AERODYNAMIC VORTEX INTERACTION WITH A FLAPPING FOIL AND BETWEEN MULTIPLE FLAPPING FOILS,

AND ITS APPLICATION TO THE DESIGN OF AERIAL AND AQUATIC SMALL VEHICLES

Interacción aerodinámica de vórtices con un perfil alar y entre dos perfiles alares batientes

y su aplicación al diseño de microvehículos aéreos y acuáticos

JAVIER ALAMINOS QUESADA

UNIVERSIDAD DE MÁLAGA

Ph.D Thesis

Ph.D Program: Mechatronic Engineering
Dpto. de Ingeniería Mecánica, Térmica y de Fluidos
Área de Mecánica de Fluidos
Escuela de Ingenierías Industriales

Universidad de Málaga

SUPERVISOR:
Dr. D. Ramón Fernández Feria

Málaga, España 2021

AUTOR: Javier Alaminos Quesada

http://orcid.org/0000-0001-5346-9273

EDITA: Publicaciones y Divulgación Científica. Universidad de Málaga

Javier Alaminos Quesada: *Aerodynamic vortex interaction with a flapping foil and between multiple flapping foils, and its application to the design of aerial and aquatic small vehicles*, Ph.D Thesis, Universidad de Málaga © 2021.

SUPERVISOR:
Dr. D. Ramón Fernández Feria

LOCATION:
Málaga, España

TIME FRAME:
2016 - 2020

You never realize what you've done; you can only see what remains to be done.
Nunca te das cuenta de lo que has hecho; sólo puedes ver lo que queda por hacer.

— Marie Curie

Dedicado a mi familia y a mi compañera de viaje.

UNIVERSIDAD
DE MÁLAGA

ANDALUCÍA TECH
Campus de Excelencia Internacional

Escuela de Doctorado

DECLARACIÓN DE AUTORÍA Y ORIGINALIDAD DE LA TESIS PRESENTADA PARA OBTENER EL TÍTULO DE DOCTOR

D./Dña JAVIER ALAMINOS QUESADA
Estudiante del programa de doctorado INGENIERÍA MECATRÓNICA de la Universidad de Málaga, autor/a de la tesis, presentada para la obtención del título de doctor por la Universidad de Málaga, titulada: INTERACCIÓN AERODINÁMICA DE VÓRTICES CON UN PERFIL ALAR Y ENTRE DOS PERFILES ALARES BATIENTES Y SU APLICACIÓN AL DISEÑO DE MICROVEHÍCULOS AÉREOS Y ACUÁTICOS.

Realizada bajo la tutorización de RAMÓN FERNÁNDEZ FERIA y dirección de RAMÓN FERNÁNDEZ FERIA (si tuviera varios directores deberá hacer constar el nombre de todos)

DECLARO QUE:

La tesis presentada es una obra original que no infringe los derechos de propiedad intelectual ni los derechos de propiedad industrial u otros, conforme al ordenamiento jurídico vigente (Real Decreto Legislativo 1/1996, de 12 de abril, por el que se aprueba el texto refundido de la Ley de Propiedad Intelectual, regularizando, aclarando y armonizando las disposiciones legales vigentes sobre la materia), modificado por la Ley 2/2019, de 1 de marzo.

Igualmente asumo, ante a la Universidad de Málaga y ante cualquier otra instancia, la responsabilidad que pudiera derivarse en caso de plagio de contenidos en la tesis presentada, conforme al ordenamiento jurídico vigente.

En Málaga, a 10 de FEBRERO de 2021

Fdo.: JAVIER ALAMINOS QUESADA

AUTORIZACIÓN

El profesor Dr. Ramón Fernández Feria Catedrático de Universidad en el departamento de Ingeniería Mecánica, Térmica y de Fluidos de la Universidad de Málaga,

CERTIFICA:

Que D. Javier Alaminos Quesada, alumno de la Universidad de Málaga, ha realizado bajo su dirección la presente tesis doctoral titulada *Interacción aerodinámica de vórtices con un perfil alar y entre dos perfiles alares batientes y su aplicación al diseño de microvehículos aéreos y acuáticos*, cumpliendo con todos los requisitos necesarios para optar al grado de Doctor Internacional, por lo que AUTORIZA SU LECTURA Y DEFENSA PÚBLICA.

Málaga, España, 2021

Dr. D. Ramón Fernández Feria

AGRADECIMIENTOS

En primer lugar quisiera mostrar mi más profundo agradecimiento a mi director de tesis, el profesor Ramón Fernández Feria, no solo por haber dirigido y tutorizado mi tesis, sino desde que comenzamos a trabajar juntos, como profesor y alumno, en el proyecto final de grado, por aquel entonces año 2014, así como en los dos proyectos finales de máster. Todo esto ha supuesto una relación académica de más de 6 años como tutor y alumno, donde siempre me ha sorprendido su habilidad para el cálculo teórico haciéndolo parecer sencillo para los demás. En teoría, con la redacción de este documento y su posterior defensa de tesis, en primera aproximación como le gusta decir a él, se pondría fin formalmente a este relación tutor-alumno, convirtiéndome así en doctor. No con ello quisiera decir, que se vaya a poner fin a esta magnífica relación que se ha forjado, porque para mí siempre será una persona de la que se puede aprender todavía más, así como una persona a la que acudir con total confianza en busca de una segunda opinión tanto en el ámbito profesional como personal, aconsejándote siempre lo mejor para tu futuro desde su punto de vista. Como se suele decir en el mundo de la investigación, ha sido y será mi padre académico.

Entre los diferentes profesores que conforman el área de Mecánica de Fluidos, de los cuales siempre he recibido su apoyo sin poner ninguna objeción a ello, quisiera mostrar un especial afecto al profesor Luis Parras Anguita, considerándolo un amigo más que un compañero de trabajo. Siempre recordaré los charlas y debates en el comedor de comercio, así como los intentos de mejora y paralelización de un código desarrollado en Matlab, haciendo que el *bicho interno* nunca duerma.

I would also like to thank Professor Jeff Eldredge of the University of California, Los Angeles, for giving me the opportunity to collaborate with him for several months. Also, for teaching me a new approach in the numerical development of a code, as well as, for including me in his group of students from the first moment.

A la Universidad de Málaga por haberme permitido llevar a cabo las simulaciones en el Centro de Supercomputación Picasso. Y al Ministerio de Ciencia, Innovación y Universidades (Proyecto DPI2016-76151-C2-1-R) por la financiación recibida durante el desarrollo de esta tesis a través de la beca FPI (BES-2017-080948).

Por último y no por ello menos importante, quisiera agradecer el incondicional apoyo de mi familia y en especial, el de mi compañera de viaje Patricia, quien ha estado y sufrido desde primera hora todo el desarrollo de esta tesis.

Por todo ello y mucho más, simplemente deciros gracias.

ABSTRACT

The dynamics of a two-dimensional vortex interacting with a flat plate at different angles of attack α is analysed using potential flow theory based on conformal mapping varying the nondimensional separation distance h/c of the upstream incoming vortex to the plate (c is the chord length of the plate) and the vortex intensity Γ_l. Transient lift forces measured in a wind tunnel are also compared with the potential theory results for a given Γ_l and several values of h/c and α. For the Reynolds number considered in the experiments (about 25 000) it is found that the potential theory predicts reasonably well the transient fluctuation in the lift force provided that the separation distance is not too close to the critical one h^*/c at which the vortex trajectory given by the potential theory bifurcates. It is found that the separation distance generating the highest induced lift is around this critical value h^*/c, which, according to the potential theory, is displaced about $-2.3(1-0.07|\Gamma_l|^{1/2})\alpha$ in relation to the zero angle of attack for the same Γ_l. Potential theory also predicts that the maximum peak of the lift fluctuation depends on α only through the relative separation $|h-h^*|/c$, and that the maximum lift is substantially larger when a clockwise vortex passes below the plate than when it passes above the plate, for the same vortex intensity Γ_l and relative separation distance. The opposite happens for a counter-clockwise vortex. This asymmetry in the maximum lift fluctuation increases slightly with $|\Gamma_l|$, approaching a ratio of almost two for large Γ_l.

On the other hand, the effect of a leading-edge vortex (LEV) on the lift, thrust and moment of a two-dimensional heaving and pitching thin airfoil is analysed within the unsteady linear potential theory. First, general expressions that take into account the effect of any set of unsteady point vortices interacting with the oscillating foil and unsteady wake are derived. Then, a simplified analysis, based on the Brown–Michael model, of the initial stages of the growing LEV from the sharp leading edge during each half-stroke is used to obtain simple expressions for its main contribution to the unsteady lift, thrust and moment. It is found that the LEV contributes to the aerodynamic forces and moment provided that a pitching motion exists, while its effect is negligible, in the present approximation, for a pure heaving motion, and for some combined pitching and heaving motions with large phase shifts which are also characterized in the present work. In particular, the effect of the LEV is found to decrease with the distance of the pivot point from the trailing edge. Further, the time-averaged lift and moment are not modified by the growing LEVs in the present approximation, and only the time-averaged thrust force is corrected, decreasing slightly in most cases in relation to the linear potential results by an amount proportional to $a_0^2k^3$ for large k , where k is the reduced frequency and a_0 is the pitching amplitude. The time-averaged input power is also modified by the LEV in the present approximation, so that the propulsion efficiency changes by both the thrust and the power, these corrections being relevant only for pivot locations behind the midchord point. Finally, the potential results modified by the LEV are compared with available experimental data.

Next, general analytical expressions are derived for the aerodynamic force and moment on a flapping flexible foil undergoing a prescribed undulatory motion in a two-dimensional, incompressible and linearized potential flow from the vortical impulse theory. It is considered a fairly broad class of foil motions, characterized by nine non-

dimensional parameters in addition to the reduced frequency. Quite simple analytical expressions are obtained in the particular case when just a chordwise flexure mode is superimposed to a pitching or heaving motion of the foil, for which the optimal conditions generating a maximum thrust force and a maximum propulsion efficiency are mapped in terms of the reduced frequency and the relative amplitude and phase shift of the deflection of the foil. These results are discussed in relation to the optimal conditions for a pitching or heaving rigid foil. The present theoretical results are compared with available numerical data for some particular undulatory motions of the flexible foil, with good agreement for small amplitudes of the oscillations and sufficiently high Reynolds number.

In order to validate the present linear theory, a numerical tool is developed to simulate the aerodynamics of a flapping rigid airfoil. The numerical scheme is developed using compact finite differences with a vorticity-streamfunction formulation in a non inertial reference frame. The present numerical tool is tested for pure heaving motions, while it remains the fine tunning for pure pitching motions, specially for high values of the Strouhal number. Thus, as a first limit of validation of the present theory, it is found that the theory becomes inaccurate for values of the Srouhal number greater than $St \simeq 0.25$ for the Reynolds number $Re = 16\,000$ and a pivot point at the quarter-chord length.

The second part of the thesis is dedicated to the aerodynamics interaction between several flapping airfoils. General expressions are derived for the aerodynamic force and moment on an arbitrary set of pitching and heaving foils from the vortical impulse theory in the limit of linearized potential, two-dimensional flow. Of special interest for studying the propulsion of some aquatic and aerial animals and small unmanned vehicles is the case of two oscillating foils in an aligned tandem configuration, for which analytical explicit expressions for the lift, thrust, and moment are obtained. In the limit of large separation distance, the expressions of a single oscillating foil for the forewing are recovered, but the hindwing is always affected by the unsteady wake of the forewing in the present inviscid model. Relatively simple expressions are obtained in the cases of two heaving foils and of two pitching foils, for which the optimal conditions generating a maximum thrust force and a maximum propulsion efficiency are mapped in terms of the nondimensional separation distance, reduced frequency, and phase shift, and discussed physically in relation to the optimal results for a single oscillating foil. The present theoretical results are compared with available experimental and numerical data, with good agreement for small amplitude of the oscillations and sufficiently high Reynolds numbers.

To conclude, the effect of prescribed flexural deflection on the propulsive performance of tandem-arranged flapping foils is analyzed using the vortex impulse formulation in the limit of two-dimensional, linear potential flow theory. Analytical expressions are given for a general configuration of tandem foils undergoing a quadratic flexural deflection coupled with heaving and pitching motions about arbitrary pitching and deflection axis, though quantitative results are focused to the cases pivoting about their leading edges. Flexural deflection may augment not only the thrust and the propulsive efficiency of the individual foils in relation to an otherwise identical rigid-foil configuration, it also modifies the wake behind the front foil, changing the wake interaction with the trailing foil and, consequently, modifying the tandem propulsive performance. The effect of the upstream wake on the thrust force of the trailing foil is analyzed using the vorticity distributions obtained analytically. Patterns of propulsive performance enhancement in both

the spacing-frequency and the spacing- phase shift planes are analyzed and discussed in relation to previous available experimental and numerical results. The present theoretical results provide some new insights for the design of small aerial or aquatic vehicles using biomimetic tandem propulsors.

RESUMEN

Se ha analizado la interacción aerodinámica de un vórtice bidimensional con una placa plana a diferentes ángulos de ataque α usando la teoría de flujo potencial, basada en un mapeado conforme variando la distancia de separación adimensional h/c de un vórtice entrante aguas arriba a la placa (c es la longitud de la cuerda de la placa) y con intensidad Γ_l. También se ha comparado la fuerza de sustentación medida en un tunel de viento con los resultados de la teoría potencial para un valor dado de Γ_l y diferentes valores de h/c y α. Para el número de Reynolds considerado (sobre 25 000) se ha encontrado que la teoría potencial predice razonablemente bien la fluctuación transitoria en la fuerza de sustentación cuando la distancia de separación no se encuentra demasiado cerca de la distancia crítica h^*/c donde la trayectoria del vórtice dada por la teoría potencial se bifurca. Se ha encontrado que la distancia de separación que genera la mayor fuerza de sustentación inducida es alrededor de la distancia crítica h^*/c, que, de acuerdo con la teoría potencial, es desplazada como $-2.3(1-0.07|\Gamma_l|^{1/2})\alpha$ en relación al ángulo de ataque cero para el mismo valor de Γ_l. La teoría potencial también predice que el pico máximo de la fluctuación de la fuerza de sustentación depende de α solo mediante la distancia relativa $|h-h^*|/c$, y que el máximo es sustancialmente mayor cuando el vórtice girando en el sentido horario pasa por debajo de la placa plana que cuando pasa por encima, para la misma intensidad del vórtice Γ_l y distancia de separación relativa. El caso opuesto ocurre para un vórtice girando en sentido antihorario. Esta asimetría en la máxima fluctuación se incrementa ligeramente con $|\Gamma_l|$, aproximándose a una proporción de casi dos para valores grandes de Γ_l.

Por otra parte, se ha analizado el efecto de un vórtice de borde de ataque (LEV) en la sustentación, propulsión y momento de un perfil aerodinámico delgado y bidimensional con un movimiento de aleteo vertical y cabeceo mediante la teoría potencial lineal transitoria. En primer lugar, se han derivado las expresiones generales que tienen en cuenta el efecto de cualquier conjunto de vórtices puntuales interactuando con el perfil aerodinámico oscilante y con su estela transitoria. A continuación, se ha usado un análisis simplificado, basado en el modelo de Brown-Michael, de las etapas iniciales del crecimiento del LEV desde el borde de ataque afilado durante cada media batida para obtener expresiones simples de su principal contribución en la sustentación, propulsión y momento transitorio. Se ha encontrado que el LEV contribuye a las fuerzas aerodinámicas y momento siempre que exista un movimiento de cabeceo, mientras que su efecto es despreciable, en la presente aproximación, para un movimiento puramente de aleteo vertical, y para algunas combinaciones de movimientos de cabeceo y aleteo vertical con grandes desfases, que también están caracterizados en el presente trabajo. En particular, se ha encontrado que el efecto del LEV decrece con la distancia del punto de pivote a partir del borde de salida de la placa. Además, la sustentación y momento promedios no son modificados por el crecimiento del LEV en la presente aproximación, y solo la fuerza de propulsión promedio es corregida, decreciendo ligeramente en la mayoría de los casos en relación a los resultados lineales potenciales por una cantidad proporcional a $a_0^2k^3$ para valores grandes de k, donde k es la frecuencia reducida y a_0 es la amplitud de cabeceo. La potencia de entrada promedio también se ve modificada por el LEV en la presente aproximación, así pues, la eficiencia propulsiva cambia tanto debido a la propulsión como a la potencia, siendo estas correcciones relevantes solamente cuando el punto

de pivote se encuentra detrás del punto medio de la placa. Finalmente, los resultados de la teoría potencial modificados por el LEV son comparados con los datos experimentales disponibles.

Por otro lado, se han derivado expresiones analíticas generales para las fuerzas aerodinámicas y momento de un perfil flexible con un movimiento ondulatorio preestablecido en un flujo bidimensional, incompresible y linealizado a partir de la teoría del impulso. Se ha considerado una variedad bastante amplía de movimientos del perfil aerodinámico, caracterizado por nueve parámetros adimensionales además de la frecuencia reducida. Se han obtenido expresiones analíticas bastante simples en el caso particular cuando solamente se considera un modo de flexión superpuesto a los movimientos de cabeceo y aleteo vertical del perfil, para el cual, se han mapeado las condiciones óptimos que generan la fuerza máxima de propulsión y la eficiencia propulsiva máxima en términos de la frecuencia reducida y de la amplitud y desfase de la deflexión del perfil. Estos resultados han sido discutidos en relación a las condiciones óptimas de un perfil rígido con movimiento de cabeceo o de aleteo vertical. Además, los presentes resultados teóricos han sido comparados con los datos numéricos disponibles para algunos movimientos particulares ondulatorios de un perfil flexible, con buena concordancia para pequeñas amplitudes de las oscilaciones y valores del número de Reynolds suficientemente altos.

Para validar los resultados teóricos se está desarrollando una herramienta numérica para simular un perfil aerodinámico batiente y rígido. El esquema numérico se ha desarrollado usando diferencias finitas compactas con una formulación basada en vorticidad-función de corriente en un plano de referencia no inercial. La presente herramienta numérica ha sido testeada con un movimiento puro vertical y solo resta poner a punto el movimiento de puro cabeceo, especialmete para valores no pequeños del número de Strouhal. Aún así, como primer límite de validez de la presente teoría, se ha encontrado que la teoría no predice los resultados numéricos para valores del número de Strouhal mayores que $St \simeq 0.25$ para un número de Reynolds $Re = 16\,000$ y un punto de pivote a un cuarto de cuerda de longitud.

La segunda parte de la tesis está dedicada a la interacción entre varios perfiles aerodinámicos batientes. Se han derivado expresiones generales para las fuerzas y momento de un conjunto arbitrario de perfiles aerodinámicos con movimientos de cabeceo y aleteo vertical a partir de la teoría del impulso en el límite de un flujo bidimensional y potencial linealizado. Para el estudio de la propulsión de algunos animales acuáticos y aéreos, y pequeños vehículos no tripulados es de especial interés el caso de dos perfiles oscilantes alineados en una configuración en tándem, para la cual se han obtenido analíticas y explícitas expresiones para la fuerza de sustentación, propulsión y momento. En el límite de una distancia de separación grande, se obtienen las expresiones de un único perfil oscilante, pero el ala trasera se ve siempre afectada por la estela transitoria del ala delantera debido al presente modelo no viscoso. Por otro lado, se han obtenido expresiones relativamente simples en los casos de dos perfiles con movimientos de aleteo vertical y movimientos de cabeceo, para los cuales se han mapeado las óptimas condiciones que generan una propulsión máxima y una eficiencia propulsiva máxima en términos de la distancia de separación adimensional, la frecuencia reducida y el desfase entre placas, discutiendo los resultados en relación a un único perfil oscilante. Por último, se han comparado los presentes resultados teóricos con los datos numéricos y experimentales disponibles, con buena concordancia para pequeñas amplitudes de las oscilaciones y valores del número de Reynolds suficienteme altos.

Para concluir, se ha analizado el efecto de una deflexión preestablecida en el rendimiento propulsivo de perfiles aerodinámicos dispuestos en una configuración en tándem usando la formulación teórica del impulso en el límite de un flujo bidimensional, lineal y potencial. Se han obtenido expresiones generales para una configuración en tándem de perfiles aerodinámicas con una deflexión cuadrática acoplada con los movimientos de aleteo vertical y cabeceo alrededor de arbitrarios ejes de deflexión y cabeceo, aunque los resultados cualitativos se han centrado en los casos de puntos de pivote fijados en los bordes de ataques. La deflexión puede aumentar no solo la propulsión y la eficiencia propulsiva de perfiles individuales en relación a uno idéntico pero rígido con la misma configuración, sino que también modifica la estela detrás del perfil delantero, cambiando la interación de la estela con el perfil trasero y, consecuéntemente, modificando el desempeño propulsivo del tándem. Se ha analizado el efecto de la estela delantera en la propulsión del ala trasera usando la distribución de vorticidad obtenida analíticamente. Consecuéntemente, se han analizado los patrones en la mejora del desempeño de la propulsión tanto en el plano separación-frecuencia como en el plano separación-desfase, y discutidos en relación con los resultados experimentales y numéricos préviamente disponibles. Finalmente, los presentes resultados teóricos proporcionan algunas ideas nuevas para el diseño de pequeños vehículos aéreos o acuáticos que utilicen propulsores consistentes en un par de alas o aletas batientes en tándem.

PUBLICATIONS

ARTICLES

Alaminos-Quesada, J. and R. Fernandez-Feria (2017). “Effect of the angle of attack on the transient lift during the interaction of a vortex with a flat plate. Potential theory and experimental results.” In: *Journal of Fluids and Structures* 74, pp. 130–141. doi: `10.1016/j.jfluidstructs.2017.07.013`.

Alaminos-Quesada, J. and R. Fernandez-Feria (2019). “Aerodynamics of Heaving and Pitching Foils in Tandem from Linear Potential Theory.” In: *AIAA Journal* 58.1, pp. 37–52. doi: `10.2514/1.J058437`.

Alaminos-Quesada, J. and R. Fernandez-Feria (2020). “Propulsion of a foil undergoing a flapping undulatory motion from the impulse theory in the linear potential limit.” In: *Journal of Fluid Mechanics* 883, A19. doi: `10.1017/jfm.2019.870`.

Alaminos-Quesada, J. and R. Fernandez-Feria (2021). “Propulsion performance of tandem flapping foils with chordwise prescribed deflection from linear potential theory.” In: *Phys. Rev. Fluids* 6 (1), p. 013102. doi: `10.1103/PhysRevFluids.6.013102`.

Fernandez-Feria, R. and J. Alaminos-Quesada (2018). “Unsteady thrust, lift and moment of a two-dimensional flapping thin airfoil in the presence of leading-edge vortices: a first approximation from linear potential theory.” In: *Journal of Fluid Mechanics* 851, pp. 344–373. doi: `10.1017/jfm.2018.505`.

CONFERENCES

Alaminos-Quesada, J. and J. Eldredge (Nov. 2019). “Vortex models for the unsteady aerodynamics of tandem foils.” In: 72^{nd} *Annual Meeting of the American Physical Society, Division of Fluid Dynamics* (Seatle, USA). Vol. 64. American Physical Society.

Alaminos-Quesada, J. and R. Fernandez-Feria (Nov. 2017). “Unsteady lift and thrust of a 2D flapping thin airfoil in the presence of additional leading edge vortices.” In: 70^{th} *Annual Meeting of the American Physical Society, Division of Fluid Dynamics* (Denver, USA). Vol. 62. American Physical Society.

Alaminos-Quesada, J. and R. Fernandez-Feria (Nov. 2018). “Linearized potential theory of flapping foils in tandem configuration.” In: 71^{st} *Annual Meeting of the American Physical Society, Division of Fluid Dynamics* (Atlanta, USA). Vol. 63. American Physical Society.

Alaminos-Quesada, J. and R. Fernandez-Feria (June 2019a). “Propulsion of flexible undulatory foils from vortical impulse theory in the limit of linearized potential flow.” In: *Fluid and Elasticity* (Málaga, Spain).

Alaminos-Quesada, J. and R. Fernandez-Feria (Mar. 2019b). “Unsteady aerodynamics of a general tandem of heaving and pitching foils from linear potential theory.” In: *Spanish Theoretical and Applied Mechanics Society* (Madrid, Spain).

CONTENTS

LIST OF FIGURES

LIST OF TABLES

1

INTRODUCTION

1.1 MOTIVATION AND OBJECTIVES

The aerodynamic interaction between a vortex and a foil has been widely modelled from two-dimensional potential flow theory based on conformal transformation to gain physical insight of some technological problems related to the blade– vortex interaction such as the enhancing of lift and propulsion (Saffman and Sheffield, 1977; Poling, Dadone, and Telionis, 1989; Streitlien, Triantafyllou, and Triantafyllou, 1996; Ford and Babinsky, 2013) or the generation of sound (Howe, 2003). Parallel blade–vortex interaction is a complex phenomena relevant for the understanding of the aerodynamic performance in general, and the unsteady loading, noise generation and vibration in particular, of a great variety of machines and engineering configurations such as helicopters, turbines, propellers, tandem wings, energy conversion systems, among others. (see, e.g. Wilder and Telionis, 1998; Rockwell, 1998; Rival, Manejev, and Tropea, 2010; Peng and Gregory, 2015).

In particular, the leading-edge vortex (LEV) has been proved to be very relevant for the generation of unsteady forces and moment on heaving and pitching airfoils, especially at relatively low Reynolds numbers, being partly responsible for the excellent aerodynamic performance of flapping wings in insects and small birds (Ellington, 1984; Dickinson and Gotz, 1993; Ellington et al., 1996; Wang, 2000; Minotti, 2002; Wang, 2005; Maxworthy, 2007; Shyy and Liu, 2007; Baik et al., 2012; Ford and Babinsky, 2013). However, the unsteady linear potential theory of Theodorsen, 1935, and Kármán and Sears, 1938, which assumes small amplitude in the airfoil oscillations, with an almost flat wake vortex sheet and no LEV generation, is surprisingly quite accurate in predicting the unsteady lift force and moment of thin flapping airfoils (McGowan et al., 2011; Baik et al., 2012; Mackowski and Williamson, 2015; Mackowski and Williamson, 2017; Cordes et al., 2017) and also the thrust force and propulsion efficiency when using the correct vortex impulse formulation (Fernandez-Feria, 2016; Fernandez-Feria, 2017). This is so even for low Reynolds number and for not so small amplitude of the oscillations, when LEV generation and shedding constitutes a relevant feature of the actual fluid motion around the airfoil. Thus, it would be of interest to explore the possibility of including the formation of weak LEVs into the linear potential theory to improve its predictive capabilities when the angle of attack is not very small.

In general, unsteady aerodynamics of flapping foils is an area of active research in part due to the recent interest in the development of small unmanned aerial and aquatic vehicles, bioinspired by flying and swimming animals. It is well known that flexible structures can enhance the propulsive performance of flapping flight and swimming (Wu, 1971b; Katz and Weihs, 1978; Prempraneerach, Hover, and Triantafyllou, 2003; Pederzani and Haj-Hariri, 2006; Heathcote and Gursul, 2007; Zhu, 2007; Alben, 2008; Kang et al., 2011; Ramananarivo, Godoy-Diana, and Thiria, 2011; Dewey et al., 2013; Moore, 2014; Huera-Huarte, 2018a) , which is supported by the fact that most flying and swimming animals take advantage of the flexibility of their flapping appendages to increase lift, thrust and/or propulsive efficiency depending on the particular circumstances of their locomotion (Wu, Brokaw, and Brennen, 1975; Lighthill, 1975; Vogel, 1981; Shyy et al., 2013). Although rigid-wing aerodynamics has been explored in more detail than flexible-wing aerodynamics (see e.g. Platzer et al., 2008), numerous experimental and numerical studies have appeared recently concerned with flexible flapping foils (see e.g. Shyy et al., 2010; Wu, 2011; Wang, He, and Zhang, 2016).

Avoiding the interesting and more complex issue of the fluid–structure interaction (Michelin and Llewellyn Smith, 2009; Dewey et al., 2013; Moore, 2014; Paraz, Schouveiler, and Eloy, 2016; Tzezana and Breuer, 2019), one of the most interesting problems is the characterization of the aerodynamic performance for prescribed kinematics of a flexible foil, which allows a search for the foil motion that maximizes thrust and/or propulsive efficiency. As in the case of a rigid flapping foil, despite the great advances in numerical simulations and experimental studies, linear unsteady potential theory still constitutes a powerful analytical tool for understanding, and estimating, the aerodynamic performance of flexible flapping foils. The theory was originally developed for two-dimensional foils undergoing an arbitrary harmonic motion by Wu and Lighthill (Wu, 1961; Lighthill, 1970; Wu, 1971a; Wu, 1971b), containing the pitching and heaving motion of a rigid foil as a particular case, which was previously studied by Theodorsen, 1935, for lift and moment, and by Garrick et al., 1936, for thrust and propulsion efficiency. Using this classical linear potential theory, the optimization problem of the propulsive performance has been addressed for the pitching and heaving oscillating motion of a rigid foil and for the more complex undulatory motion of a flexible foil by several authors (Lighthill, 1970; Wu, 1971a; Alben, 2008; Eloy and Schouveiler, 2011; Eloy, 2013; Moore, 2015; Floryan and Rowley, 2018).

Of particular relevance for addressing the problem of the unsteady aerodynamics of slender bodies at high Reynolds number is the vortical impulse theory in the limit of linearized inviscid flows, because of the insight that it provides on the effect of unsteadiness on the physics behind the aerodynamic force and moment. This approach was first utilized by Kármán and Sears, 1938, to obtain the lift force and moment on a rigid foil undergoing an arbitrary motion, and recently extended to include the thrust force and the propulsive efficiency of a pitching and heaving rigid foil (Fernandez-Feria, 2016). This latter formulation corrects, for moderate and high reduced frequencies, Garrick et al., 1936, result for the thrust force produced by a rigid oscillating foil, which was assumed to be primarily generated by the leading-edge suction. Thus, the impulse formulation substantially modifies the prediction of the kinematic conditions that optimize the propulsion efficiency of a heaving and pitching rigid foil (Fernandez-Feria, 2017), especially for high reduced frequencies.

Apart from that, within the recent interest for designing biologically inspired aerial and aquatic vehicles of flapping foils (Platzer et al., 2008; Wu, 2011), one of the most relevant strategies has been to benefit from flow interactions between flapping foils. It is well know that such interactions are exploited by the tandem wings of dragonflies to enhance lift, thrust, propulsive efficiency, or maneuverability, depending on the wing's configuration (Alexander, 1984; Azuma and Watanabe, 1988; Thomas et al., 2004; Wang and Russell, 2007; Lehmann, 2009), and also by bird flocks and fish schools to form stable aggregations that minimize energy consumption (Weihs, 1973; Bajec and Heppner, 2009). There exists a large body of numerical and experimental works that analyze the two-dimensional (2D) aerodynamic interaction between flapping foils, especially for heaving and/or pitching rigid foils (Warkentin and DeLaurier, 2007; Akhtar et al., 2007; Broering, Lian, and Henshaw, 2012; Broering and Lian, 2012; Gong, Jia, and Xi, 2015;

Gong, Jia, and Xi, 2016; Lua et al., 2016; Ortega-Casanova and Fernandez-Feria, 2016; Ramananarivo et al., 2016; Yang, Pettersen, and Xiong, 2016; Muscutt, Weymouth, and Ganapathisubramani, 2017; Newbolt, Zhang, and Ristroph, 2019; Ortega-Casanova and Fernandez-Feria, 2019). In addition, a large number of works have been published about these unsteady aerodynamic interactions between adjacent flapping foils, both to try to understand the physical mechanisms leading to the propulsion improvement and to characterize the optimal kinematics and geometric configurations generating these propulsive benefits, some of them focused on the application to the design of biomimetic aerial and aquatic vehicles. These investigations have been based on complex two-dimensional, or three-dimensional, numerical simulations of tandem flapping rigid foils in forward flight (Tuncer and Platzer, 1996; Lan and Sun, 2001; Broering and Lian, 2015; Lua et al., 2016; Ortega-Casanova and Fernandez-Feria, 2016; Muscutt et al., 2017; Lin et al., 2019; Ortega-Casanova and Fernandez-Feria, 2019; Arranz, Flores, and Garcia-Villalba, 2020), or on sophisticated experimental techniques (Thomas et al., 2004; Akhtar et al., 2007; Lua et al., 2016; Jones and Platzer, 1999; Warkentin and DeLaurier, 2007; Lehmann, 2009; Boschitsch, Dewey, and Smits, 2014; Zheng, Wu, and Tang, 2016; Ramananarivo et al., 2016; Kurt and Moored, 2018; Huera-Huarte, 2018b; Newbolt, Zhang, and Ristroph, 2019; Nagai, Fujita, and Murozono, 2019), and just a few of them making use of some theoretical, simplified approach, specially based on two-dimensional, linear potential flow theory (Bosch, 1978; Lan, 1979). On the other hand, the huge number of nondimensional geometric and kinematic parameters, as well as the computational or experimental cost of varying all of them, makes it difficult to extract from these works general trends of configurations that optimize thrust or propulsive efficiency, except for some specific kinematics and flow conditions. For this reason it is desirable to have approximate, theoretically based models that allow analyzing a wide set of configurations that generate optimal propulsion and that may help to effectively design and control air and water microvehicles with pairs of flapping foils interacting aerodynamically with each other.

1.2 THESIS OUTLINE

This document is organized in the following parts:

PART I Research relative to a single flapping foil.

- Chapter 2 analyses the interaction of a travelling vortex with a steady flat plate in terms of forces, and it is compared with experimental results provided from the wind tunnel of the Univerisdad de Málaga.
- Chapter 3 uses the vortical impulse theory to analyze the presence of leading-edge vortices of a flapping thin airfoil using a minimal model for them.
- Chapter 4 extends the vortical impulse theory to an undulatory airfoil with preescribed heaving, pitching and oscillatory deflection motion.
- Chapter 5 compares numerical results with the these from the potential theory in order to characterize its validation limit in terms of forces and efficiency for a fixed Reynolds number.

PART II Research relative to a configuration of two flapping foils.

- Chapter 6 extends the vortical impulse theory for N airfoils in tandem configuration and analyses the optimal values of the kinematic parameters in terms of thrust and propulsive efficiency for pure heaving and pitching motions of two airfoils in tandem configuration.

- Chapter 7 analyses the enhancement in thrust and efficiency when the two airfoils in tandem configuration with undergo preescribed deflections.

In the Chapter 8 is gathered all the contributions provided in this document as well as some suggestions for future works related with the thesis.

PART III Appendices.

- Appendix A provides the main functions, integrals and average coefficients for developing the formulation of one unsteady flapping airfoil.

- Appendix B presents the numerical implementation of the flapping airfoil simulation as well as the validation of the implemented code comparing with experimental and numerical results.

- Appendix C provides the main functions, integrals and average coefficients for developing the formulation of two unsteady flapping airfoils.

Part I

SINGLE FOIL

2

THE INTERACTION OF A VORTEX WITH A FLAT PLATE

2.1 INTRODUCTION

This chapter is focused on the problem of lift enhancement on a foil (a flat plate for simplicity) generated by a passing travelling vortex drifted by the stream. Particularly, it is analysed the peak intensity of the lift fluctuation in terms of the nondimensional vortex intensity Γ_l and the nondimensional upstream separation distance h/c of its centre when the angle of attack α between the plate and the incoming current is varied (c is the chord length of the plate). As demonstrated in several experimental studies, and most particularly in the recent work Peng and Gregory, 2017, significant differences in pressure and loading fluctuations may be caused by small changes in vortex trajectory, which, as it is shown here, depends strongly on the angle of attack of the target foil. Although the viscous effects are not considered, nor the possible cutting of the vortex by the plate, which are both very relevant for small separation distances (e.g. Ziada and Rockwell, 1982; Rival, Manejev, and Tropea, 2010; Peng and Gregory, 2017; Martínez-Muriel and Flores, 2020) by comparing with experimental measurements in a wind tunnel, it is shown that the most relevant features of the lift fluctuation may be captured by a two-dimensional potential theory, provided that the separation distance is not very close to the critical distance h^*/c for which the vortex trajectory bifurcates from the upper to the lower side of the foil, or vice versa. It will be shown that potential theory predicts a maximum of the lift peak at this bifurcation value of h/c, for which it is reported its dependence on α and Γ_l. When $|h - h^*|/c$ is not too small, the lift pulse predicted by the potential theory agrees reasonably well with the experimental results, allowing for a practical characterization of the peak of the lift fluctuation as a function of the nondimensional parameters. These results may be useful for explaining some features of the vortex–blade interaction found in experimental measurements and in numerical simulations, specially for a better understanding of the unsteady lift enhancement in a couple of flapping wings in a tandem configuration (e.g. Thomas et al., 2004; Ortega-Casanova and Fernandez-Feria, 2016), a problem which has motivated the present work.

2.2 POTENTIAL THEORY FORMULATION

2.2.1 *Vortex trajectory*

As a simple model for the interaction of the travelling vortex with the flat plate it is used the two-dimensional (2D) potential flow theory through the complex potential $f(z)$, where $z = x + iy$ is the complex plane of the 2D flow. It is used nondimensional variables, with lengths scaled with a quarter of the chord of the plate, $c/4$, velocities with the free stream speed U, so that time is scaled with $c/(4U)$. The plate is located in the x-axis and the free stream current forms an angle α with that axis. It is used conformal mapping from the flow on a cylinder of radius unity (that is why it is used $c/4$ as the scaling

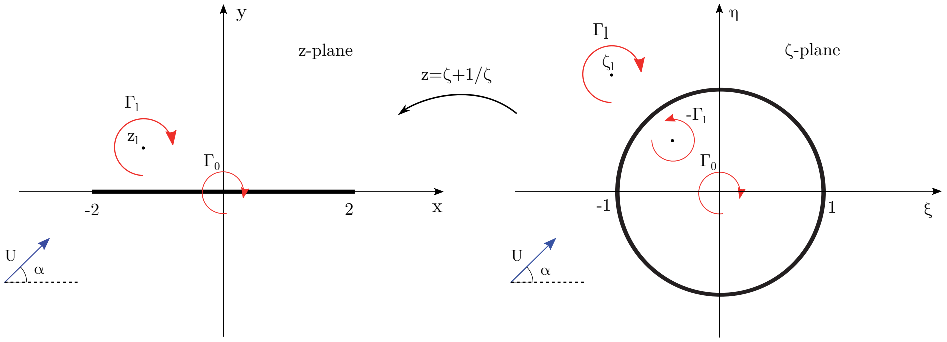

Figure 2.1: Joukowski transformation between the ζ-plane (right) and the z-plane (left). $U = 1$ in the nondimensional variables used in the text.

length) and centre at the origin of the complex plane $\zeta = \xi + i\eta$ into the complex plane $z = x + iy$ of the plate through Joukowski's transformation (see Figure 2.1.)

$$z = \zeta + \frac{1}{\zeta}. \tag{2.1}$$

It is considered the effect of a potential vortex of nondimensional circulation Γ_l (scaled with $Uc/4$) centred at $z_l = x_l + iy_l$ (Figure 2.1) at a given instant of time t. Thus, on using the circle theorem (Milne-Thomson, 1996), the nondimensional complex potential on the ζ-plane at an arbitrary instant t can be written as

$$w(\zeta) = \zeta e^{-i\alpha} + \frac{e^{i\alpha}}{\zeta} + \frac{i\Gamma_l}{2\pi} \ln\left[\frac{(\zeta - \zeta_l)\zeta}{1 - \zeta\zeta_l^*}\right], \tag{2.2}$$

where the ζ_l is the centre of the vortex in the ζ-plane, with $|\zeta_l| \geq 1$, and the asterisk superscript denotes a complex conjugate (note that, contrary to the usual notation, it is chosen $\Gamma_l > 0$ for a vortex rotating clockwise). There are two image vortices, one of strength Γ_l at the origin and another one of strength $-\Gamma_l$ at the point $\zeta = 1/\zeta_l^*$. To this potential (2.2) it is added a bound circulation centred at the origin to account for the circulation around the plate generated by the trailing-edge vortices through Kelvin circulation theorem and Kutta-Joukowski condition at the trailing-edge (see below). This bound circulation, together with the part of the vortex image centred at the origin, will be denoted by Γ_0 (nondimensional), which is the total circulation around the airfoil, so that the complex potential on the ζ-plane is written as

$$w(\zeta) = \zeta e^{-i\alpha} + \frac{e^{i\alpha}}{\zeta} + \frac{i\Gamma_0}{2\pi} \ln\zeta + \frac{i\Gamma_l}{2\pi} \ln\left[\frac{(\zeta - \zeta_l)\zeta}{1 - \zeta\zeta_l^*}\right]. \tag{2.3}$$

The nondimensional complex potential in the z-plane is $f(z) = w[\zeta(z)]$, where $\zeta(z)$ is given by the Joukowski transformation (2.1). The nondimensional velocity is given by

$$v^* = v_x - iv_y = \frac{df}{dz} = \frac{dw}{d\zeta}\frac{d\zeta}{dz} = \left[\zeta^2 e^{-i\alpha} - e^{i\alpha} + \frac{i\Gamma_0\zeta}{2\pi} + \frac{i\Gamma_l\zeta^2(1 - \zeta_l\zeta_l^*)}{2\pi(\zeta - \zeta_l)(1 - \zeta\zeta_l^*)}\right]\frac{1}{\zeta^2 - 1}. \tag{2.4}$$

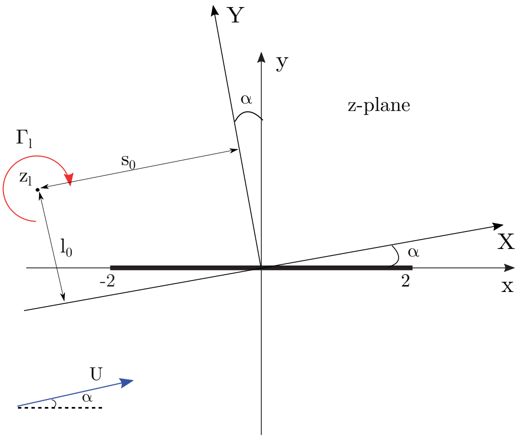

Figure 2.2: Initial position of the isolated vortex.

The bound circulation Γ_0 is obtained from the Kutta–Joukowski condition that the image of the trailing edge of the plate is a stagnation point, i.e., $dw/d\zeta = 0$ at $\zeta = 1$, yielding

$$\Gamma_0 = 4\pi \sin(\alpha) + \frac{\Gamma_l (r_l^2 - 1)}{1 + r_l^2 - 2 r_l \cos(\phi_l)} \quad \text{with} \quad \zeta_l = r_l e^{i\phi_l}, \quad r_l \geq 1. \tag{2.5}$$

With this choice, the corresponding velocity at the trailing edge of the plate, $(df/dz)^*_{z=2}$, is finite. As argued by Saffman and Sheffield, 1977, in their study for a standing vortex over a plate, only those cases where this velocity is positive should be considered as physically relevant. These authors showed that the maximum lift occurs when the trailing edge is a stagnation point. However, as recently shown experimentally by DeVoria and Mohseni, 2017, the reversed flow may describe the generation of trailing-edge vorticity that leads to lift stall, so that it is shall considered all the situations with a finite trailing- edge velocity.

The vortex with circulation Γ_l is considered as a free vortex, with its centre z_l moving with a complex velocity given by Routh's rule (Clements, 1973),

$$\frac{dz_l^*}{dt} = \frac{dx_l}{dt} - i\frac{dy_l}{dt} = \left\{ \frac{d\zeta_l^*}{dt} - \frac{i\Gamma_l}{4\pi} \left[\frac{d}{d\zeta} \ln \left(\frac{dz}{d\zeta} \right)_{\zeta=\zeta_l} \right] \right\} \left(\frac{dz}{d\zeta} \right)^{-1}, \tag{2.6}$$

with

$$\frac{d\zeta_l^*}{dt} = \lim_{\zeta \to \zeta_l} \left(\frac{dw}{d\zeta} - \frac{i\Gamma_l}{2\pi} \frac{1}{\zeta - \zeta_l} \right), \tag{2.7}$$

the complex velocity of the vortex in the ζ-plane. Initially, the isolated vortex is located far upstream, at a nondimensional distance $l_0 = 4h/c$ from the plate centre in the direction perpendicular to de free stream current, and at a nondimensional distance $s_0 = 4d/c \gg 1$ from the plate centre in the streamwise direction. Thus, the initial position of the vortex in the z-plane is (see Figure 2.2)

$$z_{l0} = x_{l0} + i y_{l0} = (-s_0 + i l_0) e^{i\alpha}. \tag{2.8}$$

The above expressions constitute a system of two ordinary differential equations for the vortex centre trajectory $[x_l(t), y_l(t)]$. It depends on the nondimensional parameters Γ_l and α, and on the initial normal distance $h/c = l_0/4$ (the upstream distance s_0 is

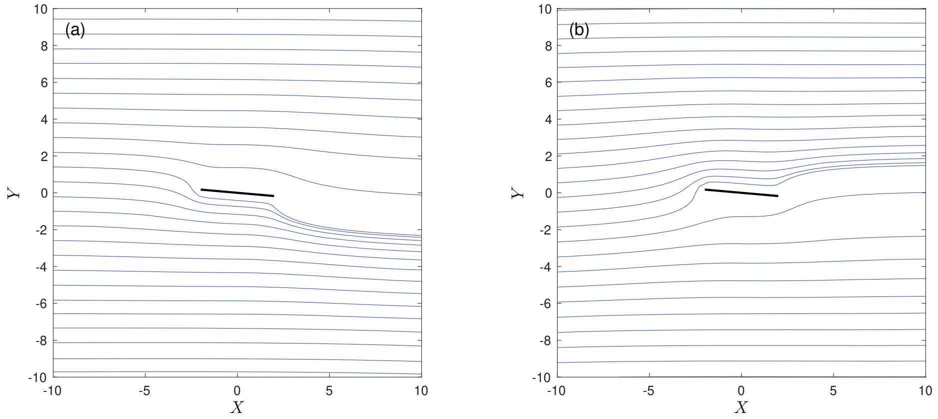

Figure 2.3: Trajectories of the vortex centre for $\alpha = 5^o$, $\Gamma_l = 3.2$ (a) and $\Gamma_l = -3.2$ (b), and for several values of h/c from -2 to 2 at intervals of $1/8$. $s_0 = 400$.

selected sufficiently large for the results to be independent of its value). These equations are integrated numerically using Matlab's ODE solver `ode15s`. Figure 2.3 shows some examples plotted in the rotated coordinates (X, Y), where the X-axis is parallel to the upstream current; i.e. (see Figure 2.2),

$$Z = X + iY = ze^{i\alpha}. \tag{2.9}$$

Note that the results are symmetrical with respect to the X-axis if one changes $\alpha \to -\alpha$, $\Gamma_l \to -\Gamma_l$ and $h/c \to -h/c$. This simplifies the mapping of the trajectories for all the values of the three parameters. An important feature observed in Figure 2.3 is that, for each Γ_l and α, there exists a critical (or bifurcation) value h^*/c such that if $h/c > h^*/c$ the vortex centre pass above the plate, and if $h/c < h^*/c$ its trajectory goes below the plate. This critical value h^*/c depends on Γ_l and α (see below). For the cases plotted in Figure 2.3 , h^*/c is slightly above zero for $\Gamma = 3.2$ and close to $-1/4$ for $\Gamma_l = -3.2$ (remember that X and Y are scaled with $c/4$).

2.2.2 *Force on the plate*

Once the trajectory is obtained, the force on the plate exerted by the flow containing the vortex can be computed as a function of time by using Blasius' theorem (Milne-Thomson, 1996). In nondimensional form, scaling forces with $\frac{1}{2}\rho U^2 c$, where ρ is the fluid density, one may write (just dividing by 2ρ the standard expression for $F_x - iF_y$, since f and z are already scaled with $Uc/4$ and $c/4$, respectively)

$$C_x - iC_y = \frac{i}{4} \oint_C \left(\frac{df}{dz} \right)^2 dz, \tag{2.10}$$

where C_x and C_y are the force coefficients in the x- and y-direction, respectively, and $\mathcal{C}$ is a contour in the z-plane tightly following the plate surface. All integrals are made in the counterclockwise direction. To evaluate the integral in (2.10) one may use Cauchy's theorem to write

$$
\begin{aligned}
\oint_{\mathcal{C}} \left(\frac{df}{dz}\right)^2 dz &= \oint_{\mathcal{C}_\infty} \left(\frac{df}{dz}\right)^2 dz - \oint_{\mathcal{C}_{\updownarrow}} \left(\frac{df}{dz}\right)^2 dz, \\
&= \oint_{\mathcal{C}'_\infty} \left(\frac{d\omega}{d\zeta}\right)^2 \left(\frac{dz}{d\zeta}\right)^{-1} d\zeta - \oint_{\mathcal{C}'_l} \left(\frac{d\omega}{d\zeta}\right)^2 \left(\frac{dz}{d\zeta}\right)^{-1} d\zeta, \qquad (2.11)
\end{aligned}
$$

where $\mathcal{C}_\infty$ (or $\mathcal{C}'_\infty$) is a contour at large distance from the origin, and $\mathcal{C}_l$ (or $\mathcal{C}'_l$) is a contour surrounding the centre of the vortex z_l (or ζ_l) at an arbitrary small radius. Writing $f(z) = f_l(z) + (i\Gamma_l/2\pi)\ln(z - z_l)$, where f_l is the regular part of f at $z = z_l$, and applying Cauchy's integral formula,

$$
\begin{aligned}
\oint_{\mathcal{C}_l} \left(\frac{df}{dz}\right)^2 dz &= \oint_{\mathcal{C}_l} \left[\left(\frac{df_l}{dz}\right)^2 + \frac{i\Gamma_l}{\pi(z - z_l)}\frac{df_l}{dz} - \frac{\Gamma_l^2}{4\pi^2(z - z_l)^2}\right] dz \\
&= 2\pi i \frac{i\Gamma_l}{\pi}\left.\frac{df_l}{dz}\right|_{z=z_l} = -2\Gamma_l \frac{dz_l^*}{dt}, \qquad (2.12)
\end{aligned}
$$

where dz^*/dt is given by (2.6). On the other hand, the first integral in the right hand side of (2.11) can be made on the path $z = Re^{i\theta}$, $0 \leq \theta \leq 2\pi$, for $R \to \infty$, resulting

$$
\oint_{\mathcal{C}'_\infty} \left(\frac{d\omega^2}{d\zeta}\right)\left(\frac{dz}{d\zeta}\right)^{-1} d\zeta = -2\Gamma_0 e^{-i\alpha}. \qquad (2.13)
$$

Thus, (2.10) becomes

$$
C_x - iC_y = -\frac{i}{2}\Gamma_0 e^{-i\alpha} + \frac{i}{2}\Gamma_l \frac{dz_l^*}{dt}. \qquad (2.14)
$$

The first term is the Kutta–Joukowski lift associated to Γ_0, a force orthogonal to the free stream current, and the second term corresponds to the force exerted by the motion of the vortex Γ_l on the plate, which has the same magnitude of the Magnus force exerted on the point vortex by the flow but with opposite sign (e.g., Zannetti and Gourjii, 2014). It is convenient to write the standard drag and lift coefficients by projecting the above force coefficients on the axes X and Y:

$$
C_D - iC_L = (C_x - iC_y)e^{i\alpha} = -\frac{i}{2}\Gamma_0 + \frac{i}{2}\Gamma_l \frac{dz_l^*}{dt} e^{i\alpha}, \qquad (2.15)
$$

so that, the drag coefficient C_D (nondimensional force component in the free stream direction X) and the lift coefficient C_L (nondimensional force component in the direction Y perpendicular to the free stream current) are given by

$$
C_D = \frac{\Gamma_l}{2}\left(\frac{dy_l}{dt}\cos\alpha - \frac{dx_l}{dt}\sin\alpha\right), \qquad (2.16)
$$

$$
C_L = \frac{\Gamma_0}{2} - \frac{\Gamma_l}{2}\left(\frac{dx_l}{dt}\cos\alpha + \frac{dy_l}{dt}\sin\alpha\right), \qquad (2.17)
$$

where Γ_0 is related to Γ_l, α and the vortex trajectory through (2.5). For $\Gamma_l = 0$ one obviously recovers the standard Kutta-Joukowski's formula, $C_L = 2\pi\sin\alpha$, and D'Alembert paradox, $C_D = 0$.

As an example, Figure 2.4 shows temporal variations of the lift coefficient C_L in terms of the horizontal coordinate of the vortex centre, $X_l(t)$, for $\Gamma_l = 3.2$, $h/c = \pm 1$, and several values of α, together with the corresponding trajectories of the vortex centre

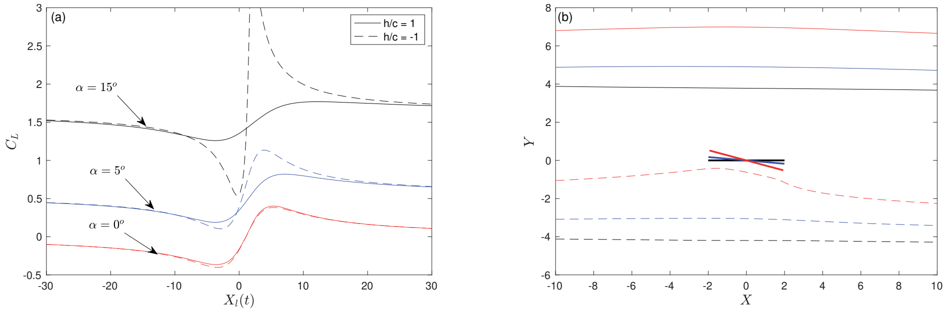

Figure 2.4: (a) C_L vs. $X_l(t)$ for $\Gamma_l = 3.2$, $h/c = \pm 1$ for three values of $\alpha \geq 0$, as indicated. (b) Corresponding trajectories of the vortex centre on the $X - Y$ plane, showing also the flat plate positions for the three values of α.

on the X-Y plane (remember that the chord-length c corresponds to four units in X or Y). In all cases the vortex-plate interaction generates a fluctuation in C_L consisting of a minimum peak when the vortex centre is closest to the leading edge $X = -2$, and a maximum peak when the vortex centre is about, or slightly downstream of, the trailing edge $X = 2$. For $\alpha = 0$, C_L obviously vanishes outside this interval of lift fluctuation, while for $\alpha > 0$ there is a circulatory lift larger than zero outside the lift pulse, increasing with α according to Kutta-Joukowski's formula. The intensity of the lift peaks is larger for h/c negative than for h/c positive, specially for the case with $\alpha = 15°$, because the vortex centre passes very close to the plate ($h/c = -1$ is near to its bifurcation value for this case, and the potential theory predicts then a quite high lift pulse for this rather large value of Γ_l). This behaviour is in qualitative agreement with recent experimental results, where a marked asymmetry is observed in the load fluctuations, with larger lift peaks when a clockwise vortex passes below the blade for similar separation distance (Peng and Gregory, 2017). In general, these lift variations are in qualitative agreement with previous numerical and experimental results (see, e.g., the similar potential results by Poling, Dadone, and Telionis, 1989, which also contains a comparison with previous experimental works). It is shall compared them with experimental results in the next section.

2.3 COMPARISON WITH EXPERIMENTAL RESULTS

Before presenting a systematic account of the results from the 2D potential theory in terms of the three nondimensional parameters, it is compared in this section some experimental data obtained in a wind tunnel with the corresponding potential flow results.

2.3.1 *Experimental setup*

The experiments were performed in a low-speed closed circuit wind tunnel with a test section of $1 \times 1\ m^2$ cross section. The tunnel is driven by four, 10-bladed fans, 15 kW each, with a maximum tunnel speed close to 50 m/s. The speed is set and controlled using a LabView code and, to ensure the uniformity of the flow in the test section, the wind tunnel is provided by honeycomb panels upstream of the flow. The tunnel is equipped with a three-components force and moment balance, with its platform in the middle of the base of the 4 m long test section. The force measurements was also controlled by the

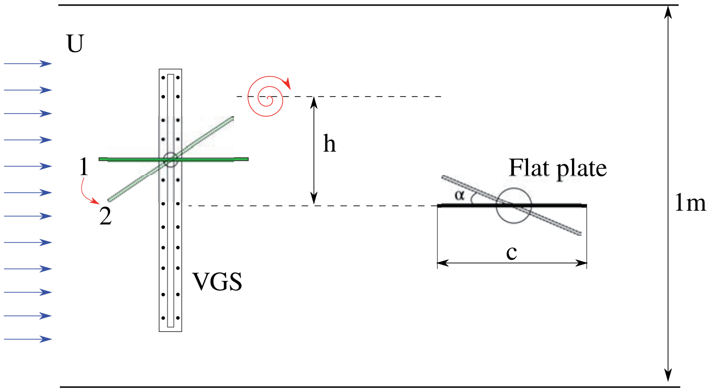

Figure 2.5: Sketch of the wind tunnel test section (top view) with the Vortex Generator System (VGS) and the flat plate with adjustable angle of attack mounted on a force and moment balance.

same LabView code. The maximum force that could be measured with the sensor in the horizontal direction was 32 N, whereas the minimum measurable force was about 0.01 N. The force sensor was calibrated previously to the series of experiments reported here using a standard dynamometer, showing a linear behaviour in the three spatial axes and an error lower than 1% for the whole measurement range. In addition, the force balance is mounted in a servomotor which allows rotations of 0.036°, providing a precise control of the angle of attack, α.

A rectangular flat plate was mounted on the platform of the force balance with adjustable angle of attack α (see Figure 2.5) . The VGS, located upstream of the flat plate, consisted of another flat plate that generated the starting vortices by a sudden pitching motion. Both plates were made of steel with 3 mm thickness, 0.98 m vertical span, and a chord length $c = 0.3$ m. The leading and trailing edges of these steel plates were both tapered on a length of about two times its thickness. The VGS was mounted on a guide on the base of the wind tunnel test section, 1 m upstream of the platform force balance, with different positions to be able to adjust the normal distance h between the vortex and the target plate. Eleven positions of the pitching axis were allowed by the guide, which generated vortices with a normal nondimensional distance h/c from their centre to the streamwise axis of the wind tunnel ranging from $-5/6$ and $5/6$, at intervals of $1/6$, approximately. This distance was measured by flow visualizations of the vortices (see Figure 2.6).

To generate isolated vortices, the flat plate of the VGS was driven by a pneumatic system very similar to that described by Peng and Gregory, 2015. The sudden pitching motion from initial position 1 to final position 2 (Figure 2.5) was actuated by an air cylinder, powered by shop air at 700 kPa through a fast valve. The amplitude and time of the sudden pitching motion was manually adjustable by the control system of the valve, as well as the returning time of the plate to its initial position. When the valve opened, the high pressure of 700 kPa was supplied to the actuator and the pitching motion of the flat plate was completed in about 0.1 s, then returning slowly to its initial position after 2 s. To generate a single vortex in this way with good enough quality, it was crucial that the time of the pitching motion was less than the time for the air to travel one chord of the

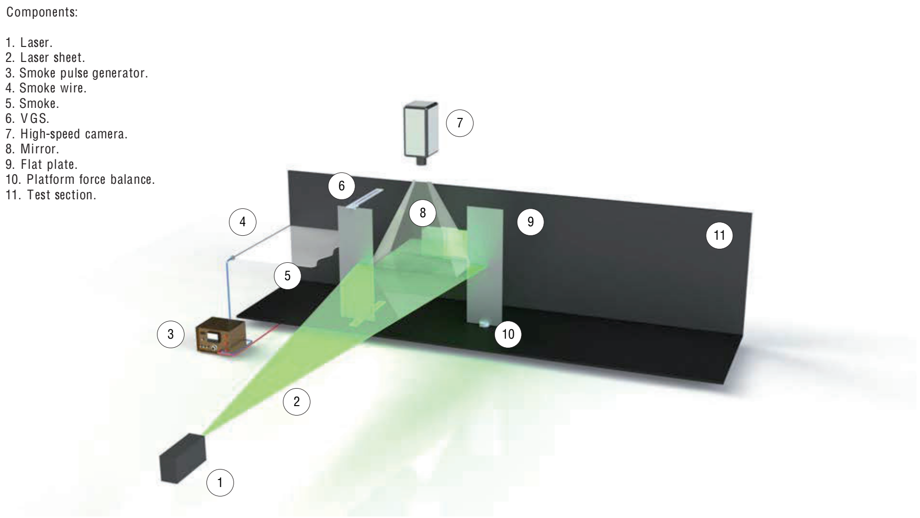

Figure 2.6: Sketch of the experimental setup with the visualization system.

pitching plate (Peng and Gregory, 2015), thus limiting the maximum free-stream velocity in the wind tunnel during the experiments to about 1.5 m/s. This quite low speed, reached by using just one fan of the wind tunnel facility, was recorded through a hot wire anemometer during the experiments, controlled by the above mentioned LabView code. Moreover, a uniform flow along the cross section is achieved due to the honeycomb panels mounted upstream of the test section, as it is mentioned above. Thus, the free stream turbulence intensity was always less than 3% for the range of velocities used in this work. This turbulence intensity was measured by taking the entire volume of the test section and using the hot wire anemometer along the cross section to take the measurements of the free-stream velocity. The selected free stream velocity in most of the reported experiments was 1.25 m/s, with a Reynolds number based on the chord length c and the free stream speed U, $Re = Uc/\nu$, where ν is the air kinematic velocity, about 23 600.

To visualize the flow it was used a smoke-wire pulse generator, a high-speed camera and a laser sheet arranged as in Figure 2.6. The smoke was generated by a 0.3 mm nicrom wire located horizontally upstream of the VGS, impregnated with a special oil (Smoke Oil 135) which was vaporized by a pulse generator (Sugawara model MS405). The pulse of 300 V and a duration of 0.3 s was synchronized manually with the sudden pitching motion of the VGS. For the laser sheet it was used a 2 W DPSS laser (Idex Optics and Photonics, model 85-GHS-301), which generated a horizontal laser sheet 0.5 m above the base of the test chamber. The high-speed camera (Phantom, model v611) was placed above the laser sheet, recording at 400 fps through the transparent glass upper wall of the wind tunnel test section. A typical visualization of a generated vortex is shown in Figure 2.7. Note that the visualization plane corresponds to the $X - Y$ plane described in §2.2.1.

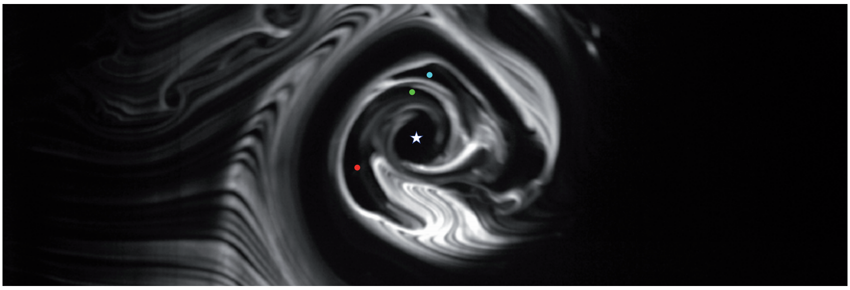

Figure 2.7: Snapshot of a vortex visualized with smoke on the X-Y plane. The vortex centre is marked with a star, and the three dots are used in the digitalized video to estimate the vortex circulation (see §2.3.3).

2.3.2 *Force measurements*

It is measured the X and Y force components (D and L) for several values of the angle of attack α of the flat plate and of the upstream distance h/c from the vortex center to the plate. The data were recorded at a rate of 1000 Hz during 5 s, enough to compute reliable averaged values of the force components at regular time intervals before the vortex reaches the plate, during the about 0.8 s that it takes to pass around the plate, and after the vortex-plate interaction. The measurement axis of the force sensor, attached to the plate, did not coincide exactly with the wind tunnel axis. Thus, to get the null angle of attack $\alpha = 0$, it was first rotated the plate around its parallel position to the wind tunnel axis and measured the force components looking for the minimum absolute force. Once the null angle of attack was thus selected, it was first measured the force components without the vortex, i.e., just with the free-stream current of the tunnel, to validate our experimental results for C_D and C_L by comparison with existing experimental data by Pelletier and Mueller, 2000, for a 2D flat plate at several angles of attack. Although the Reynolds number selected in all of our experiments, $Re \simeq 2.36 \times 10^4$, was slightly smaller than those used by these authors, Figure 2.8 shows a good agreement within the dispersion of the different experimental data. These data are used later to obtain the lift fluctuation induced by the passing vortex.

Figure 2.9 shows a typical raw measurement of $C_L(t)$ as it comes out from the force sensor, after nondimensionalization. It corresponds to an angle of attack $\alpha = 5^o$ and a vortex generated at $h/c = 1/6$. The signal contains a large amount of high frequency noise coming from structural vibrations mainly originated by the movement of the vortex generation system and transmitted through the structure of the wind tunnel to the force sensor to which the flat plate is attached. The largest peak corresponds to the fast pitching motion of the VGS to generate the vortex. It is had set $t = 0$ at the beginning of this fast motion in Figure 2.9. Then the vortex interacts with the flat plate and, after this interaction, the VGS retreats slowly to its initial position, corresponding to the last burst of noise in Figure 2.9. These two main noise fluctuations are thus outside of the interval of time of interest here. Moreover, this is a high frequency noise, much higher than the frequency corresponding to the pulse in the force originated by the physical interaction

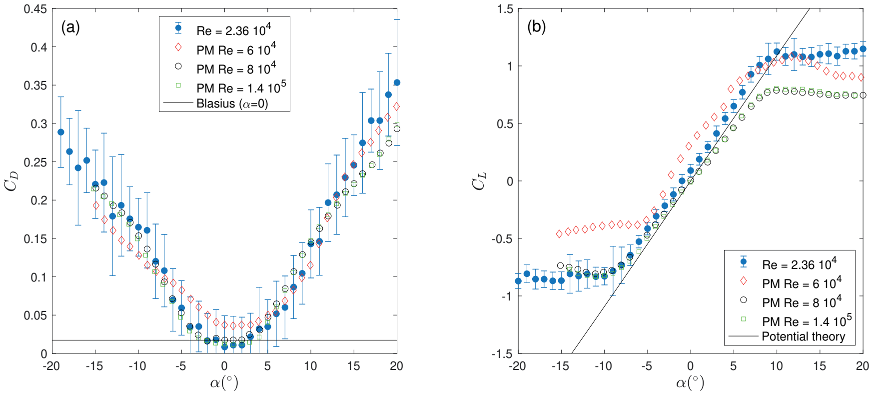

Figure 2.8: Time-averaged values of C_D (a) and C_L (b) vs. α for a free stream with $Re = 2.36 \times 104$ compared with experimental results by Pelletier and Mueller, 2000, at different Reynolds numbers (indicated in the legend after PM). As a reference, it is also plotted Blasius' boundary layer result $C_D = 2.656 Re^{-1/2} \simeq 0.0173$ in (a), and the potential lift coefficient $C_L = 2\pi \sin\alpha$ in (b).

n	1	2	3	4	5	6	7	8
$b_n \cdot 10^{-12}$	0.220	1.540	4.621	7.702	7.702	4.621	1.540	0.220
a_n	1	-6.8588	20.1629	-32.9315	32.2740	-18.9790	6.2009	-0.8683

Table 1: Low pass Butterworth digital filter coefficients of 7th order with a cut-off frequency of $f_c = 5\ Hz$.

of the vortex with the plate, so that it can be easily filtered.

In fact, by analyzing the power spectrum of the signal [see Figure 2.10(a)], one finds that there is a peak between 1 and 2 Hz, corresponding to the physical interaction between the vortex and the plate. Next, there is a higher peak at about 35 Hz, corresponding to the main structural noise, and then smaller peaks at higher frequencies (53.5 Hz is the following one). Thus, the frequency of the force fluctuations is well differentiated, by more than 30 Hz, from the main noise, and its signal can be easily filtered using a cut-off frequency. In this case, it is used a low pass Butterworth digital filter of 7th order with a cut-off frequency of $f_c = 5\ Hz$ [see Figure 2.10(b)], where its transfer function can be written as

$$H(z) = \frac{b_1 + b_2 \cdot z^{-1} + \ldots + b_{n+1} \cdot z^{-n}}{1 + a_2 \cdot z^{-1} + \ldots + a_{n+1} \cdot z^{-n}}, \tag{2.18}$$

with the coefficients a_n and b_n given by the Table 1. This is corroborated by actuating the vortex system and measuring in the absence of flow. It is found that the signal is similar to that in Figure 2.9, but with negligible low frequency fluctuations associated to the physical interaction between the vortex and the plate. The filtered signal (dashed red line in Figure 2.9) is sufficiently smooth and shows the main features of the physical interaction of the vortex with the plate described in section above (enclosed within an ellipse in the figure), but followed by smaller fluctuations due to the vortex shedding

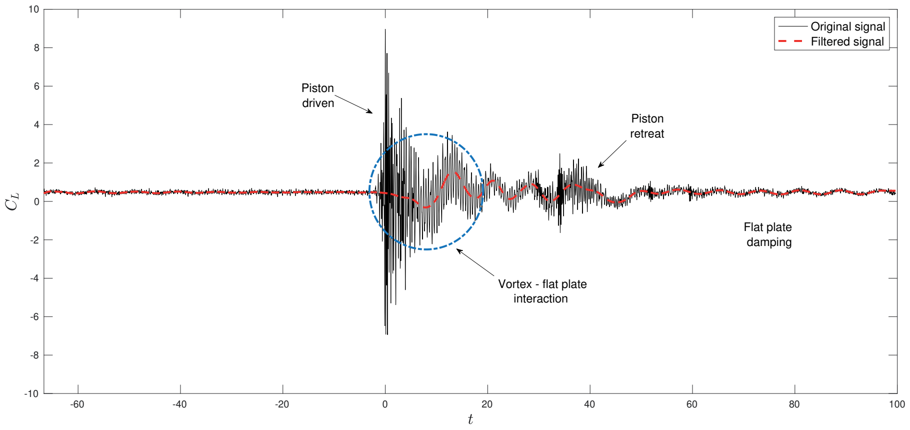

Figure 2.9: C_L vs. nondimensional time t for $\alpha = 5^\circ$ and a vortex generated at $h/c = 1/6$. The dashed red line corresponds to the filtered signal, as discussed in the text.

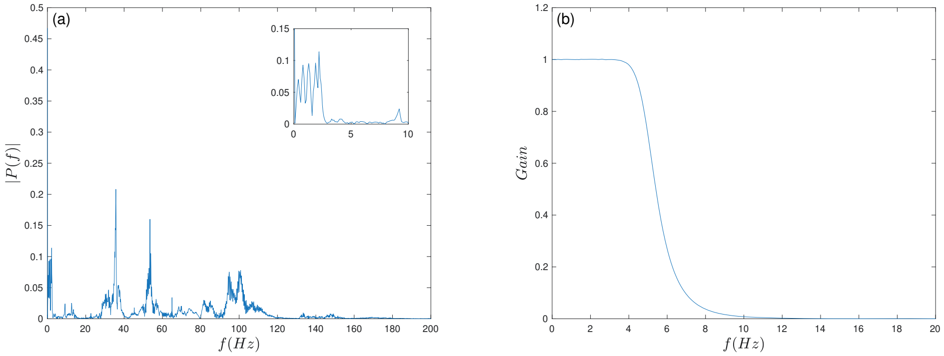

Figure 2.10: (a) Power spectrum of the original signal for the lift coefficient with $\alpha = 5^\circ$ and $h/c = 1/6$. (b) Low pass filter used to filter the original measured signal from the force sensor.

from the plate. The overall fluctuations in C_L are qualitatively similar to those measured by Booth Jr, 1990, for a NACA 0012 airfoil.

2.3.3 *Vortex circulation*

To compare the experimental results with the potential theory it was also needed an estimation of the circulation of the vortex generated experimentally. Obviously, the vortex coming out from the VGS is not a potential vortex, since it has a viscous core where the circumferential velocity grows from zero at the centre to a maximum value, and then decays outside the vortex core. This decay approximately behaves as r^{-1}, where r is the distance to the vortex centre, like in a potential vortex. It was used this fact to estimate the circulation corresponding to the equivalent potential vortex by fitting the vortex decay to $v_\theta = \widehat{\Gamma}_l/(2\pi r)$, where $\widehat{\Gamma}_l$ is the dimensional circulation.

To that end it was used the flow visualization of the vortices, and processed the digitalized video-images with several functions implemented in the software package Matlab.

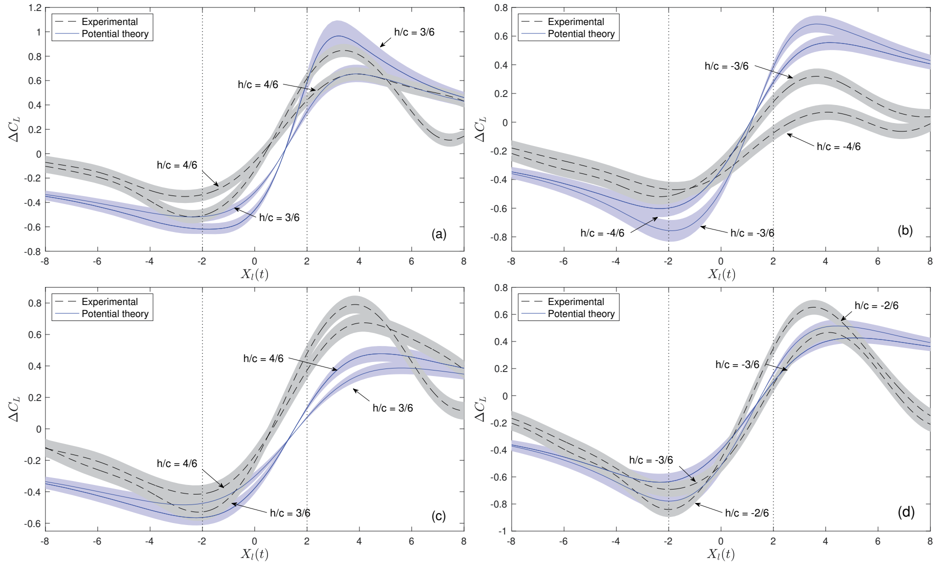

Figure 2.11: ΔC_L vs. the position $X_l(t)$ of the vortex centre for $\Gamma_l \simeq +3.3$ obtained experimentally (dashed lines) and from the potential theory (continuous lines) for $\alpha = 0$, [(a) and (b)], $\alpha = 5°$ (c), and $\alpha = -5°$ (d), for several values of h/c, as indicated in each case. The 'bands' along the curves account for the experimental uncertainty in Γ_l (theoretical curves), and the force measurements (experimental curves).

It was first identified the centre of the vortex and chosen three other points outside the vortex core (see example in Figure 2.7). For that, firstly it is binarized the images provided by the high speed camera, and then it is changed the black colors by white colors, i.e., it is obtained the complement image. In this way, one can follow the motion of the core and the external areas of the vortex marked with a star and three dots respectively, in the Figure 2.7. To choose the external areas in the complement binarized image, one must focus on areas close enough to the core of vortex, but outside of it, and large enough bigger that they can be tracked in time to compute the circumferential velocities. So, following the evolution in time of these four points from the digitalized video-images, it was computed their circumferential velocities as $v_\theta = r\Delta\theta/\Delta t$. It was checked that $v_\theta r$ remained approximately constant for the three selected points (i.e., that they were outside the vortex core) and, from the mean value of this constant, the circulation $\widehat{\Gamma}_l$ was computed. It was made this operation for several vortex visualizations, all with the same wind tunnel speed $U = 1.25$ m/s and the same pitching motion of the VGS used in all the reported experiments, and found that $\widehat{\Gamma}_l = 0.31 \pm 0.03$ m^2/s; i.e., $\Gamma_l = 3.3 \pm 0.3$. It was also computed the radius of the viscous core of the vortex as the value of r where the circumferential velocity reached a maximum, obtaining $r_c \sim 2.13$ cm.

2.3.4 *Comparison with potential lift*

Figure 2.11 compares the evolution of the lift coefficient obtained experimentally with the theoretical one computed from the potential theory for several values of α and h/c with $\Gamma_l = +3.3 \pm 0.3$. Actually it is plotted the contribution to C_L of the traveling vortex,

$$\Delta C_L(t; \alpha, h/c, \Gamma_l) = C_L(t; \alpha, h/c, \Gamma_l) - C_{L_0}(\alpha), \tag{2.19}$$

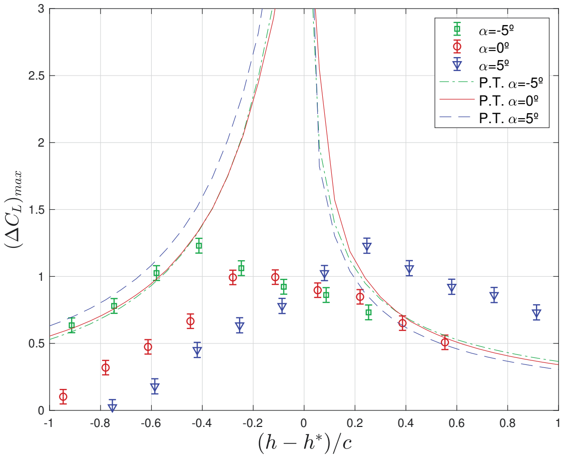

Figure 2.12: $(\Delta C_L)_{max}$ vs. $(h-h^*)/c$ for several values of α, as indicated, obtained experimentally (symbols) and from the potential theory (lines, PT in the legend).

where $C_{L_0}(\alpha)$ is the mean lift coefficient without the vortex, obtained either experimentally or from the potential theory in each case (see Figure 2.8). It is used the nondimensional position $X_l(t)$ of the centre of the vortex as it travels around the plate (as in Figure 2.8), instead of the nondimensional time t. Note that, for $\alpha = 0$, the plate is located between $X = -2$ and $X = 2$, marked in the figure for reference sake. In all cases $h/c > 0$ and the vortex, with clockwise rotation, passes above the plate.

As the vortex approaches the plate, the lift first decreases owing to the downward flow of the clockwise rotation of the vortex, and then increases due to the suction from the vortex core above the plate. This last main peak in the lift fluctuation may reach values near unity in some cases. In general, potential theory predicts reasonably well these two peaks of ΔC_L, both in intensity and separation, when $|\alpha|$ is sufficiently small and $|h/c|$ is sufficiently large, such as the cases plotted in Figure 2.11. When $|\alpha|$ is larger than about 10^o, for any value of $|h/c|$ used in the present experiments, or for $|h/c|$ smaller than about $1/3$ for any α, it is found that the agreement between the potential theory and the experimental results becomes poorer. The discrepancies are mainly due to two effects neglected in the the inviscid potential theory: viscous effects and the possibility that the vortex may be sectioned by the plate, both very relevant when the vortex core interacts directly with the plate (e.g., Ziada and Rockwell, 1982; Peng and Gregory, 2017). In addition, the present potential theory does not model the subsequent lift fluctuations with smaller amplitude caused by the vortex shedding from the trailing edge.

To better identify the ranges of the parameters α and h/c for which a reasonable good agreement exists between potential theory and experimental results, Figure 2.12 compares the maximum lift peak generated by the vortex as a function of the relative separation distance $(h-h^*)/c$ for several values of the angle of attack, where h^*/c is the bifurcation separation given by the potential theory. If $|\alpha|$ is sufficiently small, the theory predicts reasonably well the peak intensity of the lift when $(h-h^*)/c \gtrsim 0.25$, and when $(h-h^*)/c \lesssim -0.3$ if $\alpha < 0$. This is explained by the viscous interaction between the vortex core and the leading edge of the plate, which, for a given $|h|/c$, is more relevant as

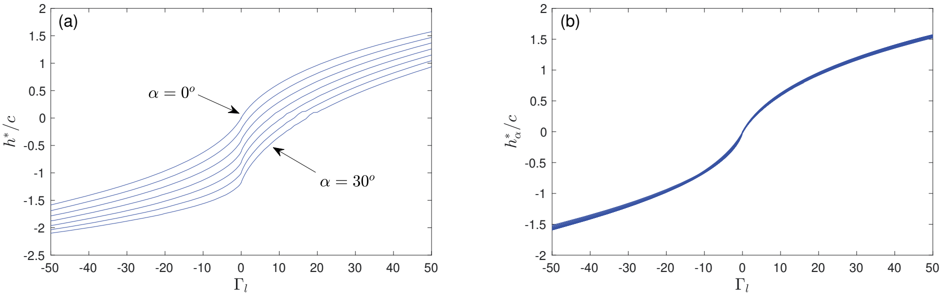

Figure 2.13: (a) h^*/c vs. Γ_l for $\alpha = 0^o, 5^o, ..., 30^o$. (b) The same curves but plotting $h^*_\alpha/c := h^*/c + 2.2858(1 - 0.07|\Gamma_l|^{1/2})\,\alpha$ vs. Γ_l.

$|\alpha|$ increases. In addition, for a clockwise vortex ($\Gamma_l > 0$), the viscous interaction between the vortex core and the blade is more relevant when the vortex passes below the plate ($h < h^*$), as already found experimentally by Peng and Gregory, 2017. This accounts for the larger variation in the experimental lift and the poorer performance of the potential theory when $h < h^*$. However, the bifurcation value h^*/c given by the potential theory provides a good estimation of the separation h/c for which the maximum peak of the lift fluctuation is reached for each Γ_l and α. Therefore, it is of practical interest to characterize h^*/c as a function of Γ_l and α for two reasons: to estimate the separation distance h/c for which the maximum lift peak is generated, and to obtain a rough idea of the range of validity of the potential theory for predicting the intensity of this peak, namely when $|h - h^*|/c$ is larger than about 0.25. This is done in the next section.

2.4 CHARACTERIZATION OF VORTEX LIFT ENHANCEMENT FROM POTENTIAL THEORY

Figure 2.13(a) shows the bifurcation distance h^*/c as a function of Γ_l for several values of $\alpha \geq 0$. The curves for different values of α approximately collapse into just one curve when plotting

$$\frac{h^*_\alpha}{c} := \frac{h^*}{c} + 2.2858(1 - 0.07|\Gamma_l|^{1/2})\,\alpha, \tag{2.20}$$

against Γ_l [Figure 2.13(b)], so that the effect of the angle of attack, for a given vortex intensity Γ_l, is to displace the separation distance h/c at which the maximum lift fluctuation is generated by an amount proportional to $-\alpha$ and almost independent of Γ_l. Note that, the equation (2.20) is obtained by doing a pure fit of the surface $\frac{h^*}{c}(\Gamma_l, \alpha)$.

The re-scaled separation h^*_α is thus only a function of Γ_l. For $|\Gamma_l| \lesssim 1$ it behaves approximately as $\Gamma_l/8$, but then saturates for large $|\Gamma_l|$. Calling this function $G(\Gamma_l)$, one may then write

$$\frac{h^*}{c} \simeq -2.2858(1 - 0.07|\Gamma_l|^{1/2})\,\alpha + G(\Gamma_l), \tag{2.21}$$

with $G(\Gamma_l)$ given by Figure 2.13(b).

As already observed in Figure 2.12, the dependence of the theoretical lift peak $(\Delta C_L)_{max}$ with the angle of attack practically disappears if one uses $(h - h^*)/c$ instead of h/c; i.e., α affects the magnitude of the lift fluctuation only through the separation h/c relative to its bifurcation value h^*/c, which depends on α as (2.21). Further, one may re-scale both $(\Delta C_L)_{max}$ and $(h - h^*)/c$ in such a way that all the theoretical results for the lift

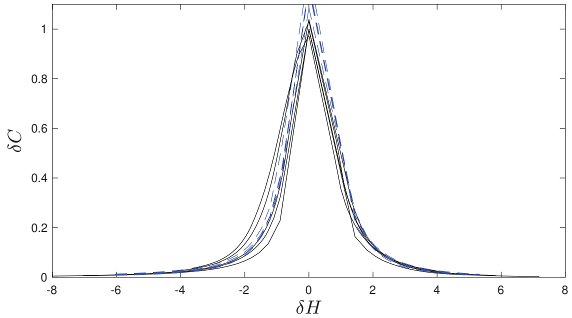

Figure 2.14: δC vs. δH, defined in (2.22)-(2.23), for $\Gamma_l = 0.1, 0.5.1, 5, 10$ with $\alpha = 0$ (continuous lines) and for $\alpha = -10^o, -5^o, 0^o, 5^o, 10^o$ when $\Gamma_l = 1$ (dased lines).

peak approximately collapse into a single curve for any Γ_l and any α. This is shown in Figure 2.14, where the peak lift is scaled as

$$\delta C := \frac{(\Delta C_L)_{max}}{2.6\sqrt{|\Gamma_l|}}, \tag{2.22}$$

while the relative separation distance δH is given by (for $\Gamma_l > 0$)

$$\delta H := \begin{cases} -\dfrac{2.7}{\Gamma_l^{0.22}} \left(\dfrac{h^* - h}{c}\right)^{1/2} & \text{for} \quad h < h^*, \\ \dfrac{3.1}{\Gamma_l^{0.13}} \left(\dfrac{h - h^*}{c}\right)^{1/3} & \text{for} \quad h > h^*. \end{cases} \tag{2.23}$$

(For $\Gamma_l < 0$ one has to substitute Γ_l for $|\Gamma_l|$ and interchange the expressions for $h < h^*$ and $h > h^*$.) All the curves in Figure 2.14 can be approximated by

$$\delta C \simeq \exp(-|\delta H|). \tag{2.24}$$

A noteworthy feature is that the scaling in δH is quite different for positive and for negative values of $h - h^*$, showing the asymmetry already mentioned of the lift enhancement, depending on whether the vortex passes above or below the foil. For positive Γ_l (clockwise vortex), the lift peak is larger when the vortex passes behind the plate, and the contrary happens when Γ_l is negative. This prediction of the present potential analysis, which qualitatively agrees with recent experimental results by Peng and Gregory, 2017, is quantified by the scaling (2.23). Thus, for a given value of the relative separation, $|h - h^*|/c = b$ (say), the corresponding values of $(\Delta C_L)_{max}$ are (for $\Gamma_l > 0$)

$$(\Delta C_L)_{max} = \begin{cases} 2.6\sqrt{\Gamma_l}\exp\left[-\dfrac{2.7}{\Gamma_l^{0.22}} b^{1/2}\right] & \text{for} \quad h < h^*, \\ 2.6\sqrt{\Gamma_l}\exp\left[-\dfrac{3.1}{\Gamma_l^{0.13}} b^{1/3}\right] & \text{for} \quad h > h^*. \end{cases} \tag{2.25}$$

As commented on above, experimental data can be approximated by the present theoretical potential results when b is about 0.25 or larger. Therefore, the above expression with $b = 0.25$ provides an estimation of the maximum of the lift fluctuations as a function of the nondimensional parameters α, Γ_l and h/c, for a (clockwise) vortex passing above, or below, the plate. For instance, for $\Gamma_l = 1$, putting $b = 0.25$ in (2.25) yields

$(\Delta C_L)_{max} \simeq 0.36$ for $h > h^*$, and $(\Delta C_L)_{max} \simeq 0.67$ for $h < h^*$; i.e., the maximum lift peak is almost twice when the clockwise vortex passes behind the plate. This ratio augments slightly as Γ_l increases, being practically 2 for large Γ_l. However, the ratio is independent of α, provided that $|h - h^*|/c$ remains the same, because the dependence of the lift enhancement with the angle of attach comes from the bifurcation value h^*/c.

2.5 CONCLUDING REMARKS

In the present chapter it is found that, although viscous effects are very relevant in the close encounter of a vortex with a flat plate, some interesting features of the lift fluctuation generated by this interaction may be derived from a relatively simple two-dimensional potential theory based on a conformal transformation. For instance, the maximum lift enhancement is approximately reached at the critical separation given by the potential theory where the vortex trajectory bifurcates from passing above to below the plate. This critical separation behaves almost linearly with the angle of attack α, and the peak of the lift depends on α only through the relative separation of the vortex to its critical value. It is also provide simple scaling laws which may be useful to estimate the intensity of the lift fluctuation in terms of the vortex circulation Γ_l and its relative separation distance $(h - h^*)/c$, showing a marked asymmetry when the vortex passes above or below the plate, depending on the sign of Γ_l, for the same $|h - h^*|/c$.

3

THE PRESENCE OF LEADING-EDGE VORTICES OF A FLAPPING THIN AIRFOIL

3.1 INTRODUCTION

In this chapter, it is analysed the interaction of arbitrary travelling point vortices with a heaving and pitching foil within the framework of the unsteady linear potential theory, and obtain general expressions for their contributions to the lift, thrust and moment on the foil by using a vortical impulse formulation (Kármán and Sears, 1938; Wu, 1981; Fernandez-Feria, 2016). To that end, it is solved the integral equation for the vortex-sheet strength of the bound vortex sheet around the foil which takes into account the effect of the point vortices in addition to the free wake vortex sheet. The resulting expressions for the forces and moment contain additional integral terms that depend on the temporal evolution of the point vortices and that, in general, have to be solved numerically.

As a difference with some previous related works, it is maintained the continuous trailing vortex wake of the linearized potential theory and add the generation of an LEV during each half-stroke as a point vortex, instead of considering the generation and shedding of both LEV and LEV as a succession of point vortices. For instance, Tchieu and Leonard, 2011, used a vortex theory formulation quite similar to the present one, but considering the trailing wake as a succession of point vortices instead of the continuous distribution of Kármán and Sears, 1938, and without considering the effect of the LEV, to obtain the lift force and moment of an unsteady thin airfoil. Ramesh et al., 2013, extended this approach to large amplitudes, combining the vortex formulation with standard potential theory. Xia and Mohseni, 2013, employed conformal mapping and the unsteady Blasius equation to model the force on a pitching flat plate by considering the effect of the LEV and TEV as successive point vortices emanating from their respective edges. These authors validated their results against experiments for the starting plate problem and for a non-sinusoidal pitching motion for which our oscillating model is not valid. The starting plate problem, or Wagner problem, was also analysed by Li and Wu, 2015, in the presence of additional LEV/TEV using a vortical impulse formulation very similar to that developed here. These authors, who only computed the lift force, considered an unsteady developing TEV instead of the long-time infinite trailing vortex wake of an oscillating plate considered here. However, as discussed below in §3.3, the general expression for the lift force of a point vortex in terms of the temporal evolution of its circulation and its position, as derived in more detail by Li and Wu, 2015, is equivalent to the general expression developed here. The results for the Wagner problem were generalized by the same authors (Li and Wu, 2016) to account for high angles of attack, and for the residual vortex sheet at both the leading and trailing edges, representing vortices being shed yet not represented by point vortices. A similar general vortex force formulation, without the thin-airfoil assumption, and considering the vortex shedding from a general-shaped airfoil with non-sharp leading edge, was more recently considered by Xia and Mohseni, 2017.

To simplify the problem and be able to obtain closed approximate expressions for the forces and moment, it is introduced several approximations. First, it is assumed that the

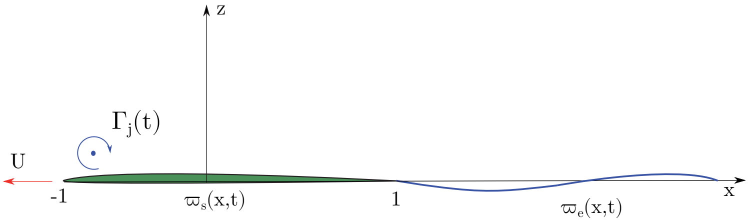

Figure 3.1: Schematic of the problem.

vortices remain sufficiently close to the foil, in accordance with the linearized approximation, and that the thin airfoil has a sharp leading edge, in addition to a sharp trailing edge (as in a flat plate). Then, knowing that the main contribution to the forces and moment is produced while the LEV is still developing close to the leading edge (Pullin and Wang, 2004; Martín-Alcántara, Fernandez-Feria, and Sanmiguel-Rojas, 2015), it is considered only the effect of a single developing LEV during each half-stroke, up to the point where it is shed. The last assumption constitutes a strong simplification of the problem, both because all the other already shed LEV are not taken into account and because the effect of the growing LEV on the wake vorticity is negligible. As a consequence, closed simple expressions for the contribution of the LEV to the forces and moment on the flapping foil can be obtained, constituting a lowest-order correction to the analytical results of the linearized potential theory when the LEV is included in the formulation.

To model the developing LEV, it is assumed that vorticity is released at the sharp leading edge, with an unsteady Kutta condition to remove the singularity of the bound vortex-sheet strength at the leading edge, similar to the condition applied at the sharp trailing edge where the free wake vortex sheet is released. Then, it is used the Brown and Michael, 1954, which ensures momentum conservation (Michelin and Llewellyn Smith, 2009) and assumes that the vortex is shed when its circulation reaches an extremum value to avoid discontinuities in temporal forces. More realistic models for the growing and shedding of the vortices could have been used (Tchieu and Leonard, 2011; Wang and Eldredge, 2013; Hemati, Eldredge, and Speyer, 2014), but they need additional parameters and equations that would complicate the formulation. The present approximation is in accordance with the simplicity of the linear potential theory, providing closed-form expressions for the contributions of the LEV to the lift, thrust and moment that depend only on flapping kinematics parameters. These results are compared with available experimental data for slender airfoils with small-to-medium maximum angle of attack.

3.2 FORMULATION OF THE PROBLEM

It is considered the two-dimensional (2D), incompressible and nearly-inviscid flow over a heaving and pitching thin airfoil of chord length c that moves with constant speed U along the negative $x-$axis (see Figure 3.1). The vertical amplitudes of the heaving and pitching motions are both very small compared to c so that the airfoil and every point of the trail of vortices which it leaves behind may be considered to be upon the $x-$axis in first approximation. In addition to the continuous wake, it is shall considered the effect of individual concentrated (point) vortices generated at the leading edge and moving downstream (only one such vortex is depicted in the sketch of Figure 3.1). For simplicity it is selected $c = 2$, so that all the lengths are scaled with the half-chord $c/2$ and the plate,

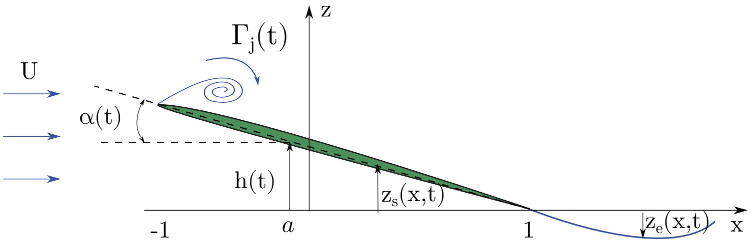

Figure 3.2: Schematic of the oscillating airfoil with a LEV.

or slender airfoil with two sharp ends, extends from $x = -1$ to $x = 1$ in a reference frame translating with it at speed U along the $x-$axis and the non-dimensional time t is scaled with $c/(2U)$. In this reference frame the motion of the airfoil is given by the vertical displacement of its mean-camber line (see sketch in Figure 3.2):

$$z_s(x,t) = h(t) - (x-a)\alpha(t), \quad -1 \le x \le 1, \tag{3.1}$$

with

$$h(t) = \Re\left[h_0 e^{ikt}\right], \quad \alpha(t) = \Re\left[\alpha_0 e^{ikt}\right], \tag{3.2}$$

and

$$k := \frac{\omega c}{2U}, \tag{3.3}$$

where k is the reduced frequency associated with the frequency ω of the harmonic motion, with non-dimensional period $\mathrm{T} = 2\pi/k$, which consists of a heaving motion, $h(t)$, and a pitching rotation $\alpha(t)$ around the horizontal axis $x = a$ [i.e., the dimensional pivoting distance from the leading-edge is $s_p = (1+a)c/2$], and $\Re$ means real part. The amplitudes h_0 and α_0 are in general complex constants (to account for any phase shift between both oscillations) satisfying $|h_0| \ll 1$ and $|\alpha_0| \ll 1$. For simplicity it is selected h_0 real and

$$\alpha_0 := a_0 e^{i\phi}, \tag{3.4}$$

with ϕ the phase shift between the plunging and pitching motions and a_0 the maximum pitching amplitude. In what follows it is shall worked with the complex functions knowing that it is had to take the real part of the results. The non-dimensional vertical velocity of the rigid airfoil is

$$v_0(x,t) = \frac{\partial z_s}{\partial t} + \frac{\partial z_s}{\partial x} = \dot{h} - (x-a)\dot{\alpha} - \alpha, \tag{3.5}$$

where a dot denotes the time derivative.

3.2.1 *General expressions for the lift, thrust, moment and input power*

The vortical impulse theory for an incompressible and unbounded flow is used to obtain the forces and moment on the airfoil. Neglecting the volume (section) of the airfoil, one may write (Wu, 1981; Saffman, 1992; Wu, Ma, and Zhou, 2006)

$$\mathbf{F} := D\mathbf{e}_x + L\mathbf{e}_z = -\rho\frac{d\mathbf{I}}{dt}, \tag{3.6}$$

where D is the drag (or minus the thrust) force, L is the lift force, ρ the fluid density, and the vortical impulse (or vorticity moment) $\mathbf{I}$ is defined as

$$\mathbf{I} := \int_{\mathcal{V}} \mathbf{x} \wedge \boldsymbol{\omega} d\mathcal{V}, \tag{3.7}$$

where $\boldsymbol{\omega} = \nabla \wedge \mathbf{v}$ is the vorticity field and $\mathcal{V}$ is the entire volume (plane in this case) occupied by the fluid plus the airfoil. In writing (3.6) it is assumed that $\mathcal{V}$ is unbounded and that the flow is potential far from the airfoil. In fact, it is shall assumed that the vorticity, which is directed along the normal $\mathbf{e}_y$ to the plane of the fluid motion, is concentrated at the airfoil surface, at the trailing wake, both considered as vortex sheets, and at the locations $[x_j(t), z_j(t)]$, $j = 1, ..., N$, of the N point vortices (e.g., LEV) present in the flow at each instant of time. Thus,

$$\mathbf{I} \simeq \sum_{j=1}^{N} \Gamma_j \left(-z_j \mathbf{e}_x + x_j \mathbf{e}_z\right) + \int_{-1}^{1} \left(-z_s \varpi_s \mathbf{e}_x + x \varpi_s \mathbf{e}_z\right) dx + \int_{1}^{\infty} \left(-z_e \varpi_e \mathbf{e}_x + x \varpi_e \mathbf{e}_z\right) dx, \tag{3.8}$$

where Γ_j is the circulation (positive clockwise) of the jth point vortex, $\varpi_s(x,t)$, $-1 \leq x \leq 1$, is the vorticity density distribution on the airfoil, $\varpi_e(x,t)$ is the vorticity density distribution in the trailing wake, and $z_e(x,t)$ is the vertical position of each point in this vortex wake. It is considered the large-time behavior in which the vortex wake sheet extends many chord lengths downstream of the airfoil, so that, in first approximation, $1 \leq x \leq \infty$ for both $\varpi_e(x,t)$ and $z_e(x,t)$, with $|z_e| \ll 1$ as commented on above. Also, although the following derivations will be for arbitrary locations of the point vortices (x_j, z_j), it is shall simplified them afterwards retaining only the lowest order approximations for $|z_j| \ll 1$ to be consistent with the present linearized approach.

Consequently, under the assumptions made, the drag (or minus the thrust) and lift forces on the airfoil are given by

$$D = \rho \sum_{j=1}^{N} \frac{d}{dt}(z_j \Gamma_j) + \rho \frac{d}{dt} \int_{-1}^{1} z_s \varpi_s dx + \rho \frac{d}{dt} \int_{1}^{\infty} z_e \varpi_e dx, \tag{3.9}$$

$$L = -\rho \sum_{j=1}^{N} \frac{d}{dt}(x_j \Gamma_j) - \rho \frac{d}{dt} \int_{-1}^{1} x \varpi_s dx - \rho \frac{d}{dt} \int_{1}^{\infty} x \varpi_e dx. \tag{3.10}$$

Similarly, the vortical impulse theory also provides the moment on the airfoil (Wu, 1981; Saffman, 1992; Wu, Ma, and Zhou, 2006):

$$\mathbf{M} = -M \mathbf{e}_y := -\rho \frac{d\mathbf{A}}{dt}, \tag{3.11}$$

where

$$\mathbf{A} := -\frac{1}{2} \int_{\mathcal{V}} |\mathbf{x} - a \mathbf{e}_x|^2 d\mathcal{V}, \tag{3.12}$$

is the angular impulse in relation to the pitching axis $x = a$ moving with speed U along the $x-$axis (note that the distance Ut is also scaled with $c/2$). Thus,

$$M \simeq \frac{1}{2} \rho \frac{d}{dt} \left[\sum_{j=1}^{N} (x_j - a)^2 \Gamma_j + \int_{-1}^{1} (x - a)^2 \varpi_s dx + \int_{1}^{\infty} (x - a)^2 \varpi_e dx \right], \tag{3.13}$$

Without considering the effect of the individual point vortices Γ_j, the lift and moment were computed by von Kármán and Sears, 1938, using similar expressions to (3.10) and (3.13), while the thrust/drag was recently computed using (3.9) in Fernandez-Feria, 2016.

Reference to these works will be made for some particular results needed in the following computations. It should be noted that the general expressions (3.6) and (3.11) were derived by Wu, 1981, for any unsteady vorticity distribution in an incompressible flow, including unsteady point vortices. They have already been used for a distribution of unsteady point vortices by Tchieu and Leonard, 2011, and Li and Wu, 2015, among others, in similar problems, and (3.6) has also been used for unsteady point vortices to estimate forces from experimental data by Graham, Ford, and Babinsky, 2017.

Finally, the input power are given by

$$P = \rho \int_{-1}^{1} \Delta p \frac{\partial z_s}{\partial t} dx, \tag{3.14}$$

where $\Delta p(x,t) := p_+(x,t) - p_-(x,t)$ is the local pressure difference between both sides of the foil, with subscripts $+$ and $-$ denoting its upper and lower surfaces, respectively. Pressure difference Δp can be obtained from the unsteady Bernoulli equation on the foil surface as

$$\Delta p = -\rho \frac{\partial}{\partial t}(\Delta\Phi) - \frac{1}{2}\rho(u_+^2 - u_-^2), \tag{3.15}$$

where Φ is the velocity potential and u the tangential velocity component. Taking into account that

$$\Delta\Phi = \int_{-1}^{x} (u_+ - u_-) dx, \quad \varpi_s = u_+ - u_-, \quad U \simeq \frac{1}{2}(u_+ + u_-), \tag{3.16}$$

and substituting into (3.14), the input power can be written in terms of the vorticity distribution as

$$P = -\rho U \int_{-1}^{1} \varpi_s \frac{\partial z_s}{\partial t} dx - \rho \int_{-1}^{1} \left(\int_{-1}^{x} \frac{\partial \varpi_s}{\partial t} d\xi \right) \frac{\partial z_s}{\partial t} dx, \tag{3.17}$$

which, after integrating by parts the double integral, can be more conveniently written as

$$P = -\rho U \int_{-1}^{1} \varpi_s \frac{\partial z_s}{\partial t} dx - \rho \int_{-1}^{1} \left(\int_{x}^{1} \frac{\partial z_s}{\partial t} d\xi \right) \frac{\partial \varpi_s}{\partial t} dx. \tag{3.18}$$

3.2.2 *Vorticity distribution*

Following von Kármán and Sears, 1938, and invoking the linearity of the problem it is separated the contributions of the vortex sheet wake and the N point vortices to ϖ_s from the bound circulation that would be produced by the motion of the airfoil as if the wake and the point vortices had no effect:

$$\varpi_s(x,t) = \varpi_0(x,t) + \varpi_{se}(x,t) + \sum_{j=1}^{N} \varpi_{sj}(x,t), \quad -1 \leq x \leq 1, \tag{3.19}$$

with

$$\Gamma_0 = \int_{-1}^{1} \varpi_0(x,t) dx, \tag{3.20}$$

being the circulation that would be obtained from the quasy-steady airfoil theory, without moving vortices nor unsteady wake, such that the corresponding lift would be $\rho U \Gamma_0$. The vorticity density ϖ_{se} is the contribution to ϖ_s induced by the wake vortex-sheet strength ϖ_e, and ϖ_{sj} is the contribution from the point vortex j. Kelvin's total-circulation conservation theorem requires that

$$\Gamma_0 + \Gamma_{se} + \sum_{j=1}^{N} (\Gamma_j + \Gamma_{sj}) + \int_1^\infty \varpi_e dx = 0, \tag{3.21}$$

with

$$\Gamma_{se}(t) = \int_{-1}^{1} \varpi_{se}(x,t)dx \quad \text{and} \quad \Gamma_{sj}(t) = \int_{-1}^{1} \varpi_{sj}(x,t)dx. \tag{3.22}$$

To obtain ϖ_0, ϖ_{se} and ϖ_{sj} one has to apply de boundary condition of the vertical velocity (3.5) at $z = 0$, $-1 \leq x \leq 1$, induced by the whole distribution of vorticity. For that, the conjugate velocity, in its integral form given by a point $z = x + i0$ in the fluid field, is given by

$$v^* = u_0 - iv_0 = 1 - \frac{i}{2\pi}\int_{-1}^{1} \frac{\varpi_s(\xi,t)}{\xi - x} d\xi - \frac{i}{2\pi}\int_{1}^{\infty} \frac{\varpi_e(\xi,t)}{\xi - x} d\xi + \sum_{j=1}^{N} \frac{i\Gamma_j}{2\pi} \frac{x - x_j(t)}{[x - x_j(t)]^2 + z_j(t)^2}. \tag{3.23}$$

As the integral related to ϖ_s is singular in the point $\xi = x$, the principal value of Cauchy has to be apply to avoid the singularity, i.e.,

$$\int_{-1}^{1} \frac{\varpi_s(\xi,t)}{\xi - x} d\xi = \fint_{-1}^{1} \frac{\varpi_s(\xi,t)}{\xi - x} d\xi \pm i\pi\varpi_s(x,t), \tag{3.24}$$

where $\fint$ denotes Cauchy's principal value of the integral (Butkov and Sposito, 1969). So, replacing it in (3.23) and taking the vertical component of the velocity,

$$v_0 - \frac{1}{2\pi}\int_{1}^{\infty} \frac{\varpi_e(\xi,t)}{\xi - x} d\xi + \sum_{j=1}^{N} \frac{\Gamma_j(t)}{2\pi} \frac{x - x_j(t)}{[x - x_j(t)]^2 + z_j(t)^2} = \frac{1}{2\pi}\fint_{-1}^{1} \frac{\varpi_s(\xi,t)}{\xi - x} d\xi. \tag{3.25}$$

In addition, invoking the linearity of the problem and with the decomposition (3.19), the equation (3.25) can be decomposed into the following integral equations

$$v_0(x,t) = \frac{1}{2\pi}\fint_{-1}^{1} \frac{\varpi_0(\xi,t)}{\xi - x} d\xi, \tag{3.26}$$

$$-\frac{1}{2\pi}\int_{1}^{\infty} \frac{\varpi_e(\xi,t)}{\xi - x} d\xi = \frac{1}{2\pi}\fint_{-1}^{1} \frac{\varpi_{se}(\xi,t)}{\xi - x} d\xi, \tag{3.27}$$

$$\sum_{j=1}^{N} \frac{\Gamma_j(t)}{2\pi} \frac{x - x_j(t)}{[x - x_j(t)]^2 + z_j(t)^2} = \frac{1}{2\pi}\sum_{j=1}^{N}\fint_{-1}^{1} \frac{\varpi_{sj}(\xi,t)}{\xi - x} d\xi. \tag{3.28}$$

The solutions of these singular and linear integral equations of the first kind with constant integration limits are given by (Polyanin, 1998)

$$\varpi_0(x,t) = \sqrt{\frac{1-x}{1+x}}\left[\frac{\Gamma_0(t)}{\pi} + (1+2x)\dot{\alpha}(t)\right], \tag{3.29}$$

$$\varpi_{se}(x,t) = \frac{1}{\pi}\sqrt{\frac{1-x}{1+x}}\int_{1}^{\infty}\sqrt{\frac{\xi+1}{\xi-1}}\frac{\varpi_e(\xi,t)}{\xi - x} d\xi, \tag{3.30}$$

$$\varpi_{sj}(x,t) = -\frac{\Gamma_j(t)}{\pi^2}\sqrt{\frac{1-x}{1+x}}\fint_{-1}^{1}\sqrt{\frac{1+\xi}{1-\xi}}\frac{1}{\xi - x}\frac{\xi - x_j(t)}{[\xi - x_j(t)]^2 + z_j(t)^2} d\xi, \tag{3.31}$$

where the regularity of ϖ_s at its corresponding trailing edge $x = 1$, or Kutta condition, has been applied (for easy reference, in the Appendix A one can see solutions of these kind of integral equations for different cases). Thus, the general expression for the vorticity distribution on the airfoil is obtained by substituting (3.29), (3.30) and (3.31) into (3.19)

$$\varpi_s(x,t) = \sqrt{\frac{1-x}{1+x}}\left[\frac{\Gamma_0(t)}{\pi} + (1+2x)\dot{\alpha}(t) + \frac{1}{\pi}\int_1^\infty \sqrt{\frac{\xi+1}{\xi-1}}\frac{\varpi_e(\xi,t)}{\xi-x}d\xi - \right.$$
$$\left. \sum_{j=1}^{N}\frac{\Gamma_j(t)}{\pi^2}\fint_{-1}^{1}\sqrt{\frac{1+\xi}{1-\xi}}\frac{1}{\xi-x}\frac{\xi-x_j(t)}{[\xi-x_j(t)]^2+z_j(t)^2}d\xi,\right]. \qquad (3.32)$$

Note that, one can obtain the same solution for ϖ_s if it is solved directly the integral equation (3.25) but by this way, one can identify the different components of ϖ_s more easily. It should be noted that this bound vortex-sheet strength is singular at the leading edge $x = -1$. However, it will be applied in §3.4.1 the Kutta condition at the leading edge while a LEV (Γ_1, say) is developing, so that ϖ_s will be also regular at $x = -1$ during the fraction of the half stroke that the LEV is growing from the leading edge. On the other hand, substituting into (3.20) and (3.22) one obtains

$$\Gamma_0(t) = 2\pi\left[\alpha(t) - \dot{h}(t) + \left(\frac{1}{2} - a\right)\dot{\alpha}(t)\right] := G_0 e^{ikt}, \qquad (3.33)$$

$$\Gamma_{se}(t) = \int_1^\infty \left(\sqrt{\frac{\xi+1}{\xi-1}} - 1\right)\varpi_e(\xi,t)d\xi, \qquad (3.34)$$

$$\Gamma_{sj}(t) = C_j(t)\Gamma_j(t), \quad \text{with} \quad C_j(t) = -\frac{1}{\pi}\fint_{-1}^{1}\sqrt{\frac{1+\xi}{1-\xi}}\frac{\xi-x_j(t)}{[\xi-x_j(t)]^2+z_j(t)^2}d\xi, \qquad (3.35)$$

and the Kelvin's total-circulation conservation theorem reduces to

$$\Gamma_0(t) + \sum_{j=1}^{N}\Gamma_j(t)[1+C_j(t)] + \int_1^\infty \sqrt{\frac{\xi+1}{\xi-1}}\varpi_e(\xi,t)dx = 0. \qquad (3.36)$$

This equation provides an integral equation for the trailing edge vortex-sheet strength ϖ_e in terms of the quasisteady circulation $\Gamma_0(t)$, given by (3.33) as a function of the foil motion, and the circulation $\Gamma_j(t)$ and trajectory $[x_j(t), z_j(t)]$ of each point vortex present in the flow, which have to be modelled independently (see §3.4 below). Thus, equations (3.32) and (3.36) suffice to obtain general expressions for the lift, thrust and moment on the foil in terms of the foil motion, $\Gamma_j(t)$ and $[x_j(t), z_j(t)]$, $j = 1, ..., N$, which are derived next.

On the other hand, to compute the temporal derivatives of terms containing ϖ_e and z_e one asumes that the vorticity in the wake is convected downstream with velocity $U = 1$, so that, both remain constant in a reference frame moving with the fluid (Kármán and Sears, 1938; Newman, 1977):

$$\varpi_e(\xi,t) = \varpi_e(X), \quad z_e(\xi,t) = z_e(X), \quad \text{with} \quad X = \xi - t. \qquad (3.37)$$

Consequently, the time derivatives of the terms containing the wake vorticity ϖ_e may be easily computed on using Leibniz's rule

$$\frac{d}{dt}\int_a^b f(\xi,t)d\xi = \int_a^b \frac{\partial f(\xi,t)}{\partial t}d\xi + \frac{db}{dt}f(b,t) - \frac{da}{dt}f(a,t), \qquad (3.38)$$

which particularized for this case

$$\frac{d}{dt}\int_a^\infty f(\xi)\varpi_e(\xi,t)d\xi = \int_{a-t}^\infty \frac{\partial}{\partial t} f(X+t)\varpi_e(X)dX - \frac{d(a-t)}{dt} f(a)\varpi_e(a-t)$$
$$= \int_a^\infty \frac{df}{d\xi}\varpi_e(\xi,t)d\xi + f(a)\varpi_e(a,t). \qquad (3.39)$$

3.3 FORCE AND MOMENT FOR ARBITRARY MOVEMENTS OF THE POINT VORTICES AND FOIL

Before simplifying the above expressions for the oscillatory motion (3.1)-(3.2) of the airfoil and before implementing models for the generation and evolution of the leading edge vortices in each stroke of the airfoil, it is instructive to write the general expressions for the forces and moment within the present linearized approximation. Taking into account the circulation conservation (3.36) and the integrals given in Appendix A, one gets the following expression for the Lift (3.10) but now in non-dimensional form:

$$C_L = \frac{L}{\frac{1}{2}\rho U^2 c} = C_{L0} + C_{L1} + C_{L2} + \sum_{j=1}^{N} C_{LIj}, \qquad (3.40)$$

where

$$C_{L0} = \Gamma_0, \quad C_{L1} = -\frac{d}{dt}\int_{-1}^{1} x\varpi_0(x,t)dx, \quad C_{L2} = \int_1^\infty \frac{\varpi_e(\xi,t)}{\sqrt{\xi^2-1}}d\xi, \qquad (3.41)$$

are the quasisteady lift, the apparent mass lift and the unsteady wake lift, respectively, obtained by von Kármán and Sears, 1938, and the contribution from each jth point vortex is

$$C_{LIj} = \Gamma_j(1+C_j) - \frac{d}{dt}\left[\Gamma_j(x_j+D_j)\right], \qquad (3.42)$$

with D_j is defined by (A.42) in Appendix A. This last expression coincides with that derived by Li and Wu, 2015, for point vortices when D_j is interpreted as the x coordinate of the image of the vortex j inside the foil. With this proviso, although obtained from a quite different approach it also agrees with the results by Xia and Mohseni, 2013, under the constant circulation assumption, with the vortices contributing to the force through vortex convection (including the image vortices) and vortex variation. The first term of (3.42) is basically the Kutta-Joukowski theorem applied to the circulation Γ_j of the individual vortex itself plus its induced circulation $\Gamma_{sj}(t) = \Gamma_j(t)C_j(t)$ around the foil. The second term is the unsteady contribution to the lift force due to the motion of the vortex and its variation in intensity, including the induced vorticity on the foil. It says that positive lift on the airfoil is generated if $\Gamma_j(t)x_j(t)$ decreases in time, as it happens, for instance, at the initial stages of the formation of the LEV at the beginning of each downstroke, when the LEV starts moving upstream of the leading edge ($x_j(t) \leq -1$, see §3.4.1 below for the details) with its circulation $\Gamma_j(t)$ growing in time. The opposite happens in the initial stages of the formation of the LEV during the beginning of the upstroke, where $\Gamma_j(t) < 0$ and decreases (remember that it is used $\Gamma > 0$ for a clockwise vortex), moving also upstream of the leading edge. When Γ_j is constant the expression coincides with the well known vortex force produced by a free vortex (Saffman, 1992; Alaminos-Quesada and Fernandez-Feria, 2017). If the free vortex (Γ_j independent of time) is far away from the foil ($x_j^2 + z_j^2 \to \infty$), and therefore moving with the free stream velocity, $dx_j/dt = 1$, one has that $C_{LIj} \to 0$ since both C_j and D_j tend to zero with the distance to the foil. Incidentally, this is the reason why it can be disregarded the effect on the lift force of the starting vortex at infinity in the present impulse formulation.

The lift expression (3.40) can be rewritten in a more convenient form by grouping together C_{L0} and the first term in C_{Lli} after using the total circulation conservation (3.36):

$$C_L = C_{La} + C_{Le} + \sum_{j=1}^{N} C_{Lj}, \tag{3.43}$$

where $C_{La} := C_{L1}$ is the added mass term given in (3.41), and the net contributions from the wake and each point vortex j are, respectively,

$$C_{Le} = -\int_1^\infty \frac{\xi \varpi_e(\xi, t)}{\sqrt{\xi^2 - 1}} d\xi, \tag{3.44}$$

$$C_{Lj} = -\frac{d}{dt}\left[\Gamma_j (x_j + D_j)\right]. \tag{3.45}$$

Note, however, that the effect of the point vortices on the wake vorticity distribution ϖ_e has to be obtained from (3.36).

In the case of the drag, it is assumed that the vertical displacement of the wake, z_e, coincides with the trailing edge location at the time $t' = t + (1 - \xi)/U$ when it was shed from the airfoil, i.e., $z_s(x = 1, t') = z_e(\xi = 1, t')$. Thus, using the Leibniz's rule given by (3.39), the time derivatives related to the vertical displacement of the wake z_e reduces to

$$\frac{d}{dt}\int_1^\infty z_e(\xi, t)\varpi_e(\xi, t) d\xi = \left[h(t) - (1 - a)\alpha(t)\right] \varpi_e(\xi = 1, t). \tag{3.46}$$

So, using (3.36) and (3.40), the thrust, $T = -D$, in non-dimensional form, can be written as

$$C_T = \frac{T}{\frac{1}{2}\rho U^2 c} = -\alpha C_L + C_{T1} + C_{T2} + \sum_{j=1}^{N} C_{Tlj}, \tag{3.47}$$

where

$$C_{T1} = \dot{\alpha}\int_{-1}^{1} x \varpi_0(x, t) dx, \tag{3.48}$$

$$C_{T2} = \int_1^\infty \left[\dot{h} - \alpha + \dot{\alpha}\left(\sqrt{\xi^2 - 1} - \xi + a\right)\right] \varpi_e(\xi, t) d\xi, \tag{3.49}$$

$$C_{Tlj} = \frac{d}{dt}\left\{\Gamma_j \left[h + (a - x_j)\alpha - z_j\right]\right\} + \dot{\alpha}\Gamma_j (x_j + D_j). \tag{3.50}$$

The first term in (3.47) is the component in the flight direction of the force normal to the airfoil, with C_L given by (3.40). The second and third terms are the contributions to the thrust from the apparent mass and from the vorticity distribution in the wake, respectively, already obtained in Fernandez-Feria, 2016, while the fourth term is the contribution from the point vortices. Note that the length in the first term of (3.50), $h + (a - x_j)\alpha - z_j$, is minus the vertical position of the point vortex in relation to the plate, $z_s(x_j) - z_j$, if $-1 \le x_j \le 1$.

Part of the contribution from the vortex j is actually included in the first term of (3.47) (inside C_L). Thus, it is convenient to use (3.43) and rewrite the thrust in a similar fashion to the lift (3.43),

$$C_T = C_{Ta} + C_{Te} + \sum_{j=1}^{N} C_{Tj}, \tag{3.51}$$

where

$$C_{Ta} = -\alpha C_{La} + C_{T1} = \frac{d}{dt}\left[\alpha \int_{-1}^{1} x\varpi_0(x,t)dx\right], \tag{3.52}$$

is the added mass thrust,

$$C_{Te} = -\alpha C_{Le} + C_{T2} = \int_{1}^{\infty}\left[\dot{h} + \dot{\alpha}\left(\sqrt{\xi^2-1} - \xi + a\right) - \alpha\left(1 + \frac{\xi}{\sqrt{\xi^2-1}}\right)\right]\varpi_e(\xi,t)d\xi, \tag{3.53}$$

is the contribution from the unsteady wake, and

$$C_{Tj} = \frac{d}{dt}\left\{\Gamma_j\left[z_s(x_j) - z_j + \alpha\left(x_j + D_j\right)\right]\right\}, \tag{3.54}$$

is the contribution from the point vortex j [note that there is an additional contribution of the point vortices in ϖ_e through the total circulation conservation (3.36)]. For a free vortex (Γ_j constant), C_{Tj} is proportional to minus the temporal variation of the vertical distance of the vortex to the plate, plus a similar contribution coming from the induced vorticity on the plate whose vertical distance is represented by $-\alpha D_j$. In general, this term C_{Tj} contributes to positive thrust when $-\Gamma_j z_j$ increases, so that the formation of the LEV generates negative thrust at the initial stages of both the downstroke and the upstroke (see §3.5 below for more details).

For the moment, using the above expressions and some integrals from Appendix A, the moment (3.13) in non-dimensional form can be written as

$$C_M = \frac{M}{\frac{1}{2}\rho U^2 c^2} = \frac{a}{2}C_L + C_{M0} + C_{M1} + C_{M2} + \sum_{j=1}^{N} C_{Mlj}, \tag{3.55}$$

where

$$C_{M0} = -\frac{1}{2}\int_{-1}^{1} x\varpi_0(x,t)dx, \quad C_{M1} = \frac{1}{4}\frac{d}{dt}\int_{-1}^{1}\left(x^2 - \frac{1}{2}\right)\varpi_0(x,t)dx, \quad C_{M2} = \frac{C_{L2}}{4}, \tag{3.56}$$

are the quasy-steady moment, apparent mass moment and the contribution of the wake respectively, obtained by von Kármán and Sears, 1938, and the contribution from each jth point vortex is

$$C_{Mlj} = \frac{1}{4}\frac{d}{dt}\left[\Gamma_j\left(x_j^2 + E_j - \frac{1}{2}\right)\right] - \frac{\Gamma_j}{2}\left(x_j + D_j\right), \tag{3.57}$$

where E_j is defined by (A.43) in Appendix A. As the case of the thrust, part of the contribution from the vortex j is actually included in the first term of (3.55) (inside C_L). Thus, it is convenient rewrite the moment in a fashion to the lift (3.43) and the thrust (3.51)

$$C_M = C_{Ma} + C_{Me} + \sum_{j=1}^{N} C_{Mj}, \tag{3.58}$$

where

$$C_{Ma} = \frac{1}{4}\frac{d}{dt}\int_{-1}^{1}\left(x^2 - 2ax - \frac{1}{2}\right)\varpi_0(x,t)dx - \frac{1}{2}\int_{-1}^{1} x\varpi_0(x,t)dx, \tag{3.59}$$

$$C_{Me} = \frac{1}{4}\int_{1}^{\infty}\frac{1-2a\xi}{\sqrt{\xi^2-1}}\varpi_e(\xi,t)d\xi, \tag{3.60}$$

$$C_{Mj} = \frac{1}{4}\frac{d}{dt}\left\{\Gamma_j\left[x_j^2 + E_j - \frac{1}{2} - 2a(x_j + D_j)\right]\right\}, \tag{3.61}$$

are the contribution from the added mass, the contribution from the unsteady wake and the contribution from the point vortex j, respectively.

Finally, the input power (3.18) in non-dimensional form is given by

$$C_P = \frac{P}{\frac{1}{2}\rho U^3 c} = -\dot{h}(t)C_L - 2\dot{\alpha}(t)C_M. \tag{3.62}$$

3.3.1 *Propulsive efficiency*

Of particular interest in forward flight flapping aerodynamics is the time-average propulsion efficiency. The propulsive efficiency is defined as the ratio between the time-averaged power output of the airfoil (thrust force multiplied by the forward speed U) and the time-averaged input power required to drive the airfoil:

$$\eta = \frac{\overline{C}_T}{\overline{C}_P}, \tag{3.63}$$

where the time-averaged quantities are defined as

$$\overline{C}_T := \frac{1}{\mathrm{T}}\int_t^{t+\mathrm{T}} C_T(t)dt, \quad \overline{C}_P := \frac{1}{\mathrm{T}}\int_t^{t+\mathrm{T}} C_P(t)dt, \tag{3.64}$$

where $\mathrm{T} = 2\pi/k$ is the time period of the oscillation.

3.4 EVOLUTION OF THE POINT VORTICES, INCLUDING THE DEVELOPING LEV

3.4.1 *General model*

In the above general expressions, the contribution of each point vortex j to the lift, thrust and moment on the airfoil depends on time through the vortex intensity $\Gamma_j(t)$ and its trajectory $[x_j(t), z_j(t)]$. Part of this dependence is inside the integrals $C_j[x_j(t), z_j(t)]$, $D_j[x_j(t), z_j(t)]$ and $E_j[x_j(t), z_j(t)]$ defined in (3.35), (A.42) and (A.43), respectively. In addition, the wake vorticity ϖ_e is also affected by the evolution of this point vortex j through Kelvin's theorem (3.36). Therefore, one needs three additional equations for each point vortex to obtain $\Gamma_j(t)$, $x_j(t)$, and $z_j(t)$, which have to be solve together with the integral equation (3.36) for $\varpi_e(x,t)$, with $\Gamma_0(t)$ given by (3.33).

As a first simplification to the problem it is assumed that, during each half-stroke, there is only one developing LEV, labeled by $j = 1$. The remaining vortices, $j = 2, ..., N$, have already been shed, so that they move with the Kirchhoff velocity and their intensities are frozen (Tchieu and Leonard, 2011; Wang and Eldredge, 2013):

$$\frac{d\Gamma_j}{dt} = 0, \quad \frac{dx_j}{dt} - i\frac{dz_j}{dt} = \mathsf{v}^*[\mathsf{z}_j(t)], \quad j = 2, 3, ..., N, \tag{3.65}$$

where $\mathsf{z}_j = x_j + iz_j$ is the position of the point vortex j on the complex plane and v^* are given by (3.23) but now evaluated in the poin vortex z_j, i.e.,

$$\mathsf{v}^*[\mathsf{z}_j(t)] = \bar{u}_j - i\bar{v}_j = 1 - \frac{i}{2\pi}\int_{-1}^{1}\frac{\varpi_s(x,t)}{x-\mathsf{z}_j}dx - \frac{i}{2\pi}\int_{1}^{\infty}\frac{\varpi_e(x,t)}{x-\mathsf{z}_j}dx + \sum_{k\neq j}^{N-j}\frac{i\Gamma_k}{2\pi}\frac{1}{\mathsf{z}_j-\mathsf{z}_k}, \tag{3.66}$$

which is the complex conjugate velocity at the vortex center z_j excluding the vortex's self-contribution. The initial conditions for these differential equations are the values of Γ_j, x_j and z_j at the shedding instant t_{js}, $j = 2, 3, ..., N$.

Since Γ_1 is developing from the sharp leading edge, one has to apply the Kutta condition at $x = -1$ to remove the singularity of ϖ_s given by (3.32). Note that this condition has already been applied at the trailing edge, where the unsteady wake is continuously generated, in the derivation of ϖ_0, ϖ_{sj} and ϖ_{se}, so that ϖ_s given by (3.32) is not singular at $x = 1$. So, the solutions of the integral equations with the regularity in both edges provide the following expresion for $\varpi_s(x,t)$ (see Appendix A)

$$\varpi_s(x,t) = \frac{1}{\pi}\sqrt{1-x^2}\left[2\pi\dot{\alpha} + \int_1^\infty \frac{\varpi_e(\xi,t)}{\sqrt{\xi^2-1}(\xi-x)}d\xi + \right.$$
$$\left. \sum_{j=1}^{N} \frac{-\Gamma_j(t)}{\pi} \fint_{-1}^{1} \frac{\xi - x_j(t)}{(\xi - x_j(t))^2 + z_j^2(t)} \frac{d\xi}{\sqrt{1-\xi^2}(\xi - x)}\right], \tag{3.67}$$

under the assumption

$$\Gamma_0 - \pi\dot{\alpha} + \sum_{j=1}^{N} \Gamma_j B_j + \int_1^\infty \frac{\varpi_e(\xi,t)}{\sqrt{\xi^2-1}}, d\xi = 0, \tag{3.68}$$

where B_j is defined as

$$B_j := -\frac{1}{\pi}\fint_{-1}^{1} \frac{\xi - x_j}{(\xi - x_j)^2 + z_j^2} \frac{d\xi}{\sqrt{1-\xi^2}}. \tag{3.69}$$

As the two additional conditions for Γ_1, x_1, and z_1 it is used the Brown and Michael, 1954, equation, which ensures the momentum conservation around the vortex and the branch cut between the point vortex and the leading-edge (Michelin and Llewellyn Smith, 2009):

$$\frac{d\mathsf{z}_1}{dt} + \frac{\mathsf{z}_1 - \mathsf{z}_{10}}{\Gamma_1}\frac{d\Gamma_1}{dt} = \mathsf{v}(\mathsf{z}_1), \tag{3.70}$$

where $\mathsf{v}(\mathsf{z}_1) = \bar{u}_1 + i\bar{v}_1$ is given by (3.66) for $\mathsf{z}_1 = x_1 + iz_1$. These are two differential equations which have to be solved with the initial condition at the beginning of each half stroke, $t = t_i$,

$$\Gamma_1(t_i) = 0, \quad x_1(t_i) = x_{10} = -1, \quad z_1(t_i) = z_{10}(t_i) = zs(-1,t_i), \tag{3.71}$$

where t_i is given by

$$\left.\frac{dz_s}{dt}\right|_{x=-1,t=t_i} = \dot{h}(t_i) + (1+a)\dot{\alpha}(t_i) = 0. \tag{3.72}$$

The point vortex with growing circulation $\Gamma_1(t)$ is shed when Γ_1 reaches an extremum value, $d\Gamma_1/dt = 0$. After that, the circulation remains constant and, according to (3.70), the vortex travels with the Kirchhoff velocity. This shedding criterium when the strength of a vortex reaches an extremum, it is frozen at that value and the vortex subsequently moves according to the Kirchhoff velocity, avoids a discontinuity in the temporal variation of the impulse, and therefore in the force. One may have used, instead of the Brown-Michael equation (3.70), the impulse matching model of Wang and Eldredge, 2013, that avoids this discontinuity even when the vortex is shed without reaching an extremum intensity. But it would need an additional, experimentally or numerically based, shedding condition which would have complicated the formulation.

On the other hand, any vortex shedding model based on just three parameters like the present one, namely the circulation Γ_1 of a point vortex moving with trajectory

$[x_1(t), z_1(t)]$ from the leading edge, cannot satisfy at the same time the Kutta condition at the sharp edge, and the conservation around the vortex and branch cut between the leading edge and the vortex of the linear momentum in both directions and the angular momentum. The Brown and Michael, 1954, model satisfies the conservation of linear momentum (Michelin and Llewellyn Smith, 2009), avoiding a spurious net force on the foil, but introducing a spurious torque (Brown and Michael, 1954; Howe, 1996; Michelin and Llewellyn Smith, 2009; Tchieu and Leonard, 2011). Howe, 1996, developed an alternative approach satisfying the conservation of angular momentum, more appropriate to determine sound generation. For that, the Brown-Michael model is more appropriate here where the main aim is to determine the forces on the foil.

3.4.2 *Simplified model*

To simplify the problem it is shall only considered the effect of the growing LEV with circulation $\Gamma_1(t)$ at each half stroke, disregarding the effect of the remaining, already shed, vortices. From (3.72) and (3.2)-(3.4), the nondimensional initial time t_i at the beginning of each half stroke is given by

$$kt_i = \arctan\left[-\frac{(1+a)a_0\sin\phi}{h_0+(1+a)a_0\cos\phi}\right] \pm n\pi, \quad n = 0, 1, 2, \ldots \tag{3.73}$$

For a pure heaving motion, $kt_i = \pm n\pi$, while for a pure pitching motion, $kt_i = -\phi \pm n\pi$, but it may be set $\phi = 0$ since there is no combined motion. Note that the nondimensional half period is π/k. For each half stroke it is reseted the nondimensional time by using

$$\tau = t - t_i, \tag{3.74}$$

and as a consequece it is defined

$$\theta(\tau) = x_{10} - x_1 = -1 - x_1(t), \quad \zeta(\tau) = z_1(t) - z_{10}(t) = z_1(t) - [h(t) + (1+a)\alpha(t)], \tag{3.75}$$

with initial conditions

$$\theta(0) = \zeta(0) = 0. \tag{3.76}$$

For the initial stages of the developing LEV it is assumed that

$$0 \leq \theta \ll 1, \quad |\zeta| \ll 1, \tag{3.77}$$

the last condition being implied by the present linearized formulation, where $|z_1| \ll 1$. In fact, it is shall used below z_1, and then substitute it by ζ according to (3.75). From (3.35), neglecting terms of order z_1^2, one obtains

$$C_1 \simeq -1 + \sqrt{\frac{x_1+1}{x_1-1}} \simeq -1 + \sqrt{\frac{\theta}{2}}. \tag{3.78}$$

Consequently, from Kelvin's circulation theorem (3.36), the growing LEV has a negligible effect of the wake vorticity ϖ_e when $\theta \ll 1$, so that ϖ_e depends, in first approximation, only on Γ_0. Thus, the wake vorticity distribution ϖ_e can be approximated by the well-known solution for the unsteady wake (Kármán and Sears, 1938; Theodorsen, 1935)

$$\varpi_e(\xi, t) = g e^{ik(t-\xi)}, \tag{3.79}$$

where g is an unknown constant. To obtain it, if one replaces the value of the wake vorticity distribution ϖ_e given by (3.79) into the Kelvin's equation (3.36) and simplifies, one obtains that

$$\varpi_e(\xi,t) = \frac{2\Gamma_0(t)}{\pi}\frac{e^{-ik\xi}}{iH_0^{(2)}(k)+H_1^{(2)}(k)}, \tag{3.80}$$

where $H_n^{(2)}(z) = J_n(z) - iY_n(z)$, $n = 0, 1$, is the Hankel function of the second kind and order n, related to the Bessel functions of the first and second kind $J_n(z)$ and $Y_n(z)$ (Olver et al., 2010).

On the other hand, from the Kutta condition (3.68) at the leading edge one can obtain Γ_1 as a function of the position of the vortex and the parameters of the problem. To that end one has first to compute the integral (3.69) defining B_1 and the integral involving ϖ_e in (3.68) (see equation (A.29)). Neglecting terms $O(z_1)^2$, B_1 is given by

$$B_1 \simeq -\frac{1}{\sqrt{x_1^2-1}} \simeq -\frac{1}{\sqrt{2\theta}}, \tag{3.81}$$

which after substituting in (3.68), yields

$$\Gamma_1(t) \simeq \sqrt{2\theta(t)}\mathcal{G}(t), \tag{3.82}$$

where

$$\mathcal{G}(t) := \Gamma_0(t)C(k) - \pi\dot{\alpha}(t), \tag{3.83}$$

and $C(k)$ is the Theodorsen function (Theodorsen, 1935; Garrick, 1938) defined in (A.32) for easy reference. It is understood that one has to take the real part of all the complex quantities separately. This expression for Γ_1 says that, at the initial stages, the LEV approximately grows as the square root of the distance to the leading edge θ, but modulated by the oscillatory motion of the airfoil through $\mathcal{G}(t)$.

To write the equations for $x_1(t)$ and $z_1(t)$ [or $\zeta(t)$] from the Brown-Michael equation (3.70) it is needed the Kirchhoff velocity components $\bar{u}_1$ and $\bar{v}_1$, which are obtained from (3.66). Since it is considered only one vortex growing at each half-stroke, disregarding the effect of the remaining, the Kirchhoff velocity (3.66) reduces to

$$\bar{u}_1 - i\bar{v}_1 = 1 - \frac{i}{2\pi}\int_{-1}^{1}\frac{\varpi_s(x,t)}{x-z_1}dx - \frac{i}{2\pi}\int_{1}^{\infty}\frac{\varpi_e(x,t)}{x-z_1}dx, \tag{3.84}$$

where using the expression for the voticity distribution ϖ_s with the regularity in both edges given by (3.67), the first integral can be writen as

$$-\frac{i}{2\pi}\int_{-1}^{1}\frac{\varpi_s(x,t)}{x-z_1}dx = \frac{i}{2\pi^2}\int_{-1}^{1}\frac{\sqrt{1-x^2}}{x-z_1}\Bigg[-2\pi\dot{\alpha} - \int_{1}^{\infty}\frac{\varpi_e(\xi,t)}{\sqrt{\xi^2-1}(\xi-x)}d\xi + \\ \frac{\Gamma_1(t)}{\pi}\fint_{-1}^{1}\frac{\xi-x_1(t)}{(\xi-x_1(t))^2+z_1^2(t)}\frac{d\xi}{\sqrt{1-\xi^2}(\xi-x)}\Bigg]dx. \tag{3.85}$$

So, developing every integral separately and, to be consistent with the present linearized theory, neglecting terms of order z_1^2, it yields to

$$\bar{u}_0 - i\bar{v}_0 := -\frac{i\dot{\alpha}}{\pi}\int_{-1}^{1}\frac{\sqrt{1-x^2}}{x-z_1}dx \simeq \frac{z_1\dot{\alpha}}{\sqrt{x_1^2-1}}\left(\frac{x_1^2}{|x_1|} - \sqrt{x_1^2-1}\right) + i\dot{\alpha}\left(x_1 - \frac{x_1}{|x_1|}\sqrt{x_1^2-1}\right), \tag{3.86}$$

$$\begin{aligned}\bar{u}_{se} - i\bar{v}_{se} &:= -\frac{i}{2\pi^2}\int_{-1}^{1}\frac{\sqrt{1-x^2}}{x-\mathsf{z}_1}\int_{1}^{\infty}\frac{\varpi_e(\xi,t)}{\sqrt{\xi^2-1}(\xi-x)}d\xi dx \\ &\simeq f_{se}^{(1)}(k) + \sqrt{\theta} f_{se}^{(2)}(k) + \theta f_{se}^{(3)}(k) + \frac{z_1}{\sqrt{\theta}}\left[g_{se}^{(1)}(k) + \sqrt{\theta} g_{se}^{(2)}(k) + \theta g_{se}^{(3)}(k)\right],\end{aligned} \tag{3.87}$$

$$\begin{aligned}\bar{u}_{s1} - i\bar{v}_{s1} &:= \frac{i}{2\pi^3}\int_{-1}^{1}\frac{\sqrt{1-x^2}}{x-\mathsf{z}_1}\Gamma_1 \fint_{-1}^{1}\frac{\xi - x_1(t)}{[\xi - x_1(t)]^2 + z_1^2(t)}\frac{d\xi}{\sqrt{1-\xi^2}(\xi-x)}d\xi dx \\ &\simeq -\frac{z_1\mathcal{G}}{16\pi\theta^{3/2}}\left(1-\theta+\frac{3\theta^2}{4}-\frac{\theta^3}{2}\right) + \frac{\mathcal{G}}{4\pi\sqrt{\theta}}\left(1-\sqrt{2\theta}+\frac{\theta}{2}+\frac{\theta^{3/2}}{2\sqrt{2}}-\frac{\theta^2}{4}\right),\end{aligned} \tag{3.88}$$

$$\bar{u}_e - i\bar{v}_e := -\frac{i}{2\pi}\int_1^{\infty}\frac{\varpi_e(x,t)}{x-\mathsf{z}_1}dx = \frac{\Gamma_0(t)}{\pi^2}\frac{\left[\mathrm{Si}(k-\mathsf{z}_1k) + i\mathrm{Ci}(k-\mathsf{z}_1k) - \frac{\pi}{2}\right]e^{-ik\mathsf{z}_1}}{iH_0^{(2)}(k) + H_1^{(2)}(k)}, \tag{3.89}$$

where $\mathrm{Si}(z)$ and $\mathrm{Ci}(z)$ are the sine integral and cosine integral functions respectively. Note that, $\Gamma_1(t)$ has been replaced by the equation (3.82). The functions $f_{se}^{(n)}(k)$ and $g_{se}^{(n)}(k)$ are given by the expressions (A.44)-(A.48) in the Appendix A. So, the Kirchhoff velocity can be decomposed into the following terms

$$\mathrm{v}_1 = \bar{u}_1 - i\bar{v}_1 = \mathrm{v}_0 + \mathrm{v}_{s1} + \mathrm{v}_{se} + \mathrm{v}_e, \tag{3.90}$$

where in v_0 is also included the contribution of the free stream current. On substituting these expressions for $\bar{u}_1$ and $\bar{v}_1$, together with (3.82) and (3.75), into the Brown-Michael equation (3.70), two differential equations for $\theta(\tau)$ and $\zeta(\tau)$ result:

$$\frac{d}{d\tau}\left(\theta^{3/2}\mathcal{G}\right) = -\mathcal{G}\theta^{1/2}\bar{u}_1, \quad \frac{d}{d\tau}\left(\zeta\theta^{1/2}\mathcal{G}\right) = \mathcal{G}\theta^{1/2}\left(\bar{v}_1 - \frac{dz_{10}}{d\tau}\right), \tag{3.91}$$

or in a more appropriate way for the numerical integration

$$\frac{d\theta}{d\tau} = -\frac{2}{3}\left(\bar{u}_1 + \frac{\theta}{\mathcal{G}}\frac{d\mathcal{G}}{d\tau}\right), \quad \frac{d\zeta}{d\tau} = -\zeta\left(\frac{1}{\mathcal{G}}\frac{d\mathcal{G}}{d\tau} + \frac{1}{2\theta}\frac{d\theta}{d\tau}\right) + \bar{v}_1 - \frac{dz_{10}}{d\tau}. \tag{3.92}$$

which have to be solved numerically with the initial contions (3.76). For the special case of $a < -1$, the plate motion is inverted, exchanging the downstroke for the upstroke in the initial time t_i. So that, the definition of ζ given by (3.75) has to be modified, changing the sign ($\zeta = z_{10} - z_1$), and consequently, the sign of z_1 in the expression of the Kirchhoff velocity (3.84). Thus, the differential equation relative to $\zeta(\tau)$ result

$$\frac{d}{d\tau}\left(\zeta\theta^{1/2}\mathcal{G}\right) = \mathrm{sign}(a+1)\mathcal{G}\theta^{1/2}\left(\bar{v}_1 - \frac{dz_{10}}{d\tau}\right), \tag{3.93}$$

taking positive sign when $a = -1$.

3.4.3 *Initial times*

Since $\tau = 0$ is a singular point of the equations, the numerical integration has to be started from an analytical approximation for $\tau \ll 1$. For small θ, the equation (3.86) can be approximated by

$$\bar{u}_0 \simeq 1 + \frac{z_1\dot{\alpha}}{\sqrt{2\theta}}\left(1-\sqrt{2\theta}+\frac{3}{4}\theta\right), \quad \bar{v}_0 \simeq \dot{\alpha}\left(1-\sqrt{2\theta}+\theta\right). \tag{3.94}$$

So, retaining only the leading terms in (3.94) for $\theta \ll 1$ and $\zeta \ll 1$ [see Eq. (3.75)], and doing the assumption that $\mathrm{v}_1 \simeq \mathrm{v}_0$, the lowest order of the equations (3.91) can be written as

$$\frac{d}{d\tau}\left(\theta^{3/2}\mathcal{G}\right) \simeq -\frac{\mathcal{G}\, z_{10}\,\dot{\alpha}}{\sqrt{2}}, \quad \frac{d}{d\tau}\left(\zeta\theta^{1/2}\mathcal{G}\right) \simeq \theta^{1/2}\mathcal{G}\,\left(\dot{\alpha} - \dot{z}_{10}\right). \tag{3.95}$$

These equations can be formally integrated to yield

$$\theta \simeq \left(-\frac{1}{\sqrt{2}\,\mathcal{G}}\int_0^{\tau} \mathcal{G}\, z_{10}\,\dot{\alpha}\, d\tau\right)^{2/3}, \quad \zeta \simeq \frac{1}{\theta^{1/2}\mathcal{G}}\int_0^{\tau} \theta^{1/2}\,\mathcal{G}\,\left(\dot{\alpha} - \dot{z}_{10}\right) d\tau. \tag{3.96}$$

The initial approximation to start the numerical integration of (3.91) can be obtained by approximating the above analytical solution for $\tau = t - t_i \ll 1$, using polynomial expansions for $z_{10}(\tau)$, $h(\tau)$, $\alpha(\tau)$ and $\mathcal{G}(\tau)$ for $\tau \ll 1$, i.e.,

$$h \simeq h_{i0} + h_{i1}\tau + h_{i2}\tau^2, \quad \alpha \simeq \alpha_{i0} + \alpha_{i1}\tau + \alpha_{i2}\tau^2, \tag{3.97}$$

with h_{i0} and α_{i0} the values of h and α at $t = t_i$, respectively, and

$$h_{i1} + (1+a)\alpha_{i1} = 0, \tag{3.98}$$

to satisfy (3.72) at $\tau = 0$. On the other hand,

$$z_{10} \simeq h_{i0} + (1+a)\alpha_{i0} + [h_{i2} + (1+a)\alpha_{i2}]\tau^2 \equiv z_{100} + z_{102}\tau^2, \tag{3.99}$$

and

$$\mathcal{G} \simeq \mathcal{G}_{i0} + \mathcal{G}_{i1}\tau. \tag{3.100}$$

All coefficients of these expressions are given in the Appendix A. So, on substituting these expansions into (3.96), at the lowest order for $\tau \ll 1$ one gets

$$\theta \simeq \left(-\frac{z_{100}\alpha_{i1}}{\sqrt{2}}\right)^{2/3}\tau^{2/3} = \left(\frac{k h_0 a_0 \sin\phi}{\sqrt{2}}\right)^{2/3}\tau^{2/3}, \quad \zeta \simeq \frac{3\alpha_{i1}}{4}\tau. \tag{3.101}$$

The time dependencies in these expressions, and the corresponding $\Gamma_1 \propto \tau^{1/3}$ after substituting into (3.82), coincide with those at the leading order of the solution for the growth of a vortex sheet from the leading-edge of a starting flat plate when considered as a point-vortex (Pullin and Wang, 2004). These expressions are not valid, and therefore cannot be used to start the numerical integration, if h_0, a_0 or $\sin\phi$ vanish. These particular cases will be considered separately below.

For $h_0 = 0$, i.e., for a pure pitching motion, $\alpha_{i0} = \pm a_0$, $\alpha_{i1} = 0$, $\alpha_{i2} = \mp a_0 k^2/2$, and $z_{10} \simeq \pm a_0(1+a)(1 - k^2\tau^2/2)$, according to the expressions given in Appendix A. Thus, (3.96) yields, at the lowest order,

$$\theta \simeq [(1+a)a_0^2k^2]^{2/3}\frac{\tau^{4/3}}{2}, \quad \zeta \simeq \pm\frac{3}{8}a_0\, a\, k^2\tau^2, \quad \tau \ll 1, \tag{3.102}$$

which have to be used to start the numerical integration of (3.91). For values of $a < -1$ one can use this same expression but taking the pivot point in absolute value.

For $\sin\phi = 0$, i.e., for a combined motion without phase shift ($\phi = 0$), or with a phase shift $\phi = 180^o$, $h_{i1} = \alpha_{i1} = 0$, $h_{i0} = \pm h_0$, $\alpha_{i0} = \pm a_0\cos\phi$ from the expressions given in Appendix A, where it has been taken into account that $\cos\phi = \pm 1$. At the lowest order when $\tau \ll 1$ one gets

$$\theta \simeq \left(k^2 a_0[(1+a)a_0 + h_0\cos\phi]\right)^{2/3}\frac{\tau^{4/3}}{2}, \quad \zeta \simeq \pm\frac{3}{8}k^2(h_0 + a_0 a\cos\phi)\tau^2. \tag{3.103}$$

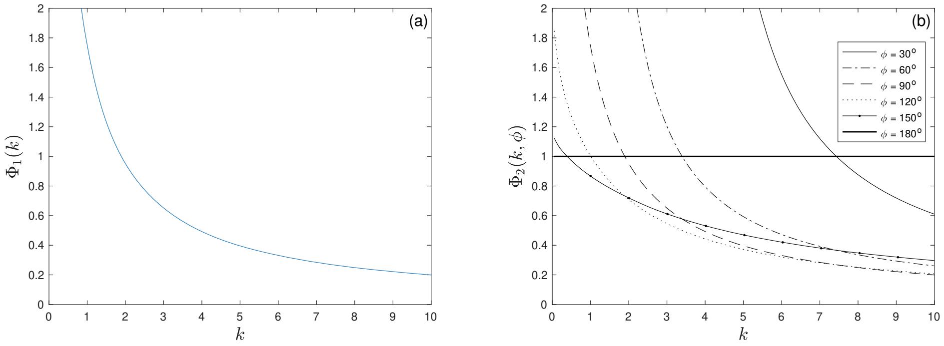

Figure 3.3: Functions a) $\Phi_1(k)$ defined in (3.105) and b) $\Phi_2(k,\phi)$ defined in (3.106) for several values of ϕ and k.

Although this starting behavior is very different to (3.101), the results as τ increases are quite similar in both cases for small ϕ or for ϕ close to 180^o.

Finally, for a pure heaving motion ($a_0 = 0$), the equations have no solution with the present approximation (3.94), which needs the presence of some pitching motion with $\dot{\alpha} \neq 0$ to generate a leading edge vortex. One would have to consider the next order effects of ϖ_{s1} in (3.88), but these second order effects are neglected to start the numerical integration.

More generally, no LEV is produced within the present approximation when Γ_1 is negative at the beginning of the downstroke (or positive at the beginning of the upstroke). From (3.82), for the downstroke for instance, it has to satisfy at the beginning that

$$\Gamma_1(t_i) \simeq \sqrt{2\theta(t_i)\mathcal{G}(t_i)} \geq 0, \quad \rightarrow \quad \mathcal{G}(t_i) \geq 0, \tag{3.104}$$

which after some algebra and taking into account the the inital condition (3.72) and the initial time (3.73), one obtains

$$\frac{h_0 \sin(\phi)}{h_0 \cos(\phi) + (1+a)a_0} \leq \Phi_1(k) := \frac{2F(k)}{k[3F(k)-1]}, \tag{3.105}$$

where $F(k)$ is the real part of the Theodorsen function $C(k)$ given by (A.32). This condition is valid for both downstroke and upstroke, like so, excludes the pure heaving motion already commented on, and allows any pure pitching motion ($h_0 = 0$) for any value of k or a. Any pitching of the foil pivoting at the leading edge ($a = -1$) is also excluded by this inequality. Apart from that, to see the effect of the phase angle ϕ in this condition, it also can be writen as

$$\frac{h_0}{(1+a)a_0} \leq \Phi_2(k,\phi) := \frac{2F(k)}{k[3F(k)-1]\sin\phi - 2F(k)\cos\phi}. \tag{3.106}$$

Figure 3.3 shows the values of Φ_1 and Φ_2 as a function of k for several values of ϕ. A solution exists, i.e., a LEV is generated, for a given motion below the corresponding curves Φ_1 or Φ_2. As one can see in Figure 3.3b, when ϕ is close to zero, the solution exists for practically any value of k and $h_0/[(1+a)a_0]$. But, as ϕ increases, the range shrinks to smaller values of both parameters. If one starts increasing $h_0/[(1+a)a_0]$ (by decreasing the pitch angle a_0, say) for given values of k and $h_0/[(1+a)a_0]$ below the curve corresponding to a given value of the phase shift ϕ, what it is found is that the maximum circulation of the LEV tends to zero as one approaches the curve, corresponding to a vanishing contribution of the LEV to the force and moment.

Condition (3.105) or (3.106) is the mathematical expression of the known physical condition that the effective angles of attack has to be sufficiently large for the flow to separate at the leading edge and develop a LEV that moves as a point vortex away from the edge (Dickinson and Gotz, 1993; Jones, 2003; Xia and Mohseni, 2013). It is a consequence of the Kutta condition imposed at the sharp leading edge while the LEV is growing. In fact, $\mathcal{G}(t)$, as defined in (3.82) proportional to the LEV's circulation, is a measure of the average slip between the plate and the adjacent fluid to the plate (Jones, 2003), which has to be positive at the beginning of the downstroke (negative for the upstroke) to generate a LEV that begins to move away from the plate. What it is remarkable here is that this condition can be written in terms of a single parameter $h_0 \sin(\phi)/[(1+a)a_0 + h_0 \cos(\phi)]$ for given k, or $h_0/[(1+a)a_0]$ for given k and ϕ.

3.4.4 *Results for the trajectories and circulations of the LEV*

Here are some examples for the different initial time behaviors discussed above. Figure 3.4(a)-(d) show some results for $h_0 = 0.1$, $a_0 = 20^o$, $a = 0$ and $k = 5$, with $\phi = 10^o$ (a),(b) and with $\phi = 90^o$ (c),(d). In Figure 3.4(a) and Figure 3.4(c) it is plotted the trajectories $\zeta(\tau)$ vs. $x_1(\tau)$ [note that the initial value of x_1 is -1, and $z_1(\tau) = z_{10}(\tau) + \zeta(\tau)$]. It is integrated numerically (3.91) starting from a sufficiently small value of τ with (3.101) until $\Gamma_1(\tau)$, plotted in Figure 3.4(b) and Figure 3.4(d), reaches a maximum value, marked with circles in the vortex trajectories. From this point on the circulation Γ_1 remains constant, and it is integrated (3.70) without the second term. For the numerical integrations it is used the assumption that $\mathrm{v}_1 \simeq \mathrm{v}_0$ for $\bar{u}_1$ and $\bar{v}_1$, valid for any x_1, and the solver `ode15s` from Matlab. Since most of the vortex contribution to the forces and moment occurs, as it is seen, before the vortex is shed, and this event happens in both plotted cases before the vortex passes above (below) the foil, it is only plotted results for $x_1 < 0$. A perfect symmetry is observed in Figure 3.4 between the downstroke and the upstroke, with $\Gamma_1 > 0$ for the downstroke (in our sign convection where Γ_1 is positive when clockwise), and $\Gamma_1 < 0$ during the upstroke.

For the case of pure pitching, $h_0 = 0$, in 3.4(e)-(f) shows results when $a_0 = 20^o$, $a = 0$ and $k = 5$. Comparing with Figure 3.4(a)-(b), which is a similar case but with $h_0 = 0.1$, the maximum of Γ_1 and the largest $|\zeta|$ travelled by the vortex are both significantly smaller.

Finally for the case of a combined motion without phase shift ($\phi = 0$ or $\phi = 180^o$), as it is commented above, when ϕ is small or close to 180^o the results are quite similar, excepting for very small τ. So that, the curves for $\phi = 0$ when $h_0 = 0.1$, $a_0 = 20^o$, $a = 0$, and $k = 5$, as are very similar to those depicted in Figure 3.4(a)-(b) for $\phi = 10^o$, these results are no plotted here.

On the other hand, in order to see the different contributions of the Kirchhoff velocity (3.90), in Figure 3.5 is represented the LEV's trayectory and circulation considering the different terms in (3.90) for the case of $h_0 = 0.05$, $a_0 = 10^o$, $a = 0$, $k = 5$ and $\phi = 0^o$. In view of the results, the contribution of v_e can be neglected. In addtion, to be consistent with the assumption $z_1^2 \ll 1$ and consequetly that $|\zeta| \ll 1$, the contribution of v_{se} is not going to be considered because of it reach values of unit order. Additionally, the contribution of the wake does not make sense to consider it, because the contribution of the vortex has not been taken into account for the calculus of the wake vorticity

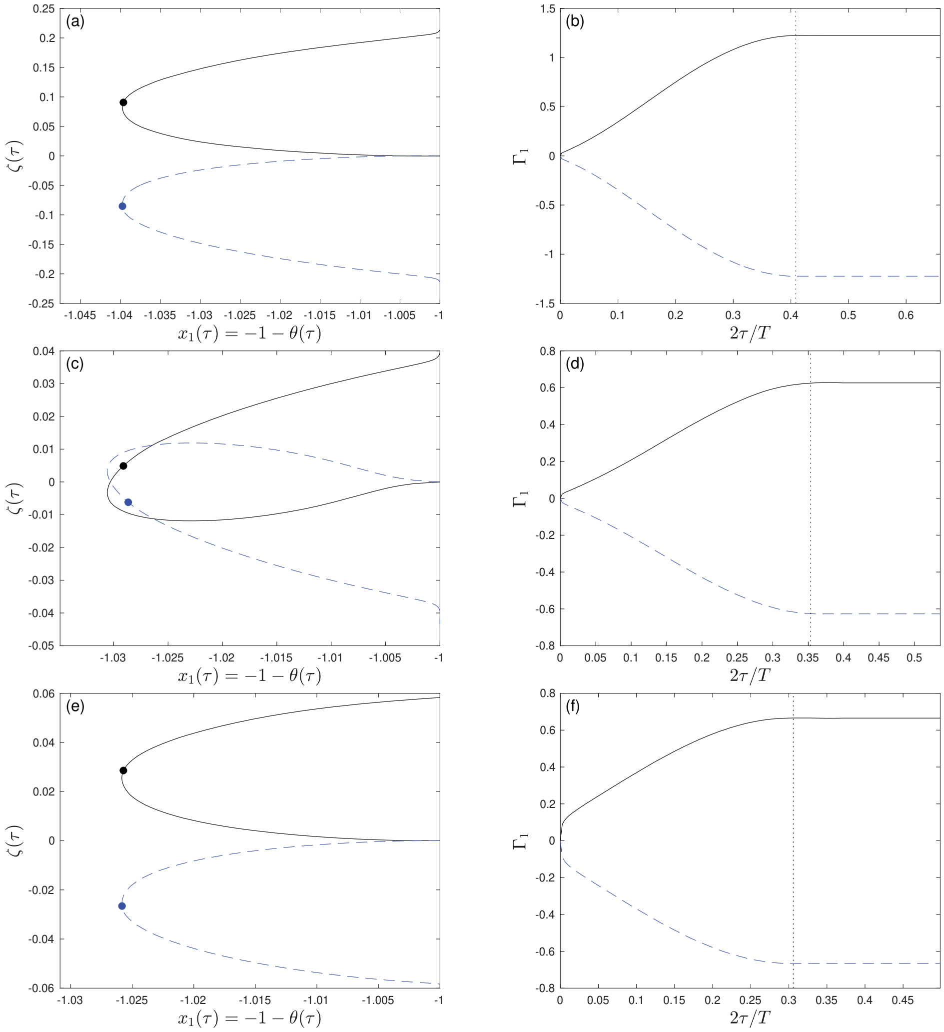

Figure 3.4: LEV's trajectory, left panels, and circulation, right panels, for $a_0 = 20^o$, $a = 0$, $k = 5$ and (a)-(b) $h_0 = 0.1$ and $\phi = 10^o$, (c)-(d) $h_0 = 0.1$ and $\phi = 90^o$, and (e)-(f) $h_0 = 0$ and $\phi = 10^o$. The continuous lines correspond to the downstroke and the dashed lines to the upstroke. The circles in the left panels mark the position at which Γ_1 reaches a maximum and the LEV is shed, whose instant is marked with a dotted vertical line in the right panels.

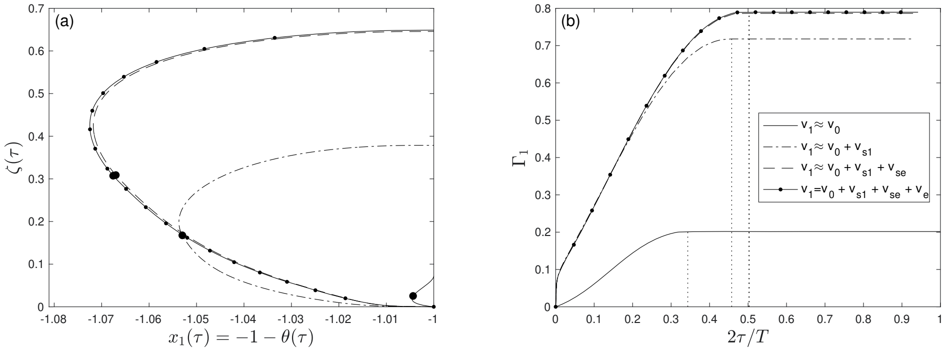

Figure 3.5: LEV's trajectory (a) and circulation (b) for the downstroke with $h_0 = 0.05$, $a_0 = 10^o$, $a = 0$, $k = 5$ and $\phi = 0^o$, considering the different components of the Kirchhoff velocity given by (3.90). The circles in (a) and dotted vertical line in (b) as in Figure 3.4.

distribution. On the other hand, although with the contribution of v_{s1}, the value of ζ is not too small, it can be considered in first approximation.

3.5 RESULTS FOR THE CONTRIBUTION OF THE LEV TO THE FORCES AND MOMENT

According to (3.45), (3.54) and (3.61), the contribution of the LEV with circulation $\Gamma_1(t)$ developed during each half stroke to the lift, thrust and moment are given, in nondimensional form, by

$$C_{L_1} = \frac{dF_{L_1}}{dt}, \quad F_{L_1} := -\Gamma_1(x_1 + D_1), \tag{3.107}$$

$$C_{T_1} = \frac{dF_{T_1}}{dt}, \quad F_{T_1} := \Gamma_1 \left[z_s(x_1) - z_1 + \alpha\,(x_1 + D_1) \right], \tag{3.108}$$

$$C_{M_1} = \frac{dF_{M_1}}{dt}, \quad F_{M_1} := \frac{\Gamma_1}{4} \left[x_1^2 + E_1 - \frac{1}{2} - 2a(x_1 + D_1) \right]. \tag{3.109}$$

The quantities D_1 and E_1, which are integrals defined in equations (A.42) and (A.43) of Appendix A, respectively, are obtained in the present linear approximation by neglecting terms of order z_1^2:

$$D_1 \simeq -x_1 - \sqrt{x_1^2 - 1}, \quad E_1 \simeq \frac{1}{2} - x_1^2 - x_1\sqrt{x_1^2 - 1}, \quad \text{for} \quad x_1 \leq -1. \tag{3.110}$$

They can also be obtained for $x_1 > -1$ with errors $O(z_1^2)$. But, since it is considering only the effect of the growing LEV up to the point where its intensity $|\Gamma_1|$ reaches a maximum, and this maximum occurs in all significant cases for $x_1 \leq -1$ (see, e.g., Figure 3.4), these expressions suffices in the present approximation. Substituting into (3.107)-(3.109), and using (3.75) and (3.82), one obtains

$$F_{L_1} = \Gamma_1 \sqrt{x_1^2 - 1} \simeq 2\mathcal{G}\theta \left(1 + \frac{\theta}{4} \right), \tag{3.111}$$

$$F_{T_1} = \Gamma_1 \left[z_s(x_1) - z_1 - \alpha\sqrt{x_1^2 - 1} \right] \simeq -2\mathcal{G}\theta \left[\zeta + \alpha \left(1 - \sqrt{\frac{\theta}{2}} + \frac{\theta}{4} \right) \right], \tag{3.112}$$

$$F_{M_1} = \frac{1}{2}\Gamma_1 \sqrt{x_1^2 - 1} \left(a - \frac{x_1}{2} \right) \simeq \mathcal{G}\theta \left[a + \frac{1}{2} + \frac{\theta}{4} \left(a + \frac{5}{2} \right) \right]. \tag{3.113}$$

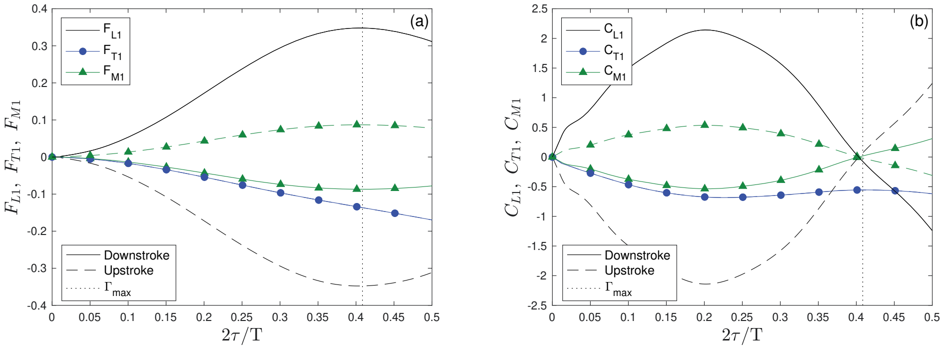

Figure 3.6: Functions (3.111)-(3.113) (a), and force and moment coefficients (3.107)-(3.109) (b) for the case depicted in Figure 3.4(a)-(b) ($h_0 = 0.1$, $a_0 = 20^o$, $a = 0$, $k = 5$ and $\phi = 10^o$), both for the downstroke (continuous lines) and for the upstroke (dashed lines). The vertical dotted line marks the instant where $|\Gamma_1|$ reaches a maximum value.

Note that it is used the approximation $\theta \ll 1$, which is quite accurate in all the cases considered (e.g., Figure 3.4). At the initial stages of each half stroke ($\tau \ll 1$) one may use (3.101) to find, at the leading order, $F_{L_1} \propto \tau^{2/3}$, $F_{T_1} \propto \tau^{4/3}$, and $F_{M_1} \propto \tau^{2/3}$, which yield, after using (3.107)-(3.109), the lift singularity at the start of the impulsive motion of a flat plate discussed by Graham, 1983, $C_{L_1} \propto \tau^{-1/3}$, together with $C_{T_1} \propto \tau^{2/3}$ and $C_{M_1} \propto \tau^{-1/3}$.

These functions (3.111)-(3.113) are very relevant because, according to (3.107)-(3.109), their values up to a given instant τ within each half stroke are proportional to the corresponding time-averaged force or moment up to that instant. Figure 3.6 shows F_{L_1}, F_{T_1} and F_{M_1}, as well as C_{L_1}, C_{T_1} and C_{M_1}, for the downstroke and for the upstroke of a typical case (that of Figure 3.4(a)-(b)) up to the point where $|\Gamma_1|$ reaches a maximum. The main feature of this and all the cases considered is that $C_{L_1}(\tau)$ and $C_{M_1}(\tau)$ for the upstroke are symmetrical in relation to the downstroke, so that the developing LEV does not contribute to the time-averaged lift and moment during a whole stroke. It only contributes to the instantaneous lift and moment, especially at the beginning of each half stroke, by the contribution cancelling out with the next half stroke. However, the evolution of $C_{T_1}(\tau)$ [and $F_{T_1}(\tau)$] for the upstroke coincides with its evolution during the downstroke. Thus, the growing LEV contributes to both the instantaneous thrust force and to its time-averaged value. In addition, for most of the cases considered, the contribution to the time-averaged thrust is negative, i.e., the growing LEV generates drag in the mean, within the present approximation. This is consistent with the discussion on the general expression for C_{T_j} given in §3.3, just below the equation (3.54).

3.6 TOTAL TIME-AVERAGED THRUST AND INPUT POWER

From (3.51), the total time-averaged thrust coefficient is then

$$\overline{C}_T \simeq \overline{C}_{T_f} + \overline{C}_{T_1}, \tag{3.114}$$

where $\overline{C}_{T_f} := \overline{C}_{T_a} + \overline{C}_{T_e}$ is the sum of the time-averaged values of C_{Ta} and C_{Te} given by (3.52)-(3.53) over a whole stroke of period $2\pi/k$ as it is defined in (3.64) (the subscript f is for 'free' of leading-edge, or any other point, vortex). The expression of $\overline{C}_{T_f}$ as a function of k, h_0, a_0, a and ϕ can be found in Fernandez-Feria, 2016; Fernandez-Feria,

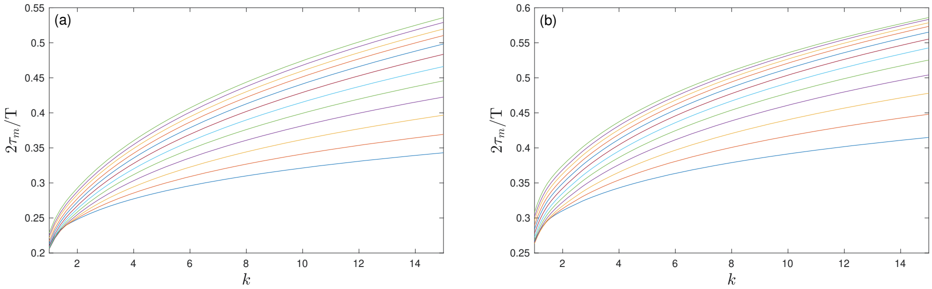

Figure 3.7: The instant τ_m as a function of k for a pure pitching motion with $a = 0$ (a) and $a = 0.5$ (b), and increasing values of a_0, from 8^o (bottom curve) to 30^o (top curve) with increments of 2^o.

2017, which modify previous ones by Garrick et al., 1936. Here the real part of the nonlinear expression of the thrust C_{T_f} is separated in a slightly different form, i.e.,

$$C_{T_f} = -\Re\left[\alpha\right] \times C_L + \Re\left[\dot{h} + a\dot{\alpha} - \alpha\right] \times \Re\left[\Gamma_0 \frac{-2i}{\pi} C_1(k)\right] + \\ \Re\left[\dot{\alpha}\right] \times \Re\left\{\pi\left(\dot{h} + a\dot{\alpha} - \alpha\right) + \Gamma_0\left[\frac{i}{k}C(k) + \left(\frac{1+ik}{k}\right)\frac{2}{\pi}C_1(k)\right]\right\}, \qquad (3.115)$$

where $C_1(k)$ is defined in (A.32) in the Appendix A. On the other hand, according to (3.108), the time-averaged thrust (actually drag in most cases) produced by the LEV during each half stroke is given by the final value of the function F_{T_1} at the half period $\tau = \pi/k$. But, since it is considering only the contribution of the LEV up to the instant τ_m where $|\Gamma_1|$ reaches a maximum value, the time-averaged thrust coefficient can be written as

$$\overline{C}_{T_1} \simeq \frac{2}{\tau_m}\int_0^{\tau_m} C_{T_1} d\tau = \frac{2}{\tau_m} F_{T_1}(\tau = \tau_m), \qquad (3.116)$$

where it has been taken into account that $C_{T_1}(t)$ coincides for the downstroke and for the upstroke, and that $F_{T_1}(\tau = 0) = 0$ (remember that $\tau = 0$ corresponds to $t = t_i$ for each half cycle). Thus, one has only to compute numerically the function F_{T_1} at $\tau = \tau_m$ from (3.112),

$$F_{T_1}(\tau = \tau_m) \simeq -2\mathcal{G}_m\theta_m\left[\zeta_m + \alpha_m\left(1 - \sqrt{\frac{\theta_m}{2}} + \frac{\theta_m}{4}\right)\right], \qquad (3.117)$$

where the subscript m means at $\tau = \tau_m$. Figure 3.7 shows $\tau_m/(T/2) = k\tau_m/\pi$, i.e., the fraction of each half stroke during which $|\Gamma_1|$ increases, as a function of k for a pure pitching motion with several values of a_0 and two pitching axis locations. It is observed that $k\tau_m/\pi$ scales, approximately, as $(a_0 k)^{1/4}$ for sufficiently large frequencies, with the proportionality constant slightly increasing with a.

Figure 3.8 shows $\overline{C}_{T_1}$ for a pure pitching motion as a function of the reduced frequency k for different values of the pitching amplitude a_0 and two values of the pitching axis location a. For small k and a_0, $|\overline{C}_{T_1}|$ is negligible, as expected. As commented on above, $\overline{C}_{T_1}$ is usually negative, i.e., the LEV produces drag in most cases within the present approximation. If this is the case, $\overline{C}_{T_1}$ is found to be roughly proportional to $-a_0^2 k^3$ for sufficiently large k, with a proportionality constant that depends on a. This constant is significantly larger for values of $a > 0$ than for $a \leq 0$ Thus, the LEV's correction to the thrust is more important when the pitching axis is downstream of the mid-chord point.

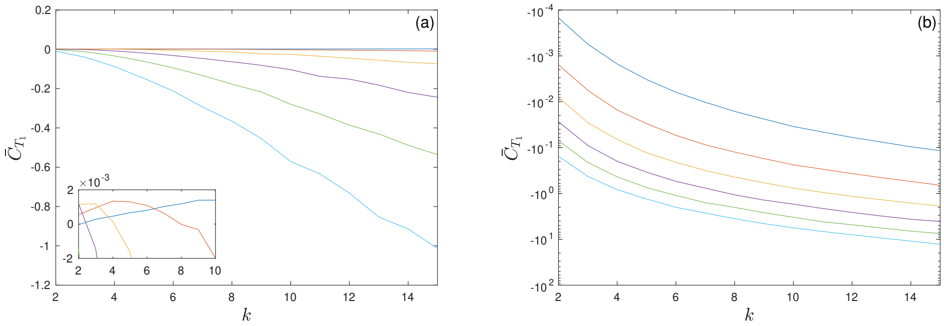

Figure 3.8: $\overline{C}_{T_1}$ vs. k for a pure pitching motion for increasing values of a_0, from 8^o (top curves) to 28^o (botom curves) with increments of 4^o, for $a = -0.5$ (a) and $a = 0$ (b).(Remember that the nondimensional pivot axis ranges from $a = -1$ at the leading edge to $a = 1$ at the trailing edge.)

For $a = -0.5$, $\overline{C}_{T_1}$ is positive and small for low a_0 and k [see inset in Figure 3.8(a)], being negative as in the other two cases for larger a_0 and k [note that the scale of $\overline{C}_{T_1}$ in Figure 3.8(b) is not logarithmic to allow for this change of sign]. For combined heaving and pitching motions that satisfy (3.105), it is found that $\overline{C}_{T_1}$ behaves in a similar fashion to the pure pitching motion in relation to k and a_0, with a weaker dependence on h_0 and ϕ.

In the case of the input power, it can be decomposed in a similar form that the thrust, from (3.62), the total time-averaged input power coefficient is then

$$\overline{C}_P \simeq \overline{C}_{P_f} + \overline{C}_{P_1}, \tag{3.118}$$

where $\overline{C}_{P_f}$ is defined as

$$\overline{C}_{P_f} = -\overline{C_{L_f}\dot{h}} - 2\overline{C_{M_f}\dot{\alpha}}, \tag{3.119}$$

with $C_{L_f} := C_{La} + C_{Le}$ given by (3.41)-(3.44) and $C_{M_f} := C_{Ma} + C_{Me}$ given by (3.59)-(3.60). Closed expression for $\overline{C}_{P_f}$ in terms of k, h_0, a_0, a and ϕ were originally derived by Theodorsen, 1935 and Garrick et al., 1936, where, for easy reference, the values of C_{L_f} and C_{M_f} are given by

$$C_{L_f} = \pi\left[\dot{\alpha} - \ddot{h} - a\ddot{\alpha}\right] + \Gamma_0 C(k), \tag{3.120}$$

$$C_{M_f} = \frac{\Gamma_0}{2}\left(\frac{1}{2} + a\right)C(k) - \frac{\pi}{2}\left[\left(\frac{1}{2} - a\right)\dot{\alpha} + a\ddot{h} + \left(\frac{1}{8} + a^2\right)\ddot{\alpha}\right]. \tag{3.121}$$

In the Appendix A one also can find the explicit expressions as for the average thrust as for the average input power, including new terms which in next chapter will be defined. Apart from that, it must be noted that, though the LEV does not contributes to the averaged lift and moment in the present approximation, i.e., $\overline{C}_{L_1} = \overline{C}_{M_1} = 0$, the LEV does contribute to the averaged input power coefficient because it comes from the time averaging of the products in (3.62), i.e.,

$$\overline{C}_{P_1} = -\overline{C_{L_1}\dot{h}} - 2\overline{C_{M_1}\dot{\alpha}} \simeq -\frac{2}{\tau_m}\int_0^{\tau_m}\left(C_{L_1}\dot{h} + 2C_{M_1}\dot{\alpha}\right)d\tau. \tag{3.122}$$

To obtain $\overline{C}_{P_1}$ one has to use the expressions (3.107) and (3.109) for C_{L_1} and C_{M_1} in (3.122). Alternatively, by integrating by parts, it can be written in terms of F_{L_1} and F_{M_1} as

$$\overline{C}_{P_1} \simeq \frac{2}{\tau_m}\left[\int_0^{\tau_m}\left(F_{L_1}\ddot{h} + 2F_{M_1}\ddot{\alpha}\right)d\tau - \left(F_{L_1}\dot{h} + 2F_{M_1}\dot{\alpha}\right)_{\tau=\tau_m}\right]. \tag{3.123}$$

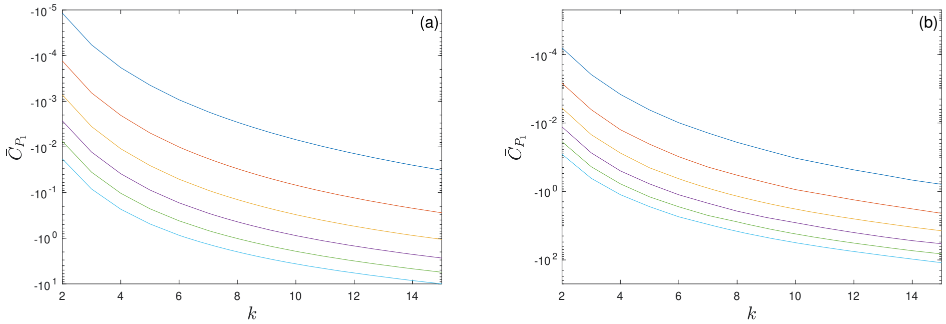

Figure 3.9: $\overline{C}_{P_1}$ vs. k for a pure pitching motion for increasing values of a_0, from 8^o (top curves) to 28^o (botom curves) with increments of 4^o, for $a = -0.5$ (a) and $a = 0$ (b).

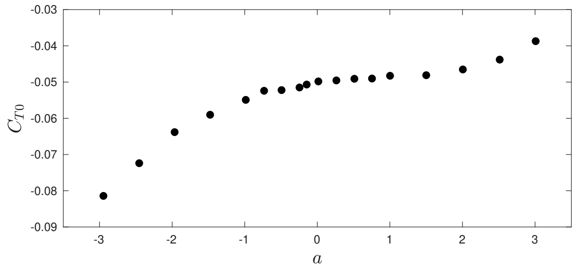

Figure 3.10: Quasisteady drag C_{T_0} vs. a measured by Mackowski and Williamson, 2017, for a NACA 0012 foil at $Re = 17000$ for $a_0 = 8^o$. Remember that $-1 \leq a \leq 1$ for a pivot location inside the foil.

Figure 3.9 shows $\overline{C}_{P_1}$ for a pitching motion vs. the reduced frequency k for different values of the pitching amplitude a_0 and two values of the pitching axis location a. For large k, $|\overline{C}_{P_1}|$ is approximately proportional to $a_0^4 k^3$, with the proportionality constant increasing with a. As in the case of $\overline{C}_{T_1}$ (Figure 3.8), the effect of the LEV is larger for a pivot location downstream the mid-chord point ($a > 0$), especially as a_0 and k increase.

3.7 COMPARISON WITH EXPERIMENTAL RESULTS

Here it is first compared the above theoretical results with the recent experimental data for a pitching foil reported by Mackowski and Williamson, 2017. These authors measured directly $\overline{C}_T$ and η for different pivot point locations and several values of the reduced frequency at a Reynolds number of 17000. To account for the viscous effects, especially relevant at low frequencies, it is added a quasisteady thrust coefficient $C_{T_0} < 0$ (actually a drag coefficient) which is experimentally computed by these authors from averaging the airfoil's static drag over the pitch angles encountered during a cycle of oscillation. By adding this C_{T_0} to $\overline{C}_T$ the results of the potential theory based on the vortical impulse agree quite well with experimental data for sufficiently small amplitude of the oscillations (Fernandez-Feria, 2017). This C_{T_0} depends, for a pitching foil, on the maximum pitch angle a_0 and on the pivot location a. Figure 3.10 shows the measured values for $a_0 = 8^o$ as a function of a.

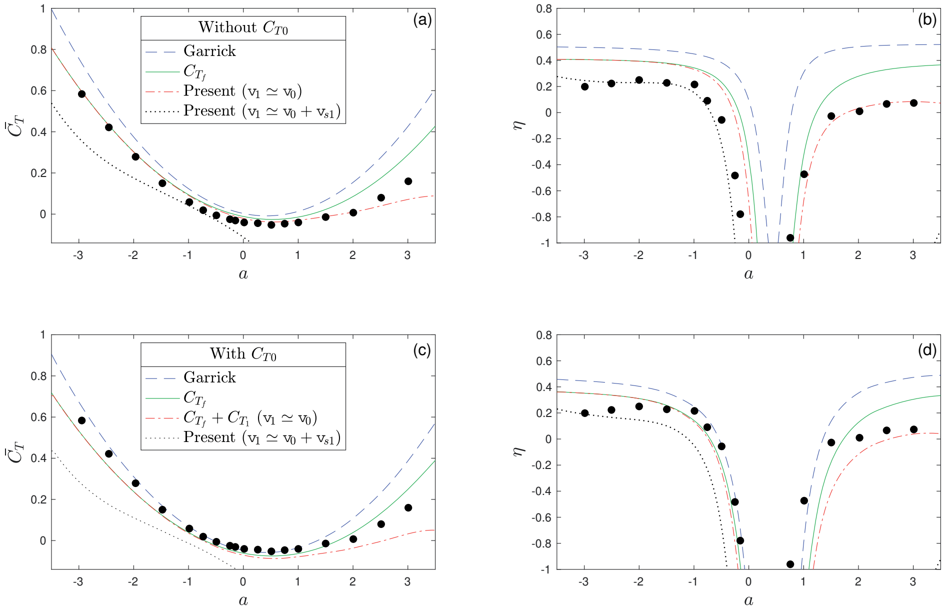

Figure 3.11: Comparison of the experimental data of Mackowski and Williamson, 2017, for $\overline{C}_T$ (a)-(c) and η (b)-(d) vs. a for $k = 2$ and $a_0 = 8^o$ (dots, from Figs. 6 and 7 of Mackowski and Williamson) with the present results (dashed-dotted and dotted lines), with the results without the LEV effect (continuous lines), and with Garrick's results (dashed lines). The different theoretical results are presented in two ways, without adding the experimental value of $C_{T_0}(a)$ given in Figure 3.10 to $\overline{C}_T$ (a)-(b), and adding it (c)-(d).

Figure 3.11 compares the experimental results for the thrust coefficient and propulsive efficiency obtained by Mackowski and Williamson, 2017, for $k = 2$, $a_0 = 8^o$, and different values of the pivot location a, with the present results for $\overline{C}_T$ and η. Also included are the results obtained without considering the LEV effect, i.e., $\overline{C}_{T_f}$ and $\eta_f \equiv \overline{C}_{T_f}/\overline{C}_{P_f}$, as well as Garrick's results for $\overline{C}_T$ and η. The theoretical results are presented in two ways: with the addition of the quasisteady constant drag $\overline{C}_{T_0}(a)$, as given in Figure 3.10, to correct $\overline{C}_T$, and also without adding the experimentally based $\overline{C}_{T_0}(a)$. The main feature arising from this figure is that the LEV's effect is relevant, within the present approximation, when $a > 0$ and one approximates $\mathrm{v}_1 \simeq \mathrm{v}_0$: the LEV's corrections to $\overline{C}_T$ and η are negligible when the pivot location is ahead of the mid-chord point ($a < 0$), while it is increasingly important as the pivot point approaches the trailing edge, or it is located further downstream. However, if it is considered next term in the Kirchhoff velocity, $\mathrm{v}_1 \simeq \mathrm{v}_0 + \mathrm{v}_{s1}$, now the effect of LEV's contribution is not negligible when $a < 0$ and it corrects the theory, matching with the experimental results but being too big the LEV's contribution when $a > 0$. The differences between Garrick's classical results and the present ones based on the vortical impulse theory are also more pronounced in these cases with $a > 0$. The correction provided by this theory, already discussed in Fernandez-Feria, 2016, is here increased when the LEV's effect is taken into account, so that the agreement of the present propulsive efficiency with the experimental data is overall better for all the pivot locations.

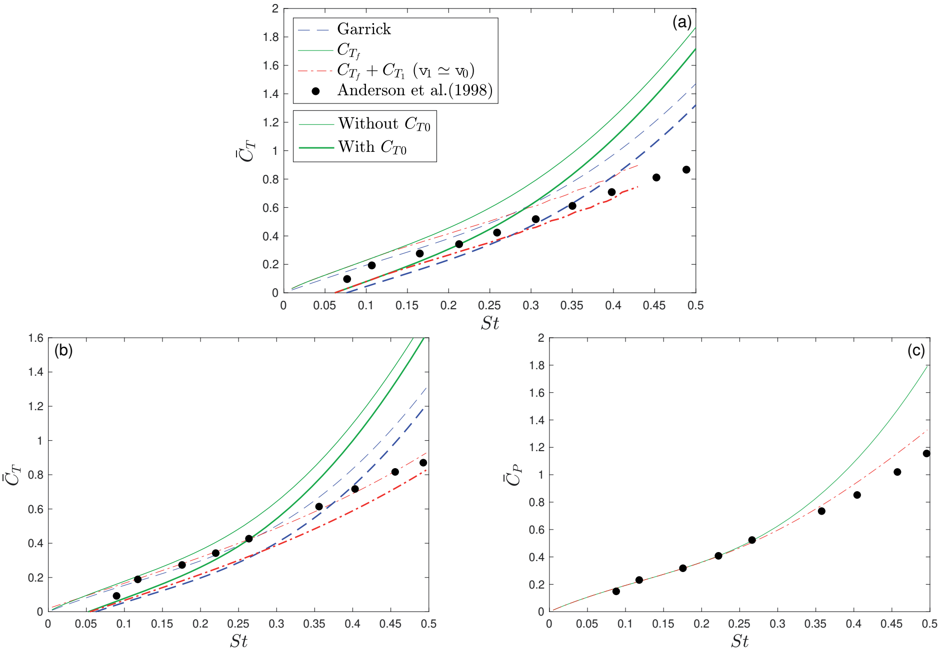

Figure 3.12: Comparison of the theoretical results with the experimental data of Anderson et al., 1998, for $\overline{C}_T$ (a)-(b) and $\overline{C}_P$ (c) vs. the Strouhal number based on the total excursion of the trailing edge St, for a combined plunging and pitching motion of a NACA 0012 airfoil with $a = -1/3$ in two cases: $h_0 = 1.5$, $\alpha_{max} = 21^o$, $\phi = 75^o$ (Case 1 from Fig. 1 of Anderson et al.) (a), and $h_0 = 1.5$, $\alpha_0 = 15^o$, $\phi = 75^o$ (from Fig. 9a of Anderson et al.)(b)-(c). The theoretical results are presented adding a constant quasisteady drag C_{T_0} to $\overline{C}_T$, $C_{T0} = -0.15$ in (a) and $C_{T0} = -0.1$ in (b) (estimated from Mackowski and Williamson, 2017, for a similar amplitude), and also without adding it.

Figure 3.12 compares the theoretical results with the experimental data for $\overline{C}_T$(a)-(b) and $\overline{C}_P$ (c) obtained by Anderson et al., 1998, for a combined pitching and plunging motion in two of the optimal cases where experiment provides very high efficiency for a NACA 0012 airfoil pivoting at one-third-chord point. These two cases, both with $\phi = 75^o$, are among the few ones of those reported by Anderson et al., 1998, that satisfy the condition (3.105). It is observed that the agreement with the experimental data improves when the present LEV's effect is taken into account, almost independently of whether it is added, or not, a constant quasisteady drag C_{T_0}, which has to be estimated from experimental data.

3.8 CONCLUDING REMARKS

General expressions have been developed for the contribution of travelling point vortices to the lift, thrust, moment and propulsion efficiency of a two-dimensional pitching and heaving airfoil from a vortical impulse formulation within the linear potential theory. Although these general formulas need additional information about the temporal evolution of the vortices, both circulation and trajectory, they provide useful qualitative information about their effect on the airfoil's unsteady aerodynamics.

Starting from these general formulas it has been derived closed-form expressions for the LEV contribution to the unsteady forces and moment on the airfoil. To that end, it has been used several simplifying assumptions for the development and shedding of the LEV. It has been considered only one point vortex during each half stroke, a LEV that is released from the sharp leading edge where one can apply the unsteady Kutta condition that regularizes the bound vortex-sheet strength at the leading edge, and used the Brown-Michael equation for the developing LEV, that ensures momentum conservation. With these assumptions, the symmetry of the problem shows that the LEV does not contribute to the time-averaged lift and moment, but only to the time-averaged thrust and to the propulsion efficiency, which are in general lowered in relation to the case without LEV. Further, by considering the effect of the developing LEV just up to its shedding point, when its circulation reaches an extremum value according to the Brown-Michael model, quite simple relations have been obtained for the LEV's effect on the thrust force and propulsion efficiency, which constitutes a lowest order correction to the analytical results from the linear potential theory. The resulting thrust coefficient and propulsion efficiency corrected by the LEV agree reasonably well with recent experimental results for a foil pitching at different pivot locations when the pitching amplitude is small enough for the linear theory to be valid.

As a general trend, it is found that the LEV's lowest order corrections to the thrust force and propulsion efficiency are more significant when the pitching axis location is behind the mid-chord point ($a > 0$), the more so the larger the pitching amplitude and the reduced frequency. These are in fact the conditions where the classical Garrick's expressions for the thrust and efficiency are in greater disagreement with experimental results for a pure pitching motion. In addition, no LEV's corrections are found within the present linear approximation for a pure heaving motion ($a_0 = 0$) or, more generally, when $h_0/(1+a)a_0$ is larger that a quantity that depends of k and ϕ.

The present contribution on the effect of the LEV to the unsteady aerodynamics of a two-dimensional airfoil is limited to thin, rigid airfoils with small-to-medium angles of attack. It may complement the large amount of information already existing in the literature about the leading-edge vortex effect on the unsteady aerodynamics of flapping wings in a great variety of kinematics and flow conditions. It is provided closed-form corrections to the very useful and long-time used analytical expressions from the linear potential theory. Better approximations can be obtained from more complete models for the development and shedding of the LEV, but at the cost of more parameters to be adjusted experimentally and probably not in a closed simple form.

A FLAPPING UNDULATORY AIRFOIL 4

4.1 INTRODUCTION

In the current chapter, the vortical impulse theory is extended to a flexible foil undergoing a quite general undulatory motion, of interest for the locomotion of a great variety of swimming and flying animals, to obtain analytical expressions for the lift, thrust, moment and propulsive efficiency. These general analytical expressions, which contain as a limit those previously obtained for a pitching and heaving rigid foil, are validated against available numerical results for some particular undulatory kinematics of the flexible foil. The analytical expressions are quite useful for characterizing the foil's kinematics that generate an optimal propulsion. In particular, it is included results for the case when a chordwise flexure mode is added to the motion of a heaving and of a pitching foil, characterizing the kinematic parameters that optimize both the thrust force and the propulsion efficiency in relation to the rigid heaving and the rigid pitching counterparts, respectively.

4.2 FORMULATION OF THE PROBLEM. KINEMATICS

In this case, superimposed to heaving and pitching motions (see Figure 4.1(a)), the plate undergoes an undulating motion with a given wavelength, defined below, and a quadratic flexure (or deflection) motion of trailing-edge amplitude δ_m (see figure Figure 4.1(b)). All the amplitudes remain small compared with the chord c, so that the airfoil, and every point of the trail of vortices that it leaves behind, may be considered to be on the horizontal plane $z = 0$ to a first approximation. In the reference frame translating with the plate at speed U along the x-axis, the vertical motion of the foil, given by the vertical displacement of its mean-chamber line z_s, can be written as

$$z_s(x,t) = h(x,t) - (x-a)\alpha(x,t) + (x-p)^2\delta(x,t), \quad -1 \le x \le 1, \tag{4.1}$$

with

$$h(x,t) = \Re\left[h_0 e^{ikt+\mathsf{b}(x+1)}\right], \quad \alpha(x,t) = \Re\left[\alpha_0 e^{ikt+\mathsf{b}(x+1)}\right], \quad \delta(x,t) = \Re\left[\delta_0 e^{ikt+\mathsf{b}(x+1)}\right], \tag{4.2}$$

$$\mathsf{b} = b_1 - ib_2, \tag{4.3}$$

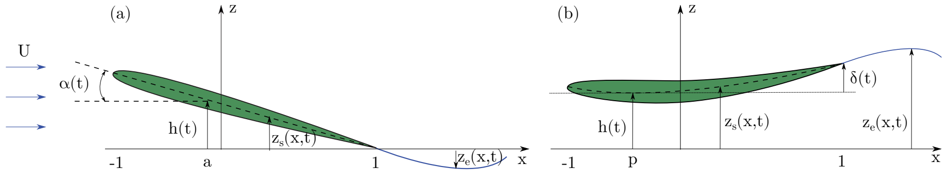

Figure 4.1: Schematic of the oscillating foil for heaving and pitching rigid motion (a) and for heaving and flexural motion (b), both in the absence of undulatory motion (i.e. for $\mathsf{b} = 0$). See (2.1)–(2.4) for the meaning of the various non-dimensional quantities.

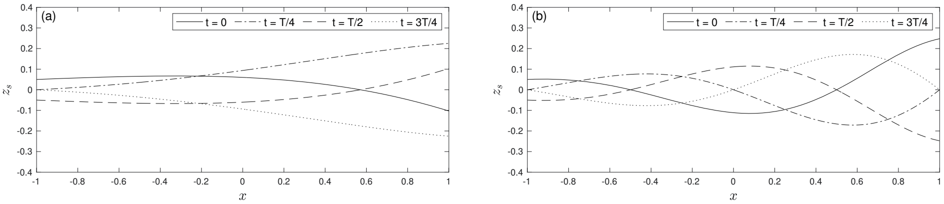

Figure 4.2: Non-dimensional vertical displacement $z_s(x,t)$ for an undulatory heaving motion ($\alpha_0 = \delta_0 = 0$) at different instants of the period's oscillation T for $h_0 = 0.05$ and $b_1 = 0.8$, with $b_2 = 1$ (a) and with $b_2 = \pi$ (b) (see (2.1)–(2.4) for the non-dimensional notation).

where k is the reduced frequency defined in (3.3) and, apart from the heaving, $h(x,t)$ and pitching, $\alpha(x,t)$ motions which in this case are functions of the position x, the function $\delta(x,t)$ is a quadratic deflection motion pivoting at $x = p$. Superimposed to each of these three displacements, it has been included an undulatory motion of the foil with non-dimensional wavenumber b_2 whose amplitude grows exponentially to the trailing edge with a non-dimensional factor b_1, both quantities grouped together in the complex number b. This form, motivated by the analysis of the carangiform fish dynamics by Lighthill, 1975, produces a travelling wave of growing amplitude that propagates from the leading edge to the trailing edge with non-dimensional phase speed k/b_2. Figure 4.2 shows some examples when the pitching and flexure motions are absent.

The amplitudes h_0, α_0 and δ_0 are, in general, complex constants satisfying $|h_0| \ll 1$, $|\alpha_0| \ll 1$ and $|\delta_0| \ll 1$. For simplicity it is selected h_0 real, α_0 is defined in (3.4) and

$$\delta_0 := \frac{\delta_m}{(1-p)^2} e^{i\psi}, \tag{4.4}$$

with ψ the phase shift between the heaving and deflection motions and δ_m the maximum amplitude of the flexure component of the motion at the trailing edge $(x = 1)$. In what follows it is shall worked with the complex expressions knowing that it will have to take the real part of the results. Equations (4.1)-(4.4) describe a fairly broad class of the flapping undulatory motion of a flexible or compliant foil, with nine non-dimensional kinematic parameters (plus the reduced frequency), for which it is shall derived analytical expressions for the force and moment using the impulse theory in the linear potential limit. General undulatory kinematics, with infinitely many wavenumbers, have been considered numerically by several authors both in the present small-amplitude inviscid limit (e.g. Alben, 2008; Moore, 2017; Tzezana and Breuer, 2019) and using direct numerical simulation of the Navier–Stokes equations (e.g. Hoover et al., 2018).

To facilitate the computations, the vertical displacement of the foil will be written as

$$z_s(x,t) = \left[\mathcal{F}(t) + \mathcal{E}(t)x + \mathcal{D}(t)x^2\right] e^{\mathsf{b}x}, \quad -1 \le x \le 1, \tag{4.5}$$

where $\mathcal{F}(t), \mathcal{E}(t)$, and $\mathcal{D}(t)$ are given by

$$\mathcal{F}(t) := \left(h_0 + b\alpha_0 + p^2\delta_0\right) e^{ikt+\mathsf{b}} := \mathcal{F}_0 e^{ikt+\mathsf{b}}, \tag{4.6}$$

$$\mathcal{E}(t) := -\left(\alpha_0 + 2p\delta_0\right) e^{ikt+\mathsf{b}} := \mathcal{E}_0 e^{ikt+\mathsf{b}}, \tag{4.7}$$

$$\mathcal{D}(t) := \delta_0 e^{ikt+\mathsf{b}}. \tag{4.8}$$

The corresponding non-dimensional vertical velocity of the foil's mean-chamber line can be written as

$$v_0(x,t) = \frac{\partial z_s}{\partial t} + \frac{\partial z_s}{\partial x} = \left[\mathcal{U}(t) + \mathcal{V}(t)x + \mathcal{C}(t)x^2\right] e^{\mathsf{b}x}, \quad -1 \le x \le 1, \tag{4.9}$$

where $\mathcal{U}(t), \mathcal{V}(t)$, and $\mathcal{C}(t)$ are given by

$$\mathcal{U}(t) := \{(ik + \mathsf{b})\mathcal{F}_0 + \mathcal{E}_0\}\, e^{ikt+\mathsf{b}} := \mathcal{U}_0 e^{ikt+\mathsf{b}}, \tag{4.10}$$

$$\mathcal{V}(t) := \{(ik + \mathsf{b})\mathcal{E}_0 + 2\delta_0\}\, e^{ikt+\mathsf{b}} := \mathcal{V}_0 e^{ikt+\mathsf{b}}, \tag{4.11}$$

$$\mathcal{C}(t) := (ik + \mathsf{b})\, \delta_0 e^{ikt+\mathsf{b}} := \mathcal{C}_0 e^{ikt+\mathsf{b}}. \tag{4.12}$$

4.3 GENERAL EXPRESSIONS FOR THE LIFT, THRUST, MOMENT AND INPUT POWER

To obtain the forces, moment and input power it is used the vortical impulse theory for an incompressible and unbounded flow as to the chapter 3 but in this case without the presence of point vortices. So that, the drag and lift with the same assumptions (see §3.2.1 for more details) are given by,

$$D = \rho \frac{d}{dt} \int_{-1}^{1} z_s \varpi_s dx + \rho \frac{d}{dt} \int_{1}^{\infty} z_e \varpi_e dx, \tag{4.13}$$

$$L = -\rho \frac{d}{dt} \int_{-1}^{1} x \varpi_s dx - \rho \frac{d}{dt} \int_{1}^{\infty} x \varpi_e dx, \tag{4.14}$$

and the moment

$$M \simeq \frac{1}{2} \rho \frac{d}{dt} \left[\int_{-1}^{1} (x-a)^2 \varpi_s dx + \int_{1}^{\infty} (x-a)^2 \varpi_e dx \right]. \tag{4.15}$$

The input power remains same given by the equation (3.18), i.e.,

$$P = -\rho U \int_{-1}^{1} \varpi_s \frac{\partial z_s}{\partial t} dx - \rho \int_{-1}^{1} \left(\int_{x}^{1} \frac{\partial z_s}{\partial t} d\xi \right) \frac{\partial \varpi_s}{\partial t} dx. \tag{4.16}$$

On the other hand, in the case of the vorticity ditribution, now $\varpi_0(x,t)$ is decomposed into the following terms:

$$\varpi_s(x,t) = \varpi_0(x,t) + \varpi_{se}(x,t), \tag{4.17}$$

without the contribution of point vortices, and where $\Gamma_0(t)$ remains same given by (3.20). Apart from that, the Kelvin's circulation theorem, in this case, is composed of the following terms

$$\Gamma_0 + \Gamma_{se} + \int_{1}^{\infty} \varpi_e dx = 0, \tag{4.18}$$

with $\Gamma_{se}(t)$ given by (3.22). To obtain $\varpi_0(x,t)$ and $\varpi_{se}(x,t)$, one has to solved the integral equations (3.26) and (3.27), obtaining the same solution for $\varpi_{se}(x,t)$ and consequetly for $\Gamma_{se}(t)$ given by (3.30) and (3.34), respectively. However, in the case of $\varpi_0(x,t)$,

$$\varpi_0(x,t) = \frac{1}{\sqrt{1-x^2}} \left\{ \frac{\Gamma_0(t)}{\pi} - \frac{2}{\pi} \int_{-1}^{1} \frac{\sqrt{1-\xi^2}}{\xi - x} \left[\mathcal{U}(t) + \mathcal{V}(t)\xi + \mathcal{C}(t)\xi^2 \right] e^{\mathsf{b}\xi} d\xi \right\}, \tag{4.19}$$

where the regularity of $\varpi_s(x,t)$ at its corresponding trailing edge $x = 1$, or Kutta condition, has been applied. In addition, substituting in the equations (3.20) one obtains

$$\Gamma_0(t) = -2\pi \left\{ \mathcal{U}(t) I_0(\mathsf{b}) + \left[\mathcal{U}(t) + \left(1 + \frac{1}{\mathsf{b}}\right) (\mathcal{V}(t) + \mathcal{C}(t)) \right] I_1(\mathsf{b}) + \right. \tag{4.20}$$

$$\left. \left[\mathcal{V}(t) + \mathcal{C}(t) \left(1 - \frac{1}{\mathsf{b}}\right) \right] I_2(\mathsf{b}) \right\}, \tag{4.21}$$

where $I_n(\mathsf{b}), n = 0, 1, 2$ is the modified Bessel function of the first kind and order n (Olver et al., 2010) applied to the complex number b. Finally, $\varpi_e(x,t)$ remains same and given by (3.80).

4.3.1 *Lift, thrust moment and input power*

Taking into account (4.14), the lift in non-dimensional form is given directly by (3.41) whose solution is

$$C_L = -2\pi \frac{ik}{\mathsf{b}} \left[\Big(\mathcal{U}+\mathcal{C}\Big) I_1(\mathsf{b}) + \left(\mathcal{V}-\frac{3}{\mathsf{b}}\mathcal{C}\right) I_2(\mathsf{b}) \right] + \Gamma_0 C(k). \tag{4.22}$$

In the case of the thrust, or minus the drag (4.13), in non-dimensional form can be written as

$$\begin{aligned} C_T = -\frac{d}{dt}\Big\{ & \Re[\Gamma_0]\times\Re[\mathcal{Q}(\mathcal{F},\mathcal{E},\mathcal{D})] + \Re[\mathcal{U}]\times\Re[\Omega_0(\mathcal{F},\mathcal{E},\mathcal{D})] + \Re[\mathcal{V}]\times\Re[\Omega_1(\mathcal{F},\mathcal{E},\mathcal{D})] + \\ & \Re[\mathcal{C}]\times\Re[\Omega_2(\mathcal{F},\mathcal{E},\mathcal{D})]\Big\} - \frac{2k}{\pi}\Re[\Gamma_0 C_1(k)]\times\Re\left\{[\mathcal{F}+\mathcal{E}+\mathcal{D}]\,e^{\mathsf{b}}\right\}, \end{aligned} \tag{4.23}$$

where the function $C_1(k)$ is defined in (A.32) in the Appendix A, and the functions $\mathcal{Q}$, Ω_n and $C_1(k)$ are defined as

$$\mathcal{Q}(\tilde{a},\tilde{b},\tilde{c}) := \tilde{a}\,(I_0(\mathsf{b}) + \mathcal{J}_0) + \tilde{b}\,(I_1(\mathsf{b}) + \mathcal{J}_1) + \tilde{c}\left(\frac{I_1(\mathsf{b})}{\mathsf{b}} + I_2(\mathsf{b}) + \mathcal{J}_2\right), \tag{4.24}$$

$$\Omega_n(\tilde{a},\tilde{b},\tilde{c}) := \tilde{a}\mathcal{I}_{0,n} + \tilde{b}\mathcal{I}_{1,n} + \tilde{c}\mathcal{I}_{2,n}, \tag{4.25}$$

with $\mathcal{I}_{n,m}(\mathsf{b})$ and $\mathcal{J}_n(\mathsf{b},k)$ defined in (A.14) and (A.17), respectively, are integrals that, in general, have to be solved numerically.

For the moment, taking into account (4.15), it in non-dimensional form is given directly by (3.55) without the contribution of point vortices, whose solution is

$$\begin{aligned} C_M = \frac{\Gamma_0}{2}\left[C(k)\left(\frac{1}{2}+a\right)-1\right] - \frac{\pi}{\mathsf{b}}(ika+1)\left[\Big(\mathcal{U}+\mathcal{C}\Big)I_1(\mathsf{b}) + \left(\mathcal{V}-\frac{3}{\mathsf{a}}\mathcal{C}\right)I_2(\mathsf{b})\right] + \\ \frac{\pi ik}{2\mathsf{b}^2}\left\{\Big[\mathcal{V}+\mathsf{b}\Big(\mathcal{U}+\mathcal{C}\Big)\Big]I_2(\mathsf{b}) + \big[\mathsf{b}\mathcal{V}-3\mathcal{C}\big]I_3(\mathsf{b})\right\}. \end{aligned} \tag{4.26}$$

Finally, the input power in non-dimensional form, are given by

$$\begin{aligned} C_P = -\Re[\Gamma_0]\times\Re[\mathcal{Q}(\dot{\mathcal{F}},\dot{\mathcal{E}},\dot{\mathcal{D}})] - \Re[\mathcal{H}]\times\Re\,[\Gamma_0 C_1(k)] + \Re[\dot{\Gamma}_0]\times\Re[\mathcal{Q}(g_1,g_2,g_3)] - \\ \Re[\mathcal{U}]\times\Re[\Omega_0(\dot{\mathcal{F}},\dot{\mathcal{E}},\dot{\mathcal{D}})] - \Re[\mathcal{V}]\times\Re[\Omega_1(\dot{\mathcal{F}},\dot{\mathcal{E}},\dot{\mathcal{D}})] - \Re[\mathcal{C}]\times\Re[\Omega_2(\dot{\mathcal{F}},\dot{\mathcal{E}},\dot{\mathcal{D}})] + \\ \Re[\dot{\mathcal{U}}]\times\Re[\Omega_0(g_1,g_2,g_3)] + \Re[\dot{\mathcal{V}}]\times\Re[\Omega_1(g_1,g_2,g_3)] + \Re[\dot{\mathcal{C}}]\times\Re[\Omega_2(g_1,g_2,g_3)], \end{aligned} \tag{4.27}$$

where a dot denotes the time derivative, and the functions $\mathcal{H}$, g_1, g_2 and g_3 are defined as

$$\mathcal{H} := \frac{e^{\mathsf{b}}}{\mathsf{b}^2}\left\{\left[2\left(1-\frac{1}{\mathsf{b}}\right)-\mathsf{b}\right]\mathcal{D} + (1-\mathsf{b})\mathcal{E} - \mathsf{b}\mathcal{F}\right\}, \tag{4.28}$$

$$g_1 := \frac{1}{\mathsf{b}^3}\left[2\mathcal{D} + \mathsf{b}(\mathsf{b}\mathcal{F}-\mathcal{E})\right], \quad g_2 := \frac{1}{\mathsf{b}^2}(\mathsf{b}\mathcal{E}-2\mathcal{D}), \quad g_3 := \frac{\mathcal{D}}{\mathsf{b}}. \tag{4.29}$$

4.4 FIRST OSCILLATION MODE OF A FLEXIBLE PLATE

The special case with $\mathsf{b} = 0$ corresponds to a quadratic flexural motion of a heaving and pitching foil, which is of particular interest because it is equivalent to the first oscillation mode of a flexible foil. The corresponding expressions for the lift, thrust, moment and input power are obtained by making the limit $\mathsf{b} \to 0$ in the above expressions.

For the lift one obtains

$$C_L = \pi \left[\dot{\alpha} + 2p\dot{\delta} - \ddot{h} - a\ddot{\alpha} - \left(p^2 + \frac{1}{4}\right)\ddot{\delta}\right] + \Gamma_0 C(k), \tag{4.30}$$

where Γ_0 now can be written as

$$\Gamma_0 = -2\pi \left[\dot{h} - \alpha + \left(a - \frac{1}{2}\right)\dot{\alpha} + (1-2p)\delta + \left(p^2 - p + \frac{1}{2}\right)\dot{\delta}\right]. \tag{4.31}$$

When $\delta_m = 0$ this expression coincides with the lift coefficient obtained by von Kármán and Sears, 1938, using the present impulse theory, and previously by Theodorsen, 1935, from a more standard potential flow approach.

For the thrust, the functions $\mathcal{Q}$ and Ω_n become

$$\lim_{\mathsf{b}\to 0} \mathcal{Q}(\tilde{a},\tilde{b},\tilde{c}) = \frac{i\tilde{b}}{k}C(k) + \left[\left(\frac{1+ik}{k}\right)\tilde{b} + i\tilde{a} + \left(\frac{2+ik}{k} - \frac{2i}{k^2}\right)\tilde{c}\right]\frac{2}{\pi}C_1(k) + \frac{\tilde{c}}{k}C_2(k), \tag{4.32}$$

$$\lim_{\mathsf{b}\to 0} \Omega_0(\tilde{a},\tilde{b},\tilde{c}) = \tilde{b}\pi, \quad \lim_{\mathsf{b}\to 0} \Omega_1(\tilde{a},\tilde{b},\tilde{c}) = \tilde{c}\frac{\pi}{4}, \quad \lim_{\mathsf{b}\to 0} \Omega_2(\tilde{a},\tilde{b},\tilde{c}) = \tilde{b}\frac{\pi}{4}, \tag{4.33}$$

where $C_2(k)$ is defined in (A.33). Consequently, the thrust coefficient can be written as

$$\begin{aligned} C_T = {} & -\Re\left[\alpha + 2p\delta\right] \times C_L + \frac{\pi}{2}\left\{\Re[\delta] \times \Re\left[\frac{\ddot{\alpha}}{2} + p\ddot{\delta} - \dot{\delta}\right] + \Re[\dot{\delta}] \times \Re\left[\frac{\dot{\alpha}}{2} + p\dot{\delta} - \delta\right]\right\} + \\ & \Re\left[\dot{\alpha} + 2p\dot{\delta}\right] \times \Re\left\{\pi\left[\dot{h} + a\dot{\alpha} + \left(p^2 + \frac{1}{4}\right)\dot{\delta} - (\alpha + 2p\delta)\right] + \Gamma_0\left[\frac{i}{k}C + \left(\frac{1+ik}{k}\right)\frac{2}{\pi}C_1\right]\right\} + \\ & \Re\left[\dot{h} + a\dot{\alpha} - (\alpha + 2p\delta) + p^2\dot{\delta}\right] \times \Re\left[\Gamma_0\frac{-2i}{\pi}C_1\right] + \Re[\delta] \times \Re\left[\Gamma_0\left(-iC_2 - 2\frac{1+ik}{k}\frac{2}{\pi}C_1\right)\right] + \\ & \Re[\dot{\delta}] \times \Re\left\{\Gamma_0\left[\left(\frac{2i}{k^2} - \frac{2+ik}{k}\right)\frac{2}{\pi}C_1 - \frac{C_2}{k}\right]\right\}. \end{aligned} \tag{4.34}$$

The complex form of this expression coincides with the thrust obtained by Fernandez-Feria, 2016, when $\delta_m = 0$, though here the real part of the nonlinear expression is separated in a slightly different form.

The moment coefficient becomes

$$\begin{aligned} C_M = {} & \frac{\Gamma_0}{2}\left(\frac{1}{2} + a\right)C(k) - \frac{\pi}{2}\left\{\left(\frac{1}{2} - a\right)\dot{\alpha} + a\ddot{h} + \left(\frac{1}{8} + a^2\right)\ddot{\alpha} + \right. \\ & \left.\left[\frac{p}{4} + a\left(p^2 + \frac{1}{4}\right)\right]\ddot{\delta} + \left[\left(\frac{1}{2} - a\right)p - 1\right]\frac{\dot{\delta}}{2} - \delta\right\}. \end{aligned} \tag{4.35}$$

As in the case of the lift, the above expression coincides with the moment obtained by von Kármán and Sears, 1938, when $\delta_m = 0$. Finally, the input power coefficient can be written in the physically relevant form

$$C_P = -\dot{h}(t)C_L - 2\dot{\alpha}(t)C_M - \dot{\delta}(t)C_F, \tag{4.36}$$

where C_F is defined as a flexural coefficient given by

$$\begin{aligned} C_F =& p\left(4C_{Mp} - pC_L\right) + \frac{C_{L2}}{2} + \int_{-1}^{1} x^2 \varpi_0(x,t) dx - \frac{1}{3}\frac{d}{dt}\int_{-1}^{1} x^3 \varpi_0(x,t) dx \\ =& p\left(4C_{Mp} - pC_L\right) + \frac{1}{2}\Gamma_0 C(k) - \frac{\pi}{4}\left[\ddot{h} + a\ddot{\alpha} + \left(p^2 + \frac{1}{3}\right)\ddot{\delta} - 2\delta\right], \end{aligned} \tag{4.37}$$

with $C_{Mp} := C_M(a = p)$ is the moment coefficient but in relation to the point $x = p$, where the flexure component of the motion vanishes, i.e, doing $a = p$ in the first term of (3.55). It must be noted that, to obtain the above input power coefficient, the limit $\mathsf{b} \rightarrow 0$ in the double integral appearing in (4.16), which now can be written as

$$\int_{-1}^{1}\left(\int_{x}^{1}\frac{\partial z_s}{\partial t} d\xi\right)\frac{\partial \varpi_s}{\partial t} dx = \int_{-1}^{1}\left[\mathcal{H} + \left(g_1 + g_2 x + g_3 x^2\right)e^{\mathsf{b}x}\right]\frac{\partial \varpi_s}{\partial t} dx, \tag{4.38}$$

has to be done collectively to all the terms inside the integrand, because the functions $\mathcal{H}$, g_1, g_2 and g_3 diverge separately as $\mathsf{b} \rightarrow 0$, but together

$$\lim_{\mathsf{b}\rightarrow 0}\left[\mathcal{H} + \left(g_1 + g_2 x + g_3 x^2\right)e^{\mathsf{b}x}\right] = \mathcal{F}(x-1) + \frac{\mathcal{E}}{2}\left(x^2 - 1\right) + \frac{\mathcal{D}}{3}\left(x^3 - 1\right). \tag{4.39}$$

Thus, the general expression (4.27) is valid when $b \neq 0$, and one has to use expression (4.36) when $\mathsf{b} = 0$. In a similar way, in the section A.4 of the Appendix A, it has been derivated the forces, moment and input power for a quartic deflection but taking the same pivot point for the pitching and deflection motion $(a = p)$.

4.4.1 *Time-averaged coefficients and propulsive efficiency*

The time-averaged coefficients (3.64) can now be written in simple closed forms. To that end it is convenient to define the following non-dimensional parameters to separate the different components of the foil's motion:

$$\theta := \frac{a_0}{kh_0}, \quad \theta_{hd} := \frac{\delta_m}{kh_0}, \quad \theta_{pd} := \frac{\delta_m}{a_0}, \tag{4.40}$$

where the first one, θ, is the well-known feathering parameter (Lighthill, 1969) for a pitching and heaving motion of a rigid foil. Thus, the time-averaged thrust coefficient can be written either normalized in relation to a pure heaving motion,

$$\begin{aligned} \hat{C}_{Th} := \frac{\bar{C}_T}{(kh_0)^2} = t_h(k) + t_{hp}(k,a,\phi)\theta + t_p(k,a)\theta^2 + \\ \left[t_{hd}(k,p,\psi) + t_{pd}(k,p,a,\psi,\phi)\theta k\right]\theta_{hd} + t_d(k,p)\theta_{hd}^2, \end{aligned} \tag{4.41}$$

or in relation to a pure pitching motion,

$$\begin{aligned} \hat{C}_{Tp} := \frac{\bar{C}_T}{a_0^2} = t_h(k)\theta^{-2} + t_{hp}(k,a,\phi)\theta^{-1} + t_p(k,a) + \\ \left[t_{hd}(k,p,\psi)\theta^{-1} + t_{pd}(k,p,a,\psi,\phi)\right]\theta_{pd} + t_d(k,p)\theta_{pd}^2, \end{aligned} \tag{4.42}$$

where the functios $t_h(k)$, $t_{hp}(k,a,\phi)$, $t_p(k,a)$, $t_{hd}(k,p,\psi)$, $t_{pd}(k,a,p,\phi,\psi)$ and $t_d(k,p)$ are giving by the equations (A.56)-(A.61) in the Appendix A. Note that for $\theta_{hd} = 0$ or $\theta_{pd} = 0$, these expressions do not coincide exactly with those for an oscillating rigid foil given in Fernandez-Feria, 2017, because here the real part of the complex nonlinear expression for the thrust force is separated in a slightly different way, but the results are practically indistinguishable.

The time-averaged input power coefficient is given by

$$\bar{C}_P = -\overline{\dot{h}(t)C_L} - 2\overline{\dot{\alpha}(t)C_M} - \overline{\dot{\delta}(t)C_F}, \tag{4.43}$$

which, similarly to the mean thrust coefficient, can be written in terms of the parameters (4.40) either as

$$\begin{aligned}\hat{C}_{Ph} := \frac{\bar{C}_P}{(kh_0)^2} = p_h(k) + p_{hp}(k,a,\phi)\theta + p_p(k,a)\theta^2 + \\ \Big[p_{hd}(k,p,\psi) + p_{pd}(k,p,a,\psi,\phi)\theta\Big]\,\theta_{hd} + p_d(k,p)\theta_{hd}^2,\end{aligned} \tag{4.44}$$

or as

$$\begin{aligned}\hat{C}_{Pp} := \frac{\bar{C}_P}{a_0^2} = p_h(k)\theta^{-2} + p_{hp}(k,a,\phi)\theta^{-1} + p_p(k,a) + \\ \Big[p_{hd}(k,p,\psi)\theta^{-1} + p_{pd}(k,p,a,\psi,\phi)\Big]\,\theta_{pd} + p_d(k,p)\theta_{pd}^2,\end{aligned} \tag{4.45}$$

where the functios $p_h(k)$, $p_{hp}(k,a,\phi)$, $p_p(k,a)$, $p_{hd}(k,p,\psi)$, $p_{pd}(k,a,p,\phi,\psi)$ and $p_d(k,p)$ are giving by the equations (A.63)-(A.68) in the Appendix A.

Finally, the propulsive efficiency (3.63) can be computed using any of the above alternative forms of $\bar{C}_T$ and $\bar{C}_P$. It is convenient to use a propulsive efficiency relative to that of a rigid oscillating foil, η_0:

$$\hat{\eta} := \eta - \eta_0, \quad \text{with} \quad \eta_0 := \frac{t_h(k) + t_{hp}(k,a,\phi)\theta + t_p(k,a)\theta^2}{p_h(k) + p_{hp}(k,a,\phi)\theta + p_p(k,a)\theta^2}. \tag{4.46}$$

4.5 MODEL VALIDATION

Before analysing in detail the results corresponding to the first oscillation mode of a flexible foil ($\mathsf{b} = 0$) considered in the previous section, it is convenient to validate the present theoretical results by comparing them with available numerical data for both $\mathsf{b} = 0$ and $\mathsf{b} \neq 0$.

It is first considered the numerical results of Le et al., 2010, who investigated the performance of a flapping wing with different chord flexures, corresponding, in the notation of the present model, to $\mathsf{b} = 0$ and $a_0 = 0$ (no pitching motion). Those authors reported results for different values of the flexure amplitude δ_m and the heave amplitude h_0, with varying phase shift ψ between the two components of the foil's motion. In particular, they considered the case of a plunging NACA0012 foil clamped at the leading edge (i.e. with $p = -1$ in our notation and without rotation at the leading edge) for $Re = 3 \times 10^4$.

Figure 4.3 compares the numerical results of Le et al., 2010, for the mean values of the thrust and input power coefficients, and for the propulsive efficiency, as functions of the phase shift ψ between the heaving and deflection motions, with the present theoretical results for two values of δ_m. For reference, the results for a rigid foil are also included, which are obviously independent of ψ. The agreement is quite good for the three mean magnitudes represented in all the range of values of ψ. But it should be noted that, since the computation of the input power is very sensitive to any temporal shift between the lift coefficient $C_L(t)$ obtained numerically and the vertical motion $\dot{h}(t)$, to fit $\bar{C}_P$ it has

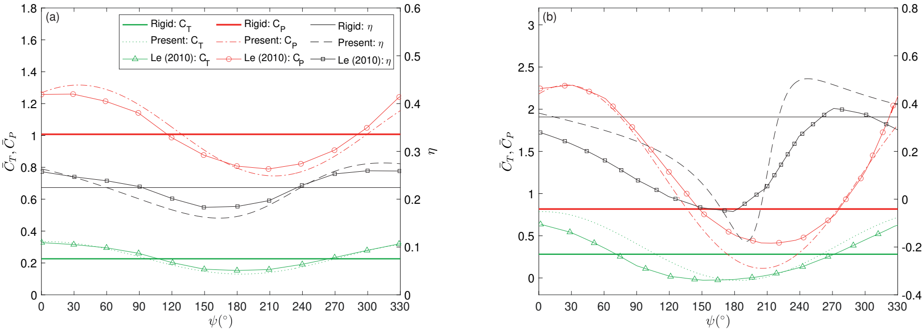

Figure 4.3: Comparison of the present results for the mean thrust, input power and efficiency with numerical results from Le et al., 2010, for pure heaving with deflection motion ($b = a_0 = 0$) with , $h_0 = 0.35$, $k = 1.82$, $p = -1$, $C_{T0} = -0.055$: (a) $\delta_m = 0.1$, with $\Delta t/T = -0.06$ for $\bar{C}_P$, for (b) $\delta_m = 0.4$, $\Delta t/T = -0.025$ for $\bar{C}_P$.

been included a very small temporal shift Δt in the lift when computing the mean value of C_P from our theoretical formulation as follows:

$$\bar{C}_P = -\frac{1}{T}\int_t^{t+T} \left[\dot{h}(t) C_L(t+\Delta t) + \dot{\delta}(t) C_F(t)\right] dt. \tag{4.47}$$

The values of Δt are given in the caption of Figure 4.3, together with all the kinematic parameters. In Figure 4.3(b), Δt is taken directly from $C_L(t)$ data in Le et al., 2010, which are not available for the case of Figure 4.3(a), and it is taken the values that best fit $\bar{C}_P$. These Δt are very small compared with the period T, justifying their use to compensate any small temporal shift in the computation of C_L from the numerical simulations. Note also the excellent agreement between the theoretical results for $\bar{C}_T$ and the numerical results obtained by Le et al., 2010, for any value of ψ, particularly in Figure 4.3(a) where the non-dimensional flexure amplitude δ_m is smaller.

Next it is considered the numerical results of Zhang et al., 2018, and of Dong and Lu, 2007, who analysed two different undulatory motions, i.e. with $b = 0$ in the present notation. As commented on in the Introduction, this kind of motion is commonly used to model fish locomotion. To put them into a biological context, the body or caudal fin of fishes can be classified into five groups that differ in the fraction of the body that is displaced laterally (coordinate z in the present notation) (Breder Jr, 1926): anguilliform (e.g. eels), sub-carangiform (e.g. trout), carangiform (e.g. jack mackerels), thunniform (e.g. tunas) and ostraciiform (e.g. boxfishes). Examples of three of these motions are plotted in Figure 4.4, with the corresponding values of the parameters in the present model given in Table 2. Also included are the values of the parameters corresponding to the selected numerical results of Zhang et al., 2018, and Dong and Lu, 2007, which are compared below with the present theoretical results, together with other references and some additional information about the numerical simulations.

Figure 4.5 compares the lift coefficient from the numerical results of Zhang et al., 2018, for several NACA profiles with the present theoretical results. The numerical results for the different foil thicknesses are all quite close to each other, and with a good agreement with the present zero-thickness theoretical results, with a slightly better agreement for the NACA-0016 profile, but for no particular reason.

Figure 4.6 compares the thrust coefficient computed numerically by Dong and Lu, 2007, with the present theoretical results, both the time-averaged values as a function of the reduced frequency k, and its temporal evolution during one cycle for $k = 1.5\pi$.

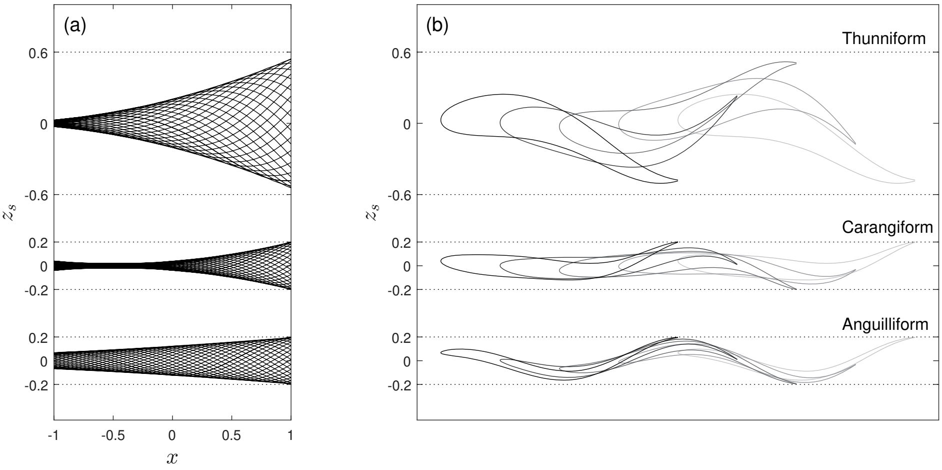

Figure 4.4: (a) Anguilliform, carangiform and thunniform motion at the mid-line. (b) Superimposed body outlines separated by $\Delta t/T = 0.25$. The corresponding values of the parameters of the present model and references are given in Table 2.

	h_0	a	a_0	ϕ	p	δm	ψ	a_1	a_2	k	Re
Anguiliform.	0	0	0	0	$-3,8243$	$0,1960$	0	0	π	$[0.5,2]\pi$	5000
	0.6346	4.1730	0.1212	π	0	0	0	0	π	$[0.3,1.3]\pi$	$[50,2\cdot 10^5]$
Carangiform.	$0,01906$	0	0	0	$-0,4923$	$0,18094$	0	0	π	$[0.5,2]\pi$	5000
	$0,1$	0	0	0	0	0	0	0.25	π	π & 2.5π	100
Thunniform.	0	0	0	0	-1.586	0.5549	0.1317	0	$\pi/1.67$	$[0.5,2]\pi$	$7.1[10^3,10^5]$

Table 2: Values of the kinematic parameters for the different motions considered in figures 4–6. Anguilliform from Tytell and Lauder, 2004, and Zhang et al., 2018, respectively; carangiform from Dong and Lu, 2007, and Zhang and Eldredge, 2009, respectively; thunniform from Chang, Zhang, and He, 2012.

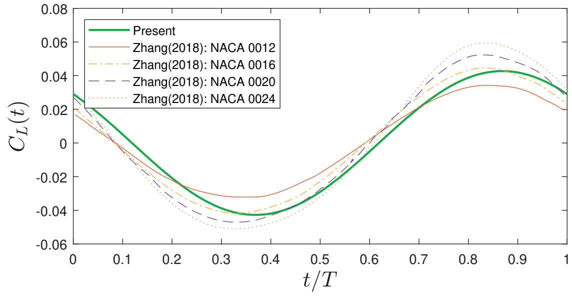

Figure 4.5: Anguilliform motion. Time-dependent lift coefficient during one cycle for $k = \pi$. Numerical results from figure 9(d) in Zhang et al., 2018, for $Re = 5 \times 10^4$. Note that those authors non-dimensionalize the lift as $L/(\rho U^2 c^2)$, so that the present $C_L/4$ is plotted. The corresponding values of the kinematic parameters in the present model are given in Table 2.

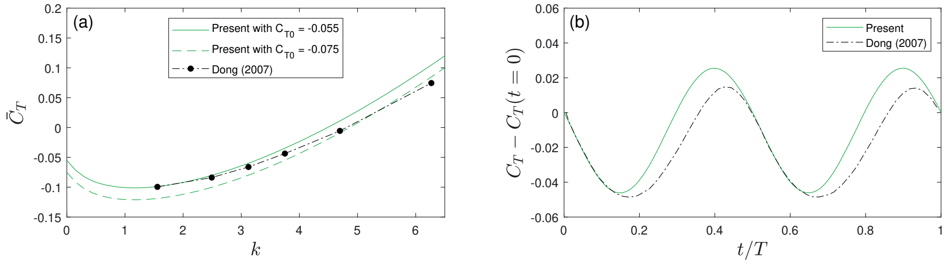

Figure 4.6: Carangiform motion. (a) Time-averaged thrust coefficient, $\bar{C}_T$, as a function of k, with two different values of the offset drag: $\bar{C}_{T0} = -0.055$ and -0.075. (b) Time-dependent thrust coefficient during one cycle for $k = 1.5\pi$. Numerical results from Dong and Lu, 2007. The corresponding values of the kinematic parameters in the present model are given in Table 2.

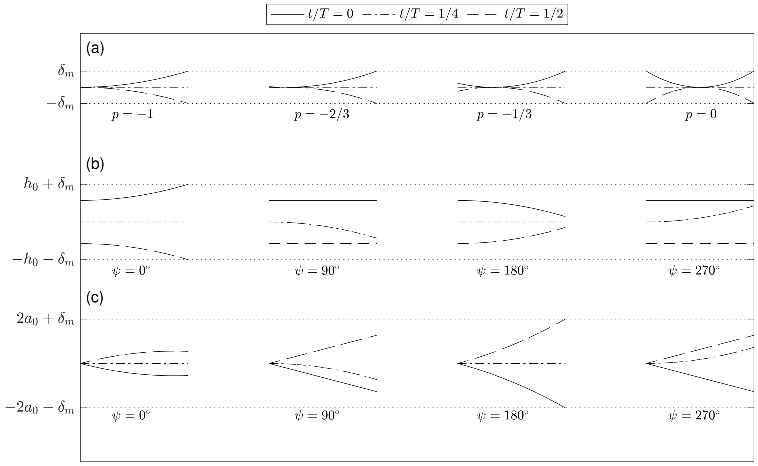

Figure 4.7: Kinematics schemes for pure flexural motion with different values of p (a), pure heaving motion with chordwise deflection for different values of ψ and $p = -1$ (b) and pure pitching motion with chordwise deflection for different values of ψ and $p = -1$ (c). In all cases the same three instants of time are plotted, as indicated.

As discussed in Fernandez-Feria, 2017, the mean values are corrected to account for the viscous drag by adding to the present theoretical results a quasi-static thrust $\bar{C}_{T0} < 0$ (i.e. by subtracting an offset quasi-static drag $-\bar{C}_{T0}$), corresponding to the numerical results for $k = 0$. Since those authors do not provide numerical results for $k = 0$, it has been selected two values of $\bar{C}_{T0}$ in Figure 4.6(a), one that yields a better fit for small values of k and the other one for higher values of k, though both values of $\bar{C}_{T0}$ are quite close to each other. Notice that no mean drag correction is needed in Figure 4.6(b) since it is plotted the instantaneous thrust coefficient minus its numerical value at $t = 0$, $C_T(t = 0)$.

4.6 RESULTS AND DISCUSSION FOR $b = 0$

Results with no undulatory motion (b = 0) are presented and discussed in this section. The kinematics of the three different cases considered are sketched in Figure 4.7.

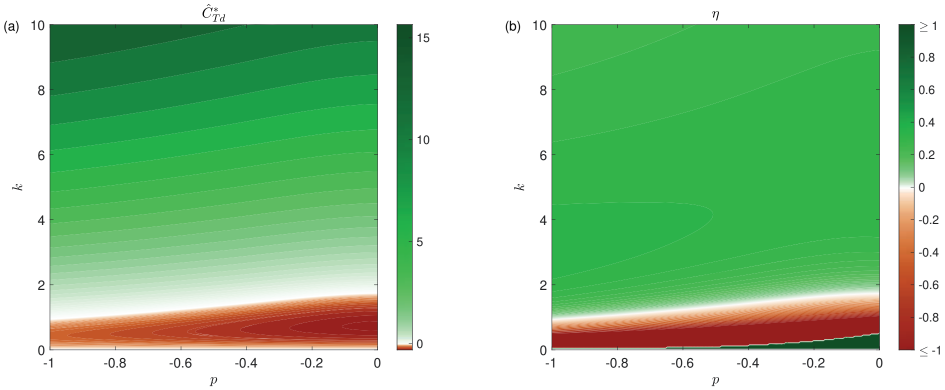

Figure 4.8: Contours of the normalized thrust $\hat{C}_{Td}$ (a) and efficiency η (b) on the (p, k)-plane in a pure flexural motion ($\mathrm{b} = h_0 = a_0 = 0$).

4.6.1 *Pure flexural motion*

It is considered first the simplest case of a pure flexural motion of the first oscillating mode, without heaving or pitching motions ($h_0 = 0$ and $a_0 = 0$). Note from (4.41) and (4.44) that in this case only the last terms of the thrust and power coefficients are different from zero, which are quadratic in the trailing-edge deflection amplitude δ_m. Thus, it is convenient to use the following normalized thrust and power coefficients

$$\hat{C}_{Td} := \frac{\bar{C}_T}{\delta_m^2} = t_d(k, p), \tag{4.48}$$

$$\hat{C}_{Pd} := \frac{\bar{C}_P}{\delta_m^2} = p_d(k, p), \tag{4.49}$$

where the functions t_d and p_d are given in Appendix A. The efficiency is $\eta = t_d / p_d$.

Figure 4.8 shows the contours of the normalized thrust $\hat{C}_{Td}$ and efficiency η as k and the location of the deflection pivot point p are varied. It is clear from this figure that no thrust is generated when $k \lesssim 1$ (i.e. $\hat{C}_{Td} < 0$). For $k \lesssim 1$, the maximum propulsive efficiency is always reached for a clamped leading edge ($p = -1$). This can be justified by the consideration that in this case all the bending of the foil is useful to generate thrust (see Figure 4.7(a)). For this reason it is only considered the cases with $p = -1$ in the results reported below when a heaving or a pitching motion is added to the flexural motion. The optimum value of the reduced frequency k in terms of propulsive efficiency for $p = -1$ is about 3.

4.6.2 *Pure heaving motion with chordwise deflection*

Next in complexity is the case of a pure heaving motion combined with a deflection motion of the foil, i.e. the first oscillation mode of a flexible airfoil for a pure heaving motion, for which (4.41) and (4.44) become

$$\hat{C}_{Th} = t_h(k) + t_{hd}(k, p, \psi)\theta_{hd} + t_d(k, p)\theta_{hd}^2, \tag{4.50}$$

$$\hat{C}_{Ph} = p_h(k) + p_{hd}(k, p, \psi)\theta_{hd} + p_d(k, p)\theta_{hd}^2, \tag{4.51}$$

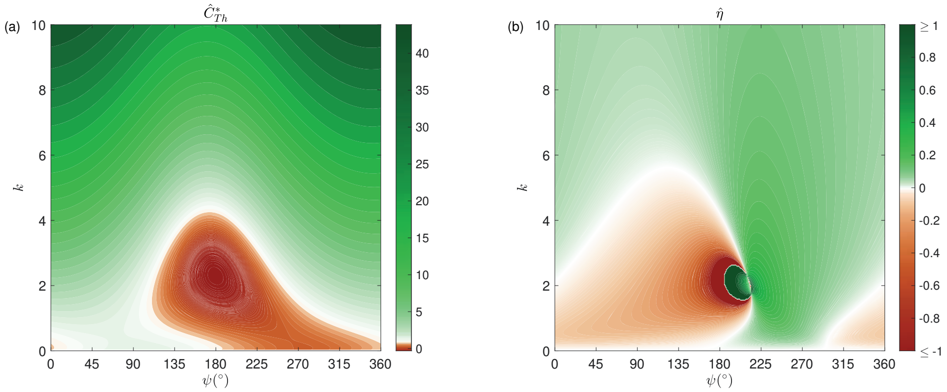

Figure 4.9: Contours of the normalized thrust $\hat{C}^*_{Th}$ (a) and efficiency $\hat{\eta}$ (b) on the (ψ, k)- plane for $\theta_{hd} = 0.75$ and $p = -1$ in a pure heaving and deflection motion ($\mathsf{b} = \theta = \theta_{pd} = 0$).

with the ratio θ_{hd} between the deflection and heaving amplitudes defined by (4.40) and the different functions given in Appendix A. To compare the thrust of the flexible foil with the thrust generated by its rigid counterpart, it is defined a normalized thrust as

$$\hat{C}^*_{Th} := \frac{\hat{C}_{Th}}{t_h(k)}, \tag{4.52}$$

which only depends on the non-dimensional parameters k, p, ψ and θ_{hd}, as does the normalized efficiency $\hat{\eta}$ defined in (4.46). In order to reduce further the number of parameters it is focused on the case of a clamped leading edge, i.e. $p = -1$, which was shown in §4.6.1 to yield the best propulsion efficiency.

Figure 4.9 shows the contours of the normalized thrust $\hat{C}^*_{Th}$ and efficiency $\hat{\eta}$ as k and ψ are varied with $\theta_{hd} = 0.75$. It is observed that, for $1 \lesssim k \lesssim 4$, the flexible foil generates more thrust than the rigid airfoil ($\hat{C}^*_{Th} > 1$) when $250^o \lesssim \psi \lesssim 100^o$, and less when $100^\circ \lesssim \psi \lesssim 250^\circ$. In fact, a phase shift ψ between 100° and 250°, approximately, corresponds to a motion of the foil with the trailing edge pointing downwards at the beginning of the downstroke, and opposite at the beginning of the upstroke (see Figure 4.7(b)), generating less thrust than its rigid counterpart. In relation to the efficiency, Figure 4.9(b) shows that the model yields a singularity for a particular combination of k and ψ due to the vanishing of the power coefficient in the present model, where η changes from $+\infty$ to $-\infty$, so that it is expected that close to this curve on the (ψ, k)-plane the propulsive efficiency reaches a local maximum, greatly enhancing the propulsive efficiency of a rigid heaving foil. For k of order unity this corresponds, approximately, to ψ between 250° and 270°.

To see the effect of θ_{hd} it is plotted the curves on the (ψ, k)-plane corresponding to $\hat{C}^*_{Th} = 1$ in Figure 4.10(a), and both the curves corresponding to $\hat{\eta} = 0$ and $\hat{\eta} = 1$ (i.e. close to the singularity) in Figure 4.10(b), for $0 < \theta_{hd} \leq 1$. Figure 4.10(a) shows that the regions of enhanced and reduced thrust in relation to a heaving rigid foil remain almost independent of θ_{hd} for k of order unity. For the efficiency (Figure 4.10b) the situation is somewhat similar, but the singularity moves towards smaller values of k as θ_{hd} increases. Thus, the present model predicts a maximum enhancement of the propulsive efficiency in relation to a rigid heaving foil when $k \approx 1$ for θ_{hd} approaching unity and $\psi \approx 260^\circ$. This result is in qualitative agreement with the experimental results of Ramananarivo, Godoy-Diana, and Thiria, 2011, for a similar foil motion, where the maximum efficiency

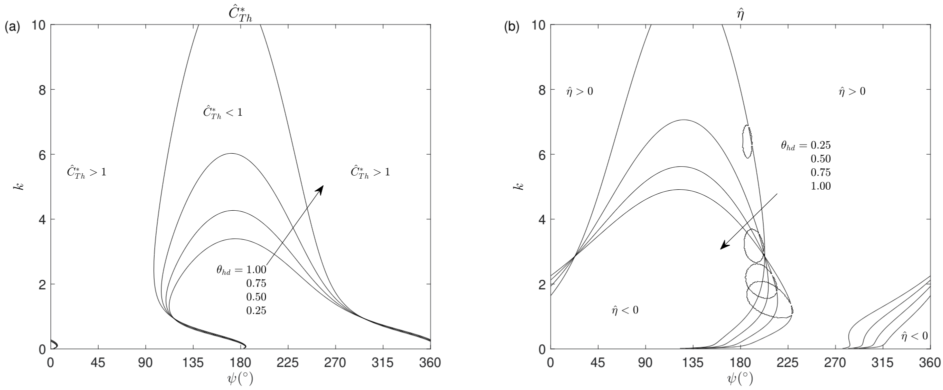

Figure 4.10: $\hat{C}^*_{Th} = 1$ (a), and both $\hat{\eta} = 0$ and $\hat{\eta} = 1$ (b) on the (ψ, k)-plane for pure heaving and deflection motion $(\mathrm{b} = \theta = \theta_{pd} = 0)$ with $0 < \theta_{hd} \leq 1$ and $p = -1$.

is found to be reached when the trailing-edge deflection angle is approximately equal to the effective angle of attack at the mid-downstroke, which is the situation for ψ approaching 270° in Figure 4.7(b).

4.6.3 *Pure pitching motion with chordwise deflection*

As the third simple case, it is considered a pure pitching motion combined with a deflection motion of the foil, i.e. the first oscillation mode of a flexible airfoil for pure pitching motion, for which (4.42) and (4.45) become

$$\hat{C}_{Tp} = t_p(k, a) + t_{pd}(k, p, a, \psi, \phi)\theta_{pd} + t_d(k, p)\theta_{pd}^2, \tag{4.53}$$

$$\hat{C}_{Pp} = p_p(k, a) + p_{pd}(k, p, a, \psi, \phi)\theta_{pd} + p_d(k, p)\theta_{pd}^2, \tag{4.54}$$

with the ratio θ_{pd} between the deflection and pitching amplitudes defined in (4.40). Since the thrust of a rigid plate may change its sign for a pure pitching motion, to avoid singularities it is convenient to redefine the normalized thrust coefficient in this case as

$$\hat{C}^*_{Tp} := \hat{C}_{Tp} - t_p(k, a). \tag{4.55}$$

Now $\hat{C}^*_{Tp} = 0$ means the same thrust coefficient as that of the equivalent pitching rigid foil. The definition of the normalized efficiency (4.46) does not change. Both $\hat{C}^*_{Tp}$ and $\hat{\eta}$ depend on the non-dimensional parameters k, a, p, ψ and θ_{pd} (note that one may set $\phi = 0$ since there is no heaving motion, and ψ is now the phase shift of the deflection in relation to the pitch). Similarly to the previous case, to reduce the number of parameters it is focused on a deflection pivoting at the leading edge $(p = -1)$, which in the present case implies also a pitching motion about the leading edge, i.e. $a = p = -1$.

Figure 4.11 shows the contours of the normalized thrust $\hat{C}^*_{Tp}$ and efficiency $\hat{\eta}$ on the (ψ, k)-plane for $\theta_{pd} = 0.75$. For the thrust (Figure 4.11a) it can be distinguished two regions: one for small k with two maxima of the relative thrust, around $\psi = 0$ and for $\psi = 270°$, and another region for $k \gtrsim 1$ where the enhanced thrust is for $90° \lesssim \psi \lesssim 270°$. Figure 4.11(b) shows that these regions approximately coincide with those of enhanced efficiency.

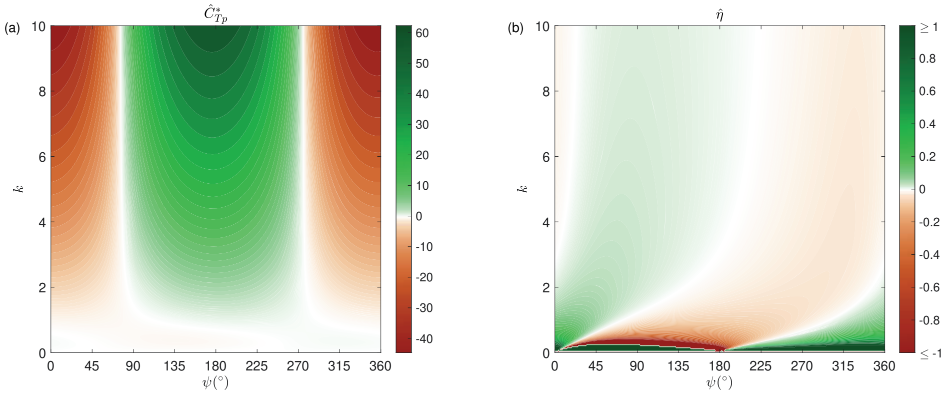

Figure 4.11: Contours of the normalized thrust $\hat{C}^*_{Tp}$ (a) and efficiency $\hat{\eta}$ (b) on the (ψ, k)- plane for $\theta_{pd} = 0.75$ and $a = p = -1$ in a pure pitching and deflection motion $(\mathsf{b} = \theta^{-1} = \theta_{hd} = 0)$.

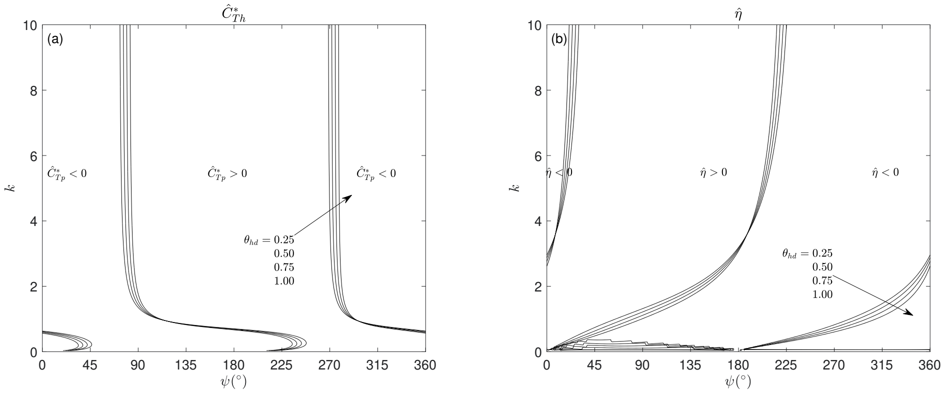

Figure 4.12: $\hat{C}^*_{Tp} = 0$ (a) and $\hat{\eta} = 0$ (b) on the (ψ, k)-plane for pure pitching and deflection motion $(\mathsf{b} = \theta^{-1} = \theta_{hd} = 0)$ with $0 < \theta_{pd} \leq 1$ and $a = p = -1$.

The effect of θ_{pd} is plotted in Figure 4.12 as curves corresponding to $\hat{C}^*_{Tp} = 0$ and $\hat{\eta} = 0$ on the (ψ, k)-plane for $0 < \theta_{pd} \leq 1$. The regions of enhanced and reduced thrust in relation to a pitching rigid foil are nearly independent of θ_{pd}, with larger variations as k increases. However, in contrast to the pure heaving motion, the regions of positive and negative relative efficiency $\hat{\eta}$ remain practically unchanged as θ_{pd} varies from zero to unity (Figure 4.12b). Therefore, the above discussed region of maximum enhancement in the propulsive efficiency of a flexible foil in relation to a pitching rigid foil about its leading edge remains practically independent of the trailing-edge deflection amplitude in relation to the pitch amplitude, within the present linearized potential theory valid for small amplitudes.

4.7 CONCLUDING REMARKS

The closed expressions obtained in the present chapter for the aerodynamic force components and moment on a two-dimensional flexible foil undergoing a quite general undulatory motion, which are validated against available numerical results for sufficiently high Reynolds numbers and small amplitude of the oscillations, constitute a convenient tool for predicting and evaluating the optimal conditions for propulsion in terms of thrust generation and efficiency in a wide range of animal and bioinspired robotic locomotion.

Relatively simple analytic expressions are obtained for the interesting cases of pitching and heaving motions superimposed to a chordwise quadratic deflection of the foil, with the additional force and moment terms in relation to an oscillating rigid foil neatly separated, and characterized by the ratio between the amplitudes of the deflection and the rigid motions. When this non-dimensional parameter vanishes one recovers previous results for a pitching and heaving rigid foil. A detailed evaluation of the propulsion performance is made for these particular cases, mapping the regions of thrust and of propulsive efficiency enhancement in relation to the rigid foil counterpart in the parameter space of the reduced frequency and the relevant deflection parameters.

The present results are limited to small amplitudes of the oscillations and sufficiently high Reynolds number for which the linearized potential theory applies. In addition, no analysis is made of the fluid–structure interaction that may produce the particular deflection or undulatory motion of the foil, which it is not the objective of this thesis.

5

NUMERICAL SIMULATION OF A FLAPPING AIRFOIL

5.1 INTRODUCTION

In the previous chapters, the potential flow theory has been extended for a flapping airfoil with the presence of leading-edge vortices and when the airfoil has a preescribed deflection motion coupled with the heaving and pitching motions. All of this, based in the vortical impulse theory and with the main assumptions of considering high Reynolds number and small oscillating amplitudes. So that, in order to find the range of validity of the developed theory, in terms of Reynolds number or oscillating amplitudes, in the present chapter, it has been implemented a numerical simulation of a flapping airfoil comparing with the theory and avalaible data in the bibliography. In addition, it has been developed the main equations in terms of vorticity and stream-function which have to be solved to do a numerical simulation of a flapping airfoil in a non-inertial reference frame, fitting a NACA-0012 with a conformal mapping.

5.2 FORMULATION OF THE PROBLEM

It is considered a two-dimensional (2D) and incompressible flow over a heaving and pitching airfoil of chord length c that moves with constant speed U along the negative x-axis (see figure 5.1). In this reference frame, the motion of the airfoil is given by the vertical displacement of its mean-camber line, i.e.,

$$\mathbf{z}_0(\mathbf{x},t) = h(t)\mathbf{e}_y + \alpha(t)\wedge\mathbf{x}, \quad \text{with} \quad \mathbf{x} = (x-\tilde{a})\mathbf{e}_x + y\mathbf{e}_y, \tag{5.1}$$

and

$$h(t) = \tilde{h}_0\cos(2kt), \quad \alpha(t) = a_0\cos(2kt+\phi), \tag{5.2}$$

where k is the reduced frequency defined in (3.3), with nondimensional period $T = \pi/k$, which consists of a heaving displacement $h(t)$ of amplitude $\tilde{h}_0$ and a pitching rotation $\alpha(t)$ of amplitude a_0 pivoting at $x = \tilde{a}$ with ϕ the phase shift between the heaving and pitching motions of the foil. Note that, now the nondimensional coordinate $\mathbf{x}$ and the amplitude of heaving motion, $\tilde{h}_0$, is scaled with the foil's chord length c ($h_0 = 2\tilde{h}_0$, $a = 2\tilde{a}$), and the time t with c/U. Thus, the corresponding nondimensional velocity of the airfoil, scaled with the velocity U, is given by

$$\mathbf{v}_0(\mathbf{x},t) = -\mathbf{e}_x + \frac{dh}{dt}\mathbf{e}_y + \boldsymbol{\Omega}(t)\wedge\mathbf{x}, \tag{5.3}$$

where $\boldsymbol{\Omega}(t) = \frac{d\alpha}{dt}\mathbf{e}_z$ is the pitching rotation velocity, which in a non-inertial frame, the airfoil does not move and the fluid domain is moving with the opposite velocity of the airfoil, i.e,

$$\mathbf{u}_\infty(\mathbf{x},t) = -\mathbf{v}_0(\mathbf{x},t). \tag{5.4}$$

As a consequence, the fluid field velocity can be decomposed into two terms,

$$\mathbf{u} = \mathbf{u}_\infty + \mathbf{u}', \tag{5.5}$$

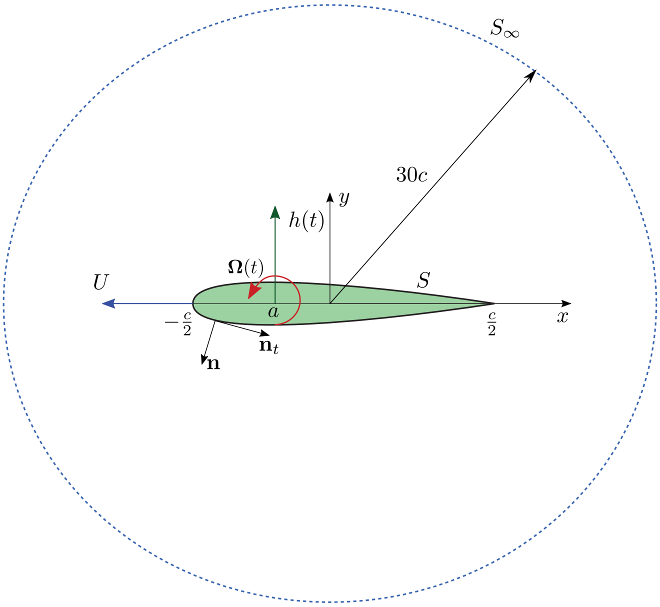

Figure 5.1: Schematic of the heaving and pitching airfoil bounded by S and the integration domain delimited by the surfaces S_∞.

where $\mathbf{u}'$ is the disturbance in the fluid field velocity. To characterize the motion of the airfoil with the kinematics parameters it is selected the Strouhal number based it in the amplitude of the trailing edge, i.e.,

$$St = \frac{fA}{U}, \tag{5.6}$$

where f is the frequency of the motion, A is the peak-to-peak excursion of the airfoil's trailing-edge and U the translating speed. For pure heaving and pure pitching motion, the Strouhal number can be written respectively as

$$St_{heave} = \frac{kh_0}{\pi}, \quad St_{pitch} = \frac{k}{\pi}(1-a)\sin(a_0). \tag{5.7}$$

5.2.1 *Governing equations*

In the non-inertial frame, the non-dimensional Navier–Stokes equations are written as

$$\frac{\partial \mathbf{u}}{\partial t} = -\frac{1}{2}\nabla p - \mathbf{u}\cdot\nabla\mathbf{u} + \frac{1}{Re}\nabla^2\mathbf{u} - \mathbf{a}_z - \mathbf{a}_{Cor} - \mathbf{a}_{tan} - \mathbf{a}_{cen}, \tag{5.8}$$

where p is the pressure (without the hydrostatic component) scaled with $\rho U^2/2$ where ρ is the fluid density, Re the Reynolds number based in the chord length of the airfoil, $\mathbf{a}_y$ the heaving motion acceleration, $\mathbf{a}_{Cor} = 2\mathbf{\Omega}\wedge\mathbf{u}$ the Coriolis acceleration, $\mathbf{a}_{tan} = \frac{d\mathbf{\Omega}}{dt}\wedge\mathbf{x}$ the tangential acceleration and $\mathbf{a}_{cen} = \mathbf{\Omega}\wedge(\mathbf{\Omega}\wedge\mathbf{x})$ is the centrifugal acceleration. Using the expresion of the two-dimensional vorticity $\boldsymbol{\omega} = (\nabla\wedge\mathbf{u})\mathbf{e}_z$ and noting that the rotational of the different accelerations are

$$\nabla\wedge(\mathbf{a}_z) = \nabla\wedge(\mathbf{a}_{Cor}) = \nabla\wedge(\mathbf{a}_{cen}) = 0, \quad \nabla\wedge(\mathbf{a}_{tan}) = 2\frac{d\mathbf{\Omega}}{dt}, \tag{5.9}$$

with the change of variable

$$\omega' = \omega + 2\Omega(t), \tag{5.10}$$

equation (5.8) reduces to

$$\frac{\partial \omega'}{\partial t} = -(\nabla \wedge \psi) \cdot \nabla \omega' + \frac{1}{Re}\nabla^2 \omega', \tag{5.11}$$

where the streamfunction, ψ, is defined by $\mathbf{u} = \nabla \wedge \psi \mathbf{e}_z$ (see Appendix B for more details). For convenience, the streamfunction is separated into background, $\boldsymbol{\psi}$, and disturbance, ψ', terms, i.e.,

$$\psi = \boldsymbol{\psi} + \psi'. \tag{5.12}$$

The most convenient choice for the background velocity is the free-stream velocity, $\mathbf{u}_\infty$, thus

$$\mathbf{u}_\infty = \nabla \wedge \boldsymbol{\psi}, \quad \mathbf{u}' = \nabla \wedge \psi'. \tag{5.13}$$

So that, the background streamfunction, $\boldsymbol{\psi}$, can be obtained directly integrating the velocity (5.4), i.e.,

$$\boldsymbol{\psi} = y + \dot{h}(t)x + \dot{\alpha}(t)\left[\frac{y^2}{2} + x\left(\frac{x}{2} - a\right)\right]. \tag{5.14}$$

On the other hand, for incompressible flows and taking into account the change of variable (5.10) and the definition (5.12), the continuity equation yields

$$\omega' = -\nabla^2 \psi'. \tag{5.15}$$

Thus, the problem has been reduced to two analytical expression (5.10) and (5.12), with two partial differential equations: the vorticity transport equation (5.11) and a Poisson equation (5.15) for the streamfunction ψ'.

5.2.2 *Boundary conditions*

Boundary conditions are required for ω' and ψ' in the equations (5.11) and (5.15) respectively in order to close the problem. The appropriate boundary conditions at infinity are that the velocity equals the free-stream velocity and the fluid is irrotational in the inertial frame. At the inlet, disturbances to the free-stream flow are neglected, so that, the boundary condition for the streamfunction, ψ', is given by

$$\left.\frac{\partial \psi'}{\partial n}\right|_{inlet} = 0, \tag{5.16}$$

where $\partial/\partial n$ refers to the normal derivative. As the wake is highly unsteady, a much more passive boundary condition is necessary for the outlet. The pressure gradient will be small at the output, neglecting it and if the viscosity is neglected too, the boundary condition at the outlet is given by

$$\left.\frac{D}{Dt}\left(\frac{\partial \psi'}{\partial n}\right)\right|_{outlet} = 0. \tag{5.17}$$

Similarly for the vorticity. In practice, the simulations are terminated before any significant vorticity becomes close to the outlet boundary. The airfoil surface has to be a streamline, $\partial\psi/\partial n = 0$, which for simplicity is selected, $\psi = 0$, so that, the boundary condition for ψ' at the airfoil is $\psi' = -\boldsymbol{\psi}$. In addition, the airfoil is a non-slip surface and for that, the vorticity at the airfoil, ω_a, can be related to the total streamfunction by

$$\omega_a = -\left.\frac{\partial^2 \psi}{\partial n^2}\right|_{airfoil}. \tag{5.18}$$

5.2.3 *Forces and input power*

Once these equations are solved, one is interested in the force (per unit length) exerted by the fluid on the foil, which in the present nondimensioal notation (the force per unit length is scaled with $1/2\rho U^2 c$) is given by

$$\mathbf{F}(t) = -\int_S p\mathbf{n}dS + \frac{2}{Re}\int_S \boldsymbol{\omega} \wedge \mathbf{n}dS = F_x\mathbf{e}_x + F_y\mathbf{e}_y, \tag{5.19}$$

where S is the foil's surface (countour in 2D) oriented with normal vector $\mathbf{n}$ towards the fluid. The x and y components of this force have to be proyected to the parallel and perpendicular axis of the free stream current, to obtain the drag and the lift coefficients, respectively, i.e,

$$\tilde{C}_D(t) = F_x(t)\cos[\alpha(t)] - F_y(t)\sin[\alpha(t)], \tag{5.20}$$

$$\tilde{C}_L(t) = F_x(t)\sin[\alpha(t)] + F_y(t)\cos[\alpha(t)], \tag{5.21}$$

In order to compare with the theoretical results, which are scaled with $c/2$, the forces (5.20) and (5.21) have to be multiplied by a factor of 2, i.e.,

$$C_D(t) = 2\tilde{C}_D(t), \quad C_L(t) = 2\tilde{C}_L(t). \tag{5.22}$$

On the other hand, the nondimensional moment can be computed as follows

$$\mathbf{M}(t) = -\int_S p\,(\mathbf{x} \wedge \mathbf{n})\,dS + \frac{2}{Re}\int_S \mathbf{x} \wedge (\boldsymbol{\omega} \wedge \mathbf{n})\,dS, \tag{5.23}$$

which only has one component, perpendicular to the airfoil surface plane, in the present 2D flow. It will be defined as $C_M(t)$. Moreover, the input power coefficient is given by

$$C_P(t) = \int_S (p\mathbf{n})\frac{\partial z_0}{\partial t}dS - \frac{2}{Re}\int_S (\boldsymbol{\omega} \wedge \mathbf{n})\,\frac{\partial z_0}{\partial t}dS, \tag{5.24}$$

which, after substituting (5.1), can be written as

$$C_P(t) = -\dot{h}(t)C_L(t) - 2\dot{\alpha}(t)C_M(t). \tag{5.25}$$

Finally, to obtain the pressure on the airfoil surface, a simplified procedure is used based on the pressure gradient along the no-slip surface to the normal derivative of vorticity modified for the non-inertial reference frame, i.e,

$$\frac{1}{2}\nabla p \cdot \mathbf{n}_t = -\frac{1}{Re}\,(\nabla \wedge \boldsymbol{\omega}) \cdot \mathbf{n}_t - \left[\mathbf{a}_z + \frac{d\boldsymbol{\Omega}}{dt} \wedge \mathbf{x} + \boldsymbol{\Omega} \wedge (\boldsymbol{\Omega} \wedge \mathbf{x})\right] \cdot \mathbf{n}_t, \tag{5.26}$$

where $\mathbf{n}_t$ is the unit tangent vector to the surface of the airfoil. The pressure force at every point on the airfoil is found by assuming an arbitrary value of pressure at one point (the trailing edge) and marching through successive grid points using (5.26).

5.3 NUMERICAL IMPLEMENTATION

The governing equations are discretized using a conformal map. A rectangular, r, θ domain is first mapped to a circular domain using a log-polar transformation (Lin, Pepper, and Lee, 1976), and the circular cylinder is mapped into an airfoil by the Kármán-Trefftz transformation

$$mb\frac{(\zeta + b)^m + (\zeta - b)^m}{(\zeta + b)^m - (\zeta - b)^m} = x + iy, \tag{5.27}$$

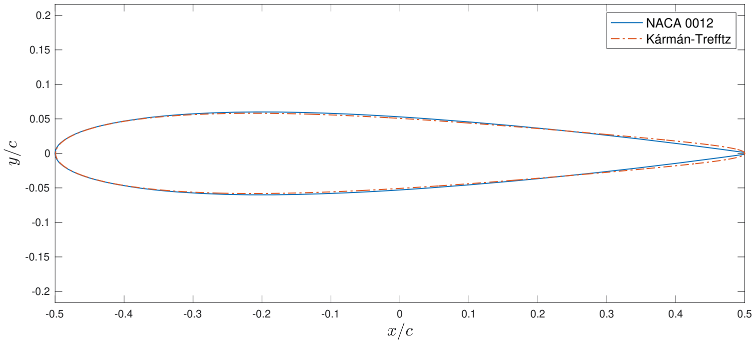

Figure 5.2: Comparison of the NACA-0012 profile with Kármán Trefftz profile. The values of the parameters are $m = 2.0257$, $b = 0.2566$ and $\zeta = -0.01765 + e^{0.29+i\theta}$ with $\theta \in [0, 2\pi)$ and $R^2 = 0.9971$.

where m is related to angle of trailing edge, obtaining the Joukwoski's profiles when $m = 2$, b measures the thickness of the airfoil which becomes in a flate plate when $b = 1$ and in a cilinder when $b = 0$, for $m = 2$, and ζ is the plane in the circular domain. The different values used of the previous parameters are presented in the caption of the Figure 5.2. The airfoil is constructed fitting a NACA-0012 profile, but to avoid numerical singularities at the trailing edge, it has been rounded as one can see in the Figure 5.2, where also it has been compared to the actual NACA profile. A portion of the typical mesh is showed in Figure B.1 in the Appendix B, which also contains some more details about the conformal mapping described above in the .

The vorticity transport equation in the computational space is given by

$$h_r h_\theta \frac{\partial \boldsymbol{\omega}'}{\partial t} = -(\nabla_{r,\theta} \wedge \psi) \cdot \nabla_{r,\theta} \boldsymbol{\omega}' + \frac{1}{Re} \nabla^2_{r,\theta} \boldsymbol{\omega}', \tag{5.28}$$

where h_r and h_θ are the grid transformation metrics which links the physical (x, y)-space with the computational (r, θ)-space. The subscripts $_{r,\theta}$ refer to derivatives in the r, θ domain.

The Poisson equation for ψ' becomes

$$\nabla^2_{r,\theta} \psi' = -h_r h_\theta \boldsymbol{\omega}'. \tag{5.29}$$

One must take into account that $h_r = h_\theta$ as a result of the log-polar transformation in the first mapping to a circular domain, turning the gorverning equations into cartesian equations multiplied by the factor $h_r h_\theta$. So that, after spatial discretization, the semi-discrete scheme (5.28) is equivalent to the first ODE system, i.e.,

$$\frac{\partial \omega'}{\partial t} = R(\omega'), \quad \text{with} \quad R(\omega') = \frac{1}{h_r h_\theta} \left[\frac{1}{Re} \left(\frac{\partial^2 \omega'}{\partial r^2} + \frac{\partial^2 \omega'}{\partial \theta^2} \right) - \frac{\partial \psi}{\partial r} \frac{\partial \omega'}{\partial \theta} + \frac{\partial \psi}{\partial \theta} \frac{\partial \omega'}{\partial r} \right], \tag{5.30}$$

and the Poisson equation for the streamfunction (5.29) yields

$$\frac{\partial^2 \psi'}{\partial r^2} + \frac{\partial^2 \psi'}{\partial \theta^2} = -h_r h_\theta \omega', \tag{5.31}$$

where the spatial discretization is carried out on a uniform grid of width Δ in both r and θ directions.

5.3.1 *Discretization and initial condition*

For time-marching, a second order Runge-Kutta scheme is used for the vorticity transport equation. For spacial terms, sixth-order compact centred scheme differencing is used (Mehra and Patel, 2017). For easy reference, the first and second derivative, $\partial f / \partial \theta$ and $\partial^2 f / \partial \theta^2$, are given, respectively, by

$$\frac{1}{3} f'_{i,j-1} + f'_{i,j} + \frac{1}{3} f'_{i,j+1} = \frac{14}{9} \frac{f_{i,j+1} - f_{i,j-1}}{2\Delta} + \frac{1}{9} \frac{f_{i,j+2} - f_{i,j-2}}{4\Delta}, \tag{5.32}$$

$$\frac{2}{11} f''_{i,j-1} + f''_{i,j} + \frac{2}{11} f''_{i,j+1} = \frac{12}{11} \frac{f_{i,j-1} - 2f_{i,j} + f_{i,j+1}}{\Delta^2} + \frac{2}{11} \frac{f_{i,j-2} - 2f_{i,j} + f_{i,j+2}}{4\Delta^2}. \tag{5.33}$$

In the case of the first and second derivative in the radial direction, $\partial f / \partial r$ and $\partial^2 f / \partial r^2$, the nodes $i = 1, i = 2, i = N_r$ and $i = N_r - 1$ have to be approximated with forward or backward compact finite differences, i.e.,

- $i = 1$

$$f'_1 + 5f'_2 = \frac{1}{\Delta} \left[-\frac{197}{60} f_1 - \frac{5}{12} f_2 + 5 f_3 - \frac{5}{3} f_4 + \frac{5}{12} f_5 - \frac{1}{20} f_6 \right], \tag{5.34}$$

$$f''_1 + \frac{126}{11} f''_2 = \frac{1}{\Delta^2} \left[\frac{13097}{990} f_1 - \frac{2943}{110} f_2 + \frac{573}{44} f_3 + \frac{167}{99} f_4 - \frac{18}{11} f_5 + \frac{57}{110} f_6 - \frac{131}{1980} f_7 \right], \tag{5.35}$$

- $i = 2$

$$\frac{2}{11} f'_1 + f'_2 + \frac{2}{11} f'_3 = \frac{1}{\Delta} \left[-\frac{20}{33} f_1 - \frac{35}{132} f_2 + \frac{34}{33} f_3 - \frac{7}{33} f_4 + \frac{2}{33} f_5 - \frac{1}{132} f_6 \right], \tag{5.36}$$

$$\frac{11}{128} f''_1 + f''_2 + \frac{11}{128} f''_3 = \frac{1}{\Delta^2} \left[\frac{585}{512} f_1 - \frac{141}{64} f_2 + \frac{459}{512} f_3 + \frac{9}{32} f_4 - \frac{81}{512} f_5 + \frac{3}{64} f_6 - \frac{3}{512} f_7 \right]. \tag{5.37}$$

For $i = N_r$ and $i = N_r - 1$, the compact finite difference coefficients are the same for the second derivative and with the opposite sign for the first derivative on the right hand side, but taking into account that the evaluation has to be done in the backward direction ($i = N_r, ..., N_r - 6$, for the right hand side). Note that the factor $2077/157$ in the first term of the second derivative for $i = 1$ on the right hand side reported by Mehra and Patel, 2017, has been corrected in (5.35).

For the Poisson equation for the streamfunction, the equations are discretized using a sixth-order compact centered scheme (Sutmann, 2007), and solved using a SIP (Strongly Implicid Procedure) solver with a Cholesky factorization. For the boundary condition on the airfoil surface in the case of the vorticity is used the fourth order Briley formula (Briley, 1971), i.e.,

$$\omega'_a = \frac{1}{18 \Delta n^2} \left[85\psi_a - 108\psi_{a+1} + 27\psi_{a+2} - 4\psi_{a+3} \right] + 2\Omega. \tag{5.38}$$

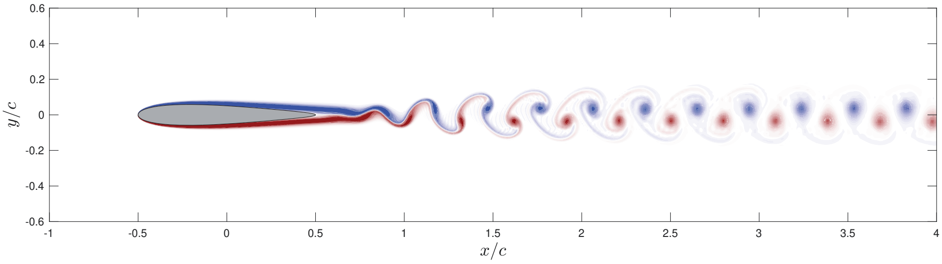

Figure 5.3: Vorticity contours around the static horizontal airfoil used as initial condition ($t = 0$) for every numerical simulation of the flapping foil for $Re = 16000$.

Step grid size (Δ)	Mesh size ($N_r \times N_\theta$)	Nodes on foil	$\bar{C}_T$	$\bar{C}_P$
$\pi/600$	886×1200	1200	0.531	2.942
$\pi/800$	1182×1600	1600	0.504	3.011
$\pi/1000$	1477×2000	2000	0.499	3.056

Table 3: Properties of the three meshes for the grid convergence study (three first columns), and the corresponding results for $\bar{C}_T$ and $\bar{C}_P$ when $Re = 16\,000$, $a = -1$, $a_0 = 8°$ and $St = 0.4$ (last column).

For more information about the different tested methods and boundary conditions see Appendix B.

On the other hand, in order to avoid nonphysical starting flows when simulating a flapping motion, the permanent von Kármán vortex street wake behind the airfoil is previously obtained, when it is horizontally at rest. In the Figure 5.3 one can see a snapshoot of the vorticity contours around the static horizontal airfoil used as initial condition for every numerical sumulation of the flapping foil.

5.3.2 *Mesh convergence and validation of the code*

A grid sensitivity analysis was performed using three meshes whose main characteristics are given in Table 1, together with the results for the time-averaged thrust coefficient for $Re = 16\,000$, $a = -1$, $a_0 = 8°$ and $St = 0.4$, which is the highest value of the Strouhal number considered in the present study, and therefore the most adverse case in terms of trailing edge velocity. After a large number of simulations, it is selected a step grid size $\Delta = \pi/800$ assuming a relative error below 2%.

For the first validation case, it is selected the numerical results of Martín-Alcántara and Fernandez-Feria, 2019, and the experimental ones of McGowan et al., 2011, for pure heaving motion for the lift coefficient at $Re = 10000$, $h_0 = 0.05$, and $k = 7.86$ (see Figure 5.4). The numerical results, which are strictly periodic for this value of $kh_0 \simeq 0.4$, practically coincide with the theoretical results by Theodorsen and agree quite well with the experimental results.

As a second validation case, it is selected the numerical results of Senturk and Smits, 2019, for pure pitching motion for the time-average thrust, $\bar{C}_T$, and input power coefficient, $\bar{C}_P$ as a function of St for $Re = 16\,000$, $a_0 = 8°$, and $a = -0.5$. The results agree

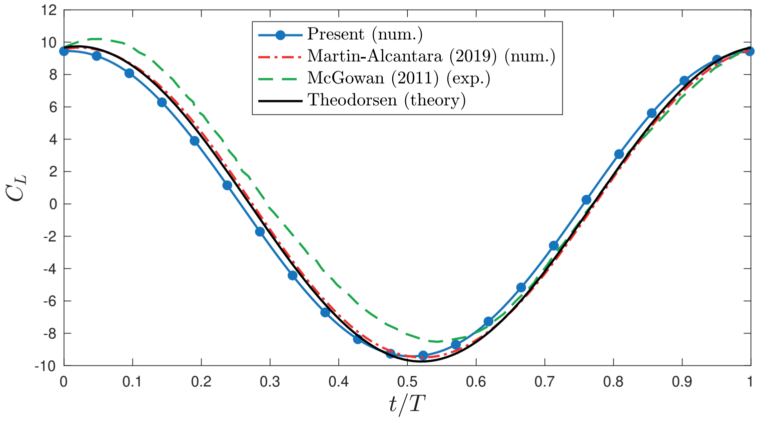

Figure 5.4: Lift coefficient $C_L(t)$ during a cycle compute for $Re = 10\ 000$, $h_0 = 0.05$, and $k = 7.86$ compared with the experimental results of McGowan et al., 2011, the numerical results of Martín-Alcántara and Fernandez-Feria, 2019, and the theoretical ones by Theodorsen, 1935.

quite well with these by Senturk and Smits, 2019, for the input power coefficient. However, the time-average thrust coefficient and consequetly the efficiency, compare well only for small values of St. On the other hand, taking as reference the numerical results from Senturk and Smits, 2019, the theoretical results only coincide for $St \lesssim 0.25$, which can be considered as a limit for the present theory, in first approximation for pitching foils.

Appendix B report addional comparisons with other numerical and experimental cases, testing and validating the code with a impulsively started cylinder for several Reynolds number, comparing the temportal evolution of the drag coefficient with numerical results from Koumoutsakos and Leonard, 1995, and the closed wake length, the location of the main eddy core and the velocity at the mean line of the cylinder wake with the theory and the experimental results from Bouard and Coutanceau, 1980, and Loc and Bouard, 1985.

5.4 CONCLUDING REMARKS

The equations and their discretizations which have to be solved numerically in terms of vorticity and stream function have been presented, considering a flapping rigid airfoil in a non inertial reference frame. To map the airfoil, in this case a NACA-0012, it has been used the Kármán-Trefftz conformal mapping transformation. In addition, it has been tested the code with several numerical and experimental results available in the bibliography (see also Appendix B). However, this is a numerical work in progress. The results for pitching foils are not estricly satisfacting yet and have to be checked. These and other comparisons with further numerical and experimental results will be under taken in the future using the developed code here in order to finish the main objective in this chapter which is to obtain the validation limit of the present theoretical results.

Part II

TWO FOILS

6

UNSTEADY AERODYNAMICS OF FOILS IN TANDEM

6.1 INTRODUCTION

Configurations with more than one flapping foil are used to enhance propulsion and efficiency taking advantage of their positive aerodynamic interaction for some particular settings. However, the aerodynamic optimization of these configurations becomes cumbersome when using numerical or experimental techniques owing to the huge number of nondimensional geometric and kinematic parameters. For this reason, it is desirable to have approximate, theoretically based models that allow analyzing a wide set of configurations that generate optimal propulsion and that may help to effectively design and control air and water microvehicles with pairs of flapping foils interacting aerodynamically with each other. This is the main aim of the present and next chapters, where analytical expressions for the lift, thrust, moment, and propulsive efficiency of a pair of general pitching and heaving foils in tandem configuration are derived within the framework of linearized potential flow theory. To that end it is generalized the impulse theory of Kármán and Sears, 1938, for the lift and moment of an oscillating foil in the limit of linear potential flow, including the thrust force and propulsive efficiency in the same framework of the impulse theory, as derived in Fernandez-Feria, 2016. It is applied to a general set of flapping foils, but closed analytical expressions are given for two general pitching and heaving foils in tandem configurations. The expressions are valid for any separation between the foils, with independent and arbitrary heaving and pitching motions.

The 2D potential flow over a tandem configuration of two pitching and heaving plates has been previously considered by several authors using standard methods of potential flow theory (Bosch, 1978; Lan, 1979; Tanida, 2003). All of them use Garrick's approximation for the thrust force (Garrick et al., 1936), which only considers the suction force at the leading edge of each airfoil, instead of the more accurate results from the impulse theory that considers the effect on the thrust force of all the vorticity distribution on the foils and in their wakes. For a single airfoil, this impulse approach has been proved to be more accurate for computing the thrust force and the propulsive efficiency in all the range of reduced frequencies (Fernandez-Feria, 2016; Fernandez-Feria, 2017). In addition, the present potential flow approach based on the impulse theory is more coherent in the sense that both force components come from the same vector formula. It is compared the present theoretical results with available numerical and experimental results for large Reynolds numbers and small amplitudes of the plate oscillations, for which the present theory is limited in practice. But the general trends of thrust and propulsion efficiency from the present theory may reasonably be extrapolated to higher amplitudes and lower Reynolds numbers of practical interest. In particular, numerical simulations and experimental results show that linearized potential results for thrust and propulsive efficiency of pitching and heaving foils are sufficiently accurate above a Reynolds number, based on the chord length and flight speed, of about 10^4 , provided that the amplitude remains sufficiently small to preclude the formation of significant leading-edge vortices, and that, for three- dimensional (3D) wings, the aspect ratio is large enough (Fernandez-Feria, 2017; Martín-Alcántara and Fernandez-Feria, 2019; Fernandez-Feria

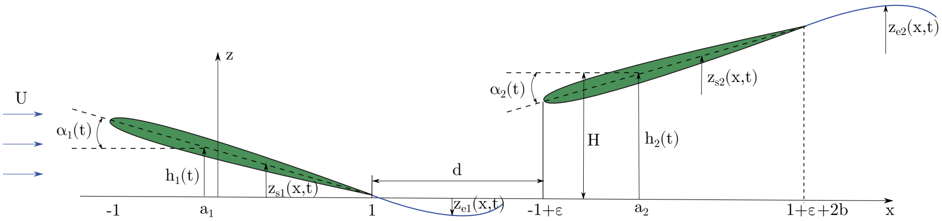

Figure 6.1: Schematic of the oscillating airfoils (non-dimensional).

and Sanmiguel-Rojas, 2019; Senturk and Smits, 2019; Fernandez-Feria and Alaminos-Quesada, 2018; Gonzalo et al., 2018). For flapping animals or robotic devices with 3D low-aspect-ratio wings or fins, flying, swimming, or maneuvering at low Reynolds numbers or at high angles of attack, the results of the present chapter are inapplicable.

6.2 FORMULATION OF THE PROBLEM

In this case it is considered N pitching and heaving thin airfoils of chord length c_i that move with constant speed U along the negative x-axis. As to the single airfoil, the amplitudes of the heaving and pitching motions are both very small compared with each c_i, so that, the airfoils, and every point of each trail of vortices that they leave behind, may be considered to be on a horizontal plane (constant z) in first approximation.

For simplicity it is selected the first plate with $c_1 = 2$, so that all the lengths are scaled with the half-chord $c_1/2$, and this plate extends from $x = -1$ to $x = 1$ in a reference frame translating with it at speed U along the x-axis (see Figure 6.1). The rest of airfoils $i = 2, 3, ..., N$, are separated a horizontal non-dimensional distance d_i from the trailing edge of the front plate, so that plate i extends from $x = -1 + \varepsilon_i$ to $x = 1 + \varepsilon_i^*$, with

$$\varepsilon_i = \sum_{j=1}^{i-1} \left(d_j + 2C_j \right), \quad \varepsilon_i^* = \varepsilon_i + 2b_i, \quad i = 1, \ldots, N, \tag{6.1}$$

where C_j is the relationship between chords with respect to the first plate $C_i = c_i/c_1 = c_i/2$, and b_i denotes the chord increment of plate i, $b_i = C_i - 1$. In this reference frame the motion of plate or airfoil i is given by the vertical displacement of its mean-camber line:

$$z_{si}(x,t) = h_i(t) - (x - \varepsilon_i - a_i)\alpha_i(t), \quad -1 + \varepsilon_i \leq x \leq 1 + \varepsilon_i^*, \tag{6.2}$$

with

$$h_i(t) = \Re[H_{0i} e^{ikt}] + H_i, \quad \alpha_i(t) = \Re[\alpha_{0i} e^{ikt}], \tag{6.3}$$

where H_i is the mean non-dimensional vertical distance between airfoil i and the x-axis. The amplitudes H_{0i} and α_{0i} are, in general, complex constants to allow for phase shifts between the different harmonic motions satisfying $|H_{0i}| \ll 1$ and $|\alpha_{0i}| \ll 1$. For simplicity it is selected $H_{01} = h_{01}$ real and

$$H_{0i} = h_{0i} e^{i\varphi_i}, \quad \alpha_{0i} = a_{0i} e^{i(\phi_i + \varphi_i)}, \tag{6.4}$$

with ϕ_i the phase shift between the heaving and pitching motions of plate i, φ_i the phase shift between the heaving motion of the first plate and the plate i, and a_{0i} the maximum pitching amplitude of plate i. Note that $H_1 = \varphi_1 = \varepsilon_1 = 0$. In what follows it is shall worked with the complex functions knowing that it has to be taken the real part of the results. The dimensionaless vertical velocity of each airfoil is

$$v_{0i}(x,t) = \dot{h}_i - (x - \varepsilon_i - a_i)\dot{\alpha}_i - \alpha_i, \quad -1 + \varepsilon_i \le x \le 1 + \varepsilon_i^*, \tag{6.5}$$

where a dot denotes the time derivative.

6.3 GENERAL EXPRESSIONS FOR THE FORCES, MOMENT AND INPUT POWER

To obtain the forces, moment and input power it is used the vortical impulse theory for an incompressible and unbounded flow as to the chapter 4 but in this case extending to the presence of N plates in the flow field. So that, the drag and lift with the same assumptions (see §3.2.1 for more details) are given by,

$$D = \rho \sum_{i=1}^{N} \frac{d}{dt} \left[\int_{-1+\varepsilon_i}^{1+\varepsilon_i^*} z_{si}\varpi_{si} dx + \int_{1+\varepsilon_i^*}^{\infty} z_{ei}\varpi_{ei} dx \right] := \sum_{i=1}^{N} D^{(i)}, \tag{6.6}$$

$$L = -\rho \sum_{i=1}^{N} \frac{d}{dt} \left[\int_{-1+\varepsilon_i}^{1+\varepsilon_i^*} x\varpi_{si} dx + \int_{1+\varepsilon_i^*}^{\infty} x\varpi_{ei} dx \right] := \sum_{i=1}^{N} L^{(i)}, \tag{6.7}$$

where $D^{(i)}$ and $L^{(i)}$ are the drag and lift on each airfoil i, respectively. Similarly for the moment,

$$M \simeq \frac{1}{2}\rho \frac{d}{dt} \sum_{i=1}^{N} \left[\int_{-1+\varepsilon_i}^{1+\varepsilon_i^*} (x - a_i)^2 \varpi_{si} dx + \int_{1+\varepsilon_i^*}^{\infty} (x - a_i)^2 \varpi_{ei} dx \right] := \sum_{i=1}^{N} M^{(i)}, \tag{6.8}$$

with $M^{(i)}$ the moment of each airfoil i. On the other hand, the input power remains same but extending it for N plates, given by the equation (3.18), i.e.,

$$P = \sum_{i=1}^{N} \left\{ -\rho U \int_{-1+\varepsilon_i}^{1+\varepsilon_i^*} \varpi_{si} \frac{\partial z_{si}}{\partial t} dx - \rho \int_{-1+\varepsilon_i}^{1+\varepsilon_i^*} \left(\int_{x}^{1+\varepsilon_i^*} \frac{\partial z_{si}}{\partial t} d\xi \right) \frac{\partial \varpi_{si}}{\partial t} dx \right\} := \sum_{i=1}^{N} P^{(i)}. \tag{6.9}$$

6.3.1 *Vorticity distributions*

As to the single airfoil, invoking the linearity of the problem the vorticity distribution of each plate i, ϖ_{si}, can be decomposed into the following terms:

$$\begin{gathered} \varpi_{si}(x,t) = \varpi_{0i}(x,t) + \varpi_{sei}(x,t) + \sum_{\substack{j=1 \\ j \neq i}}^{N} \left\{ \varpi_{ji}(x,t) + \varpi_{seji}(x,t) \right\}, \\ i = 1, \ldots, N, \quad -1 + \varepsilon_i \le x \le 1 + \varepsilon_i^*. \end{gathered} \tag{6.10}$$

The first term ϖ_{0i}, with associated circulation

$$\Gamma_{0i}(t) = \int_{-1+\varepsilon_i}^{1+\varepsilon_i^*} \varpi_{0i}(x,t) dx, \tag{6.11}$$

is the quasi-steady contribution, i.e., that for a single airfoil i without considering the effect of the other moving airfoils nor their unsteady wakes, including its own, such that the corresponding lift would be $\rho U \Gamma_{0i}$. The meanings of the other terms in (6.10) are the following: ϖ_{sei} is the contribution to ϖ_{si} induced by its wake vortex-sheet, of strength ϖ_{ei}; ϖ_{seji} is the contribution to ϖ_{si} induced by the wake of airfoil j, of strength ϖ_{ej}, and

ϖ_{ji} is the contribution to ϖ_{si} associated with airfoil j, of bound vorticity ϖ_{sj}. On the other hand, the Kelvin's total-circulation conservation theorem requires that

$$\Gamma_{0i} + \Gamma_{sei} + \sum_{\substack{j=1\\ j\neq i}}^{N} \left\{ \Gamma_{ji} + \Gamma_{seji} \right\} + \int_{1+\varepsilon_i^*}^{\infty} \varpi_{ei} dx = 0, \quad i = 1, \dots, N, \tag{6.12}$$

with

$$\Gamma_{sei}(t) = \int_{-1+\varepsilon_i}^{1+\varepsilon_i^*} \varpi_{sei}(x,t) dx, \tag{6.13}$$

$$\Gamma_{ji}(t) = \int_{-1+\varepsilon_i}^{1+\varepsilon_i^*} \varpi_{ji}(x,t) dx, \quad \Gamma_{seji}(t) = \int_{-1+\varepsilon_i}^{1+\varepsilon_i^*} \varpi_{seji}(x,t) dx. \tag{6.14}$$

To obtain the different vorticity distributions, one has to apply the boundary condition of the vertical velocity (6.5) at $z = 0$, $-1 \leq x \leq 1$, induced by the whole distribution of vorticity. For more details see §3.2.2. So that, after some algebra, one obtains the following integral equations

$$v_{0i}(x,t) = \frac{1}{2\pi} \fint_{-1+\varepsilon_i}^{1+\varepsilon_i^*} \frac{\varpi_{0_i}(\xi,t)}{\xi - x} d\xi, \tag{6.15}$$

$$-\frac{1}{2\pi} \int_{1+\varepsilon_i^*}^{\infty} \frac{\varpi_{ei}(\xi,t)}{\xi - x} d\xi = \frac{1}{2\pi} \fint_{-1+\varepsilon_i}^{1+\varepsilon_i^*} \frac{\varpi_{sei}(\xi,t)}{\xi - x} d\xi, \tag{6.16}$$

$$-\frac{1}{2\pi} \sum_{\substack{j=1\\ j\neq i}}^{N} \int_{-1+\varepsilon_j}^{1+\varepsilon_j^*} \frac{(\xi - x)\varpi_{sj}(\xi,t)}{(\xi - x)^2 + (H_i - H_j)^2} d\xi = \frac{1}{2\pi} \sum_{\substack{j=1\\ j\neq i}}^{N} \fint_{-1+\varepsilon_i}^{1+\varepsilon_i^*} \frac{\varpi_{ji}(\xi,t)}{\xi - x} d\xi, \tag{6.17}$$

$$-\frac{1}{2\pi} \sum_{\substack{j=1\\ j\neq i}}^{N} \int_{1+\varepsilon_j^*}^{\infty} \frac{(\xi - x)\varpi_{ej}(\xi,t)}{(\xi - x)^2 + (H_i - H_j)^2} d\xi = \frac{1}{2\pi} \sum_{\substack{j=1\\ j\neq i}}^{N} \fint_{-1+\varepsilon_i}^{1+\varepsilon_i^*} \frac{\varpi_{seji}(\xi,t)}{\xi - x} d\xi. \tag{6.18}$$

The solutions of these singular and linear integral equations of the first kind with constant integration limits are given by (Polyanin, 1998)

$$\begin{aligned} \varpi_{0i}(x,t) = & \frac{1}{\sqrt{(1 - \varepsilon_i + x)(1 + \varepsilon_i^* - x)}} \left\{ \frac{\Gamma_{0i}}{\pi} + 2\left(\dot{h}_i + (\varepsilon_i + a_i)\dot{\alpha}_i - U\alpha_i\right)(x - \varepsilon_i - b_i) + \right. \\ & \left. \dot{\alpha}_i \left[1 + 2b_i \left(1 + \frac{b_i}{2} + x \right) + 2(\varepsilon_i - x)x \right] \right\}, \end{aligned} \tag{6.19}$$

$$\varpi_{sei}(x,t) = \frac{1}{\pi} \sqrt{\frac{1 + \varepsilon_i^* - x}{1 - \varepsilon_i + x}} \int_{1+\varepsilon_i^*}^{\infty} \sqrt{\frac{\xi + 1 - \varepsilon_i}{\xi - 1 - \varepsilon_i^*}} \frac{\varpi_{ei}(\xi,t)}{\xi - x} d\xi, \tag{6.20}$$

where the regularity of ϖ_{si} at its corresponding trailing edge $x = 1 + \varepsilon_i^*$, or Kutta condition, has been applied for each airfoil. It must be noted that Kelvin's theorem is applied to each airfoil separately, and Kutta condition at the trailing edge of each airfoil separately to each vorticity distribution component, invoking the linearity of the problem as to the case of single airfoil (see §3.2.2). Integration between $x = -1 + \varepsilon_i$ and $x = 1 + \varepsilon_i^*$ yields

$$\Gamma_{0i}(t) := G_{0i} e^{i\omega t}, \quad G_{0i} = 2\pi \left\{ U\alpha_{0i} - i\omega h_{0i} e^{i\varphi_i} - i\omega\alpha_{0i} \left[a_i - \frac{1}{2} - 2b_i \left(1 + \frac{3b_i}{4} \right) \right] \right\}, \tag{6.21}$$

$$\Gamma_{sei}(t) = \int_{1+\varepsilon_i^*}^{\infty} \left(\sqrt{\frac{\xi + 1 - \varepsilon_i}{\xi - 1 - \varepsilon_i^*}} - 1 \right) \varpi_{ei}(\xi, t) d\xi. \tag{6.22}$$

Since the objective is the aligned tandem configuration, it is obtained the solutions of the remaining two integral equations (6.17) and (6.18) in the limit $(H_i - H_j)^2 \ll 1$, considering only the first order in the expansion in this small parameter. Beginning with equation (6.18), it is first identified airfoils $j < i$ as those in front of airfoil i, while those labelled $j > i$ are located behind airfoil i; i.e., the wakes ϖ_{ej} for $j > i$ are rear-wakes for computing ϖ_{seji}, while they are front-wakes for $j < i$. Thus, the solution for $j > i$ is similar to the above solution for ϖ_{sei} in terms of ϖ_{ei}, but now with ϖ_{ej} displaced; i.e., one only has to change the lower integration limit and the vorticity density distribution:

$$\varpi_{seji}(x, t) = \frac{1}{\pi} \sqrt{\frac{1 + \varepsilon_i^* - x}{1 - \varepsilon_i + x}} \int_{1+\varepsilon_j^*}^{\infty} \sqrt{\frac{\xi + 1 - \varepsilon_i}{\xi - 1 - \varepsilon_i^*}} \frac{\varpi_{ej}(\xi, t)}{\xi - x} d\xi, \tag{6.23}$$

$$\Gamma_{seji}(t) = \int_{1+\varepsilon_j^*}^{\infty} \left(\sqrt{\frac{\xi + 1 - \varepsilon_i}{\xi - 1 - \varepsilon_i^*}} - 1 \right) \varpi_{ej}(\xi, t) d\xi. \tag{6.24}$$

For the case of front-wakes ($j < i$), the integration has to be divided into three terms because the integral is singular in $-1 + \varepsilon_i \leq x \leq 1 + \varepsilon_i^*$: a front part, a middle part, and the region behind the airfoil. One obtains

$$\varpi_{seji}(x, t) = \frac{1}{\pi} \sqrt{\frac{1 + \varepsilon_i^* - x}{1 - \varepsilon_i + x}} \left[\int\limits_{1+\varepsilon_i^*}^{\infty} \sqrt{\frac{\xi + 1 - \varepsilon_i}{\xi - 1 - \varepsilon_i^*}} \frac{\varpi_{ej}(\xi, t)}{\xi - x} d\xi - \int\limits_{1+\varepsilon_j^*}^{-1+\varepsilon_i} \sqrt{\frac{\xi + 1 - \varepsilon_i}{\xi - 1 - \varepsilon_i^*}} \frac{\varpi_{ej}(\xi, t)}{\xi - x} d\xi \right], \tag{6.25}$$

$$\Gamma_{seji}(t) = \int\limits_{1+\varepsilon_i}^{\infty} \sqrt{\frac{\xi + 1 - \varepsilon_i}{\xi - 1 - \varepsilon_i^*}} \varpi_{ej}(\xi, t) d\xi - \int\limits_{1+\varepsilon_j^*}^{-1+\varepsilon_i} \sqrt{\frac{\xi + 1 - \varepsilon_i}{\xi - 1 - \varepsilon_i^*}} \varpi_{ej}(\xi, t) d\xi - \int\limits_{1+\varepsilon_j^*}^{\infty} \varpi_{ej}(\xi, t) d\xi. \tag{6.26}$$

Finally, equation (6.17) is in fact an integral equation system since the vorticity distribution ϖ_{si} contains ϖ_{ji}. The solution can be formally written as

$$\varpi_{ji}(x, t) = \frac{1}{\pi^2} \sqrt{\frac{1 + \varepsilon_i^* - x}{1 - \varepsilon_i + x}} \fint_{-1+e_i}^{1+\varepsilon_i^*} \sqrt{\frac{1 - \varepsilon_i + \xi}{1 + \varepsilon_i^* - \xi}} \frac{1}{\xi - x} \fint_{-1+\varepsilon_j}^{1+\varepsilon_j} \frac{\varpi_{sj}(\xi', t)}{\xi' - \xi} d\xi' d\xi, \tag{6.27}$$

with the different contributions to ϖ_{sj}, defined in (6.10), already given above.

6.3.2 *Forces, moment and input power*

Taking into account (6.7), the lift in non-dimensional form, after some algebra, can be written as

$$C_L = \sum_{i=1}^{N} C_L^{(i)}, \quad C_L^{(i)} := C_{L0}^{(i)} + C_{L1}^{(i)} + C_{L2}^{(i)} + C_{Le}^{(i)}, \tag{6.28}$$

where the different components of the lift on each airfoil i are

$$C_{L0}^{(i)} := \Gamma_{0i} + \sum_{\substack{j=1 \\ j \neq i}}^{N} \Gamma_{0ji}, \tag{6.29}$$

$$C_{L1}^{(i)} := -\frac{d}{dt}\int_{-1+\varepsilon_i}^{1+\varepsilon_i^*}(x-\varepsilon_i-b_i)\left(\varpi_{0i}+\sum_{\substack{j=1\\ j\neq i}}^{N}\varpi_{0ji}\right)dx, \tag{6.30}$$

$$C_{L2}^{(i)} := \int_{1+\varepsilon_i^*}^{\infty}\frac{(1+b_i)\,\varpi_{ei}(\xi,t)}{\sqrt{(\xi+1-\varepsilon_i)(\xi-1-\varepsilon_i^*)}}d\xi, \tag{6.31}$$

$$\begin{aligned}
C_{Le}^{(i)} := \sum_{j=i+1}^{N}&\left\{\int_{1+\varepsilon_j^*}^{\infty}\frac{(1+b_i)\,\varpi_{ej}(\xi,t)}{\sqrt{(\xi+1-\varepsilon_i)(\xi-1-\varepsilon_i^*)}}d\xi+\right.\\
&\left.\left(1+\varepsilon_j^*-\varepsilon_i-b_i-\sqrt{(2+\varepsilon_j^*-\varepsilon_i)(\varepsilon_j^*-\varepsilon_i^*)}\right)\varpi_{ej}(\xi=1+\varepsilon_j^*,t)\right\}+\\
&\sum_{j=1}^{i-1}\left\{\int_{1+\varepsilon_j^*}^{\infty}\frac{(1+b_i)\,\varpi_{ej}(\xi,t)}{\sqrt{(\xi+1-\varepsilon_i)(\xi-1-\varepsilon_i^*)}}d\xi-\int_{-1+\varepsilon_i}^{1+\varepsilon_i^*}\varpi_{ej}(\xi,t)d\xi\right.\\
&-\int_{-1+\varepsilon_i^*}^{\infty}\frac{(1+b_i)\,\varpi_{ej}(\xi,t)}{\sqrt{(\xi+1-\varepsilon_i)(\xi-1-\varepsilon_i^*)}}d\xi+\\
&\left(1+\varepsilon_j^*-\varepsilon_i-b_i+\sqrt{(2+\varepsilon_j^*-\varepsilon_i)(\varepsilon_j^*-\varepsilon_i^*)}\right)\varpi_{ej}(\xi=1+\varepsilon_j^*,t)+\\
&\left.\varpi_{ej}(\xi=-1+\varepsilon_i,t)+(1+2b_i)\varpi_{ej}(\xi=1+\varepsilon_i^*,t)\right\}.
\end{aligned} \tag{6.32}$$

They are the quasi-steady lift, the apparent-mass lift, the lift induced by its own unsteady wake, and the lift induced by the other airfoils' wakes, respectively. For a single airfoil, the above expressions coincide with the lift obtained by von Kármán and Sears, 1938, using the present impulse theory, and previously by Theodorsen, 1935, from a more standard potential flow approach. For easy reference, it is given by the equation (3.41).

To compute (6.6), one makes the same assumptions that for the single plate, i.e, one assumes that the vertical displacement of the wakes ϖ_{ei} coincides with the trailing edge location at the time $t' = t + (1-\xi)/U$ when it was shed from the airfoil, $z_{si}(x = 1 + \varepsilon_i^*, t')$ (see §3.3). Therefore, by using the integrals (C.19), (C.21) and (C.23) given in the Appendix C, the thrust, or minus the drag (6.6), in non-dimensional form can be written as

$$C_T := \sum_{i=1}^{N} C_T^{(i)}, \quad C_T^{(i)} := -\Re[\alpha_i]C_L^{(i)} + C_{T1}^{(i)} + C_{T2}^{(i)} + C_{Te}^{(i)}, \tag{6.33}$$

where

$$C_{T1}^{(i)} := \dot{\alpha}_i\int_{-1+\varepsilon_i}^{1+\varepsilon_i^*}(x-\varepsilon_i-b_i)\left(\varpi_{0i}+\sum_{\substack{j=1\\ j\neq i}}^{N}\varpi_{0ji}\right)dx, \tag{6.34}$$

$$C_{T2}^{(i)} := \int_{1+\varepsilon_i^*}^{\infty}\left[h_i-\alpha_i+\dot{\alpha}_i\left(a_i+\sqrt{(\xi+1-\varepsilon_i)(\xi-1-\varepsilon_i^*)}-(\xi-\varepsilon_i)\right)\right]\varpi_{ei}(\xi,t)d\xi, \tag{6.35}$$

$$
\begin{aligned}
C_{Te}^{(i)} =& \sum_{j=1}^{i-1} \dot{\alpha}_i \int_{1+\varepsilon_j^*}^{\infty} \left(\sqrt{(\xi+1-\varepsilon_i)(\xi-1-\varepsilon_i^*)} - (\xi-\varepsilon_i) + b_i\right) \varpi_{ei}(\xi,t) d\xi + \\
& \sum_{j=i+1}^{N} \left\{ \dot{\alpha}_i \int_{1+\varepsilon_i^*}^{\infty} \left(\sqrt{(\xi+1-\varepsilon_i)(\xi-1-\varepsilon_i^*)} - (\xi-\varepsilon_i) + b_i\right) \varpi_{ej}(\xi,t) d\xi \right. \\
& \left. - \dot{\alpha}_i \int_{1+\varepsilon_j^*}^{-1+\varepsilon_i} \left(\sqrt{(\xi+1-\varepsilon_i)(\xi-1-\varepsilon_i^*)} - (\xi-\varepsilon_i) - b_i\right) \varpi_{ej}(\xi,t) d\xi \right\}. \qquad (6.36)
\end{aligned}
$$

The first term in Eq.(6.33) is the projection in the flight direction of the normal force to the plate i, where $C_L^{(i)}$ is given by (6.28). The following terms of $C_T^{(i)}$ are the apparent-mass thrust, the contribution of its own unsteady wake, and the contributions of the other airfoils' wakes, respectively. For a single airfoil, the above expressions coincide with the thrust obtained by Fernandez-Feria, 2016. For easy reference, it is given by the equation (3.47) but with the presence of N point vortices.

On the other hand, using the integrals (C.19)-(C.24) given in the Appendix C, the moment (6.8) in non-dimensional form, can be written as

$$
C_M = \sum_{i=1}^{N} C_M^{(i)}, \quad C_M^{(i)} := C_{M0}^{(i)} + C_{M1}^{(i)} + C_{M2}^{(i)} + C_{Me}^{(i)} + \frac{a_i}{2} C_L^{(i)}, \qquad (6.37)
$$

where

$$
C_{M0}^{(i)} := -\frac{1}{2} \int_{-1+\varepsilon_i}^{1+\varepsilon_i^*} (x-\varepsilon_i) \left(\varpi_{0i} + \sum_{\substack{j=1 \\ j\neq i}}^{N} \varpi_{0ji} \right) dx, \qquad (6.38)
$$

$$
C_{M1}^{(i)} := \frac{1}{4} \frac{d}{dt} \int_{-1+\varepsilon_i}^{1+\varepsilon_i^*} \left[(x-\varepsilon_i)^2 - \frac{1}{2} - b_i \left(1 + \frac{3b_i}{2}\right) \right] \left(\varpi_{0i} + \sum_{\substack{j=1 \\ j\neq i}}^{N} \varpi_{0ji} \right) dx, \qquad (6.39)
$$

$$
\begin{aligned}
C_{M2}^{(i)} :=& \frac{1}{4} \left\{ \int_{1+\varepsilon_i^*}^{\infty} \frac{(1-b_i^2)\varpi_{ei} d\xi}{\sqrt{(\xi+1-\varepsilon_i)(\xi-1-\varepsilon_i^*)}} + \sum_{j=i+1}^{N} \int_{1+\varepsilon_j^*}^{\infty} \frac{(1-b_i^2)\varpi_{ej} d\xi}{\sqrt{(\xi+1-\varepsilon_i)(\xi-1-\varepsilon_i^*)}} + \right. \\
& \left. \sum_{j=1}^{i-1} \left[\int_{1+\varepsilon_i^*}^{\infty} \frac{(1-b_i^2)\varpi_{ej} d\xi}{\sqrt{(\xi+1-\varepsilon_i)(\xi-1-\varepsilon_i^*)}} - \int_{1+\varepsilon_j^*}^{-1+\varepsilon_i} \frac{(1-b_i^2)\varpi_{ej} d\xi}{\sqrt{(\xi+1-\varepsilon_i)(\xi-1-\varepsilon_i^*)}} \right] \right\},
\end{aligned}
\qquad (6.40)
$$

$$
\begin{aligned}
C_{Me}^{(i)} :=& \frac{1}{4} \sum_{j=i+1}^{N} \sqrt{(2+\varepsilon_j^*-\varepsilon_i)(\varepsilon_j^*-\varepsilon_i^*)} \left(1+\varepsilon_j^*-\varepsilon_i+b_i\right) \varpi_{ej}(\xi=1+\varepsilon_j^*,t) + \\
& \frac{1}{4} \sum_{j=1}^{i-1} \left\{ -\sqrt{(2+\varepsilon_j^*-\varepsilon_i)(\varepsilon_j^*-\varepsilon_i^*)} \left(1+\varepsilon_j^*-\varepsilon_i+b_i\right) \varpi_{ej}(\xi=1+\varepsilon_j^*,t) + \right. \\
& \left. \varpi_{ej}(\xi=-1+\varepsilon_i,t) - (1+2b_i)^2 \varpi_{ej}(\xi=1+\varepsilon_i^*,t) \right\} + \\
& \frac{1}{4} \sum_{\substack{j=1 \\ j\neq i}}^{N} \left[\frac{1}{2} + b_i \left(1+\frac{3b_i}{2}\right) - (1+\varepsilon_j^*-\varepsilon_i)^2 \right], \qquad (6.41)
\end{aligned}
$$

are the quasi-steady moment on airfoil i, the apparent-mass moment, the moment induced by its own wake, and the moment induced by the other airfoils' unsteady wakes, respectively. The last term in (6.37) is the moment induced by the normal force to the plate in relation to its pivot point. As in the case of the lift, for a single airfoil the above expressions coincide with the moment obtained by von Kármán and Sears, 1938. For easy reference, it is given by the equation (3.56).

Finally, the input power (6.9) in non-dimensional form is given by

$$C_P = \sum_{i=1}^{N} C_P^{(i)}, \quad C_P^{(i)} = -\dot{h}_i(t) C_L^{(i)} - 2\dot{\alpha}_i(t) C_M^{(i)}. \tag{6.42}$$

6.4 FORCES AND MOMENT FOR TWO AIRFOILS IN TANDEM CONFIGURATION

The configuration of greatest interest is that of just two airfoils with the same chord length oscillating at the same frequency in aligned tandem configuration. In this section, it is simplified the general expressions obtained in §6.3.2 for this particular configuration, and arbitrary values of the remaining parameters.

Since the vorticity ϖ_{ji} in (6.27) is not trivially solved, to simplify it is assumed that the contribution of the hindwing vorticity distribution to the forewind vorticity distribution is negligible in (6.27), as shown by numerical and experimental results (Broering, Lian, and Henshaw, 2012; Gong, Jia, and Xi, 2015; Gong, Jia, and Xi, 2016; Lua et al., 2016; Yang, Pettersen, and Xiong, 2016). But it is retained the effect of the hindwing wake vorticity on the forewing through (6.23). Thus, in first approximation, it is only considered ϖ_{12}, computed with the assumption that the main contribution from ϖ_{s1} in (6.27) comes from ϖ_{01}. So that, with these assumptions, in first approximation,

$$\begin{aligned}
\varpi_{12}(x,t) =& \frac{1}{\pi^2}\sqrt{\frac{1+\varepsilon-x}{1-\varepsilon+x}} \int_{-1+\varepsilon}^{1+\varepsilon} \sqrt{\frac{1-\varepsilon+\xi}{1+\varepsilon-\xi}} \frac{1}{\xi-x} \int_{-1}^{1} \frac{\varpi_{s1}(\xi',t)}{\xi'-\xi} d\xi' d\xi, \\
\simeq& \frac{1}{\pi}\sqrt{\frac{1+\varepsilon-x}{1-\varepsilon+x}} \int_{-1}^{1} \sqrt{\frac{\xi+1-\varepsilon}{\xi-1-\varepsilon}} \frac{\varpi_{01}(\xi,t)}{\xi-x} d\xi, \\
\simeq& \frac{1}{\pi}\sqrt{\frac{1+\varepsilon-x}{1-\varepsilon+x}} \Big[\Gamma_{01}(t) f_{\gamma}(x) + \dot{\alpha}_1(t) f_{\gamma\alpha}(x) \Big],
\end{aligned} \tag{6.43}$$

and consequently

$$\begin{aligned}
\Gamma_{12}(t) \simeq& \frac{1}{\pi} \int_{-1+\varepsilon}^{1+\varepsilon} \sqrt{\frac{1+\varepsilon-x}{1-\varepsilon+x}} \int_{-1}^{1} \sqrt{\frac{\xi+1-\varepsilon}{\xi-1-\varepsilon}} \frac{\varpi_{01}(\xi,t)}{\xi-x} d\xi, \\
=& \Gamma_{01}(t) f_{\Gamma} + \dot{\alpha}_1(t) f_{\Gamma\alpha}, \quad \Gamma_{12}(t) := G_{12} e^{ikt},
\end{aligned} \tag{6.44}$$

where the functions $f_{\gamma}(x), f_{\gamma\alpha}(x), f_{\Gamma}$ and $f_{\Gamma\alpha}$ are given by (C.13)-(C.16), respectively in the Appendix C. Thus, the vorticity distribution of each plate from (6.10)

$$\begin{aligned}
\varpi_{s1}(x,t) \simeq& \frac{1}{\pi}\sqrt{\frac{1-x}{1+x}} \Bigg\{ \Gamma_{01} + \dot{\alpha}_1(1+2x)\pi + \int_{1}^{\infty} \sqrt{\frac{\xi+1}{\xi-1}} \frac{\varpi_{e1}(\xi,t)}{\xi-x} d\xi + \\
& \int_{1+\varepsilon}^{\infty} \sqrt{\frac{\xi+1}{\xi-1}} \frac{\varpi_{e2}(\xi,t)}{\xi-x} d\xi \Bigg\},
\end{aligned} \tag{6.45}$$

$$\varpi_{s2}(x,t) \simeq \frac{1}{\pi}\sqrt{\frac{1+\varepsilon-x}{1-\varepsilon+x}}\left\{\Gamma_{02}+\dot{\alpha}_2\left[1+2(x-\varepsilon)\right]\pi+\int_{1+\varepsilon}^{\infty}\sqrt{\frac{\xi+1-\varepsilon}{\xi-1-\varepsilon}}\frac{\varpi_{e2}(\xi,t)}{\xi-x}d\xi+\right.$$
$$\int_{1+\varepsilon}^{\infty}\sqrt{\frac{\xi+1-\varepsilon}{\xi-1-\varepsilon}}\frac{\varpi_{e1}(\xi,t)}{\xi-x}d\xi-\int_{1}^{-1+\varepsilon}\sqrt{\frac{\xi+1-\varepsilon}{\xi-1-\varepsilon}}\frac{\varpi_{e1}(\xi,t)}{\xi-x}d\xi+$$
$$\left.\Gamma_{01}f_{\gamma}(x)+\dot{\alpha}_1 f_{\gamma\alpha}(x)\right\}. \tag{6.46}$$

On the other hand, from Kelvin's circulation theorem (6.12), in first approximation with the assumptions made,

$$\int_{1}^{\infty}\sqrt{\frac{\xi+1}{\xi-1}}\varpi_{e1}(\xi,t)d\xi+\int_{1+\varepsilon}^{\infty}\left(\sqrt{\frac{\xi+1}{\xi-1}}-1\right)\varpi_{e2}(\xi,t)d\xi \simeq -\Gamma_{01}, \tag{6.47}$$

$$\int_{1+\varepsilon}^{\infty}\sqrt{\frac{\xi+1-\varepsilon}{\xi-1-\varepsilon}}\varpi_{e2}(\xi,t)d\xi+\int_{1}^{\infty}\left(\sqrt{\frac{\xi+1-\varepsilon}{\xi-1-\varepsilon}}-1\right)\varpi_{e1}(\xi,t)d\xi \simeq -\Gamma_{02}-\Gamma_{12}. \tag{6.48}$$

So, substituting the value of Γ_{01} and Γ_{02} given by (6.21), Γ_{12} by (6.44) and the well-known solution for the unsteady wakes (Theodorsen, 1935; Kármán and Sears, 1938), which remains same but now displaced the distance ε_i, i.e,

$$\varpi_{ei}(\xi,t) = g_i e^{ik[t-(\xi-\varepsilon_i)]}, \tag{6.49}$$

one can obtain the following system of linear equations for the unknown constants g_1 and g_2:

$$\left.\begin{aligned} \mathsf{a}(k)g_1-\mathsf{b}(k,\varepsilon)g_2 &= G_{01} \\ \mathsf{a}(k)g_2-\mathsf{c}(k,\varepsilon)g_1 &= G_{02}+G_{12} \end{aligned}\right\}, \tag{6.50}$$

where $\mathsf{a}(k), \mathsf{b}(k,\varepsilon)$ and $\mathbf{c}(k,\varepsilon)$ are given by the expressions (C.4),(C.5) and (C.6), respectively in the Appendix C. Thus, simplifying and solving, the constants g_1 and g_2 are:

$$g_1 = \frac{F_a(k,\varepsilon)}{\mathsf{a}(k)}G_{01}+\frac{F_b(k,\varepsilon)}{\mathsf{a}(k)}\left(G_{02}+G_{12}\right), \tag{6.51}$$

$$g_2 = \frac{F_a(k,\varepsilon)}{\mathsf{a}(k)}\left(G_{02}+G_{12}\right)+\frac{F_c(k,\varepsilon)}{\mathsf{a}(k)}G_{01}, \tag{6.52}$$

with F_a, F_b and F_c given by (C.7) and (C.8) in the Appendix C.

6.4.1 *Coefficients and average quantities*

Once the vorticity distributions are computed, the forces and moment coefficients given by (6.28), (6.33) and (6.37), respectively, can be written as

$$C_L^{(i)} = \mathcal{L}_0(t)+\Gamma_{01}(t)\mathcal{L}_{01}+\left[\Gamma_{02}(t)+\Gamma_{12}(t)\right]\mathcal{L}_{02}, \tag{6.53}$$

$$C_T^{(i)} = -\alpha_i(t)C_L^{(i)}(t)+\dot{\alpha}_i(t)\mathcal{T}_0(t)+\Gamma_{01}(t)\mathcal{T}_{01}(t)+\left[\Gamma_{02}(t)+\Gamma_{12}(t)\right]\mathcal{T}_{02}(t), \tag{6.54}$$

$$C_M^{(i)} = \frac{a_i}{2}C_L^{(i)}(t)+\mathcal{M}_0(t)+\Gamma_{01}(t)\mathcal{M}_{01}+\left[\Gamma_{02}(t)+\Gamma_{12}(t)\right]\mathcal{M}_{02}. \tag{6.55}$$

It must be noted that the functions of time and coefficients $\mathcal{L}, \mathcal{T}$ and $\mathcal{M}$ are different for each airfoil i. Full expressions for both airfoils are given in the Appendix C. In the limit of very large distance between airfoils ($d := d_2 \to \infty$ or $\varepsilon := \varepsilon_2 \to \infty$), it is easy to check that the forewing lift tends to the lift of a single airfoil given in Kármán and Sears, 1938:

$$\lim_{\varepsilon\to\infty} \mathcal{L}_0(t) = \pi\left(\dot{\alpha}_1 - \ddot{h}_1 - a_1\ddot{\alpha}_1\right), \quad \lim_{\varepsilon\to\infty} \mathcal{L}_{01} = C(k), \quad \lim_{\varepsilon\to\infty} \mathcal{L}_{02} = 0. \tag{6.56}$$

However, for the hindwing, the coefficient $\mathcal{L}_{01}$ do not vanish because in the present inviscid model, the forewing's wake extends to infinite since there is no viscosity to dissipate it. In the same way, the thrust and moment of the forewing tend to those for a single airfoil (given in Fernandez-Feria, 2016 and Kármán and Sears, 1938, respectively) when $\varepsilon \to \infty$, but the coefficients $\mathcal{T}_{01}$ and $\mathcal{M}_{01}$ do not vanish for the hindwind.

On the other hand, for combined pitching and heaving motions it is convenient to define the following nondimensional parameters

$$\theta_i := \frac{a_{0i}}{kh_{0i}}, \quad \theta_{ij} := \frac{a_{0i}}{kh_{0j}}. \tag{6.57}$$

For a single airfoil θ is already defined in (4.40). In addition, it is convenient to define the ratios of the amplitudes of heaving and pitching motions, respectively, i.e.,

$$\Theta_h := \frac{h_{0j}}{h_{0i}}, \quad \Theta_a := \frac{a_{0j}}{a_{0i}}, \tag{6.58}$$

So that, using the above parameters, (6.57) and (6.58), the time-averaged thrust and input power coefficients, defined in (3.64) for a single plate and extensible for each plate i, can be written in a compact form as

$$\frac{\bar{C}_T^{(i)}}{(kh_{0i})^2} = t_h\left(k,\varepsilon,\varphi,\Theta_h\right) + t_{hp}\left(k,\varepsilon,\varphi,\phi_i,\phi_j,a_i,a_j,\Theta_h,\Theta_a\right)\theta_i + t_p\left(k,\varepsilon,\varphi,a_i,a_j,\Theta_a\right)\theta_i^2, \tag{6.59}$$

$$\frac{\bar{C}_P^{(i)}}{(kh_{0i})^2} = p_h\left(k,\varepsilon,\varphi,\Theta_h\right) + p_{hp}\left(k,\varepsilon,\varphi,\phi_i,\phi_j,a_i,a_j,\Theta_h,\Theta_a\right)\theta_i + p_p\left(k,\varepsilon,\varphi,a_i,a_j,\Theta_a\right)\theta_i^2, \tag{6.60}$$

for $i = 1, 2$ and $j \neq i$ when appearing in the expression for the airfoil i. The functions $t_h, t_{hp}, t_p, p_h, p_{hp}$ and p_p are given in the Appendix C. Note that, these functions which appearing in these expressions are different for each airfoil i. Alternatively, they can be written factoring out the square of the pitching amplitude a_{0i}^2, instead of the square of the heaving amplitude $(kh_{0i})^2$, in terms of the inverse of the feathering parameter and the same functions of the non-dimensional parameters (see e.g. (4.42) and (4.45) in the case of one single airfoil).

Another quantity of interest is the propulsive efficiency of each airfoil i, or ratio of the time-averaged power output of the airfoil (thrust force multiplied by the forward speed U) and the time-averaged input power required to drive the airfoil,

$$\eta_i = \frac{\bar{C}_T^{(i)}}{\bar{C}_P^{(i)}}. \tag{6.61}$$

Similarly to the time-average coefficients, the efficiency of each airfoil (6.61) is conveniently written in terms of the above functions and the feathering parameter θ_i:

$$\eta_i = \frac{t_h\left(k,\varepsilon,\varphi,\Theta_h\right) + t_c\left(k,\varepsilon,\varphi,\phi_i,\phi_j,a_i,a_j,\Theta_h,\Theta_a\right)\theta_i + t_p\left(k,\varepsilon,\varphi,a_i,a_j,\Theta_a\right)\theta_i^2}{p_h\left(k,\varepsilon,\varphi,\Theta_h\right) + p_c\left(k,\varepsilon,\varphi,\phi_i,\phi_j,a_i,a_j,\Theta_h,\Theta_a\right)\theta_i + p_p\left(k,\varepsilon,\varphi,a_i,a_j,\Theta_a\right)\theta_i^2}, \tag{6.62}$$

for $i = 1,2$ and $j \neq i$ when appearing in the expression for the airfoil i. Finally, the global propulsive efficiency is given by

$$\eta = \frac{\bar{C}_T^{(1)} + \bar{C}_T^{(2)}}{\bar{C}_P^{(1)} + \bar{C}_P^{(2)}}. \tag{6.63}$$

6.5 ANALYSIS OF THE IMPACT OF THE UPSTREAM WAKE ON THE BACK-FOIL THRUST

The main contribution to the amplification (or reduction) in the propulsion capabilities of flapping foils in tandem configuration, in relation to an isolated flapping foil, obviously comes from the interaction of the front-foil wake with the back foil, which may enhance (or reduce) the thrust generated by the trailing foil in relation to a single foil undergoing the same motion, and therefore increase (or reduce) the propulsive efficiency of the tandem system. In the present linear potential theory, where no leading- or trailing-edge vortices are intermittently shed by the flapping foils, but vorticity is continuously shed in concentrated free (wake) vortex sheets, in addition to the vorticity inside the thin bound vortex sheets on the flapping foils, this contribution is characterized by (6.25), or contribution to the vorticity distribution along the back foil, ϖ_{s2}, due to the vorticity distribution ϖ_{e1} in the upstream wake.

In particular, it is well known that the intensity of the bound vorticity distribution ϖ_s on a plate at the leading edge is related, within the linear potential theory, to the suction force at the leading edge (Kármán and Sears, 1938): ϖ_s is singular at the leading edge, but generates a finite suction force. This was used, for example, by Garrick et al., 1936, to quantify the suction component of the thrust force generated by a pitching and heaving rigid plate within the linear potential theory. This suction thrust force is given by $T_S = \pi \rho K^2$, where $K = \lim_{x \to c/2} \sqrt{x + c/2}\varpi_s(x,t)/2$ for an airfoil with the leading edge at $x = -c/2$. Thus, taking into account the above argument and using the present dimensionless variables, the main contribution to the thrust force amplification in the back foil in relation to an isolated foil can be obtained from (6.25), when the singularity at the leading edge $x = -1 + \varepsilon$ is removed (particularized for two airfoils in tandem configuration); i.e., from the quantity

$$m(x,t) := \int_{1+\varepsilon}^{\infty} \sqrt{\frac{\xi + 1 - \varepsilon}{\xi - 1 - \varepsilon}} \frac{\varpi_{e1}(\xi,t)}{\xi - x} d\xi - \int_{1}^{-1+\varepsilon} \sqrt{\frac{\xi + 1 - \varepsilon}{\xi - 1 - \varepsilon}} \frac{\varpi_{e1}(\xi,t)}{\xi - x} d\xi, \tag{6.64}$$

which, after substituting the upstream wake vorticity ϖ_{e1} from (6.49), results

$$\begin{aligned} m(x,t) = \left[\frac{F_a(k,\varepsilon)}{\mathsf{a}(k)} \Gamma_{01}(t) + \frac{F_b(k,\varepsilon)}{\mathsf{a}(k)} \left(\Gamma_{02}(t) + \Gamma_{12}(t) \right) \right] \times \\ \left[\int_{1+\varepsilon}^{\infty} \sqrt{\frac{\xi + 1 - \varepsilon}{\xi - 1 - \varepsilon}} \frac{e^{-ik\xi}}{\xi - x} d\xi - \int_{1}^{-1+\varepsilon} \sqrt{\frac{\xi + 1 - \varepsilon}{\xi - 1 - \varepsilon}} \frac{e^{-ik\xi}}{\xi - x} d\xi \right]. \end{aligned} \tag{6.65}$$

The relevant value of this magnitude is the time-average of the square of the real part of this quantity at the leading edge of the back foil, which as argued above characterizes (is proportional to) the main contribution to the nondimensional amplification in the suction thrust of the trailing foil due to the upstream wake:

$$\mathcal{M} := \frac{k}{2\pi} \int_{t}^{t+2\pi/k} \Re[m(x = -1 + \varepsilon, t)] \times \Re[m(x = -1 + \varepsilon, t)] dt. \tag{6.66}$$

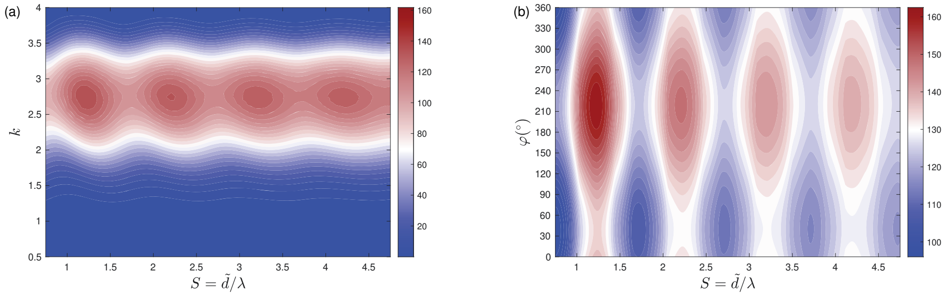

Figure 6.2: Contour values of $\mathcal{M}/h_0^2$ for purely heaving motion in the schooling number-frequency plane with $\varphi=0$ (a) and in the schooling number-phase shift plane with $k=2.75$ (b).

The maxima in $\mathcal{M}$ as the geometrical and kinematic parameters are varied will provide relevant information about the optimal configurations of the tandem in terms of thrust and, most likely, in terms of propulsive efficiency, since the main propulsive advantage of the tandem configuration is the amplification in the thrust force of the trailing foil. For purely heaving foils with the same amplitude h_0, $\mathcal{M}/h_0^2$ depends only on k, d and φ for rigid foils. This quantity is plotted in Figure 6.2(a), with both plates in phase $(\varphi=0)$, as a function of the reduced frequency, k, and the so-called schooling number, S (Ramananarivo et al., 2016),

$$S=\frac{\tilde{d}}{\lambda},\quad \frac{\lambda}{c}=\frac{\pi}{k}, \tag{6.67}$$

so that, S measures the separation between airfoils in units of the wake's wavelength. It is noticeable that the thrust amplification pattern has a frequency band containing peaks at selected values of the schooling number which are slightly larger than the successive natural numbers, in good agreement with the experimental results by Ramananarivo et al., 2016. There exist similar bands at higher frequencies, but only the lowest frequency one is shown in Figure 6.2(a). On the other hand, Figure 6.2(b) shows the effect of φ on $\mathcal{M}/h_0^2$ for the optimal frequency in Figure 6.2(a) $(k\simeq 2.75)$. It is observed that the optimal phase shift for thrust enhancement of the trailing foil due to its interaction with the upstream wake is about 220°.

It must be remarked that this analysis considers only the (arguably) most relevant contribution to the suction force at the leading edge of the trailing foil, not all contributions to the total thrust force. But it serves to illustrate the physical origin of the thrust (and efficiency) enhancement in a tandem configuration in comparison with an isolated foil.

6.6 RESULTS AND DISCUSSION

6.6.1 *Pure heaving motion*

It is considered first the simplest case of a pure heaving motion of both airfoils, for which (6.59)-(6.60) become

$$\bar{C}_T^{(i)}=(kh_0)^2 t_h(k,\varepsilon,\varphi,\Theta_h),\quad \bar{C}_P^{(i)}=(kh_0)^2 p_h(k,\varepsilon,\varphi,\Theta_h). \tag{6.68}$$

If, additionally, the heave amplitudes of both airfoils are the same, $h_{01}=h_{02}=h_0$, i.e., $\Theta_h=1$, the function t_h of the time-averaged thrust coefficients, p_h of the mean value of the input power, and the propulsive efficiency depent on only of k, ε and φ, where the propulsive efficiency is independent of the amplitude of heaving motion, $\eta = t_h/p_h$.

In order to define a thrust coefficient independent of the amplitude of the oscillations, one can normalize it with the thrust of a single airfoil, C_{T0}, which is also proportional to $(kh_0)^2$,

$$\hat{C}_T^{(i)} := \frac{\bar{C}_T^{(i)}}{\bar{C}_{T0}} = \hat{C}_T^{(i)}(k, \varepsilon, \varphi), \quad \text{and} \quad \hat{C}_T := \frac{\bar{C}_T}{2\bar{C}_{T0}} = \hat{C}_T(k, \varepsilon, \varphi), \tag{6.69}$$

for the airfoil i and for the whole tandem system, respectively, which are functions only of the reduced frequency k, the non-dimensional distance between leading edges, $\varepsilon = 2 + d$, and the phase shift φ between the two heaving motions. Similarly, one can define an efficiency relative to that of a single airfoil, η_0, as

$$\hat{\eta}_i := \eta_i - \eta_0, \quad \text{and} \quad \hat{\eta} := \eta - \eta_0. \tag{6.70}$$

with η_0 defined in (4.46) but in this case for a rigid plate. In the Figure 6.3 is shown these normalized quantities as functions of the reduced frequency k and the non-dimensional distance between airfoils, $\tilde{d}/c = d/2$ (the 'tilde' over d means dimensional quantity), when the two heaving motions are in phase ($\varphi = 0$). It is observed that the thrust and the efficiency of the forewing tend to the values of a single airfoil as the distance between airfoils increases to infinity; i.e., $\hat{C}_T^{(1)} \to 1$ and $\hat{\eta}_1 \to 0$ as $\tilde{d}/c \to \infty$. However, this is not so for the hindwing, and consequently for the global values, as a result of the non-viscous wake of the forewing extending to infinite. Another consequence of this anomaly of the present inviscid model is that the input power of the hindwing may be negative for some values of the parameters (in contrast, the forewing's input power is always positive). Thus, to discard cases where the hind wind supplies energy to the system, it has been plotted in Figure 6.3 (d) and (f) only the cases where the hindwing's input power coefficient is positive.

It is also observed in Figure 6.3 that the thrust and the efficiency are magnified in relation to a single airfoil ($\hat{C}_T > 1$ and $\hat{\eta} > 0$, respectively) in several regions of the $(\tilde{d}/c, k)-$plane where the reduced frequency is inversely proportional to the distance between airfoils. Particularly, these two quantities reach a relative maximum when $k = k^*$ given by

$$k^* \simeq \frac{k_t^{(n)}(\varphi)}{d/2+1} = \frac{k_t^{(n)}(\varphi)}{\varepsilon/2} \quad \text{for} \quad \hat{C}_T, \quad \text{and} \quad k^* \simeq \frac{k_\eta^{(n)}(\varphi)}{d/2+1} = \frac{k_\eta^{(n)}(\varphi)}{\varepsilon/2} \quad \text{for} \quad \hat{\eta}, \tag{6.71}$$

where $k_t^{(n)}(\varphi)$ and $k_\eta^{(n)}(\varphi)$ are functions of φ, and $n = 1, 2, \ldots$ identifies the different modes of amplification. These functions are plotted in Figure 6.4 for the first three modes. Note that $k_t^{(n)}(\varphi)$ is the value of the reduced frequency of the corresponding mode for $\tilde{d}/c = 0$ (compare Figure 6.4 for $\varphi = 0$ with Figure 6.3). However, to compute $k_\eta^{(n)}(\varphi)$, it is selected a specific combination of $\tilde{d}/c$ and k related to the schooling number S given by (6.67).

This optimal behavior can be better understood by writing the reduced frequency in terms of the wavelength λ of the wake and the so-called schooling number S given by (6.67), measuring the separation between airfoils in units of the wake's wavelength. Figure 6.5(a) shows the same contours of $\hat{\eta}$ given in Figure 6.3(f) but now plotted on

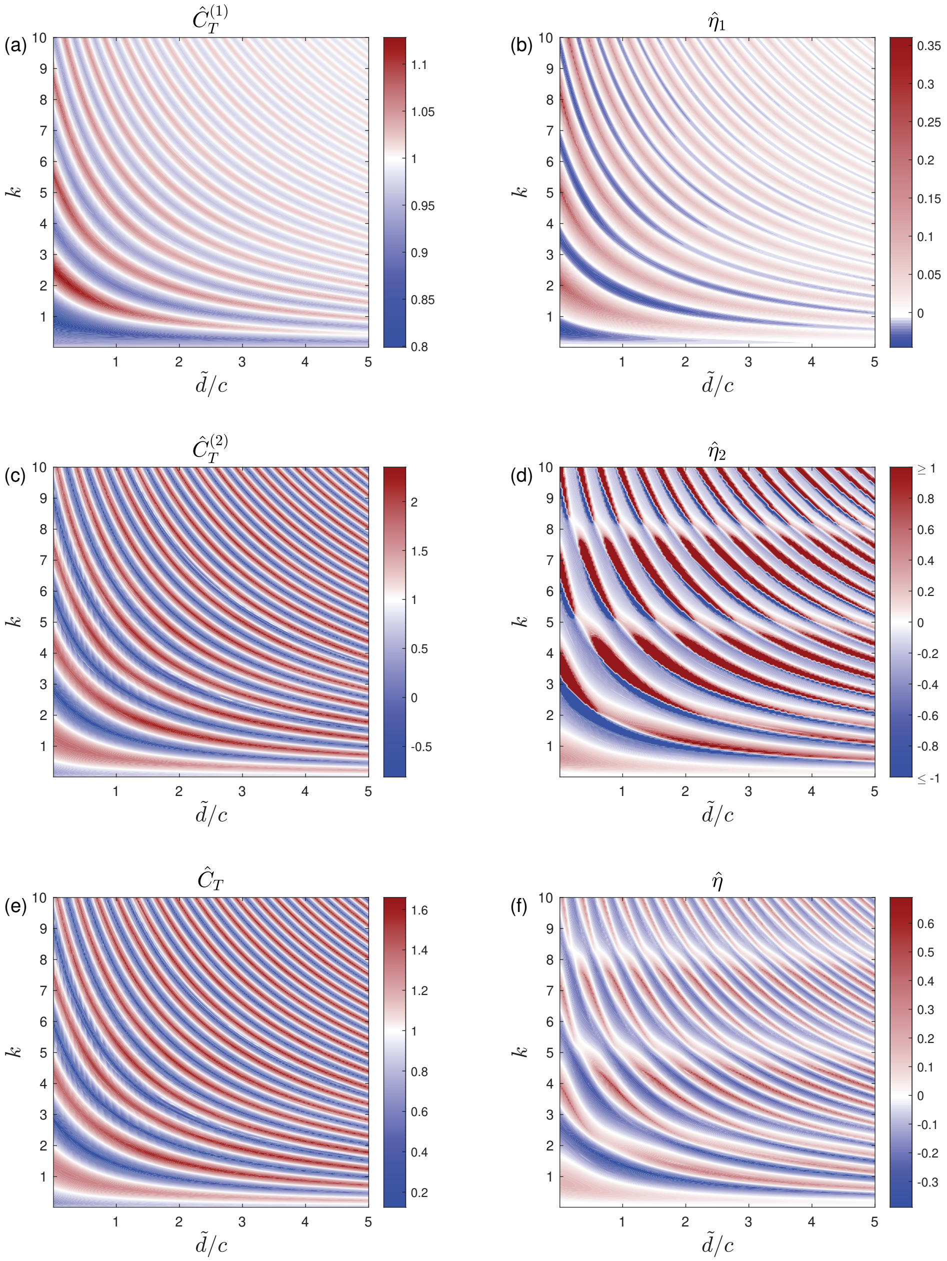

Figure 6.3: Contours of the normalized thrust $\hat{C}_T$ (left panels) , and propulsive efficiency $\hat{\eta}$ (right panels), for a pure heaving motion in a $(\tilde{d}/c, k)-$plane for $\varphi = 0$. (a)-(b) Forewing, (c)-(d) hindwing, and (e)-(f) global values.

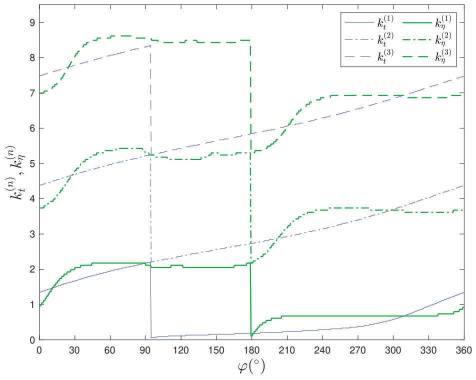

Figure 6.4: Functions $k_t^{(n)}(\varphi)$ and $k_\eta^{(n)}(\varphi)$ for $n = 1, 2$ and 3.

the $(\lambda/c, S)$-plane, showing that the different modes of propulsive efficiency magnification correspond to integer values of the schooling number S, provided that λ is sufficiently large (k is not too large). This is in agreement with the experimental results by Ramananarivo et al., 2016, for two self-propelled heaving wings, which are also plotted in Figure 6.5(a). These authors found that the self-propelled foils undergoing a heaving motion at high Reynolds numbers spontaneously assume one of multiple arrangements due to flow interactions that correspond, approximately, to an integer multiple of the wavelength λ. These stable locations are shown here to correspond to relative maxima of the global propulsive efficiency of the tandem configuration, as also argued by Ramananarivo et al., 2016, but here computed analytically from the linearized potential theory. Higher modes predicted by the present theory ($S > 4$, say) are not observed in practice because the wake dissipation by viscosity is obviously not considered by the present potential theory. For the same reason, the theory fails for high values of k.

Since the theory agrees better with the experimental results for sufficiently large values of λ/c (i.e., for k of order unity or below), to obtain the values of $k_\eta^{(n)}(\varphi)$ for the different modes plotted in Figure 6.4 and Figure 6.5 it has been used a (sufficiently small) value of k corresponding to the region with constant S for each n, for given φ.

Figure Figure 6.5(b) shows also a good agreement between the stable locations found experimentally by Newbolt, Zhang, and Ristroph, 2019, for two foils undergoing heaving motions with the same frequency and amplitude, but for different phase φ, and the present theoretical results for the maximum values of $\hat{\eta}$. Note that the theory predicts two local maxima of the efficiency for each mode, one around $\varphi = 130^\circ$ and the other one for $\varphi \simeq 300^\circ$.

Finally, Figure 6.6 summarizes the optimal results for two heaving airfoils in tandem configuration, representing the maximum values of the normalized global thrust coefficient and global propulsive efficiency corresponding to the three first modes as the phase lag φ is varied, together with the corresponding values of the optimal reduced frequency k^* according to (6.71). Since the functions are periodic with φ, the three modes are plotted continuously. Figure 6.6(a) shows the contours of $\hat{C}_T$, with the corresponding value of k^* in Figure 6.6(c). It is observed that the local maxima of the normalized thrust are always larger than unity for the three modes plotted, i.e, the tandem configuration can

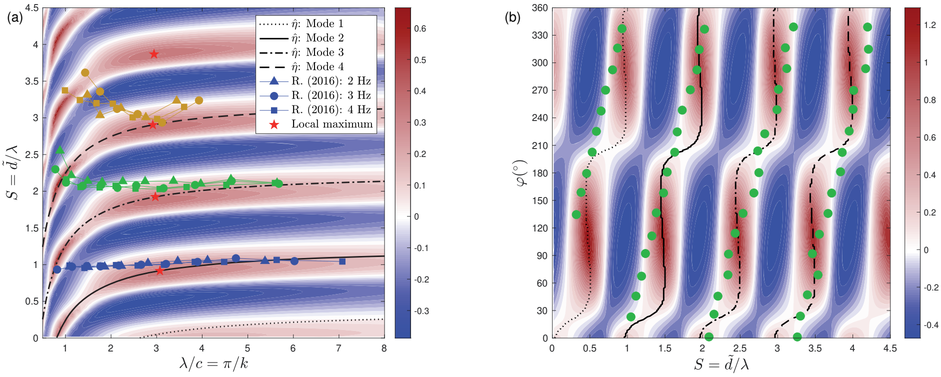

Figure 6.5: Contours of the normalized global efficiency $\hat{\eta}$ in the $(\lambda/c, S)$-plane for phase lag $\varphi = 0$ (a), and in the (S, φ)-plane for $\lambda/c = 4$ (b), both for pure heaving motions. The symbols correspond to experimental values of stable positions obtained by Ramananarivo et al., 2016, for different frequencies with $\varphi = 0$ in (a) (from their Fig. 3), and by Newbolt, Zhang, and Ristroph, 2019, for different values of φ and the same frequency and amplitude of both airfoils in (b) (from their Fig. 2). Also shown are the lines corresponding to the first four modes of global efficiency enhancement (6.71), and the locations of the local maxima of $\hat{\eta}$ for each mode with $\varphi = 0$ in (a).

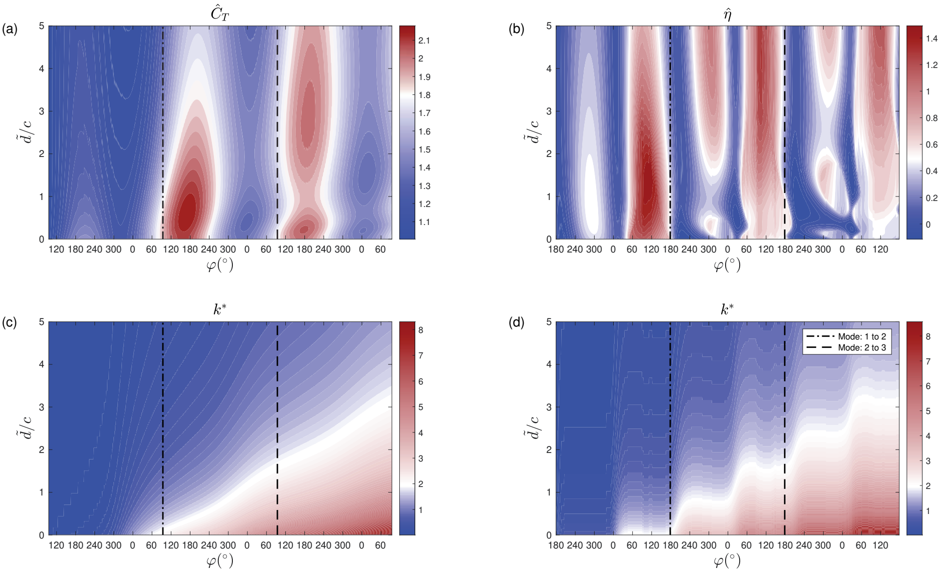

Figure 6.6: Contour plots in the $(\varphi, \tilde{d}/c)$-plane of $\hat{C}_T$ (a) and $\hat{\eta}$ (b) for the first three modes of thrust and efficiency enhancement given in Figure 6.4. The corresponding frequencies k^* are given in (c) and (d), respectively.

always generate more propulsion than a single airfoil if one selects the non-dimensional parameters corresponding to these three modes. For distances $\tilde{d}/c \lesssim 2$, the maximum value of $\hat{C}_T$ is found at the second mode around $\varphi \simeq 170°$. However, for $\tilde{d}/c \gtrsim 2$, the maximum is found at the third mode, again around $\varphi \simeq 170°$. In both cases $k^* < 2$.

For $k^* \lesssim 2$, the global efficiency [Figure 6.6(b) for $\hat{\eta}$ and Figure 6.6(d) for the corresponding k^* in each mode] presents two local maxima around $\varphi = 120°$ and $\varphi = 300°$ in each mode. On the other hand, for $\varphi \simeq 0°$ in the first mode, and around $\varphi = 30°$ in the second mode, the normalized efficiency is negative, i.e., lower than for a single airfoil [see also Figure 6.5(b)], contrary to the normalized thrust, which is always larger than unity for the three modes represented in Figure 6.6. Note also that regions with higher propulsive efficiency correspond to relatively low thrust.

6.6.2 *Pure pitching motion*

As the next simplest case it is considered that of two pitching plates, for which (6.59)-(6.60) become

$$\bar{C}_T^{(i)} = a_{0i}^2 t_p(k,\varepsilon,\varphi,a,\Theta_a), \quad \bar{C}_P^{(i)} = a_{0i}^2 p_p(k,\varepsilon,\varphi,a,\Theta_a). \tag{6.72}$$

If $a_{01} = a_{02} = a_0$, i.e., $\Theta_a = 1$, all the coefficients are proportional to a_0^2 and consequetly, the propulsive efficiency is independent of the amplitude of the pitching motion. Since C_{T0} for a single airfoil may change its sign depending on the values of the kinematics parameters (Fernandez-Feria, 2016), to avoid singularities it is convenient to redefine the normalize thrust coefficient as

$$\hat{C}_{Tp}^{(i)} := \frac{\bar{C}_T^{(i)} - \bar{C}_{T0}}{a_0^2} = \hat{C}_{Tp}(k,\varepsilon,\varphi,a), \quad \hat{C}_{Tp} := \frac{\bar{C}_T - \bar{C}_{T0}}{a_0^2} = \hat{C}_{Tp}(k,\varepsilon,\varphi,a). \tag{6.73}$$

The definitions of the normalized efficiencies (6.70) do not change. The normalized thrust and propulsive efficiency present similar magnification modes as in pure heaving motion, with reduced frequency inversely proportional to the distance between airfoils, so that they correspond approximately to constant values of the schooling number. Several of these modes can be observed in the contour plots of the normalized thrust coefficient and global efficiency of Figure 6.7 for two values of φ (now φ is the phase shift between the two pitching motions). However, expressions like (6.71) cannot be used now for all the range of k or ε because there are shifts in the proportionality constant at certain values of k. The lines plotted in Figure 6.7 representing the first few modes has been computed numerically from the local maxima in the contour plots. It is found that the global thrust coefficient and the global propulsive efficiency are both negative for small values of k when $\varphi \lesssim 180°$, and both positive otherwise, as it can be observed in Figure 6.7 for $\varphi = 90°$ and $\varphi = 270°$.

The results in Figure 6.7 are for a pivot axis located at the center of each airfoil ($a_1 = a_2 = a = 0$). Figure 6.8 shows the normalized thrust coefficient and the propulsive efficiency as a function of the pivot axis location a and the separation distance $\tilde{d}/c$ corresponding to the first three magnification modes when $\varphi = 150^o$. It is observed that higher thrust is reached for pivot points located close to the leading edge ($a = -1$), while higher propulsive efficiency is obtained when the pivot point is close the three-quarter chord length from the leading edge ($a = 0.5$), where the efficiency presents a singularity,

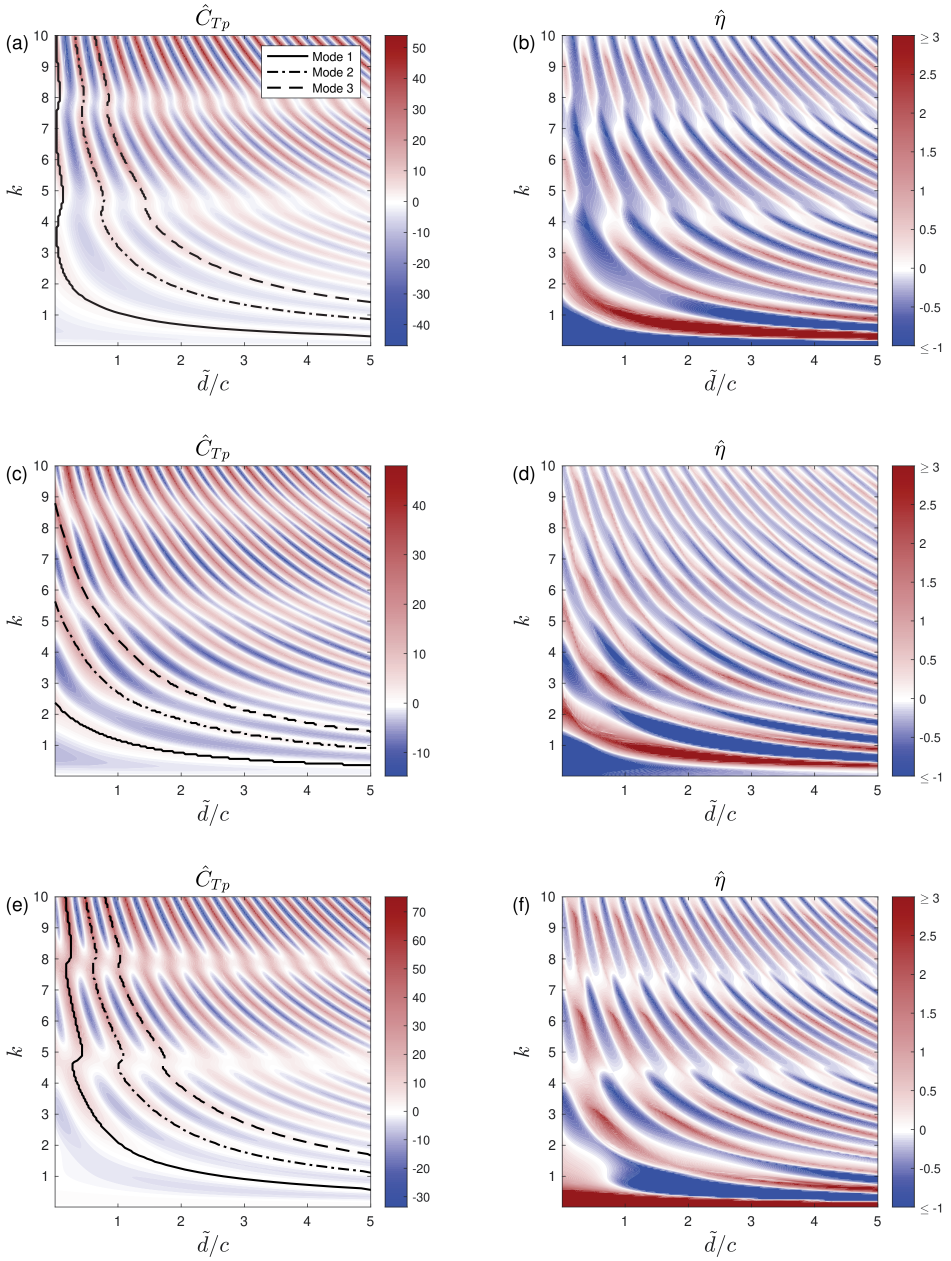

Figure 6.7: Contours of the normalized global thrust $\hat{C}_{Tp}$ (left panels) and global propulsive efficiency $\hat{\eta}$ (right panels) in a $(\tilde{d}/c, k)-$plane for pure pure pitching motion with $a = 0$. Panels (a)-(b) are for $\varphi = 90°$, (c)-(d) for $\varphi = 180°$ and (e)-(f) for $\varphi = 270°$. The lines corresponding to the first three modes are plotted in (a)-(b) and (c).

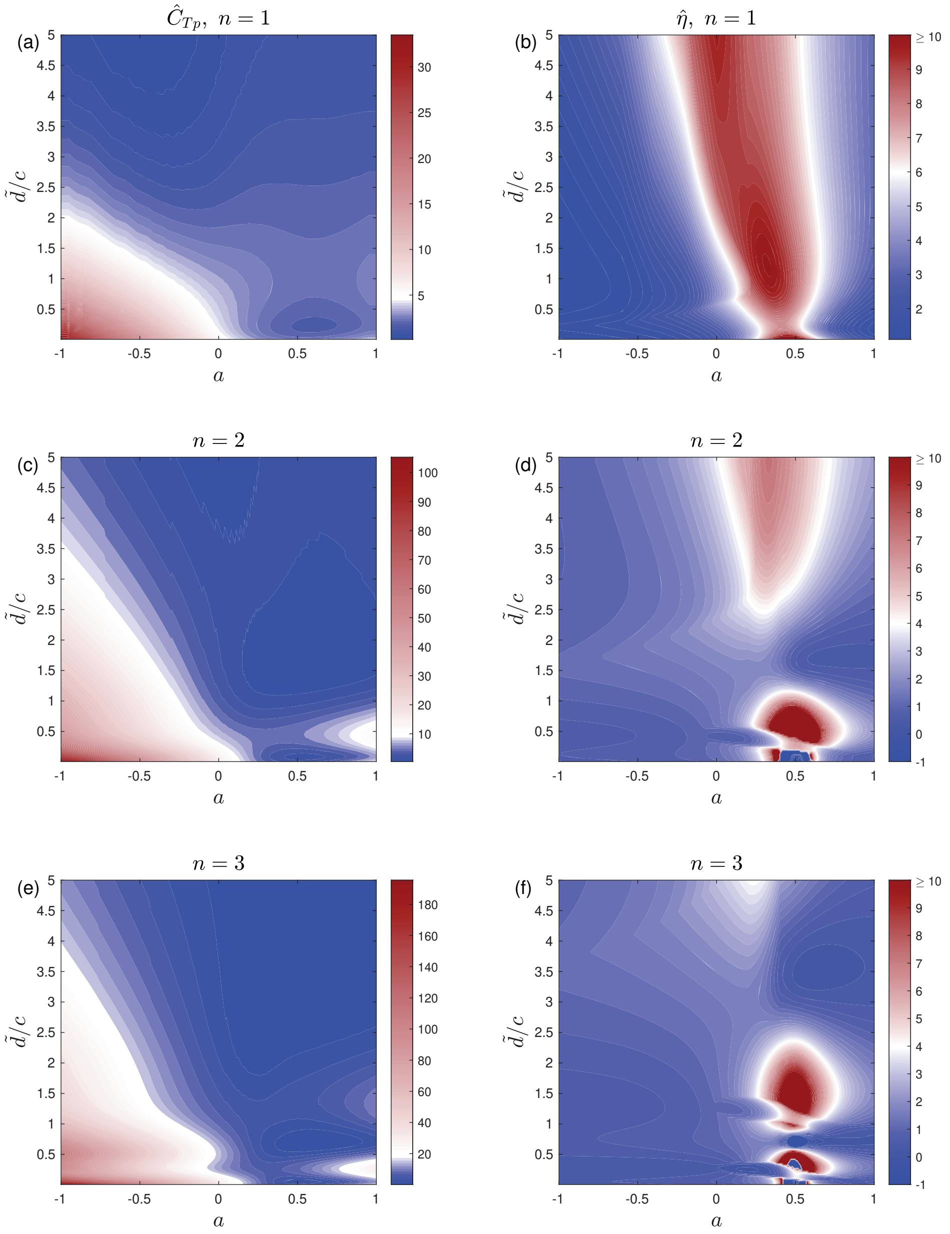

Figure 6.8: Contour plots in the $(a, \tilde{d}/c)$-plane of $\hat{C}_{Tp}$ (left panels), and $\hat{\eta}$ (right panels) corresponding to the first mode (a)-(b), the second mode (c)-(d) and the third mode (e)-(f) of thrust and efficiency magnification for a pure pitching motion with $\varphi = 150^o$.

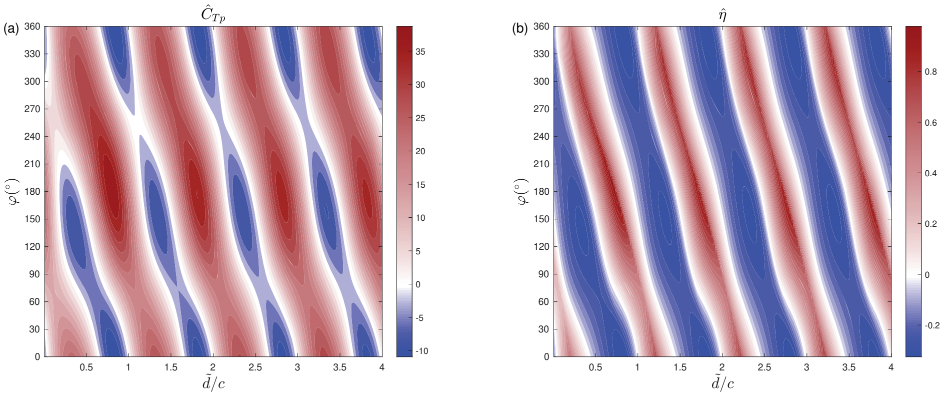

Figure 6.9: Contours of the tandem normalized thrust (a) and the normalized propulsive efficiency (b) in the $(\tilde{d}/c, \varphi)$-plane for purely pitching motions with $k = \pi$ and $a = -1$.

similarly to what happens for a single airfoil (Fernandez-Feria, 2017).

Finally, in the Figure 6.9 is shown the normalized thrust $\hat{C}_{Tp}$ and the normalized propulsive efficiency $\hat{\eta}$ in the spacing-phase shift plane pitching about their leading edges ($a_1 = a_2 = a = -1$), following Boschitsch, Dewey, and Smits, 2014, with the same reduced frequency, $k = \pi$. Boschitsch, Dewey, and Smits, 2014, plotted in their Fig. 8 the same normalized values but for the downstream foil. However, since the trailing foil is by far the main contributor to the tandem thrust and efficiency enhancement, the banded patterns in Figure 6.9 practically coincide with those reported in Fig. 8 of Boschitsch, Dewey, and Smits, 2014, but obviously with different contour values since it is representing different quantities. In fact, they were the first to observe these angled band patterns experimentally for the thrust amplification of the trailing foil in an in-line configuration of rigid foils pitching about their leading edges. In this case, it is found that the slope of the banded patterns is $\varphi \sim -2\pi\tilde{d}/c$.

6.6.3 *Combined motion*

Expressions (6.59) and (6.62) for combined pitching and heaving motions depend on so many non-dimensional parameters that it would be difficult to give here a brief account about the optimal conditions for maximum thrust force or maximum propulsive efficiency. So, it is only presented here a few representative results.

First, Figure 6.10 compares the present theoretical results with numerical results obtained by Broering, Lian, and Henshaw, 2012 for the temporal evolution of C_L and C_T for two flat plates in a given tandem configuration with a mean pitch angle different from zero ($\alpha_m = 5^o$) and for two distances between the plates. The numerical results are for relatively low amplitudes of the oscillations and a high Reynolds number, so that they agree quite well with the present potential results, working better for the largest distance between the plates ($\tilde{d}/c = 1$), when viscous effects near the plates are less relevant for their flow interaction than in the case with $\tilde{d}/c = 0.5$.

To put these results in a wider perspective, Figure 6.11 shows the global thrust coefficient and the global propulsive efficiency as functions of the distance between airfoils,

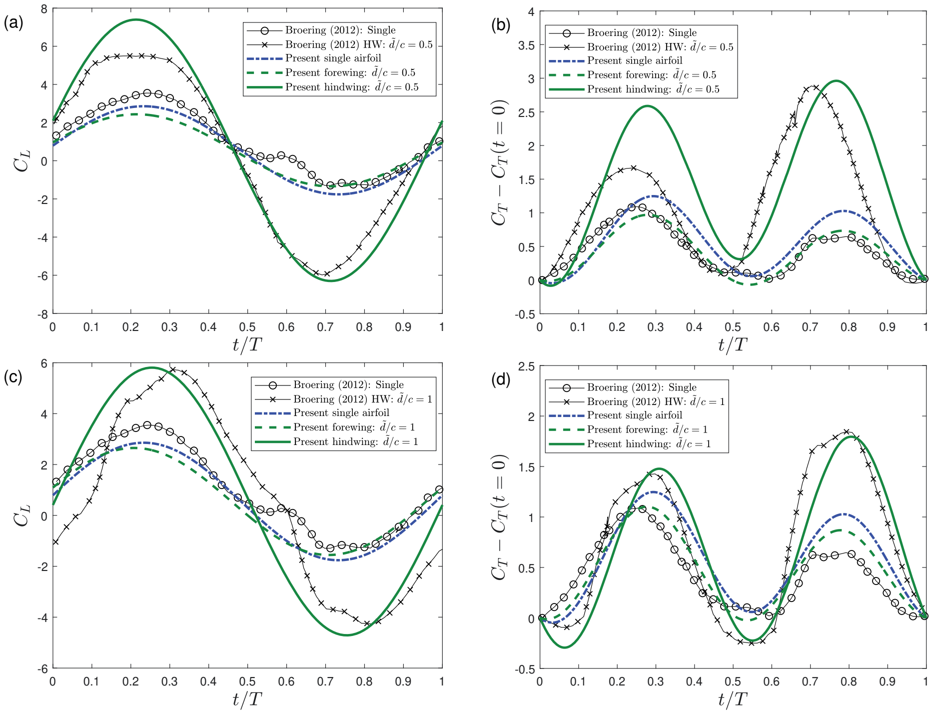

Figure 6.10: Comparison of the temporal evolution of C_L (left panels) and C_T (right panels) with numerical results from Broering, Lian, and Henshaw, 2012, for two different distances between airfoils, $\tilde{d}/c = 0.5$ (top panels) and $\tilde{d}/c = 1$ (bottom panels). $h_0/c = 0.5$, $a_0 = 20^\circ$, $\alpha_m = 5^\circ$, $a = -0.5$, $\phi = 90^\circ$, $\varphi = 0^\circ$, $k = 0.9425$, $\theta = 0.3704$ and $Re = 5000$. Also shown are the results for a single airfoil, both from the present theory and from the numerical simulations.

either varying k for a fixed value of the feathering parameter $\theta = a_0/kh_0$ (that selected in the numerical simulations of Broering, Lian, and Henshaw, 2012), or varying θ for the value of k in the results plotted in 6.10. The cases plotted in Figure 6.10 are marked with symbols in the contour plot of Figure 6.11, showing that they correspond to a relatively low thrust and low propulsive efficiency. If one keeps constant the value of the reduced frequency and varies θ, the optimal propulsion conditions are reached as θ approaches unity for two specific values of the distance between airfoils, $\tilde{d}/c < 0.5$ and $\tilde{d}/c \approx 3.5$.

6.7 CONCLUDING REMARKS

General expressions have been developed for the lift, thrust, moment and propulsive efficiency of an arbitrary set of two-dimensional pitching and heaving airfoils from the impulse theory in the limit of linear potential flow. In particular, it is provided closed analytical expressions for two airfoils in tandem configuration. For pure heaving motions of the airfoils it is found that there exist combinations of the reduced frequency and the normalized distance between airfoils, that depend on the phase shift of the two motions, for which the global propulsive efficiency of the tandem reaches a local maximum. These combinations, or modes, correspond to specific values of the so-called schooling number, in very good agreement with recent experimental results (Ramana-

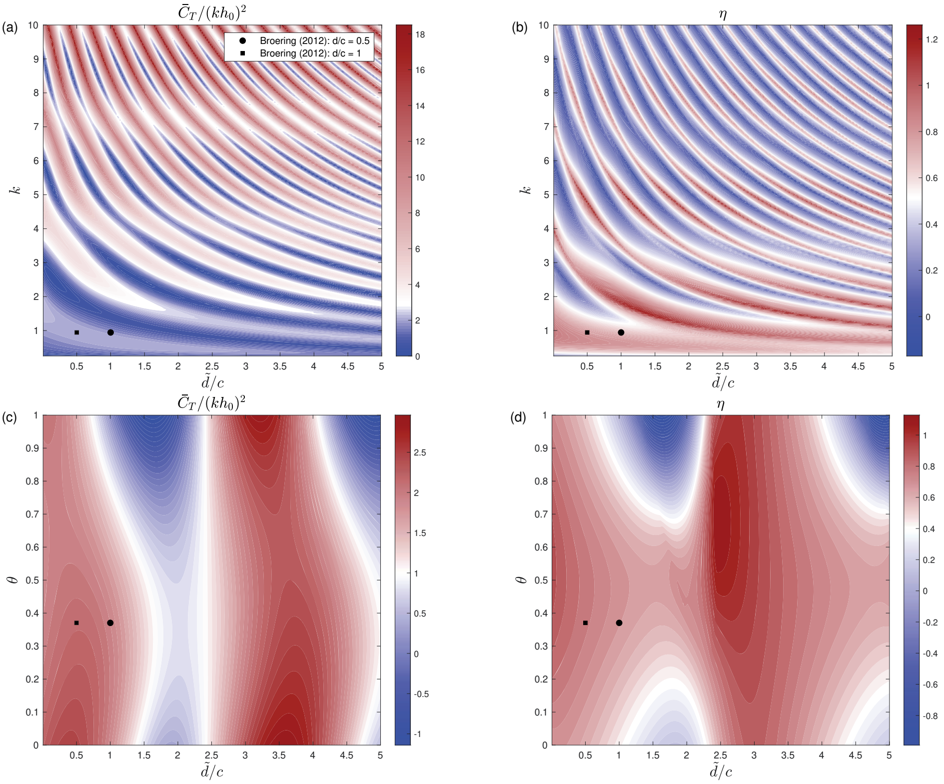

Figure 6.11: Contours of the normalized global thrust coefficient (left panels), and global propulsive efficiency η (right panels), in the $(\tilde{d}/c, k)$-plane for $\theta = a_0/kh_0 = 0.3704$ (top panels), and in the $(\tilde{d}/c, \theta)$-plane for $k = 0.9425$ (bottom panels). The remaining parameters of the combined pitching and heaving motions are the following: $\alpha_m = 5^\circ$, $a = -0.5$, $\phi = 90^\circ$ and $\varphi = 0^\circ$. The symbols mark the locations corresponding to the results by Broering, Lian, and Henshaw, 2012, plotted in Figure 6.10.

narivo et al., 2016; Newbolt, Zhang, and Ristroph, 2019). Similar modes are found for pure pitching motions. In general, the present formulation permits the identification of optimal conditions in terms of either thrust force or propulsive efficiency with much less effort than using numerical simulations or experiments. In addition to the comparison with experimental results for pure heaving motion, the present theoretical results have been also checked with numerical simulations for a complex pitching and heaving motion with small amplitudes and high Reynolds number for which the theory is limited, showing a good agreement. The theory is also limited to intermediate distances between the airfoils: for distances smaller than about one chord length viscous effects become important in the flow interaction between airfoils, while for distances much larger that the chord length the present results do not consider the viscous decay of the vortex wake. Nonetheless it is believed that the present analytical results constitute a good tool for the preliminary aerodynamic design, and a guide for the subsequent control, of MAVs based on pairs of flapping wings in tandem configuration.

7

FIRST OSCILLATION MODE OF TWO FLEXIBLE PLATES

7.1 INTRODUCTION

Though the validity of the theoretical approach so far is limited to high Reynolds number flow and to small flapping amplitudes, i.e., the flow does not separate and the wakes remain almost flat, it provides useful insight on the combined effect of the huge number of geometric and kinematic parameters on the propulsive performance of the tandem flapping foils. This insight is valuable in spite of the fact that some interesting configurations in terms of thrust and propulsive efficiency are often found in the range of high amplitudes where the linearized theory fails. For instance, using two-dimensional, potential flow theory, Bosch, 1978, showed that a lifting surface at rest located behind a pitching or a heaving foil considerably improves the propulsive efficiency of the resulting tandem arrangement, almost independently of the reduced frequency and the backward position of the trailing surface. This theory explained a previous experimental finding by Schmidt, 1965, that a stationary wing placed in the oscillatory wake of a flapping wing could generate additional thrust by recovering some of the energy released in the wake of the flapping airfoil. Later numerical simulations at high Reynolds numbers, without considering viscous effects (Tuncer and Platzer, 1996), corroborated the theoretical results, finding that with appropriate selection of the frequency, amplitude and separation of the leading foil, the tandem propulsive efficiency could be augmented more than 40% in relation to a single airfoil. However, later experiments and numerical simulations at low to moderate Reynolds numbers (Ortega-Casanova and Fernandez-Feria, 2016; Jones and Platzer, 1999), though in qualitative agreement with the inviscid results, showed that this benefit was greatly outweighed by the effect of viscous drag.

Using potential flow theory for two heaving foils in tandem configuration, Lan, 1979, showed that the maximum thrust can be generated with maximum power efficiency if the trailing foil flaps in advance to the front one by 90° to 180°, depending on the reduced frequency and the foil separation. For two pitching foils this author found that for a reduced frequency of 0.75 and a separation between half and one chord length the best propulsive efficiency is obtained when pitch leads heave by about 90°, while the maximum thrust is obtained for 45°. These results are again in qualitative agreement with later experimental studies, where it was shown that aerodynamic power requirement can be reduced up to 22% compared with a pair of isolated wings when the trailing wing leads the front one by about 90° in hovering flight (Lehmann, 2009; Usherwood and Lehmann, 2008), while the maximum thrust and propulsive efficiency in wind tunnel experiments where observed at phase angles from 0 to 50° (Warkentin and DeLaurier, 2007), depending on the reduced frequency and the foil spacing, in any case when the trailing foil leads the flapping motion.

A general analytical formulation of the aerodynamics performance of two heaving and pitching rigid foils in tandem configuration, based on the linearized potential flow theory, has been developed in the previous chapter, with the thrust forces computed following the vortex impulse theory (Fernandez-Feria, 2016). These theoretical results showed that the thrust and the propulsive efficiency are greatly enhanced in relation to

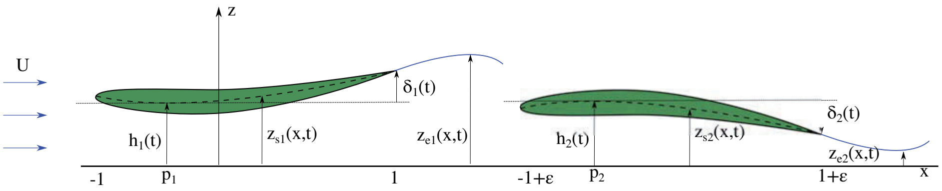

Figure 7.1: Schematic of the oscillating airfoils for heaving and flexural motion (nondimensional).

those of an isolated flapping foil when certain combinations of the reduced frequency and the dimensionless separation between the foils are used, that depend on the phasing between their oscillatory motions. For heaving foils, these combinations, or aerodynamic amplification modes, correspond to specific values of the so-called schooling number, in very good agreement with experimental results by Ramananarivo et al., 2016, and by Newbolt, Zhang, and Ristroph, 2019.

All these works are for rigid foils in a tandem arrangement. Flexibility of flapping wings and fins is known to greatly enhance the propulsive performance of natural fliers and swimmers. For single foils, its effect on the thrust force and the propulsive efficiency has been extensively analyzed (Heathcote, Martin, and Gursul, 2004; Heathcote and Gursul, 2007; Wu, 2011; Quinn, Lauder, and Smits, 2015; Olivier and Dumas, 2016; Wang, He, and Zhang, 2016; Smits, 2019). For tandem arrangements of flapping foils only a few recent works based on two-dimensional flow simulations are available, either assuming potential flow (Alben, 2009), or by solving the full Navier-Stokes equations coupled with the flexible foil dynamics (Maertens, Gao, and Triantafyllou, 2017; Park and Sung, 2018; Cong, Teng, and Cheng, 2020; Ryu et al., 2020). As aforementioned, owing to the complexity of the numerical simulations, specially for the moderate Reynolds numbers of interest in biomimetic aerial or aquatic vehicles, only very limited ranges of just a few of the many parameters governing the problem can be realistically analyzed. For this reason it is of interest to dispose of some analytical foresight from the two-dimensional, linear potential flow theory, even if the results are limited to high Reynolds numbers without flow separation, i.e., for small flapping amplitudes, which on many occasions of physical interest are far from the optimal propulsion configurations. This is the aim of the present chapter, to extend the analytical results of the chapter §6 to tandem flapping foils with prescribed chordwise deflection, so that the propulsive benefits of flexibility in these tandem arrangements may be characterized over an ample range of parameters. It is shall considered the case in which a prescribed quadratic deflection of small amplitude is added to the pitching and heaving motions of each foil, so that the effect of a flexural motion of small amplitude on the propulsive performance of the tandem arrangement is characterized with a lowest order model. Though it is sometimes used the word ”flexible” for short, it is not considered here the fluid-structure interaction.

7.2 FORMULATION OF THE PROBLEM

In chapter 6, the theory for N rigid airfoils in tandem configuration with prescribed heaving and pitching motions has been derived. In order to simplify the algebra and focusing on the most relevant case, it is going to be considered only two airfoils with prescribed deflection motion. So that, the 2D, incompressible, and nearly inviscid flow is considered over two pitching and heaving thin airfoils of chord length c that move with constant speed U along the negative x axis. Superimposed to theses motions, the plates undergo a quadratic flexure (or deflection) motion of trailing-edge amplitudes δ_{mi}. As the case of the rigid plates, all these heaving, pitching, and now, deflection motions, which are prescribed oscillatory motions given below, have very small amplitudes compared with c, so that the airfoils, and every point of each trail of vortices that they leave behind, may be considered to be on a horizontal plane $(z = 0)$ in first approximation.

It is continued using dimensionless variables, with all the lengths scaled with the half-chord $c/2$ and the time t scaled with $c/(2U)$. Thus, the front foil extends from $x = -1$ to $x = 1$ in a reference frame translating with it at speed U along the x axis (see Figure 7.1). The trailing foil is separated by a horizontal dimensionless distance d from the trailing edge of the front foil, i.e., $\varepsilon = d + 2$ from the leading edge of the front foil, so that it is located between $x = -1 + \varepsilon$ and $x = 1 + \varepsilon$. In this reference frame, the dimensionless vertical displacement of the mean-camber line of each foil i, with $i = 1$ and 2 for the front and back foil, respectively, is given by

$$z_{si}(x,t) = h_i(t) - (x - \varepsilon_i - a_i)\alpha_i(t) + (x - \varepsilon_i - p_i)^2\delta_i(t), \quad -1 + \varepsilon_i \leq x \leq 1 + \varepsilon_i, \tag{7.1}$$

where $h_i(t)$ and $\alpha_i(t)$ are given by (6.3). Following the deflection definition for the case of the one single plate given by (4.2) but now extended for the plate i and considering only the first oscillating mode, i.e, $\mathsf{b} = 0$, $\delta_i(t)$ is defined as

$$\delta_i(t) = \Re[\delta_{0i}e^{i(kt)}]. \tag{7.2}$$

The amplitude δ_{0i} is, in general, a complex constant satisfying $|\delta_{0i}| \ll 1$, where it is given by

$$\delta_{0i} = \frac{d_{mi}}{(1 - p_i)^2}e^{i(\psi_i + \varphi_i)}, \tag{7.3}$$

ψ_i the phase shift between the heaving and deflection motions and d_{mi} the maximum amplitude of the flexure component of the motion at the trailing edge $(x = 1)$. In what follows it is shall worked with the complex expressions knowing that it has to be taken the real part of the results. Note that $\varphi_1 = \varepsilon_1 = 0$. To facilitate the computations in a similar way that the flapping undulatory airfoil, derivative in the chapter 4, the vertical displacement of the foil will be written as

$$z_{si}(x,t) = \mathcal{F}_i(t) + \mathcal{E}_i(t)(x - \varepsilon_i) + \mathcal{D}_i(t)(x - \varepsilon_i)^2, \tag{7.4}$$

where, in this case, the functions $\mathcal{F}_i(t)$, $\mathcal{E}_i(t)$ and $\mathcal{D}_i(t)$ are specific to each airfoil i but in the absence of undulatory motion, i.e. for $\mathsf{b} = 0$,

$$\mathcal{F}_i(t) = h_i(t) + a_i\alpha_i(t) + p_i^2\delta_i(t), \quad \mathcal{E}_i(t) = -\alpha_i(t) - 2p_i\delta_i(t), \quad \mathcal{D}_i(t) = \delta_i(t), \tag{7.5}$$

The corresponding non-dimensional vertical velocity of each foil's mean-chamber line can be written as

$$v_{0i}(x,t) = \mathcal{U}_i(t) + \mathcal{V}_i(t)(x - \varepsilon_i) + \dot{\mathcal{D}}_i(t)(x - \varepsilon_i)^2, \tag{7.6}$$

with

$$\mathcal{U}_i(t) = \dot{\mathcal{F}}_i(t) + \mathcal{E}_i(t), \quad \mathcal{V}_i(t) = \dot{\mathcal{E}}_i(t) + 2\mathcal{D}_i(t), \tag{7.7}$$

where a dot denotes the time derivative.

7.3 GENERAL EXPRESSIONS FOR THE LIFT, THRUST, MOMENT AND INPUT POWER

7.3.1 *Vorticity distributions and time-dependent coefficients*

The normal velocities (7.6) are used to compute the vorticity distributions on both airfoils and along their wakes considering all the mutual interactions, as done for the case of two rigid airfoils in tandem configuration, but now with the additional terms coming from the quadratic flexural motions. So that, the vorticity distribution and the corresponding circulation to each airfoil is given by

$$\varpi_{0i}(x,t) = \sqrt{\frac{1-x+\varepsilon_i}{1+x-\varepsilon_i}}\left\{\frac{\Gamma_{0i}}{\pi} - [1+2(x-\varepsilon_i)]\mathcal{V}_i - 2(x-\varepsilon_i)[1+(x-\varepsilon_i)]\dot{\mathcal{D}}_i\right\}, \tag{7.8}$$

$$\Gamma_{0i}(t) = -\pi\left[2\mathcal{U}_i(t) + \mathcal{V}_i(t) + \dot{\mathcal{D}}_i(t)\right]. \tag{7.9}$$

To be consistent with the hypothesis made in the case of two rigid airfoils in tandem configuration (see §6.4), the same hypothesis will be made about the contribution of the forewing to the hindwing in terms of vorticity. So that, the circulation $\Gamma_{12}(t)$ in this case reduces to

$$\Gamma_{12}(t) \simeq \Gamma_{01} f_\Gamma(\varepsilon) - \mathcal{V}_1 f_{\Gamma\alpha}(\varepsilon) - \dot{\mathcal{D}}_1 f_{\Gamma\delta}(\varepsilon), \tag{7.10}$$

where $f_{\Gamma\delta}$ is given by the equation (C.31). Regarding the vorticity distributions of the wakes and those contributions over the plates, they remain formally the same but using the expressions (7.9) and (7.10).

Once the vorticity distributions and their respective circulations are known, to obtain the forces, moment and input power, one has to use the same integral expressions that for the two airfoils in tandem configuration given by (6.6)-(6.9), respectively. The resulting lift coefficient can be written as

$$C_L^{(i)} = \mathcal{L}_0(t) + \Gamma_{01}(t)\mathcal{L}_{01} + \left[\Gamma_{02}(t) + \Gamma_{12}(t)\right]\mathcal{L}_{02}, \tag{7.11}$$

where the only term that changes in relation to the tandem of rigid foils is $\mathcal{L}_0(t)$, maintaining the same expressions for the terms $\mathcal{L}_{01}$ and $\mathcal{L}_{02}$, which are given in the Appendix C.

In the case of the thrust force, being a quadratic expression of the different components of the foils motion, the new deflection term modifies its general form in relation to the rigid foil version. Thus, the thrust coefficient can be written as

$$C_T^{(i)} = \mathcal{E}_i C_L^{(i)} - \mathcal{D}_i C_{Td}^{(i)} + C_{T1}^{(i)} + C_{T2}^{(i)} + C_{Te}^{(i)}. \tag{7.12}$$

This expression mainly differs from that of a tandem of rigid foils in the new term, $-\mathcal{D}_i C_{Td}^{(i)}$, which is the projection in the flight direction of the normal force and moment to the plate i produced by the flexural motion. The different terms for the front $(i=1)$ and trailing $(i=2)$ foils are the following:

- Forewing

$$C_{Td}^{(1)} = C_{L2} + 4\left(C_{M1} + C_{Me}\right), \tag{7.13}$$

$$C_{T1}^{(1)} = -\dot{\mathcal{E}}_1 \int_{-1}^{1} x\left(\varpi_{01} + \varpi_{21}\right) dx - \dot{\mathcal{D}}_1 \int_{-1}^{1}\left(x^2 - \frac{1}{2}\right)\left(\varpi_{01} + \varpi_{21}\right) dx, \tag{7.14}$$

$$C_{T2}^{(1)} = \int_1^\infty \left[\dot{\mathcal{F}}_1 + \mathcal{E}_1 - (\dot{\mathcal{E}}_1 + 2\mathcal{D}_1 + \xi\dot{\mathcal{D}}_1)\left(\sqrt{\xi^2-1} - \xi\right)\right] \varpi_{e1} d\xi, \tag{7.15}$$

$$C_{Te}^{(1)} = -\int_{1+\varepsilon}^\infty \left[\frac{\dot{\mathcal{D}}_1}{2} + (\dot{\mathcal{E}}_1 + 2\mathcal{D}_1 + \xi\dot{\mathcal{D}}_1)\left(\sqrt{\xi^2-1} - \xi\right)\right] \varpi_{e2} d\xi. \tag{7.16}$$

- Hindwing

$$C_{Td}^{(2)} = C_{L2} + 4\left(C_{M1} + C_{Me}\right) + \int_{-1+\varepsilon}^{1+\varepsilon} \varpi_{e1} d\xi, \tag{7.17}$$

$$C_{T1}^{(2)} = -\dot{\mathcal{E}}_2 \int_{-1+\varepsilon}^{1+\varepsilon} (x-\varepsilon)\left(\varpi_{02} + \varpi_{12}\right) dx - \dot{\mathcal{D}}_2 \int_{-1+\varepsilon}^{1+\varepsilon} \left[(x-\varepsilon)^2 - \frac{1}{2}\right]\left(\varpi_{02} + \varpi_{12}\right) dx, \tag{7.18}$$

$$C_{T2}^{(2)} = \int_{1+\varepsilon}^\infty \left[\dot{\mathcal{F}}_2 + \mathcal{E}_2 - (\dot{\mathcal{E}}_2 + 2\mathcal{D}_2 + (\xi-\varepsilon)\dot{\mathcal{D}}_2)\left(\sqrt{(\xi-\varepsilon)^2-1} - (\xi-\varepsilon)\right)\right] \varpi_{e2} d\xi, \tag{7.19}$$

$$\begin{aligned} C_{Te}^{(2)} = & -\int_{1+\varepsilon}^\infty (\dot{\mathcal{E}}_2 + 2\mathcal{D}_2 + (\xi-\varepsilon)\dot{\mathcal{D}}_2)\left(\sqrt{(\xi-\varepsilon)^2-1} - (\xi-\varepsilon)\right) \varpi_{e1} d\xi + \\ & \int_1^{-1+\varepsilon} (\dot{\mathcal{E}}_2 + 2\mathcal{D}_2 + (\xi-\varepsilon)\dot{\mathcal{D}}_2)\left(\sqrt{(\xi-\varepsilon)^2-1} + (\xi-\varepsilon)\right) \varpi_{e1} d\xi - \frac{\dot{\mathcal{D}}_2}{2}\int_1^\infty \varpi_{e1} d\xi. \end{aligned} \tag{7.20}$$

Solving the different integrals, the thrust coefficient can be written as

$$C_T^{(i)} = \mathcal{E}_i C_L^{(i)} + \dot{\mathcal{E}}_i \mathcal{T}_0 + \mathcal{D}_i \mathcal{T}_{\delta 1} + \dot{\mathcal{D}}_i \mathcal{T}_{\delta 2} + \Gamma_{01}\mathcal{T}_{01} + \left[\Gamma_{02} + \Gamma_{12}\right]\mathcal{T}_{02}, \tag{7.21}$$

where all $\mathcal{T}$ functions are different respect to the two rigid airfoils in tandem configuration.

In the case of the moment coefficient, its general form remains the same as that of the tandem of rigid foils, as it happens for the lift coefficient, since both are linear functions of the foil's harmonic motion. The corresponding moment coefficient is given by

$$C_M^{(i)} = \frac{a_i}{2} C_L^{(i)} + \mathcal{M}_0(t) + \Gamma_{01}\mathcal{M}_{01} + \left[\Gamma_{02}(t) + \Gamma_{12}(t)\right]\mathcal{M}_{02}, \tag{7.22}$$

where only the function $\mathcal{M}_0(t)$ changes when including the flexural motios, and it is given in the Appendix C together with $\mathcal{M}_{01}$ and $\mathcal{M}_{02}$, which maintain the same expressions that the two rigid airfoils.

Finally, for the input power coefficient, a new term associated to the deflection appears in relation to the tandem of rigid foils (already obtained for an isolated foil in §4.4):

$$C_P^{(i)} = -\dot{h}_i C_L^{(i)} - 2\dot{\alpha} C_M^{(i)} - \dot{\delta}_i C_F^{(i)}, \tag{7.23}$$

where the flexural coefficient, $C_F^{(i)}$, is given by

- Forewing

$$\begin{aligned} C_F^{(1)} = & \, p_1\left(4C_{Mp}^{(1)} - p_1 C_L^{(1)}\right) + \frac{C_{L2}^{(1)}}{2} + \int_{-1}^{1} x^2\left(\varpi_{01} + \varpi_{21}\right) dx - \frac{1}{3}\frac{d}{dt}\int_{-1}^{1} x^3\left(\varpi_{01} + \varpi_{21}\right) dx + \\ & \frac{1}{3}\left[(1+\varepsilon)^3 - \left((1+\varepsilon)^2 + \frac{1}{2}\right)\sqrt{\varepsilon(\varepsilon+2)}\right] \varpi_{e2}(1+\varepsilon, t). \end{aligned} \tag{7.24}$$

- Hindwing

$$C_F^{(2)} = p_2 \left(4C_{Mp}^{(2)} - p_2 C_L^{(2)}\right) + \frac{C_{L2}^{(2)}}{2} + \frac{1}{2}\int_{-1+\varepsilon}^{1+\varepsilon} \varpi_{e1} d\xi + \int_{-1+\varepsilon}^{1+\varepsilon} (x-\varepsilon)^2 \left(\varpi_{02} + \varpi_{12}\right) dx$$
$$- \frac{1}{3}\frac{d}{dt}\int_{-1+\varepsilon}^{1+\varepsilon} (x-\varepsilon)^3 \left(\varpi_{02} + \varpi_{12}\right) dx + \frac{1}{3}\left[\varpi_{e1}(-1+\varepsilon, t) + \varpi_{e1}(1+\varepsilon, t)\right] +$$
$$\frac{1}{3}\left[(1-\varepsilon)^3 + \left((1-\varepsilon)^2 + \frac{1}{2}\right)\sqrt{\varepsilon(\varepsilon-2)}\right]\varpi_{e1}(1,t). \tag{7.25}$$

Solving theses expressions, they can be written as

$$C_F^{(i)} = p_i \left[4C_{Mp}^{(i)} - p_i C_L^{(i)}\right] + \mathcal{F}_0(t) + \Gamma_{01}(t)\mathcal{F}_{01} + \left[\Gamma_{02}(t) + \Gamma_{12}(t)\right]\mathcal{F}_{02}, \tag{7.26}$$

where $C_{Mp}^{(i)}$ is the moment coefficient (7.22) replacing $a_i/2$ by $p_i/2$ in its first term, and the different functions and coefficients $\mathcal{F}_0(t)$, $\mathcal{F}_{01}$ and $\mathcal{F}_{02}$ are summarized in Appendix C.

7.3.2 *Average coefficients*

The time-averaged thrust and input power coefficients can be decomposed in two terms,

$$\bar{C}_T = \bar{C}_{Tr} + \bar{C}_{Td}, \quad \bar{C}_P = \bar{C}_{Pr} + \bar{C}_{Pd}, \tag{7.27}$$

where $\bar{C}_{Tr}$ and $\bar{C}_{Pr}$ are the average thrust and input power of the two rigid airfoils respectively given by (6.59) and, $\bar{C}_{Td}$ and $\bar{C}_{Pd}$ are the contributions of the deflection motion. In a similar way that the case of the two rigid airfoils, the contribution of the deflection motion can be written in terms of the feathering parameters

$$\bar{C}_{Td}^{(i)} = (kh_{0i})^2 \Big\{ \left[t_{hd}(k,\varepsilon,\varphi,p_i,p_j,\psi_i,\psi_j,\Theta_h,\Theta_d) + \right.$$
$$\left. t_{pd}(k,\varepsilon,\varphi,a_i,a_j,p_i,p_j,\phi_i,\phi_j,\psi_i,\psi_j,\Theta_a,\Theta_d)\theta_i\right]\theta_{hdi} +$$
$$t_d(k,\varepsilon,\varphi,p_i,p_j,\psi_i,\psi_j,\Theta_d)\theta_{hdi}^2 \Big\}, \tag{7.28}$$

$$\bar{C}_{Pd}^{(i)} = (kh_{0i})^2 \Big\{ \left[p_{hd}(k,\varepsilon,\varphi,p_i,p_j,\psi_i,\psi_j,\Theta_h,\Theta_d) + \right.$$
$$\left. p_{pd}(k,\varepsilon,\varphi,a_i,a_j,p_i,p_j,\phi_i,\phi_j,\psi_i,\psi_j,\Theta_a,\Theta_d)\theta_i\right]\theta_{hdi} +$$
$$p_d(k,\varepsilon,\varphi,p_i,p_j,\psi_i,\psi_j,\Theta_d)\theta_{hdi}^2 \Big\}, \tag{7.29}$$

where

$$\Theta_d := \frac{d_{mj}}{d_{mi}}, \tag{7.30}$$

is the ratio of the amplitudes of the deflection motions and the functions $t_{hd}, t_{pd}, t_d, p_{hd}, p_{pd}$ and p_d are given in the Appendix C. Finally, the propulsive efficiency of each airfoil is conveniently written in terms of these functions and the feathering parameters:

$$\eta_i = \frac{\bar{C}_T^{(i)}}{\bar{C}_P^{(i)}} = \frac{t_h + t_{ph}\theta_i + t_p\theta_i^2 + \left(t_{hd} + t_{pd}\theta_i\right)\theta_{hdi} + t_d\theta_{hdi}^2}{p_h + p_{ph}\theta_i + p_p\theta_i^2 + \left(p_{hd} + p_{pd}\theta_i\right)\theta_{hdi} + p_d\theta_{hdi}^2}, \tag{7.31}$$

with the global propulsive efficiency of the tandem defined in (6.63).

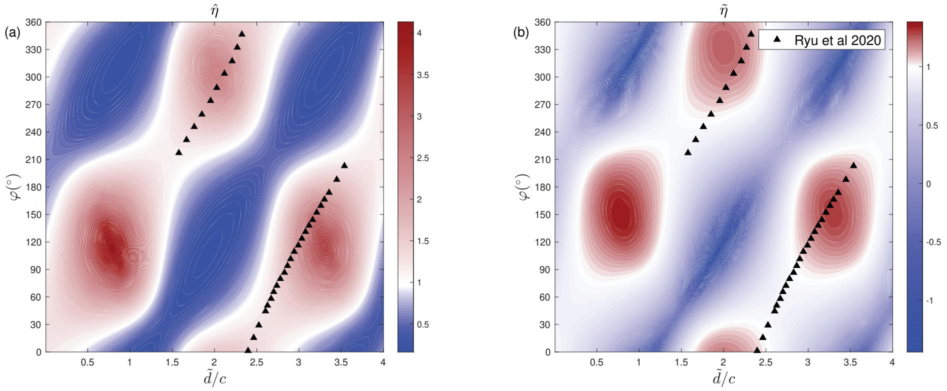

Figure 7.2: Contours of the normalized propulsive efficiency in the $\tilde{d}/c - \varphi$ plane for tandem heaving foils with $k = 1.25$ and $p = -1$. (a) $\hat{\eta}$ for a pair of rigid foils. (b) $\tilde{\eta}$ for a pair of flexible foils with $d_m/h_0 = 1/4$ and $\psi = 90°$. The symbols correspond to equilibrium gap distances obtained by Ryu et al., 2020, in their numerical simulations for two self-propelled flexible plates in tandem for the same values of k and p, and $h_0 = 0.4$ (i.e., their tandem flapping (TF) modes in Fig.2(d) of Ryu et al., 2020; note that their $\bar{G}_x$ is our $\tilde{d}/c + 1$, while their $\Delta\phi$ is our φ).

7.4 RESULTS

For a tandem flapping flexible foils, the available numerical or experimental data for validation is scarce, specially for high enough Reynolds numbers and small amplitude, with the additional difficulty that most of the published works do not provide information about the flexural deflection amplitudes and phase, d_{mi} and ψ_i, which are needed to evaluate the force expressions derived in this work. However, like in the rigid-foils case, available results for the equilibrium separation distances between two self-propelled plates in tandem arrangement can be used as an alternative. In the chapter §6, it is showed that the equilibrium separations between two self-propelled heaving rigid plates in tandem arrangement found experimentally by Ramananarivo et al., 2016, and Newbolt, Zhang, and Ristroph, 2019, correspond to configurations with maximum amplification of the tandem propulsive efficiency computed from the linear potential theory.

The recent work by Ryu et al., 2020, with numerical simulations for two self-propelled heaving flexible plates in a tandem arrangement, reports such kind of results in the separation-phase plane ($\tilde{d}/c - \varphi$ plane, where the tilde over d means dimensional quantity). Figure 7.2 shows that, similarly to the results reported in Ramananarivo et al., 2016, for rigid foils, the bands of maximum propulsive efficiency of the tandem obtained with the present theory roughly correspond to equilibrium separation distances between the self-propelled plates obtained numerically by Ryu et al., 2020. The results given by these authors are for flexible plates with the conditions given in the caption of Figure 7.2, but, since no data can be extracted for d_m or ψ from their reported results, they are compared in Figure 7.2 with the efficiency amplification obtained from the present theory for both a tandem of rigid foils and a tandem of flexible foils with the same kinematics of the reported numerical results and selected values of the flexural deflection amplitude and phase. The normalized efficiencies plotted in this figure are

$$\hat{\eta} := \frac{\eta_r}{\eta_s}, \quad \tilde{\eta} := \frac{\eta}{\eta_r}, \tag{7.32}$$

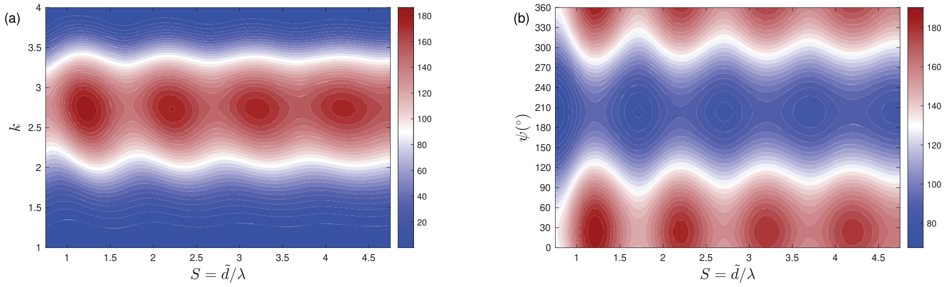

Figure 7.3: Contour values of $\mathcal{M}/h_0^2$ for purely heaving motion with flexural deflection amplitude $d_m/h_0 = 1/4$ and $p = -1$ in the schooling number-frequency plane with $\psi = \varphi = 0$ (a) and in the schooling number-phase shift plane with $k = 2.75$ (b).

for rigid foils and flexible foils, respectively, where η is the total efficiency defined in (6.63), the subscript s stands for a single airfoil undergoing the same motion, and the subscript r, as in (6.63), means rigid foils, for which it is used the same expression (6.63) but setting to zero the flexural deflection amplitude d_m. Though the contour values inside the bands of efficiency amplification and reduction are obviously different in each case, the slope and location of the banded patterns are practically the same and agree quite well with the numerical results by Ryu et al., 2020. It should be noted that though the amplitude $h_0 = 0.4$ does not seem sufficiently small for a linear theory, the present theory for pure heave of a single airfoil works remarkably well even for not too small amplitudes, as shown in Fernandez-Feria, 2016, comparing theoretical results for the thrust coefficient and the efficiency with experimental data by Heathcote and Gursul, 2007, for $h_0 = 0.35$.

On the other hand, analyzing the magnitude $\mathcal{M}$ defined in (6.66), one can obtain relevant information about the optimal configurations of the tandem in terms of thrust and, most likely, in terms of propulsive efficiency. So, in the case of pure heaving motion with the same amplitude h_0, the magnitude $\mathcal{M}/h_0^2$ depends only on k, d and φ for rigid foils, and additionally on d_m/h_0, ψ and p for flexible foils. For simplicity, taking the same values as for the rigid case ($\psi = \varphi = 0$ with $p = -1$), it is noticeable that the thrust amplification pattern is the same in both cases (see Figure 6.2(a) and Figure 7.3(a)). On the other hand, the thrust amplification in the foil with flexural deflection is significantly larger than that of a rigid foil for the selected values of the parameters. In fact, $p = -1$ is usually the best deflexion axis location in terms of propulsion performance of a foil with quadratic flexural deflection, as it has been shown in the Chapter 4, and the thrust increases quadratically with d_m in the present linear theory, so that, the most relevant parameter to quantify the effect of the flexural motion on the thrust enhancement for given φ is the phase shift ψ between the heaving and flexural motions. In the Figure 7.3(b) is plotted this magnitude in the (S, ψ)-plane for $d_m/h_0 = 1/4$ where one can see the effect of ψ on $\mathcal{M}/h_0^2$ for the optimal frequency in Figure 7.3, ($k \simeq 2.75$). It is observed that the optimal phase shift for thrust enhancement of the trailing foil due to its interaction with the upstream wake is about 25°, close to the case plotted in Figure 7.3(a).

As for the rigid case, it must be remarked that this analysis considers only the (arguably) most relevant contribution to the suction force at the leading edge of the trailing foil, not all contributions to the total thrust force. But it serves to illustrate the physical origin of the thrust (and efficiency) enhancement in a tandem configuration in comparison with an isolated foil.

On the other hand, owing to the large number of geometric and kinematic parameters, only the cases of purely heaving or pitching motions pivoting about the leading edges, combined with chordwise deflection, will be considered here with some detail.

7.4.1 *Pure heaving motions with chordwise deflections*

In this case, the time-averaged coefficients reduce to

$$\bar{C}_{Td}^{(i)} = (kh_{0i})^2 \left\{ t_{hd}(k,\varepsilon,\varphi,p_i,p_j,\psi_i,\psi_j,\Theta_h,\Theta_d)\theta_{hdi} + t_d(k,\varepsilon,\varphi,p_i,p_j,\psi_i,\psi_j,\Theta_d)\theta_{hdi}^2 \right\}, \tag{7.33}$$

$$\bar{C}_{Pd}^{(i)} = (kh_{0i})^2 \left\{ p_{hd}(k,\varepsilon,\varphi,p_i,p_j,\psi_i,\psi_j,\Theta_h,\Theta_d)\theta_{hdi} + p_d(k,\varepsilon,\varphi,p_i,p_j,\psi_i,\psi_j,\Theta_d)\theta_{hdi}^2 \right\}. \tag{7.34}$$

To simplify further, it is shall considered the same heaving and deflection amplitudes for both plates ($\Theta_h = \Theta_d = 1$), with the same phase shifts ($\psi_1 = \psi_2 = \psi$) and pivoting about their leading edges ($p_1 = p_2 = p = -1$). First, it is compared in Figure 7.4 the patterns of thrust and efficiency enhancement (or reduction) in the schooling number-frequency plane for the rigid-foils case with the present results when chordwise deflection is added. The normalized efficiencies are defined in (7.32), while the normalized time-averaged thrust coefficients are similarly defined as

$$\hat{C}_T := \frac{\bar{C}_{Tr}}{\bar{C}_{Ts}}, \quad \tilde{C}_T := \frac{\bar{C}_T}{\bar{C}_{Tr}}, \tag{7.35}$$

for rigid and flexible foils, respectively, where $\bar{C}_T$ is the total thrust coefficient defined in (7.27), the subscript s stands for a single foil undergoing the same motion, and the subscript r means rigid foils, for which it is used the same expression (7.27) but setting to zero the flexural deflection amplitude d_m. All the normalized quantities are independent of the amplitude of the oscillations, in this case of the heave amplitude h_0. It must be noted that, though the magnitude of the amplifications in Figure 7.4 seems unrealistic in some cases, these amplifications are in relation to the isolated rigid foil in (a) and (c), or to the tandem of rigid foils in (b) and (d), for the same values of k and S, which obviously do not always coincide with their respective maxima.

For comparison sake, Figure 7.4(a) and (b) reproduce results from Figure 6.3(e)-(f) for a tandem of rigid foils in phase ($\varphi = 0$), but now in the (S, k) plane, with S defined in (6.67), instead of the $(\tilde{d}/c, k)$ plane. As shown in Figure 6.5, the maxima in the efficiency magnification shown in Figure 7.4(b) approximately follow the multiple arrangements that self-propelled foils undergoing a heaving motion at high Reynolds numbers spontaneously assume due to flow interactions, roughly corresponding to integer values of the schooling number (Ramananarivo et al., 2016).

Figure 7.4(c) and (d) show the corresponding normalized quantities for a tandem arrangement of heaving foils with flexural deflection amplitude $d_m/h_0 = 1/4$ and phase shift $\psi = 270°$. It is observed that the amplification pattern remains, now in relation to the tandem rigid foils, but with a slight shift in the S-k plane that partially overlaps the adjacent regions of reduction in the propulsive performance of the tandem rigid foils. For

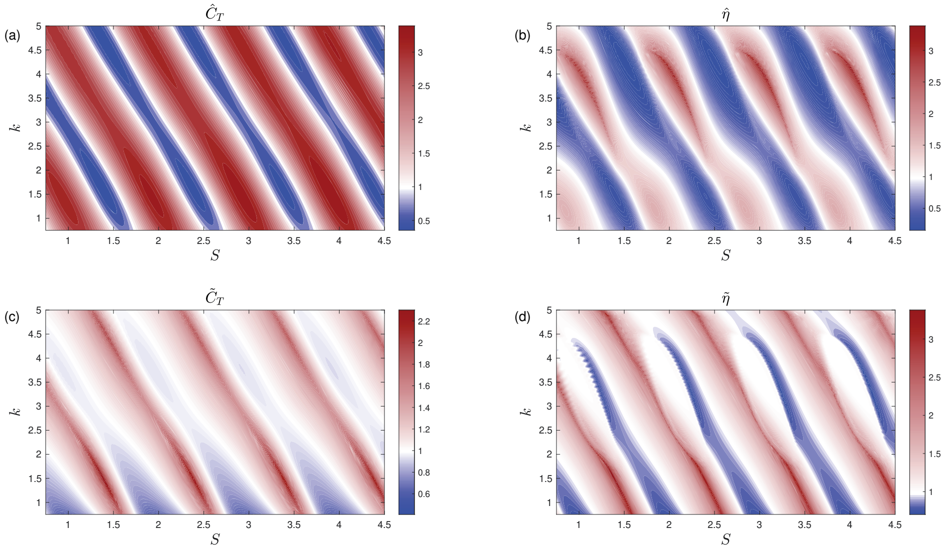

Figure 7.4: Contours of normalized thrust (left panels) and normalized propulsive efficiency (right panels) of the tandem in the (S, k)-plane for pure heave with $\varphi = 0$ and $p = -1$. (a) and (b) are for a tandem of rigid foils, with quantities normalized by those of an otherwise identical single foil. (c) and (d) are for a tandem of flexible foils with chordwise deflection when $d_m/h_0 = 1/4$ and $\psi = 270°$, now normalized by the corresponding values for the tandem of rigid foils.

given φ, this shift in the amplification pattern depends on the flexural deflection phase ψ. For the case $\psi = 270°$ plotted in Figure 7.4(c)-(d) the net effect is that a quadratic deflection may augment further the thrust and the propulsive efficiency of the tandem arrangement in several banded regions of the S-k plane. Particularly relevant is the first amplification mode (lower S), specially at the lowest frequencies, which are the most interesting conditions from a physical point of view, and for that reason is explored with more detail next.

Apart from that, it is observed similar regions where the magnitudes are magnified in relation to the two rigid airfoils ($\tilde{C}_T > 1$ and $\tilde{\eta} > 1$) of the $(\tilde{d}/c, k)$ plane, or in this case the (S, k) plane, where the reduced frequency is inversely proportional to the distance between airfoils. Particularly, these two quantities reach a relative maximum when $k = k^*$, in a similar way that the two rigid airfoils, given by

$$k^* \simeq \frac{k_t^{(n)}(\varphi, \psi)}{d/2 + 1} = \frac{k_t^{(n)}(\varphi, \psi)}{\varepsilon/2}, \quad \text{for} \quad \tilde{C}_T, \tag{7.36}$$

$$k^* \simeq \frac{k_\eta^{(n)}(\varphi, \psi)}{d/2 + 1} = \frac{k_\eta^{(n)}(\varphi, \psi)}{\varepsilon/2}, \quad \text{for} \quad \tilde{\eta}, \tag{7.37}$$

but in this case the constants $k_t^{(n)}$ and $k_\eta^{(n)}$ are functions of the phase of the two heaving motions, φ, and the phase of heaving and deflection motion, ψ, in addition to the amplification mode n. The value of this constant for the first mode is shown in the Figure 7.5. The jumps which one can see in the contour plots correspond to the appearance of new amplification modes as ψ or φ is increased, shifting the numeration of the modes.

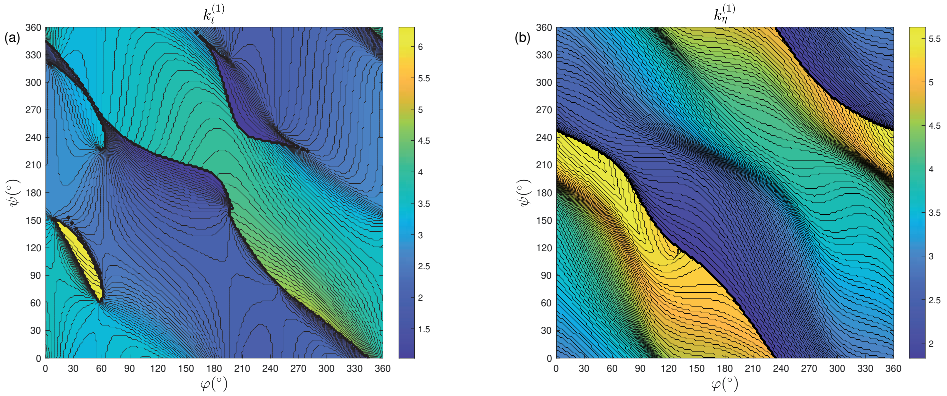

Figure 7.5: Functions $k_t^{(n)}(\varphi, \psi)$ and $k_\eta^{(n)}(\varphi, \psi)$ for the first mode with $d_m/h_0 = 1/4$ and $p = -1$. The jumps correspond to the appearance of new amplification modes as ψ or φ is increased, shifting the numeration of the modes.

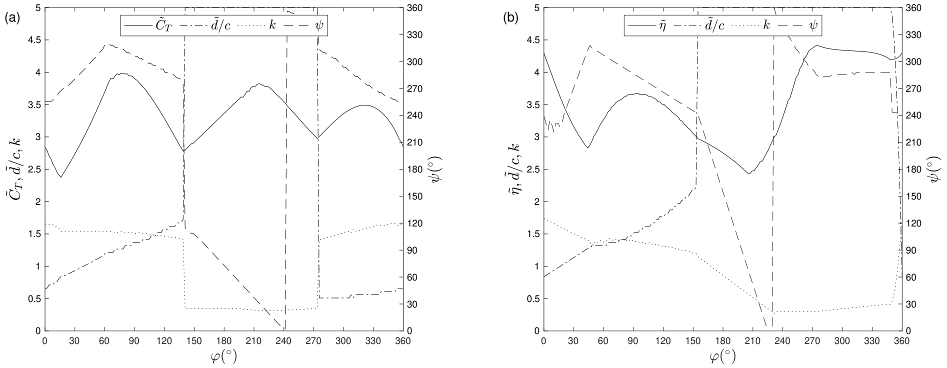

Figure 7.6: Maxima in $\tilde{C}_T$ (a) and $\tilde{\eta}$ (b) within the first amplification modes (with lower frequencies) plotted in Figure 7.4(c) and (d), respectively, as a function of the phase shift φ, and the corresponding optimal values of k, $\tilde{d}/c$ and ψ.

Figure 7.6 plots the maximum values of the thrust and efficiency corresponding to the first amplification mode with the lowest frequencies shown in Figure 7.4(c-d) as the phase shift φ is varied from the value $\varphi = 0$ used in Figure 7.4, maintaining the flexural deflection amplitude $d_m/h_0 = 1/4$ and varying also the defection phase shift ψ. This figure also contains the corresponding optimal values of k, $\tilde{d}/c$ and ψ for both thrust and efficiency enhancement by flexibility. Note that the deflection amplitude is not varied because the thrust coefficient goes as d_m^2 and the efficiency is almost independent of d_m in the present linear theory. The maximum thrust enhancement by flexibility is obtained for a heave phase shift $\varphi \approx 75^\circ$, corresponding to $k \approx 1.5$, $\psi \approx 300^\circ$ and $\tilde{d}/c \approx 1.25$. For a similar value of φ there is a local peak of efficiency enhancement though it is not the absolute maximum in Figure 7.6(b) it is the most interesting one in view of the corresponding optimal values of the parameters. It is obtained with practically the same values of φ, k and ψ of the maximum thrust, but for a slightly larger separation, about 1.5 chord lengths. The other local maxima of thrust and efficiency enhancement are less interesting physically because they are obtained for either too large or too low separations between the foils, for which the present inviscid theory is less accurate. Thus,

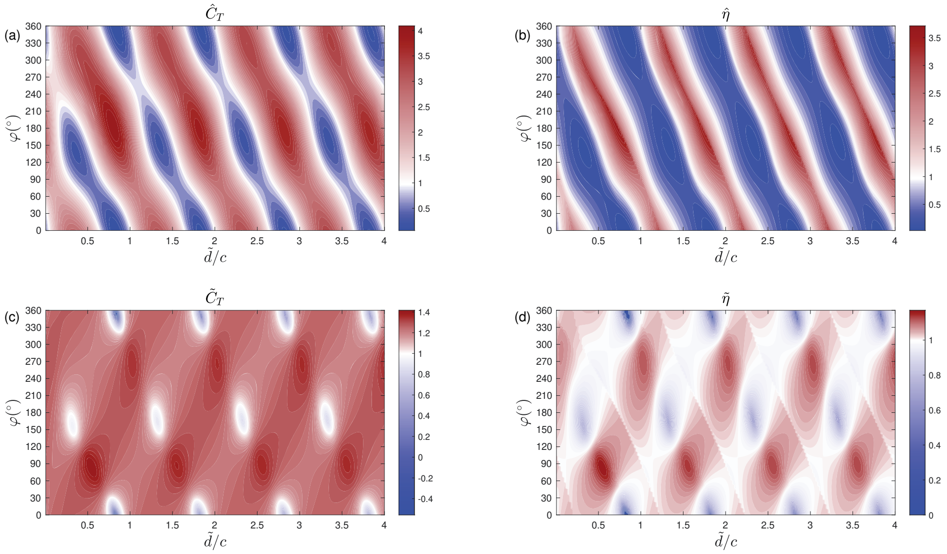

Figure 7.7: Contours of the tandem normalized thrust (left panels) and the tandem normalized propulsive efficiency (right panels) in the $(\tilde{d}/c, \varphi)$ plane for purely pitching motions with $k = \pi$ and $a = p = -1$. Figures (a) and (b) are for a tandem of rigid foils, with quantities normalized by those of an otherwise identical single foil, while Figs. (c) and (d) are for a tandem of flexible foils with trailing-edge deflection amplitude $d_m/a_0 = 1/4$ and $\psi = 180^\circ$, now normalized by the corresponding values for the tandem of rigid foils.

though there are other local maxima in the efficiency or in the thrust force amplifications, this one appears within the range of physically relevant values of the parameters where the present theory is more accurate and it is robust in the sense that both thrust and efficiency enhancement reach local maxima at these optimal conditions.

7.4.2 *Pure pitching motions with chordwise deflections*

Similarly to the case of purely heaving motions, for pitching foils with quadratic chordwise deflection it is considered only configurations with the same pitching and deflection amplitudes for both plates $(\Theta_a = \Theta_d = 1)$, with the same deflection phase shifts $(\psi_1 = \psi_2 = \psi)$ and pivoting about their leading edges $(a_1 = a_2 = a = p_1 = p_2 = p = -1)$. Figure 7.7(c)-(d) show the effect of a quadratic flexural deflection on the rigid-foils case plotted in Figure 7.7(a)-(b) when the deflection amplitude is $d_m/a_0 = 1/4$ and its phase shift $\psi = 180^\circ$ (Figure 7.7(a) and (b) are the same as Figure 6.9 but are reproduced here again for easy comparison). The banded patterns for thrust and efficiency basically remain, but with spots of thrust and efficiency enhancement by the quadratic deflection in relation to their rigid foil counterparts.

Figure 7.8 shows the maxima in the thrust and efficiency enhancement corresponding to the first amplification mode shown in Figure 7.7(c)-(d) as the deflection phase shift ψ is varied [note that $\psi = 180^\circ$ in Figure 7.7(c)- (d)], maintaining the flexural deflection amplitude at $d_m/a_0 = 1/4$ and the reduced frequency at $k = \pi$. This figure also contains the corresponding optimal values of $\tilde{d}/c$ and φ for both thrust and efficiency enhancement by flexural deformation. The deflection amplitude is not varied because the thrust

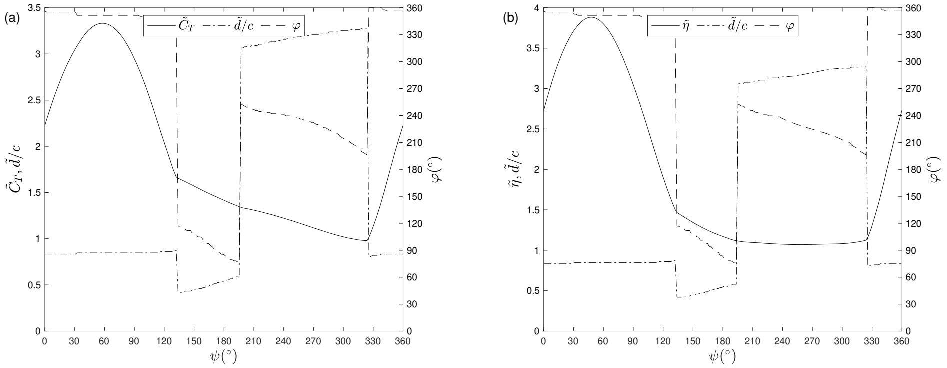

Figure 7.8: Maxima in $\tilde{C}_T$ (a) and $\tilde{\eta}$ (b) in the first amplification modes plotted in Figure 7.7(c) and (d), respectively, as a function of the deflection phase shift ψ, and the corresponding optimal values of φ and $\tilde{d}/c$ for $k = \pi$.

coefficient increases quadratically with d_m/a_0 and the efficiency is almost independent of d_m/a_0 in the present linear theory. The maximum thrust and efficiency enhancement by flexural deflection are both obtained at roughly the same values of the parameters, namely $\psi \approx 60°$, $\tilde{d}/c \approx 0.8$, and $\varphi \approx 350°$. This optimal separation and the selected frequency are well within the range of validity of the present theory and this maximum is robust in the sense that at these optimal conditions both thrust and efficiency enhancement reach local maximum values.

7.5 CONLUDING REMARKS

The effect of chordwise flexural deflection has been analyzed on the propulsive performance of a tandem arrangement of two-dimensional flapping foils in the linearized inviscid limit. General expressions for the vorticity distributions, the thrust, moment, power input and propulsive efficiency are given analytically in terms of the huge number of geometric and kinematic parameters characterizing the complex aerodynamic problem. This is the main advantage of the present approach: though limited to small amplitudes of the flapping and deflection motions and to high Reynolds number flows, the effect on the propulsive performance of all these parameters is readily available, while in numerical and experimental studies only the effect of a very reduced number of parameters can be taken into account simultaneously. In addition, the analytical expressions for the vorticity distributions are used to analyze the effect of the front-foil wake on the thrust of the trailing foil, thus extracting relevant qualitative information about the optimal configurations for thrust and efficiency enhancement, both for a tandem of rigid foils and for the case with the additional flexural deflection.

From these general expressions, results for two particular configurations have been presented consisting of purely heaving and purely pitching motions of the foils about their leading edges. These configurations have been selected because there exists a good agreement with available experimental and numerical data for the case of rigid foils, some of these validations made in the previous chapter for tandem rigid foils, and new comparisons presented here. It has been analyzed with some detail how a small-amplitude chordwise deflection improves the propulsive performance of the tandem flapping foils. For heaving foils, it is found that thrust enhancement by flexibility is maximized for a phase shift between the two heaving motions of about 75°, for a separation distance about 1.25 chord lengths, a reduced frequency around 1.5, and a deflection phase shift of about 300°. Maximum propulsive efficiency enhancement is obtained for basically the same values of these parameters, but for a slightly larger spacing between the foils. For pitching foil about their leading edges, a particular value of the reduced frequency has been selected to compare with a previous experimental work for rigid foils (Boschitsch, Dewey, and Smits, 2014), and find that both the maximum thrust and the maximum efficiency enhancement by flexural deflection is obtained for almost in phase pitching foils, separated a little less than one chord length and with a deflection phase shift of about 60°. All these results, both the general analytical expressions and the findings for the particular flapping configurations, may be of interest as a first guide in the design of small aerial or aquatic vehicles using tandem propulsors.

8

CLOSURE

8.1 CONTRIBUTION OF THIS THESIS

To conclude, the main contributions of this thesis are summarized below.

Firstly, it is found that, although viscous effects are very relevant in the close encounter of a vortex with a flat plate, some interesting features of the lift fluctuation generated by this interaction may be derived from a relatively simple two-dimensional potential theory based on a conformal transformation. It mainly provides simple scaling laws which may be useful to estimate the intensity of the lift fluctuation in terms of the vortex circulation Γ_l and its relative separation distance $(h - h^*)/c$, showing a marked asymmetry when the vortex passes above or below the plate, depending on the sign of Γ_l, for the same $|h - h^*|/c$.

On the other hand, it has been developed general expressions for the contribution of travelling point vortices to the lift, thrust, moment and propulsion efficiency of a two-dimensional pitching and heaving airfoil from a vortical impulse formulation within the linear potential theory. In order to see the effect of these point vortices on the aerodynamics forces, it has been considered just one point vortex, in particular a LEV during each half stroke which is released from the sharp leading edge. The development of the LEV follows the Brown-Michael model that ensures momentum conservation. The symmetry of the problem shows that the LEV does not contribute to the time-averaged lift and moment, but only to the time-averaged thrust and to the propulsion efficiency, which are in general lowered in relation to the case without LEV. Further, by considering the effect of the developing LEV just up to its shedding point, when its circulation reaches an extremum value according to the Brown-Michael model, quite simple relations have been obtained for the LEV's effect on the thrust force and propulsion efficiency, which constitutes a lowest order correction to the analytical results from the linear potential theory.

As a general trend, it is found that the LEV's lowest order corrections to the thrust force and propulsion efficiency are more significant when the pitching axis location is behind the mid-chord point ($a > 0$), the more so the larger the pitching amplitude and the reduced frequency. In addition, no LEV's corrections are found within the present linear approximation for a pure heaving motion ($a_0 = 0$) or, more generally, when $h_0/(1+a)a_0$ is larger that a quantity that depends of k and ϕ. Better approximations can be obtained from more complete models for the development and shedding of the LEV, but at the cost of more parameters to be adjusted experimentally and probably not in a closed simple form.

Next, the vortical impulse theory has been extended to obtain closed expressions for the aerodynamic force components and moment on a two-dimensional flexible foil undergoing a quite general undulatory motion. It constitutes a convenient tool for predicting and evaluating the optimal conditions for propulsion in terms of thrust generation and efficiency in a wide range of animal and bioinspired robotic locomotion. Relatively simple analytic expressions have been obtained for the interesting cases of pitching and heaving motions superimposed to a chordwise flexibility of the foil, with the additional force and moment terms in relation to an oscillating rigid foil neatly separated, and characterized by the ratio between the amplitudes of the deflection and the rigid motions. When this non-dimensional parameter vanishes one recovers previous results for a pitching and heaving rigid foil. A detailed evaluation of the propulsion performance is made for these particular cases, mapping the regions of thrust and of propulsive efficiency enhancement in relation to the rigid foil counterpart in the parameter space of the reduced frequency and the relevant deflection parameters.

In order to obtain the validation limit of the present linear developed theory, in terms of Reynolds number and values of the amplitude motions, a numerical tool has been developed for the simulation of a flapping rigid airfoil using compact finite differences in a vorticity-streamfunction formulation. It has already been checked for pure heaving motions and compared with numerical and experimental results, remaining only to fine tune the case of pure pitching motions for not small values of the strouhal number.

As a second part of this thesis, general expressions have been developed for the lift, thrust, moment and propulsive efficiency of an arbitrary set of two-dimensional pitching and heaving airfoils from the impulse theory in the limit of linear potential flow. In particular, it is provided closed analytical expressions for two airfoils in tandem configuration. For pure heaving motions of the airfoils it is found that there exist combinations of the reduced frequency and the normalized distance between airfoils, that depend on the phase shift of the two motions, for which the global propulsive efficiency of the tandem is a local maximum. These combinations, or modes, correspond to specific values of the so-called schooling number, in very good agreement with recent experimental results (Ramananarivo et al., 2016; Newbolt, Zhang, and Ristroph, 2019). Similar modes are found for pure pitching motions.

Also, it has been analyzed the effect of chordwise flexural deflection on the propulsive performance of a tandem arrangement of two-dimensional flapping foils in the linearized inviscid limit. General expressions for the vorticity distributions, the thrust, moment, power input and propulsive efficiency are given analytically in terms of the huge number of geometric and kinematic parameters characterizing the complex aerodynamic problem. In general, the present formulation permits the identification of optimal conditions in terms of either thrust force or propulsive efficiency with much less effort than using numerical simulations or experiments. This is the main advantage of the present approach: though limited to small amplitudes of the flapping and deflection motions and to high Reynolds number flows, the effect on the propulsive performance of all these parameters is readily available, while in numerical and experimental studies only the effect of a very reduced number of parameters can be taken into account simultaneously. In addition, it is used the analytical expressions for the vorticity distributions to analyze the effect of the front-foil wake on the thrust of the trailing foil, thus extracting relevant qualitative information about the optimal configurations for thrust and efficiency enhancement, both for a tandem of rigid foils and for the case with the additional flexural deflection.

In addition to the comparison with experimental results for pure heaving motion, the present theoretical results have been also checked with numerical simulations for a complex pitching and heaving motion with small amplitudes and high Reynolds number for which the theory is limited, showing a good agreement. In the case of considering flexural deflection motions it has been presented results for two particular configurations consisting of purely heaving and purely pitching motions of the foils about their leading edges. These configurations have been selected because there exists a good agreement with available experimental and numerical data for the case of rigid foils. It has been analyzed with some detail how a small-amplitude chordwise deflection improves the propulsive performance of the tandem flapping foils.

The theory is limited to intermediate distances between the airfoils: for distances smaller than about one chord length viscous effects become important in the flow interaction between airfoils, while for distances much larger that the chord length the present results do not consider the viscous decay of the vortex wake. Nonetheless, all these results, both the general analytical expressions and the findings for the particular flapping configurations, it is believed that the present analytical results constitute a good tool for the preliminary aerodynamic design, and a guide for the subsequent control, of MAVs based on pairs of flapping wings in tandem configuration.

8.2 WORK IN PROGRESS

The present results are limited to small amplitudes of the oscillations and sufficiently high Reynolds number for which the linearized potential theory applies. In addition, no analysis is made of the fluid–structure interaction that may produce the particular deflection or undulatory motion of the foil. Previous works that have analysed this fluid–structure interaction have shown that, in some particular pitching and heaving motions of the foil, the regions of optimal propulsion are related to structural resonant frequencies of the foil (Michelin and Llewellyn Smith, 2009; Dewey et al., 2013; Moore, 2014; Paraz, Schouveiler, and Eloy, 2016; Moore, 2017; Floryan and Rowley, 2018). The present analytical results are independent of the material properties of the foil, depending only on the prescribed kinematics of the flexible foil. Although to analyse the fluid–structure interaction one needs to model a truly general motion of the deformable foil, with infinite kinematic parameters, as recently done numerically in this limit of linear potential theory by Tzezana and Breuer, 2019, it is believed that with the present fairly broad class of flapping undulatory motion, with nine non-dimensional parameters, one may undertake a similar, but more limited, analysis of the fluid-structure interaction to obtain approximately these kinematic parameters for given properties of the flexible or compliant material and the boundary conditions at the leading and trailing edges, with the advantage that now the aerodynamic force and moment are obtained analytically in terms of these parameters from a general impulse theory. This research has just been started with the following articles:

- Fernandez-Feria, R. and Alaminos-Quesada, J. (2021). "Analytical results for the propulsion performance of a flexible foil with prescribed pitching and heaving motions and passive small deflection". In: *Journal of Fluid Mechanics* 910, A43. DOI: doi.org/10.1017/jfm.2020.1015
- Fernandez-Feria, R. and Alaminos-Quesada, J. (2021). "Propulsion and energy harvesting performances of a flexible thin airfoil undergoing forced heaving motion with passive pitching and deformation of small amplitude". *Journal of Fluids and Structures*, (under review),

which are out of the initial scope of this thesis and for that reason are not included here.

Another point of interest is to define clearly the validation limit of the present theory in terms of Reynolds number and values of the amplitude motions, because one always assumes that the amplitudes have to be small and the Reynolds number has to be high, but it would be of practical interest to characterize more precisely the value of these magnitudes above for which the present linear theory is no longer valid. The numerical tool for this task is presented in the present terms and it is ready, but the numerical work is in progress.

Finally, although the present linear theory has, in its majority, explicit analytical expressions, many of them are very involved and one can make mistakes when they are programmed. For that reason, a repository to share with the scientific comunity all the analytical results presented here is being developed. It remains to be tested.

Part III

APPENDIX

A

ONE PLATE FUNCTIONS, INTEGRALS AND COEFFICIENTS

A.1 SOLUTION OF THE INTEGRAL EQUATIONS

The integral equations which appear in the present document are defined as singular and linear integral equations of the first kind with constant limits of integration (Polyanin, 1998), and they can be written as

$$\frac{1}{\pi}\fint_a^b \frac{\varpi(\xi,t)}{\xi - x} d\xi = f(x,t), \quad a \leq x \leq b, \tag{A.1}$$

The solution of this integral equation depends on if it is bounded or unbounded at the endpoints. For easy reference, some of them are presented below.

1. Unbounded at both endpoints:

$$\varpi(x,t) = -\frac{1}{\pi}\frac{1}{\sqrt{(x-a)(b-x)}}\left[\Gamma(t) + \fint_a^b \frac{\sqrt{(\xi-a)(b-\xi)}}{\xi - x} f(\xi,t) d\xi\right], \tag{A.2}$$

   where $\Gamma(t)$ is an arbitrary constant (independent of x) which satisfies

$$\int_a^b \varpi(x,t)dx = \Gamma(t). \tag{A.3}$$

2. Bounded at the endpoint a and unbounded at the endpoint b:

$$\varpi(x,t) = -\frac{1}{\pi}\sqrt{\frac{x-a}{b-x}}\fint_a^b \sqrt{\frac{b-\xi}{\xi-a}}\frac{f(\xi,t)}{\xi - x} d\xi. \tag{A.4}$$

3. Bounded at both endpoints:

$$\varpi(x,t) = -\frac{1}{\pi}\sqrt{(x-a)(b-x)}\fint_a^b \frac{f(\xi,t)}{\sqrt{(\xi-a)(b-\xi)}}\frac{d\xi}{\xi - x}, \tag{A.5}$$

   under the condition that

$$\fint_a^b \frac{f(\xi,t)}{\sqrt{(\xi-a)(b-\xi)}} d\xi = 0. \tag{A.6}$$

A.2 SOME INTEGRALS AND FUNCTIONS

The integrals of the vorticity distribution ϖ_0 can be written as

$$\int_{-1}^{1} x^n e^{sbx}\varpi_0(x,t) = \int_{-1}^{1}\frac{x^n e^{sbx}}{\sqrt{1-x^2}}\left[\frac{\Gamma_0(t)}{\pi} - \frac{2}{\pi}\fint_{-1}^{1}\left(\frac{\sqrt{1-\xi^2}}{\xi - x} e^{b\xi}\sum_{m=0}^{2} f_m(t)\xi^m\right) d\xi\right] dx. \tag{A.7}$$

where n, m and s are integer values and $f_m(t)$ are the dependent factors of the time which appear in the airfoil velocity ($f_0(t) = \mathcal{U}(t)$, $f_1(t) = \mathcal{V}(t)$, and $f_2(t) = \mathcal{C}(t)$ defined in (4.10)-(4.12)). To obtain the lift and moment the integrals which appear are for $s = 0$, whose solutions are the following

$$\int_{-1}^{1} \varpi_0(x,t) = \Gamma_0(t), \tag{A.8}$$

$$\int_{-1}^{1} x\varpi_0(x,t) = \frac{2\pi}{\mathsf{b}}\left\{[\mathcal{U}(t)+\mathcal{C}(t)]\, I_1(\mathsf{b}) + \left[\mathcal{V}(t) - \frac{3}{\mathsf{b}}\mathcal{C}(t)\right] I_2(\mathsf{b})\right\}, \tag{A.9}$$

$$\int_{-1}^{1} x^2\varpi_0(x,t) = \frac{\Gamma_0(t)}{2} + \frac{2\pi}{\mathsf{b}}\left\{\left[\frac{\mathcal{V}(t)}{\mathsf{b}} + \mathcal{U}(t) + \mathcal{C}(t)\right] I_2(\mathsf{b}) + \left[\mathcal{V}(t) - \frac{3}{\mathsf{b}}\mathcal{C}(t)\right] I_3(\mathsf{b})\right\}, \tag{A.10}$$

where $I_r(\mathsf{b})$ is the modified Bessel function of the first kind and order $r = 0, 1, ..., 4$. In the case of the thrust and input power, $s = 1$, the first part of (A.7) has analytical solution. For some values of n, it reduces to

$$\frac{1}{\pi}\int_{-1}^{1} \frac{e^{\mathsf{b}x}}{\sqrt{1-x^2}}dx = I_0(\mathsf{b}), \tag{A.11}$$

$$\frac{1}{\pi}\int_{-1}^{1} \frac{xe^{\mathsf{b}x}}{\sqrt{1-x^2}}dx = I_1(\mathsf{b}), \tag{A.12}$$

$$\frac{1}{\pi}\int_{-1}^{1} \frac{x^2e^{\mathsf{b}x}}{\sqrt{1-x^2}}dx = \frac{I_1(\mathsf{b})}{\mathsf{b}} + I_2(\mathsf{b}). \tag{A.13}$$

The second part, in general, has to be solved numerically and it will be defined as

$$\mathcal{I}_{n,m}(\mathsf{b}) := -\frac{2}{\pi}\int_{-1}^{1} \frac{x^n e^{\mathsf{b}x}}{\sqrt{1-x^2}}\left(\fint_{-1}^{1} \frac{\sqrt{1-\xi^2}}{\xi - x}\xi^m e^{\mathsf{b}\xi}d\xi\right)dx = \mathcal{I}^R_{n,m} + i\mathcal{I}^I_{n,m}. \tag{A.14}$$

It should be noted that $\mathcal{I}_{1,1} = \mathcal{I}_{2,2} = 0$ and $\mathcal{I}_{0,0} = \mathcal{I}_{2,0}$. In addition, when the growth factor of the undulatory motion vanishes ($b_1 = 0$) then

$$\mathcal{I}^R_{0,0} = \mathcal{I}^I_{0,1} = \mathcal{I}^R_{0,2} = 0, \quad \mathcal{I}^I_{1,0} = \mathcal{I}_{1,1} = \mathcal{I}^I_{1,2} = 0, \quad \mathcal{I}^R_{2,0} = \mathcal{I}^I_{2,1} = \mathcal{I}_{2,2} = 0. \tag{A.15}$$

The integrals of the vorticity distribution ϖ_{se} can be written as

$$\int_{-1}^{1} x^n e^{\mathsf{b}x}\varpi_{se}(x,t) = \frac{\Gamma_0(t)2/\pi^2}{iH_0^{(2)}(k) + H_1^{(2)}(k)}\int_{-1}^{1} x^n e^{\mathsf{b}x}\sqrt{\frac{1-x}{1+x}}\left(\int_{1}^{\infty}\sqrt{\frac{\xi+1}{\xi-1}}\frac{e^{-ik\xi}}{\xi - x}d\xi\right)dx. \tag{A.16}$$

This integral, in general, has to be solved numerically and it will be defined as

$$\mathcal{J}_n(\mathsf{b},k) := \frac{2/\pi^2}{iH_0^{(2)}(k) + H_1^{(2)}(k)}\int_{-1}^{1} x^n e^{\mathsf{b}x}\sqrt{\frac{1-x}{1+x}}\left(\int_{1}^{\infty}\sqrt{\frac{\xi+1}{\xi-1}}\frac{e^{-ik\xi}}{\xi - x}d\xi\right)dx = \mathcal{J}^R_n + i\mathcal{J}^I_n. \tag{A.17}$$

In the Figure A.1 and Figure A.2 one can see the value of these integral definitions for the special case of $b_1 = 0$ and several values of b_2 and k. In the special case of $\mathsf{b} = 0$, the above integrals have analytical solutions and they are given by

$$\int_{-1}^{1} x\varpi_0(x,t) = \pi\left[\mathcal{U}(t) + \frac{\mathcal{C}(t)}{4}\right], \tag{A.18}$$

$$\int_{-1}^{1} x^2\varpi_0(x,t) = \frac{\Gamma_0(t)}{2} + \frac{\pi}{4}\mathcal{V}(t), \tag{A.19}$$

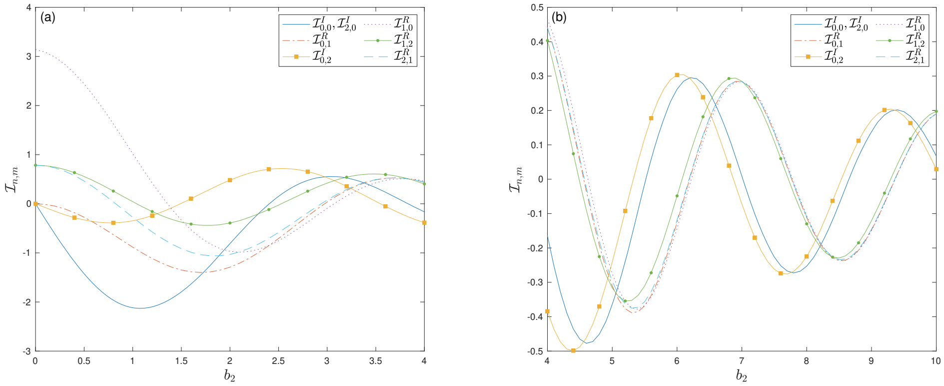

Figure A.1: Value of the integral definition $\mathcal{I}_{n,m}$ for the case $b_1 = 0$.

$$\int_{-1}^{1} x^3 \varpi_0(x,t) = -\frac{\pi}{8}\left[\frac{3}{\pi}\Gamma_0(t) + 3\mathcal{V}(t) + \mathcal{C}(t)\right]. \tag{A.20}$$

For the vorticity distribution ϖ_{se}, it is convenient to solve the integral of the variable x before the final solution, i.e,

$$\int_{-1}^{1} x\varpi_{se}(x,t) = \int_{1}^{\infty}\left(\sqrt{\xi^2-1}-\xi\right)\varpi_e(\xi,t)d\xi, \tag{A.21}$$

$$\int_{-1}^{1} x^2\varpi_{se}(x,t) = \int_{1}^{\infty}\left(\frac{1}{2}\sqrt{\frac{\xi+1}{\xi-1}}+\xi\sqrt{\xi^2-1}-\xi^2\right)\varpi_e(\xi,t)d\xi, \tag{A.22}$$

$$\int_{-1}^{1} x^3\varpi_{se}(x,t) = \int_{1}^{\infty}\left[\sqrt{\xi^2-1}\left(\frac{1}{2}+\xi^2\right)-\xi^3\right]\varpi_e(\xi,t)d\xi. \tag{A.23}$$

After some operations in the calculus of forces and input power, the most common integrals which one has to solve are the following

$$\int_{1}^{\infty}\varpi_e(\xi,t)d\xi = \Gamma_0(t)g_0(k), \tag{A.24}$$

$$\int_{1}^{\infty}\left(\sqrt{\xi^2-1}-\xi\right)\varpi_e(\xi,t)d\xi = -\Gamma_0(t)g_1(k), \tag{A.25}$$

$$\int_{1}^{\infty}\xi\left(\sqrt{\xi^2-1}-\xi\right)\varpi_e(\xi,t)d\xi = -\Gamma_0(t)g_2(k), \tag{A.26}$$

$$\int_{1}^{\infty}\xi^2\left(\sqrt{\xi^2-1}-\xi\right)\varpi_e(\xi,t)d\xi = -\Gamma_0(t)g_3(k), \tag{A.27}$$

$$\int_{1}^{\infty}\xi^3\left(\sqrt{\xi^2-1}-\xi\right)\varpi_e(\xi,t)d\xi = -\Gamma_0(t)g_4(k), \tag{A.28}$$

$$\int_{1}^{\infty}\frac{1}{\sqrt{\xi^2-1}}\varpi_e(\xi,t)d\xi = \Gamma_0(t)\left[C(k)-1\right], \tag{A.29}$$

$$\int_{1}^{\infty}\frac{\xi}{\sqrt{\xi^2-1}}\varpi_e(\xi,t)d\xi = -\Gamma_0(t)C(k), \tag{A.30}$$

$$\int_{1}^{\infty}\frac{\xi^2}{\sqrt{\xi^2-1}}\varpi_e(\xi,t)d\xi = -\Gamma_0(t)\frac{C_3(k)}{k}, \tag{A.31}$$

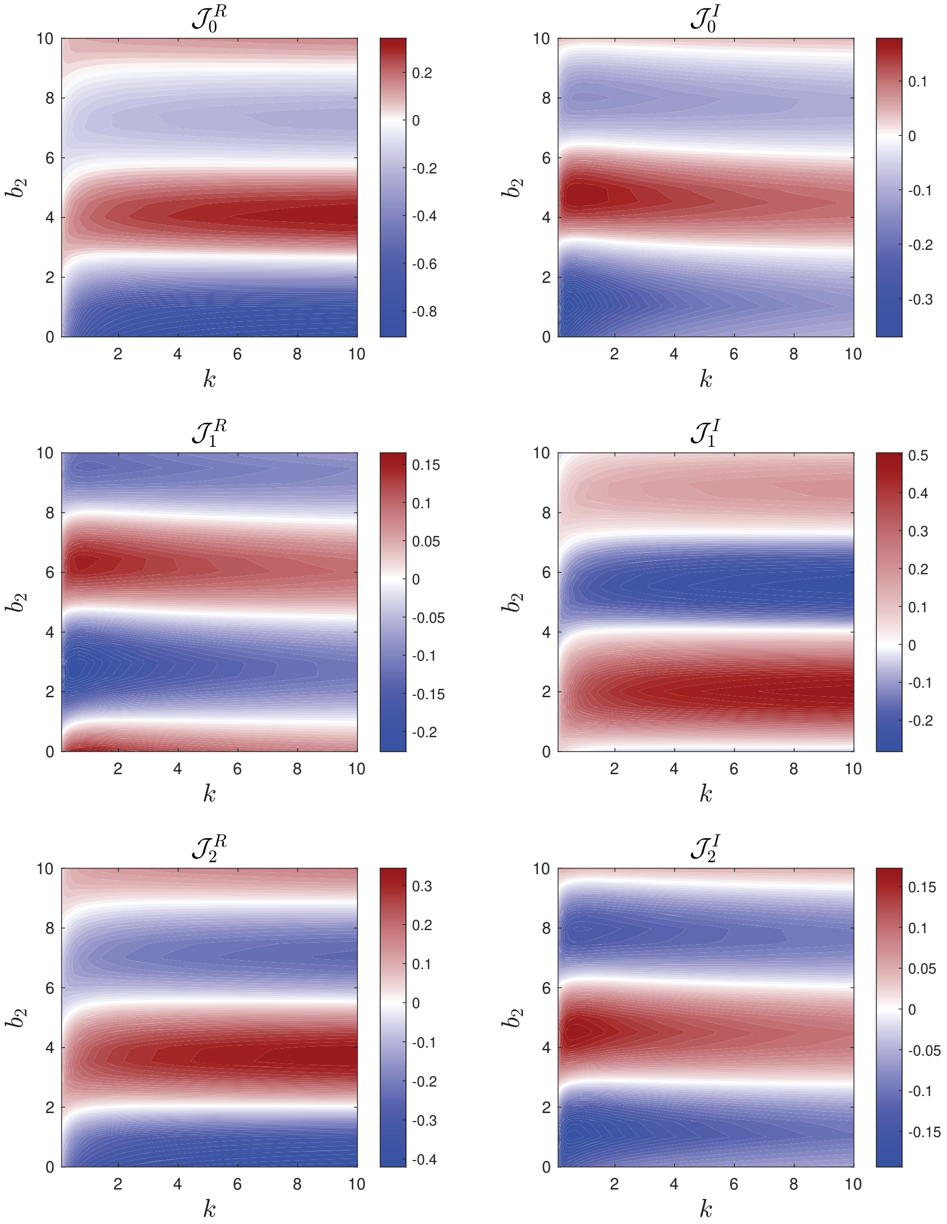

Figure A.2: Value of the integral definition $\mathcal{J}_n$ for the case $b_1 = 0$.

where the functions $C(k), C_1(k)$, $C_2(k)$ and $C_3(k)$ are defined as

$$C(k) := \frac{H_1^{(2)}(k)}{iH_0^{(2)}(k) + H_1^{(2)}(k)}, \quad C_1(k) := \frac{\frac{1}{k}e^{-ik}}{iH_0^{(2)}(k) + H_1^{(2)}(k)}, \tag{A.32}$$

$$C_2(k) := \frac{H_2^{(2)}(k)}{iH_0^{(2)}(k) + H_1^{(2)}(k)}, \quad C_3(k) := \frac{Y_0(k) - iJ_2(k) + iH_1^{(1)}(k)}{iH_0^{(2)} + H_1^{(2)}(k)}, \tag{A.33}$$

and the functions $g_j(k)$, $j = 1, 2, 3, 4$ are given by

$$g_0(k) := \frac{-2i}{\pi}C_1(k), \quad g_1(k) := -\frac{2}{\pi k}(1 + ik)C_1(k) - \frac{i}{k}C(k), \tag{A.34}$$

$$g_2(k) := -\frac{1}{k}C_2(k) + \left(\frac{2i}{k^2} - \frac{2 + ik}{k}\right) C_1(k), \tag{A.35}$$

$$g_3(k) := \frac{3Y_2(k) - kY_1(k) + iJ_3(k) - iJ_2(k)}{k^2\left[iH_0^{(2)} + H_1^{(2)}(k)\right]} + \frac{6}{\pi k}(1 + ik)\left(\frac{2}{k^2} - 1\right) C_1(k), \tag{A.36}$$

$$\begin{aligned} g_4(k) :=& \frac{1}{iH_0^{(2)} + H_1^{(2)}(k)} \left\{ \frac{1}{k^2}\left[kJ_4(k) - 3J_3(k)\right] + \frac{ik}{4}G^{2,0}_{1,3}\left(\frac{k^2}{4} \middle| \begin{matrix} -\frac{3}{2} \\ -3, 0, -\frac{1}{2} \end{matrix} \right) \right\} + \\ & \frac{2}{\pi}\left[\frac{24}{k^4}(k - i) - \frac{4}{k^2}(k - 3i) - i\right] C_1(k), \end{aligned} \tag{A.37}$$

where $G^{m,n}_{p,q}\left(z|\mathbf{a}_p; \mathbf{b}_q\right)$ is the Meijer G-function.

On the other hand, the integrals of the vorticity distribution ϖ_{sj} associated to the point vortex jth are the following

$$\int_{-1}^{1} \varpi_{sj}(x,t) = C_j(t)\Gamma_j(t), \tag{A.38}$$

$$\int_{-1}^{1} x\varpi_{sj}(x,t) = D_j(t)\Gamma_j(t), \tag{A.39}$$

$$\int_{-1}^{1} x^2\varpi_{sj}(x,t) = \left[\frac{C_j(t)}{2} + E_j(t)\right]\Gamma_j(t), \tag{A.40}$$

where

$$C_j(t) = -\frac{1}{\pi}\fint_{-1}^{1}\sqrt{\frac{1+\xi}{1-\xi}}\,\frac{\xi - x_j(t)}{[\xi - x_j(t)]^2 + z_j(t)^2}d\xi, \tag{A.41}$$

$$D_j(t) = \frac{1}{\pi}\fint_{-1}^{1}\sqrt{1-\xi^2}\,\frac{\xi - x_j(t)}{[\xi - x_j(t)]^2 + z_j(t)^2}d\xi, \tag{A.42}$$

$$E_j(t) = \frac{1}{\pi}\fint_{-1}^{1}\xi\sqrt{1-\xi^2}\,\frac{\xi - x_j(t)}{[\xi - x_j(t)]^2 + z_j(t)^2}d\xi. \tag{A.43}$$

Other functions associated to the wake over plate contribution for the Kirchhoff velocity, v_{se}, are the following

$$f_{se}^{(1)}(k) = -\frac{H_0^{(2)}(k)}{4} + \frac{e^{ik}}{2\pi}[\pi - i\mathrm{Ei}(-2ik)], \tag{A.44}$$

$$f_{se}^{(2)}(k) = \frac{k}{2\sqrt{2}}\left[H_1^{(2)}(k) - iH_0^{(2)}(k)\right], \tag{A.45}$$

$$f_{se}^{(3)}(k) = \frac{e^{-ik}}{4\pi}\left\{2e^{2ik}k[\mathrm{Ei}(-2ik)+i\pi]-i\right\}, \tag{A.46}$$

$$g_{se}^{(1)}(k) = -\frac{k}{4\sqrt{2}}\left[H_0^{(2)}(k)+iH_1^{(2)}(k)\right], \tag{A.47}$$

$$g_{se}^{(2)}(k) = \frac{e^{-ik}}{2\pi}\left[-\frac{1}{2}+e^{2ik}k\left(\frac{\pi}{2}-i\mathrm{Ci}(2k)-\mathrm{Si}(2k)\right)\right], \tag{A.48}$$

$$g_{se}^{(3)}(k) = \frac{k}{16\sqrt{2}}\left[(8k+i)H_1^{(2)}(k)-(3+8ik)H_0^{(2)}(k)\right], \tag{A.49}$$

where $\mathrm{Si}(z)$, $\mathrm{Ci}(z)$ and $\mathrm{Ei}(z)$ are the sine integral, the cosine integral and the exponential integral function, respectively. Apart from these functions, the coefficients for the inital time of the vortex evolution are the following

$$h_{i0} = \frac{\pm h_0[h_0+(1+a)a_0\cos\phi]}{[h_0^2+(1+a)^2a_0^2+2h_0a_0(1+a)\cos\phi]^{1/2}}, \tag{A.50}$$

$$h_{i1} = \frac{\pm kh_0(1+a)a_0\sin\phi}{[h_0^2+(1+a)^2a_0^2+2h_0a_0(1+a)\cos\phi]^{1/2}}, \quad h_{12} = -\frac{k^2}{2}h_{i0}, \tag{A.51}$$

$$\alpha_{i0} = \frac{\pm a_0[h_0\cos\phi+(1+a)a_0]}{[h_0^2+(1+a)^2a_0^2+2h_0a_0(1+a)\cos\phi]^{1/2}}, \quad \alpha_{i1} = -\frac{h_{i1}}{1+a}, \quad \alpha_{i2} = -\frac{k^2}{2}\alpha_{i0}, \tag{A.52}$$

where the upper sign is for the downstroke and the lower sign for the upstroke. On the other hand,

$$\mathcal{G}_{i0} = 2\pi\left[\alpha_{i0}-h_{i1}-\left(a-\frac{1}{2}\right)\alpha_{i1}\right]F(k)-\pi\alpha_{i1}, \tag{A.53}$$

$$\mathcal{G}_{i1} = 2\pi\left[\alpha_{i1}-h_{i2}-\left(a-\frac{1}{2}\right)\alpha_{i2}\right]F(k)-2\pi\alpha_{i2}. \tag{A.54}$$

A.3 TIME-AVERAGED COEFFICIENTS

A.3.1 *Thrust coefficient*

The time-average thrust coefficient can be written in terms of the feathering paremeters as

$$\bar{C}_T = (kh_0)^2\left[t_h+t_{hp}\theta+t_p\theta^2+\left(t_{hd}+t_{pd}\theta\right)\theta_{hd}+t_d\theta_{hd}^2\right] \tag{A.55}$$

where the functions t_h, t_{hp}, t_p, t_{hd}, t_{pd} and t_d are given by

$$t_h = -2G_1, \tag{A.56}$$

$$t_{hp} = [(3-4a)G_1k-2F_1]\cos(\phi)+(2G_1-F_1k)\sin(\phi), \tag{A.57}$$

$$t_p = 2(1-a)k\left[F_1-\left(\frac{1}{2}-a\right)G_1k\right], \tag{A.58}$$

$$\begin{aligned} t_{hd} =& \frac{4}{(1-p)^2}\left\{F_1\left(\frac{1}{2}-p\right)-G_1k\left[\left(p-\frac{3}{2}\right)p+\frac{3}{4}\right]\right\}\cos(\psi)+ \\ & \frac{4}{(1-p)^2}\left(p-\frac{1}{2}\right)\left(G_1-\frac{F_1k}{2}\right)\sin(\psi), \end{aligned} \tag{A.59}$$

$$
\begin{aligned}
t_{pd} = & \frac{4k}{(1-p)^2}\left\{F_1\left[a\left(\frac{1}{2}-p\right)+2\left(1-\frac{p}{4}\right)p-1\right]+\right. \\
& \left. G_1 k\left[\left(\frac{3}{4}-a\right)p^2+\frac{3}{2}a\left(p-\frac{1}{2}\right)-p+\frac{1}{2}\right]\right\}\cos(\phi-\psi)+ \\
& \frac{4k}{(1-p)^2}\left[a\left(\frac{1}{2}-p\right)+\frac{p^2}{2}\right]\left(G_1-\frac{F_1 k}{2}\right)\sin(\phi-\psi),
\end{aligned} \tag{A.60}
$$

$$
t_d = \frac{2k}{(1-p)^2}\left\{2F_1\left(\frac{1}{2}-p\right)-G_1 k\left[(p-1)p+\frac{1}{2}\right]\right\}. \tag{A.61}
$$

$F(k)$ and $G(k)$ are the real and imaginary parts of Theodorsen's function (A.32), and likewise $F_j(k)$ and $Gj(k)$, $j = 1, 2, 3,$, in relation to the complex functions $C_j(k)$ given by (A.32)-(A.33).

A.3.2 *Input power coefficient*

The time-average input power coefficient can be written in terms of the feathering paremeters as

$$
\bar{C}_P = (kh_0)^2\left[p_h + p_{hp}\theta + p_p\theta^2 + \left(p_{hd} + p_{pd}\theta\right)\theta_{hd} + p_d\theta_{hd}^2\right], \tag{A.62}
$$

where the functions p_h, p_{hp}, p_p, p_{hd}, p_{pd} and p_d are given by

$$
p_h = \pi F, \tag{A.63}
$$

$$
p_{hp} = \pi\left(2aFk - G - \frac{k}{2}\right)\cos(\phi) + \pi(Gk - F)\sin(\phi), \tag{A.64}
$$

$$
p_p = \pi k\left[-\left(\frac{1}{4}-a^2\right)Fk - \left(a+\frac{1}{2}\right)G + \frac{1}{2}\left(\frac{1}{2}-a\right)k\right], \tag{A.65}
$$

$$
\begin{aligned}
p_{hd} = & \frac{2\pi}{(1-p)^2}\left\{\left[Fk\left(p^2+\frac{1}{2}\right)+G\left(\frac{1}{2}-p\right)-\frac{kp}{2}\right]\cos(\psi)+\right. \\
& \left.\left[F\left(\frac{1}{2}-p\right)+Gkp\right]\sin(\psi)\right\},
\end{aligned} \tag{A.66}
$$

$$
\begin{aligned}
p_{pd} = & \frac{k\pi}{(1-p)^2}\left\{Fk\left(2ap^2+a-p\right)-G\left[p(p+2)+2a\left(p-\frac{1}{2}\right)\right]-\right. \\
& \left. k\left[p\left(a+\frac{p}{2}-1\right)+\frac{1}{4}\right]\right\}\cos(\phi-\psi)+\frac{k\pi}{(1-p)^2}\left\{F\left(2ap-a-p^2-1\right)+\right. \\
& \left. Gk\left[p(p-2a)+\frac{1}{2}\right]+k^2p^2(a-p)+\frac{1}{2}\right\}\sin(\phi-\psi),
\end{aligned} \tag{A.67}
$$

$$
p_d = \frac{k\pi}{(1-p)^4}\left\{kF\left(p^4+\frac{1}{4}\right)-pk\left[(p-1)p+\frac{1}{2}\right]+G\left[\frac{1}{2}-p^2(2p+1)\right]\right\}. \tag{A.68}
$$

$F(k)$ and $G(k)$ are the real and imaginary parts of Theodorsen's function (A.32), and likewise $F_j(k)$ and $Gj(k)$, $j = 1, 2, 3,$, in relation to the complex functions $C_j(k)$ given by (A.32)-(A.33).

A.4 CUARTIC DEFLECTION

In this approximation of z_s as a quartic polynomial, the cubic and the quartic terms are related to the quadratic one by the boundary conditions of a *free* trailing edge, namely $\partial^2 z_s/\partial x^2 = \partial^3 z_s/\partial x^3 = 0$ at $x = 1$, in addition to the conditions $z_s = h$ and $\partial z_s/\partial x = -\alpha$ at $x = a$, already satisfy by the quadratic deflection. One must take into account that in this case the pivot point from the pithcing and deflection motion are the same $a = p$ for simplicity. Thus, this yields to

$$z_s(x,t) = h(t) - (x-a)\alpha(t) + (x-a)^2 \left(1 - \frac{2}{3}\frac{x-a}{1-a} + \frac{1}{6}\frac{(x-a)^2}{(1-a)^2}\right)\delta(t). \tag{A.69}$$

To facilitate the computations, the vertical displacement of the foil will be written as

$$z_s(x,t) = \sum_{n=0}^{4} \mathcal{Z}_n(t)x^n, \tag{A.70}$$

where

$$\mathcal{Z}_0(t) = h(t) + a\alpha(t) + A(a)\delta(t), \quad \mathcal{Z}_1(t) = -\alpha(t) - B(a)\delta(t), \tag{A.71}$$

$$\mathcal{Z}_2(t) = D(a)\delta(t), \quad \mathcal{Z}_3(t) = -E(a)\delta(t), \quad \mathcal{Z}_4(t) = J(a)\delta(t), \tag{A.72}$$

and the following functions of the pivot point location a have been defined:

$$A(a) = a^2\left(1 + \frac{2a}{3(1-a)} + \frac{a^2}{6(1-a)^2}\right), \quad B(a) = 2a\left(1 + \frac{a}{1-a} + \frac{a^2}{3(1-a)^2}\right), \tag{A.73}$$

$$D(a) = 1 + \frac{2a}{1-a} + \frac{a^2}{(1-a)^2}, \quad E(a) = \frac{2}{3(1-a)}\left(1 + \frac{a}{1-a}\right), \quad J(a) = \frac{1}{6(1-a)^2}. \tag{A.74}$$

Thus, the corresponding non-dimensional foil's velocity in the z direction ca be written as

$$v_0(x,t) = \sum_{n=0}^{4} \mathcal{V}_n(t)x^n, \quad \mathcal{V}_n(t) = \begin{cases} \dot{\mathcal{Z}}_n(t) + (n+1)\mathcal{Z}_{n+1}(t), & 0 \le n \le 3, \\ \dot{\mathcal{Z}}_n(t) & n = 4. \end{cases} \tag{A.75}$$

So, after solving the different integrals corresponding to the forces and moment, the non-dimensional coefficients can be written as

$$C_L(t) = -\pi\left[\ddot{h} + a\ddot{\alpha} - \dot{\alpha} + A_{l1}(a)\dot{\delta} + A_{l2}(a)\ddot{\delta}\right] + \Gamma_0 C(k), \tag{A.76}$$

$$C_M(t) = \frac{1}{2}\Gamma_0 C(k)\left(\frac{1}{2} + a\right) - \frac{\pi}{2}\left[a\ddot{h} + \ddot{\alpha}\left(\frac{1}{8} + a^2\right) + \dot{\alpha}\left(\frac{1}{2} - a\right) + \right. \tag{A.77}$$

$$\left. A_{m0}(a)\delta + A_{m1}(a)\dot{\delta} + A_{m2}(a)\ddot{\delta}\right], \tag{A.78}$$

$$\begin{aligned} C_T(t) = {} & \mathcal{Z}_1 C_L + \sum_{n=1}^{4} \dot{\mathcal{Z}}_n f_n + \sum_{n=2}^{4} \mathcal{Z}_n \dot{f}_n + \left[\dot{h} + a\dot{\alpha} - \alpha\right]\left[\Gamma_0 g_0(k)\right] - \dot{\alpha}\left[\Gamma_0 g_1(k)\right] + \\ & \delta\left[\Gamma_0 A_{d0}(k,a)\right] + \dot{\delta}\left[\Gamma_0 A_{d1}(k,a)\right], \end{aligned} \tag{A.79}$$

$$C_F(t) = \left(\frac{1}{2} + a + a^2\right)\Gamma_0 C(k) + \pi\Bigg[-\left(\frac{1}{4} + a^2\right)\ddot{h} - \ddot{\alpha}\left(\frac{1}{2} + a^2\right) + \dot{\alpha}\,(a-1)\,a + \\ A_{f0}(a)\delta + A_{f1}(a)\dot{\delta} + A_{f2}(a)\ddot{\delta}\Bigg], \tag{A.80}$$

where

$$\Gamma_0 = -2\pi\left[\dot{h} + \dot{\alpha}\left(a - \frac{1}{2}\right) - \alpha + A_{g0}(a)\delta + A_{g1}(a)\dot{\delta}\right], \tag{A.81}$$

and the following functions of the pivot point location a have been defined:

$$A_{g0}(a) := \frac{3 - 24a + 24a^2 - 8a^3}{12(1-a)^2}, \quad A_{g1}(a) := \frac{15 - 48a + 96a^2 - 80a^3 + 24a^4}{48(1-a)^2}, \tag{A.82}$$

$$A_{l1}(a) := -\frac{3 + 12a - 12a^2 + 4a^3}{6(1-a)^2}, \quad A_{l2}(a) := \frac{13 + 48a^2 - 64a^3 + 24a^4}{48(1-a)^2}, \tag{A.83}$$

$$A_{m0}(a) := \frac{-3}{4(1-a)^2}, \quad A_{m1}(a) := \frac{-16a^4 + 56a^3 - 72a^2 + 12a - 9}{24(a-1)^2}, \tag{A.84}$$

$$A_{m2}(a) := \frac{2 + 25a - 12a^2 + 52a^3 - 64a^4 + 24a^5}{48(1-a)^2}, \tag{A.85}$$

$$A_{f0}(a) := \frac{7 + 18a}{12(1-a)^2}, \quad A_{f1}(a) := \frac{1 + 8a - 18a^2 + 48a^3 - 32a^4 + 8a^5}{12(1-a)^2}, \tag{A.86}$$

$$A_{f2}(a) := -\frac{192a^6 - 512a^5 + 496a^4 - 320a^3 + 392a^2 + 32a + 35}{384(1-a)^2}, \tag{A.87}$$

and with

$$f_1(t) := -\pi\left(\mathcal{V}_0 + \frac{\mathcal{V}_2}{4} + \frac{\mathcal{V}_4}{8}\right), \quad f_2(t) := -\pi\left(\frac{\mathcal{V}_1}{4} + \frac{\mathcal{V}_3}{8}\right), \tag{A.88}$$

$$f_3(t) := -\pi\left(\frac{3\mathcal{V}_0}{4} + \frac{\mathcal{V}_2}{4} + \frac{9\mathcal{V}_4}{64}\right), \quad f_4(t) := -\pi\left(\frac{\mathcal{V}_1}{4} + \frac{9\mathcal{V}_3}{64}\right). \tag{A.89}$$

The complex functions $A_{d0}(k,a)$ and $A_{d1}(k,a)$ are given by

$$A_{d0}(k,a) := -Bg_0 + D[1 + 2g_1 - C] - E\left[\frac{1}{2} + 3g_2 + \frac{C}{2}\right] + J\left[4g_3 + \frac{C}{2} + \frac{C_3}{k}\right], \tag{A.90}$$

$$A_{d1}(k,a) := Ag_0 - Bg_1 + Dg_2 - E\left[g_3 - \frac{i}{2k}C\right] + J\left[g_4 - \frac{C_2}{2k}\right]. \tag{A.91}$$

A.4.1 *Time-averaged coefficients*

For the time-averaged coefficients only the components of deflection motion are different respect to the quadratic deflection. So, the new functions t_{hd}, t_{pd}, t_d, p_{hd}, p_{pd} and p_d are given by

$$t_{hd} = \Bigg\{\Bigg[\pi\left(A^I_{d0} - kA^R_{d1} - DG\right) - 2AG_1k + \frac{3}{2}(E-J)\left(\pi G - \frac{G_1k}{2}\right) - Q\Bigg(F_1 - \frac{G_1k}{2} + \\ \frac{\pi G}{2}\Bigg)\Bigg]\cos(\psi) + \left[\pi\left(-A^R_{d0} - kA^I_{d1} + DF\right) - 2AF_1k + \frac{3}{2}(E-J)\left(-\frac{F_1k}{2} - \pi F\right) + \\ Q\left(\frac{F_1k}{2} + \frac{\pi F}{2} + G_1\right)\right]\sin(\psi)\Bigg\}\frac{1}{(1-a)^2}, \tag{A.92}$$

$$
\begin{aligned}
t_{pd} ={}& \Bigg\{ \pi \left[\left(\frac{1}{2} - a \right) k \left(-A^I_{d0} + kA^R_{d1} + DG \right) + A^R_{d0} + kA^I_{d1} - DF \right] + 2Ak\Big[-aG_1k + F_1 \\
& + \frac{\pi}{2} \left(kg^R_1 - G \right) \Big] + \frac{3}{2}(E-J) \left[\pi \left(F - \left(\frac{3}{4} - a \right) Gk + \frac{k^2}{4} g^R_1 \right) + \frac{k}{2} \left(F_1 - aG_1k \right) \right] - \\
& Q\left[\pi \left(\frac{k}{2}(a-1)G + F + \frac{kg^I_1}{2} + \frac{k^2}{4} g^R_1 \right) + \left(a + \frac{1}{2} \right) F_1k + G_1 \left(1 - \frac{ak^2}{2} \right) \right] \Bigg\} \times \\
& \frac{\cos(\phi - \psi)}{(1-a)^2} + \Bigg\{ \pi \left[- \left(\frac{1}{2} - a \right) k \left(A^R_{d0} + kA^I_{d1} - DF \right) - A^I_{d0} + kA^R_{d1} + DG \right] + \\
& 2Ak \left(aF_1k + \frac{\pi}{2} \left(F + kg^I_1 \right) + G_1 \right) + \frac{3}{2}(E-J) \Bigg[\frac{k}{2} \left(aF_1k + G_1 \right) - \\
& \pi \left(G + \left(\frac{1}{4} - a \right) Fk - \frac{k^2}{4} g^I_1 \right) \Bigg] - Q\Bigg[\frac{\pi}{2}k \left(aF + \frac{kg^I_1}{2} - g^R_1 \right) - F_1 \left(1 - \frac{ak^2}{2} \right) + \\
& \left(a + \frac{1}{2} \right) G_1k \Bigg] \Bigg\} \frac{\sin(\phi - \psi)}{(1-a)^2},
\end{aligned}
\tag{A.93}
$$

$$
\begin{aligned}
t_d ={}& \frac{\pi}{4(1-a)^4} \Bigg\{ Q\Bigg[-kA^I_{d0} + 2A^R_{d0} + 2kA^I_{d1} + k^2A^R_{d1} - 2AGk + D(Gk - 2F) + \\
& (E-J) \left(3F - \frac{9Gk}{4} \right) \Bigg] + k \left(4A + \frac{3E}{2} - \frac{3J}{2} \right) \left[A^I_{d0} - kA^R_{d1} + G \left(-D + \frac{3E}{2} - \frac{3J}{2} \right) \right] + \\
& Q^2 \left(\frac{Gk}{2} - F \right) \Bigg\},
\end{aligned}
\tag{A.94}
$$

$$
\begin{aligned}
p_{hd} ={}& \frac{\pi}{(1-a)^2} \left[Fk \left(a(a+1) + A_{g1} + \frac{1}{2} \right) + A_{g0}G + \frac{A_{l1}k}{2} \right] \cos(\psi) + \\
& \frac{\pi}{(1-a)^2} \left[\frac{k^2}{2} \left(a^2 - A_{l2} + \frac{1}{4} \right) + Gk \left(a(a+1) - A_{g1} + \frac{1}{2} \right) + A_{g0}F \right] \sin(\psi),
\end{aligned}
\tag{A.95}
$$

$$
\begin{aligned}
p_{pd} ={}& \pi k \Bigg\{ Fk \left[\left(a + \frac{1}{2} \right) \left(a^2 + A_{g1} \right) - \frac{1}{4} \right] + G \left[\left(a + \frac{1}{2} \right) A_{g0} - a(a+1) - \frac{1}{2} \right] + \\
& \frac{k}{2}[(1-a)a + A_{m1}] \Bigg\} \frac{\cos(\phi - \psi)}{(1-a)^2} + \pi k \Bigg\{ Gk \left[\frac{1}{4} - \left(a + \frac{1}{2} \right) \left(a^2 - A_{g1} \right) \right] - \\
& \frac{k^2}{2} \left[\left(a^2 - A_{m2} \right) + \frac{1}{2} \right] - F \left[\left(a + \frac{1}{2} \right) A_{g0} + (a+1)a + \frac{1}{2} \right] - \frac{A_{m0}}{2} \Bigg\} \frac{\sin(\phi - \psi)}{(1-a)^2},
\end{aligned}
\tag{A.96}
$$

$$
p_d = \frac{\pi k}{(1-a)^4} \left[\left(a(a+1) + \frac{1}{2} \right) \left(A_{g0}G + A_{g1}Fk \right) - \frac{A_{f1}k}{2} \right], \tag{A.97}
$$

where $F(k)$ and $G(k)$ are the real and imaginary parts of Theodorsen's function (A.32), and likewise $F_j(k)$ and $Gj(k)$, $j = 1,2,3$, in relation to the complex functions $C_j(k)$ given by (A.32)-(A.33), and the $g^R_j(k)$ and $g^I_j(k)$, $j = 1,2,3,4$, in relation to the complex functions (A.34)-(A.37). Finally, $A^R_{dj}(k,a)$ and $A^I_{dj}(k,a)$ are the real and imaginary parts of the functions (A.90) and (A.91), and $Q(a)$ is defined as

$$
Q(a) = 2B(a) - 2D(a) + 3E(a) - 3J(a). \tag{A.98}
$$

B

NUMERICAL IMPLEMENTATION OF THE FLOW AROUND A FLAPPING AIRFOIL

B.1 CONFORMAL MAPPING

To compute geometry of the airfoil, the Kármán-Trefftz transformation has been used which maps an airfoil from an off-centered cylinder. This transformation is given by

$$mb\frac{(\zeta+b)^m+(\zeta-b)^m}{(\zeta+b)^m-(\zeta-b)^m}=x+\hat{i}z, \tag{B.1}$$

where m is related to angle of trailing edge, obtaining the Joukwoski's profiles when $m=2$, b measures the thickness of the airfoil, which it becomes in a flate plate when $b=1$ and in a cilinder when $b=0$, for $m=2$, and ζ is the plane in the circular domain. Apart from that, the cylinder is mapped using a log-polar transformation (Lin, Pepper, and Lee, 1976)

$$\zeta=\zeta_0+e^{r+\hat{i}\theta}, \quad r\in[\ln(r_0),\ln(r_f)], \quad \theta\in[0,2\pi), \tag{B.2}$$

where ζ_0 is the origin of the cylinder, r_0 is the radius of the cylinder and r_f is the radius of the grid. The reason of using a log-polar transformation for the cylinder, apart from it concentrates the nodes near the surface, is that provides the same scale factor for both variables simplifying the equations as it will be seen later. So, the parameters to fix are ζ_0, r_0, m, and b. Obviously, these parameters have to be fixed iteratively minimizing the error between the airfoil, which one wants to approximate, and the Kármán-Trefftz transformation. An algorithm to do that is presented in Yükselen and Erim, 1984. In that case the selected airfoil is the NACA-0012. In the Figure B.1 one can see a portion of the generated grid for $\Delta=\pi/80$ and with the corresponding values of the parameters for the Kármán-Trefftz transformation. It should be noted that the trailing edge has been rounded to avoid singularities in the numerical simulation.

B.2 POISSON EQUATION FOR THE STREAM FUNCTION

The Poisson equation for the stream function is given by the vorticity as $\boldsymbol{\omega}=-\nabla^2\psi\mathbf{e}_z$, but for simplicity, from now on it is going to be consider a cartesian Poisson equation with an independent term f, which is a known function or a vector of known values, i.e,

$$\nabla^2\psi=\frac{\partial^2\psi}{\partial r^2}+\frac{\partial^2\psi}{\partial\theta^2}=f. \tag{B.3}$$

If one uses finite differences of second order to discretize the two dimensional Poisson equation, one obtains the following stencil scheme:

$$\begin{pmatrix} 0 & \beta^2 & 0 \\ 1 & -2(1+\beta^2) & 1 \\ 0 & \beta^2 & 0 \end{pmatrix}\psi_{i,j}=\Delta_r^2 f_{i,j}, \tag{B.4}$$

where $\beta=\Delta_r/\Delta_\theta$ is the space relation between both variables. This scheme provides a linear system of equations which has to be solved. For that, there are several options, like

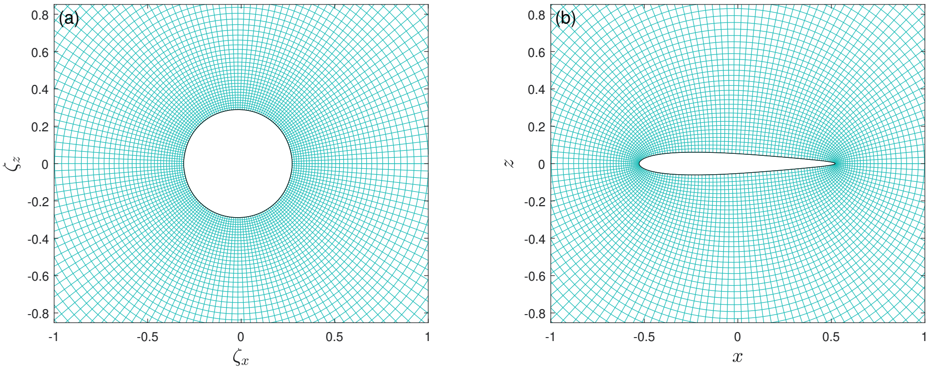

Figure B.1: A portion of the generated grid in the circular domain a) and in the physical space b) for the parameters $\zeta_0 = -0.01765$, $r_0 = 0.29$, $m = 2.0257$ and $b = 0.2566$, and a spaced grid $\Delta = \pi/80$.

iterative methods, multigrid methods, eigenvalues-eigenvectors based methods, or some kind of decomposition (LU, Cholesky, ...) to obtain the solution directly. Regardless of the method that one uses to solve the Poisson equation, a scheme of second order accuracy is useful and enough when the Reynolds number is low. However, the required grid size increases as the Reynolds number is higher. Thus, to avoid to use big grids, and because of that long time simulations, a high order scheme is necessary. So, following the derivation scheme from Sutmann, 2007, but maintaining the factor β, the stencil of the fourth compact order scheme (4COS) is given by

$$\begin{pmatrix} (1+\beta^2)/2 & -1+5\beta^2 & (1+\beta^2)/2 \\ 5-\beta^2 & -10(1+\beta^2) & 5-\beta^2 \\ (1+\beta^2)/2 & -1+5\beta^2 & (1+\beta^2)/2 \end{pmatrix} \psi_{i,j} = \frac{\Delta_r^2}{2} \begin{pmatrix} 0 & 1 & 0 \\ 1 & 8 & 1 \\ 0 & 1 & 0 \end{pmatrix} f_{i,j}, \tag{B.5}$$

The advantage of this scheme is that it uses a nine compact points stencil instead of a cross-shaped stencil of the completed fourth order scheme, accessing to the nodes ± 2 in both variables, where one must be careful not to access outside grid points. On the other hand, in the special case of $\beta = 1$, a sixth compact order scheme (6COS) can be obtained (see Sutmann, 2007) and it is given by

$$\begin{pmatrix} 1 & 4 & 1 \\ 4 & -20 & 4 \\ 1 & 4 & 1 \end{pmatrix} \psi_{i,j} = \Delta_r^2 \left[\frac{1}{30} \begin{pmatrix} 2 & 11 & 2 \\ 11 & 128 & 11 \\ 2 & 11 & 2 \end{pmatrix} - \frac{1}{40} \left(\delta_r^4 + \delta_\theta^4 \right) \right] f_{i,j}, \tag{B.6}$$

where the fourth order derivatives in the right hand side have the following stencil

$$\left(\delta_r^4 + \delta_\theta^4 \right) f_{i,j} = \begin{pmatrix} 0 & 0 & 1 & 0 & 0 \\ 0 & 0 & -4 & 0 & 0 \\ 1 & -4 & 12 & -4 & 1 \\ 0 & 0 & -4 & 0 & 0 \\ 0 & 0 & 1 & 0 & 0 \end{pmatrix} f_{i,j}, \quad \text{with} \quad i = 3, \ldots, N_r - 2, \quad \forall j. \tag{B.7}$$

Taking into account that the nodes $i = 2$ and $i = N_p - 1$ have to be approximated with forward and backward finite differences of second order accuracy respectively, i.e,

$$\delta_r^4 f_{2,j} = 3f_{2,j} - 14f_{3,j} + 26f_{4,j} - 24f_{5,j} + 11f_{6,j} - 2f_{7,j}, \tag{B.8}$$

$$\delta_r^4 f_{Nr-1,j} = 3f_{Nr-1,j} - 14f_{Nr-2,j} + 26f_{Nr-3,j} - 24f_{Nr-4,j} + 11f_{Nr-5,j} - 2f_{Nr-6,j}, \tag{B.9}$$

Apart from that, if one pays attention to the stencil for the unknown variable ψ, it is the same that the 4COS when $\beta = 1$, i.e, the matrix which one has to invert is the same, changing only the independent vector of the linear system of equations. So, to obtain the solution, one has the same computationally cost using 4COS or 6COS because the independent vector is known in both cases.

Another possible scheme is to use the fast Fourier transform (FFT) for the azimuthal variable taking advantage of the periodic boundary conditions, maintaining finite differences in the radial variable. So, the inverse discrete Fourier transform (iDFT) is given by

$$\psi_j = \frac{1}{2\pi} \sum_{k=-N_\theta/2+1}^{N_\theta/2} e^{\hat{i}k\theta_j} \hat{\psi}_k, \tag{B.10}$$

where $\hat{i} = \sqrt{-1}$ is the complex number and k is the wave number. So, replacing in the Poisson equation and simplifying, one obtains the following scheme

$$\left[\frac{\partial^2}{\partial r^2} - k^2\right] \hat{\psi}_{i,k} = \hat{f}_{i,k}, \tag{B.11}$$

where $\hat{f}_{i,k}$ is the discrete Fourier transform (DFT) of $f_{i,j}$. Regardless of which finite difference scheme one implements to discretize the radial variable, one have to solve a linear system of equations for every mode k (N_θ systems of equations of $N_p - 2$ unknowns) and then make use of the inverse fast Fourier transform (iFFT) to obtain the solution in the physical space. This scheme can be easily parallelizable, solving every linear system of equations in one single processor. It should be noted that the azimuthal distribution of the nodes is being done with a constant value of Δ_θ and not with a Fourier collocation in order to simplify the equation. To test the previously mentioned schemes, the Poisson equation has been solved with the following example

$$\nabla^2\psi = 2r^3 \cos(r) \cos(\theta)^2 - 3r \left[\left(r^2 - 2\right) \cos(r) + 2r \sin(r)\right] \sin(\theta)^2, \tag{B.12}$$

whose analytical solution is

$$\psi_e(p, \theta) = r^3 \cos(r) \sin(\theta)^2, \tag{B.13}$$

which satisfies the periodical boundary condition in the azimuthal variable. In the figure Figure B.2a one can see the representation of the maximum error using the previously mentioned schemes. It should be noted that maximum error using FFT for the azimuthal variable, it is preset according to what order of accuracy is being used to discretize the radial variable. On the other hand, in the figure Figure B.2b one can see the computational time to solve the Poisson equation using a CPU with 16 cores. For every value of Δ, the Poisson equation has been solved 100 times and then its mean has been obtained. As one can see in the figure Figure B.2b, the number of cores used for the FFT scheme is not enough to exceed the computational time of the compact schemes. In addition, as it has been mentioned before, as the matrix which one has to invert is the same in the compact schemes, the computational cost to solve the Poisson equation does not change, i.e, one has sixth order accuracy with the computational time of a second order scheme. It is worth mentioning that the method to solve the Poisson equation has been a Cholesky decomposition for high order schemes and the Thomas algorithm for the second order scheme. In view of the results, the 6COS has been selected to solve the Poisson equation.

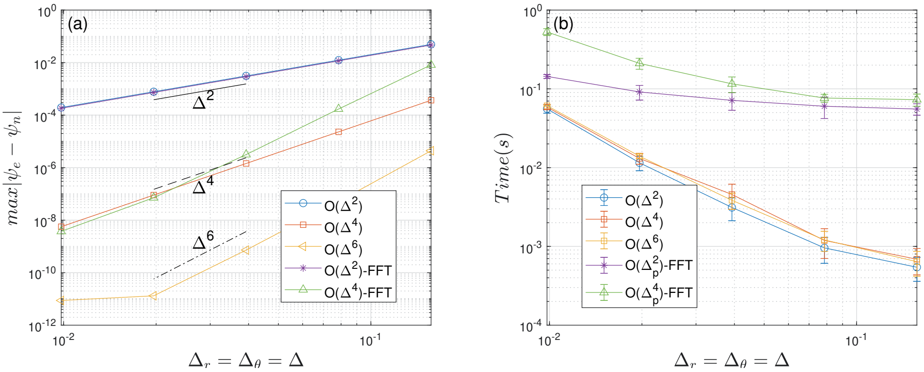

Figure B.2: a) Representation of the maximum numerical error and b) the computational time depending on the spaced grid Δ for the test function ψ_e using different schemes to solve the Poisson equation.

To conclude, the Poisson equation for the stream function in curvilinear coordinates is given by

$$\omega = \frac{-1}{h_r h_\theta}\left[\frac{\partial}{\partial r}\left(\frac{h_\theta}{h_r}\frac{\partial \psi}{\partial r}\right) + \frac{\partial}{\partial \theta}\left(\frac{h_r}{h_\theta}\frac{\partial \psi}{\partial \theta}\right)\right], \tag{B.14}$$

where h_r and h_θ are the scale factors for the radial and azimuthal variables respectively. But, as a result of the conformal mapping used, both scale factors are equals and the Poisson equation reduces to

$$\omega = \frac{-1}{h_s^2}\left(\frac{\partial^2 \psi}{\partial r^2} + \frac{\partial^2 \psi}{\partial \theta^2}\right), \tag{B.15}$$

which is a cartesian Poisson equation multiplied by a geometric factor h_s^2, where $h_s := h_r = h_\theta$. In that case, to implement the 6COS, the independent term is defined as $f := -\omega h_s^2$.

B.2.1 *Compute efficiently the right hand side*

Although the right hand side is known, one must compute it in the most efficient way in order to save computational time. After some algebraic manipulations, the right hand side of the 6COS can be written as

$$I = \frac{\Delta_r^2}{120}\left[A \cdot F + F \cdot B^T + 8C \cdot (F_{-1} + F_{+1})\right], \tag{B.16}$$

where F is the matrix of $f_{i,j}$ values ordered by rows the radial component and by columns the azimuthal component, i.e,

$$F = \begin{pmatrix} f_{1,1} & \cdots & f_{1,N_\theta} \\ \vdots & \ddots & \vdots \\ f_{N_r,1} & \cdots & f_{N_r,N_\theta} \end{pmatrix}. \tag{B.17}$$

The matrices F_{+1} and F_{-1} correspond to the matrix F but evaluated in the node $j \pm 1$ respectively. Must take into account that, by the periodicity condition in azimuthal variable, when it is accessing to the node $j = N_\theta + 1$, it corresponds to the first node, $j = 1$, and in the same way for the node $j = 0 = N_\theta$. So, they are given by

$$F_{-1} = \begin{pmatrix} f_{1,N_\theta} & f_{1,1} & \cdots & f_{1,N_\theta-1} \\ \vdots & \vdots & \vdots & \vdots \\ f_{N_r,N_\theta} & f_{N_r,1} & \cdots & f_{N_r,N_\theta-1} \end{pmatrix}, \quad F_{+1} = \begin{pmatrix} f_{1,2} & \cdots & f_{1,N_\theta} & f_{1,1} \\ \vdots & \cdots & \vdots & \vdots \\ f_{N_r,2} & \cdots & f_{N_r,N_\theta} & f_{N_r,1} \end{pmatrix}. \tag{B.18}$$

Finally, the matrices A, B and C, given by (B.19)-(B.21) respectively, are the coefficient resultant matrices. It should be noted the matrix B is symmetric and therefore, $B^T = B$. In addition, the nodes $i = 1$ and $i = N_r$, corresponding to the boundaries, have not been considered in the independent vector, specifically in the matrices A and C. It must not be confused with the values of ψ in the boundaries that they have to past as a vector to the right hand side, obtaining a linear system of equations with $(N_r - 2) \times N_\theta$ unknowns.

$$A = \begin{pmatrix} 44 & 503 & 86 & -78 & 72 & -33 & 6 & & 0 \\ -3 & 56 & 494 & 56 & -3 & & & & \\ 0 & -3 & 56 & 494 & 56 & -3 & & & \vdots \\ & & \ddots & \ddots & \ddots & \ddots & \ddots & & \\ \vdots & & & & & & & & 0 \\ & & & & -3 & 56 & 494 & 56 & -3 \\ 0 & & 6 & -33 & 72 & -78 & 86 & 503 & 44 \end{pmatrix}_{(N_r-2)\times N_r}, \tag{B.19}$$

$$B = \begin{pmatrix} -18 & 56 & -3 & 0 & \ldots & 0 & -3 & 56 \\ 56 & -18 & 56 & -3 & & & 0 & -3 \\ -3 & 56 & -18 & 56 & -3 & & & 0 \\ 0 & -3 & 56 & -18 & 56 & -3 & & \\ & & & & & & & \vdots \\ \vdots & & \ddots & \ddots & \ddots & \ddots & \ddots & \\ & & & & & & & 0 \\ 0 & & & -3 & 56 & -18 & 56 & -3 \\ -3 & 0 & & & -3 & 56 & -18 & 56 \\ 56 & -3 & 0 & \ldots & 0 & -3 & 56 & -18 \end{pmatrix}_{N_\theta \times N_\theta}, \tag{B.20}$$

$$C = \begin{pmatrix} 1 & 0 & 1 & & & \\ 0 & 1 & 0 & 1 & & \vdots \\ \vdots & & \ddots & \ddots & \ddots & 0 \\ & & & 1 & 0 & 1 \end{pmatrix}_{(N_r-2)\times N_r}. \tag{B.21}$$

B.3 TRANSPORT EQUATION FOR THE VORTICITY

To obtain the transport equation for the vorticity, one has to take the curl of the momentum Navier-Stokes equation given by (5.8). So, taking the curl term by term

$$\nabla \wedge \frac{\partial \mathbf{u}}{\partial t} = \frac{\partial}{\partial t}\left(\nabla \wedge \mathbf{u}\right) = \frac{\partial \boldsymbol{\omega}}{\partial t}, \tag{B.22}$$

$$\nabla \wedge \nabla p = 0, \tag{B.23}$$

$$\nabla \wedge \left[\left(\mathbf{u}\cdot\nabla\right)\mathbf{u}\right] = \nabla \wedge \left[\nabla\frac{|\mathbf{u}|^2}{2} - \mathbf{u}\wedge\boldsymbol{\omega}\right] = \mathbf{u}\cdot\nabla\boldsymbol{\omega}, \tag{B.24}$$

$$\nabla \wedge \nabla^2\mathbf{u} = \nabla \wedge \left[\nabla\left(\nabla\cdot\mathbf{u}\right) - \nabla\wedge\boldsymbol{\omega}\right] = \nabla^2\boldsymbol{\omega}, \tag{B.25}$$

$$\nabla \wedge \left(\boldsymbol{\Omega}\wedge\mathbf{u}\right) = \left[\mathbf{u}\cdot\nabla + \nabla\cdot\mathbf{u}\right]\boldsymbol{\Omega} - \left[\boldsymbol{\Omega}\cdot\nabla + \nabla\cdot\boldsymbol{\Omega}\right]\mathbf{u} = 0, \tag{B.26}$$

$$\nabla \wedge \left(\frac{d\boldsymbol{\Omega}}{dt}\wedge\mathbf{x}\right) = \left[\mathbf{x}\cdot\nabla + \nabla\cdot\mathbf{x}\right]\frac{d\boldsymbol{\Omega}}{dt} - \left[\frac{d\boldsymbol{\Omega}}{dt}\cdot\nabla + \nabla\cdot\frac{d\boldsymbol{\Omega}}{dt}\right]\mathbf{x} = 2\frac{d\boldsymbol{\Omega}}{dt}, \tag{B.27}$$

$$\nabla \wedge \left[\boldsymbol{\Omega}\wedge\left(\boldsymbol{\Omega}\wedge\mathbf{x}\right)\right] = \nabla \wedge \left[\left(\boldsymbol{\Omega}\cdot\mathbf{x}\right)\boldsymbol{\Omega} - \boldsymbol{\Omega}^2\mathbf{x}\right] = -\boldsymbol{\Omega}^2\ \nabla\wedge\mathbf{x} = 0, \tag{B.28}$$

and with the change of variable (5.10) the transport equation for the vorticity in non dimensional form can be written as

$$\frac{\partial \boldsymbol{\omega}'}{\partial t} = -\left(\nabla\wedge\psi\right)\cdot\nabla\boldsymbol{\omega}' + \frac{1}{Re}\nabla^2\boldsymbol{\omega}', \tag{B.29}$$

where the relation between the velocity and stream function has been used, $\mathbf{u} = \nabla\wedge\psi\mathbf{e}_z$. If one uses finite differences the transport equation reduces to

$$\frac{\omega'^{n+1}_{i,j} - \omega'^{n}_{i,j}}{\Delta t} = \frac{1}{h_s^2}\left[-NLT(\psi,\omega') + \frac{1}{Re}L(\omega')\right], \tag{B.30}$$

where NLT are the non-linear terms and L is the laplacian operator, which both are given respectively by

$$NLT(\psi,\omega') = -\delta_\theta\psi_{i,j}\,\delta_r\omega'_{i,j} + \delta_r\psi_{i,j}\,\delta_\theta\omega'_{i,j}, \quad L(\omega) = \delta_r^2\omega'_{i,j} + \delta_\theta^2\omega'_{i,j}. \tag{B.31}$$

with δf and $\delta^2 f$ the finite differences of the first and second derivative with sixth order of accuracy. To solve the discrete equation (B.30) there are many different options, one of them is to use a semi-implicit scheme in order to maintain a constant matrix to invert. For that, NLT are approximated with a explicit scheme and L is obtained using an implicit scheme. Some of these kind of semi-implicit methods are presented in Ascher, Ruuth, and Wetton, 1995, which for easy reference are shown below

$$\text{AB2CN2}: \left(1 - \frac{\Delta t}{h_s^2 Re}L\right)\omega'^{n+1}_{i,j} = \omega'^{n}_{i,j} + \frac{\Delta t}{h_s^2}\left[\frac{1}{Re}L^n_{i,j} - \frac{3}{2}NLT^n_{i,j} + \frac{1}{2}NLT^{n-1}_{i,j}\right], \tag{B.32}$$

$$\text{MABCN}: \left(1 - \frac{9\Delta t}{16h_s^2 Re}L\right)\omega'^{n+1}_{i,j} = \omega'^{n}_{i,j} + \frac{\Delta t}{h_s^2}\left[\frac{3}{8Re}L^n_{i,j} + \frac{1}{16Re}L^{n-1}_{i,j} - \frac{3}{2}NLT^n_{i,j} + \frac{1}{2}NLT^{n-1}_{i,j}\right], \tag{B.33}$$

$$
\begin{array}{c|cc}
0 & & \\
\frac{1}{2} & \frac{1}{2} & \\
\hline
 & 0 & 1
\end{array}
\qquad
\begin{array}{c|ccc}
0 & & & \\
\frac{1}{2} & \frac{1}{2} & & \\
\frac{3}{4} & 0 & \frac{3}{4} & \\
\hline
 & \frac{2}{9} & \frac{1}{3} & \frac{4}{9}
\end{array}
\qquad
\begin{array}{c|cccc}
0 & & & & \\
\frac{1}{2} & \frac{1}{2} & & & \\
\frac{1}{2} & 0 & \frac{1}{2} & & \\
1 & 0 & 0 & 1 & \\
\hline
 & \frac{1}{6} & \frac{1}{3} & \frac{1}{3} & \frac{1}{6}
\end{array}
\qquad
\begin{array}{c|cccccc}
0 & & & & & & \\
\frac{1}{4} & \frac{1}{4} & & & & & \\
\frac{1}{4} & \frac{1}{8} & \frac{1}{8} & & & & \\
\frac{1}{2} & 0 & -\frac{1}{2} & 1 & & & \\
\frac{3}{4} & \frac{3}{16} & 0 & 0 & \frac{9}{16} & & \\
1 & -\frac{3}{7} & \frac{2}{7} & \frac{12}{7} & -\frac{12}{7} & \frac{8}{7} & \\
\hline
 & \frac{7}{90} & 0 & \frac{32}{90} & \frac{12}{90} & \frac{32}{90} & \frac{7}{90}
\end{array}
$$

Table 4: RK parameters in Butcher's notation (Butcher, 1964) from left to right: RK2, RK3, RK4 and RK5.

$$
\text{BDF2} \; : \; \left(1-\frac{2\Delta t}{3h_s^2 Re}L\right)\omega'^{n+1}_{i,j} \; = \; \frac{1}{3}\left(4\omega'^{n}_{i,j}-\omega'^{n-1}_{i,j}\right)+\frac{\Delta t}{h_s^2}\left[-4NLT^{n}_{i,j}+2NLT^{n-1}_{i,j}\right], \tag{B.34}
$$

$$
\begin{aligned}
\text{BDF3} : \left(1-\frac{6\Delta t}{11h_s^2 Re}L\right)\omega'^{n+1}_{i,j} = \frac{6}{11}\left(3\omega'^{n}_{i,j}-\frac{3}{2}\omega'^{n-1}_{i,j}+\frac{1}{3}\omega'^{n-2}_{i,j}\right)+ \\
\frac{6\Delta t}{11h_s^2}\left[-3NLT^{n}_{i,j}+3NLT^{n-1}_{i,j}-NLT^{n-2}_{i,j}\right],
\end{aligned} \tag{B.35}
$$

where AB2CN2 is the well-known second order Adams-Bashforth and Crank-Nicholson, MABCN is a modification of the last, BDF2 is backward differentation of second order and BD3 is of third order scheme. As one can see the different schemes, the number of operations and the memory storage increase as the scheme has a smaller truncation error because it is necessary to store the values of the vorticity and the stream function at other time moments. Other option to solve the discrete equation (B.30) is to use directly explicit methods. The equation (B.29) also can be written as

$$
\frac{\partial\omega'}{\partial t} = R(\omega'), \quad \text{with} \quad R(\omega') := \frac{1}{h_s^2}\left[\frac{1}{Re}\left(\frac{\partial^2\omega'}{\partial r^2}+\frac{\partial^2\omega'}{\partial\theta^2}\right)-\frac{\partial\psi}{\partial r}\frac{\partial\omega'}{\partial\theta}+\frac{\partial\psi}{\partial\theta}\frac{\partial\omega'}{\partial r}\right], \tag{B.36}
$$

which is equivalent to the first ODE system. In that case, the spatial derivatives are computed with sixth order compact finite difference schemes (Mehra and Patel, 2017). The most common methods to solve this kind of equation is the Runge-Kutta methods. In the Table 4, it is presented the RK parameters in Butcher's notation (Butcher, 1964) for the second, third, fourth and fifth order scheme. As one can see in the Table 4, the number of evaluations increase as the order sheme is higher although the time step decrease too.

In the Figure B.3 it is compared the drag coefficient using the different schemes shown above with the numerical results from Koumoutsakos and Leonard, 1995. As one can see, the semi-implicit methods do not work well with the sixt compact order scheme. However, the Runge-Kutta explicit methods reproduce the numerical results from Koumoutsakos and Leonard, 1995. In addition, the semi-implicit methods present oscillations at the beginning of motion. On the other hand, to use a high order Runge-Kutta method is not worth it because the improvement in Δt is too small comparing with the total time required to do the simulation. So that, it is selected the second order Runge-Kutta method to solve the vorticity transport equation.

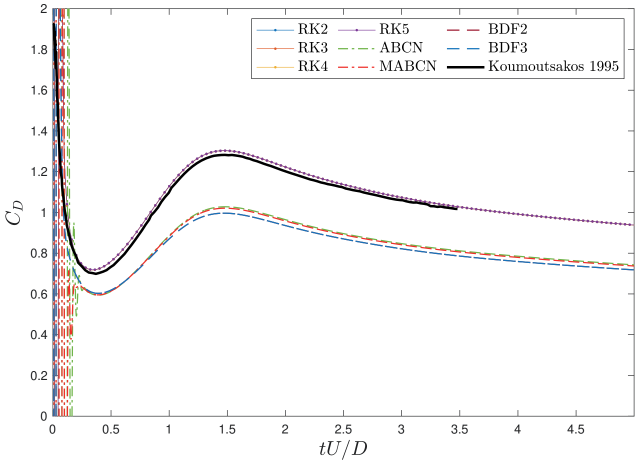

Figure B.3: Drag coefficient of a impulsively started cylinder for different resolution schemes of the vorticity transport equation for $Re = 550$ with $\Delta = \pi/200$; and comparing with the numerical results from Koumoutsakos and Leonard, 1995.

B.4 PRESSURE EQUATION

To obtain the equation for the pressure, one has to take the divergence of the momentum Navier-Stokes equation given by (5.8). So, taking the divergence term by term

$$\nabla \cdot \frac{\partial \mathbf{u}}{\partial t} = \frac{\partial}{\partial} \left(\nabla \cdot \mathbf{u} \right) = 0, \tag{B.37}$$

$$\nabla \cdot \left[\left(\mathbf{u} \cdot \nabla \right) \mathbf{u} \right] = \nabla^2 \frac{1}{2} |\mathbf{u}|^2 - \boldsymbol{\omega}^2 - \mathbf{u} \cdot \nabla^2 \mathbf{u}, \tag{B.38}$$

$$\nabla \cdot \nabla^2 \mathbf{u} = \nabla^2 \left(\nabla \cdot \mathbf{u} \right) = 0, \tag{B.39}$$

$$\nabla \cdot \nabla p = \nabla^2 p, \tag{B.40}$$

$$\nabla \cdot \left(\boldsymbol{\Omega} \wedge \mathbf{u} \right) = -\Omega \omega, \tag{B.41}$$

$$\nabla \cdot \left(\frac{d\Omega}{dt} \wedge \mathbf{x} \right) = \left(\nabla \wedge \frac{d\Omega}{dt} \right) \mathbf{x} - \frac{d\Omega}{dt} \left(\nabla \wedge \mathbf{x} \right) = 0, \tag{B.42}$$

$$\nabla \cdot \left[\Omega \wedge \left(\Omega \wedge \mathbf{x} \right) \right] = -\nabla \cdot \left(\nabla \frac{1}{2} |\Omega \wedge \mathbf{x}|^2 \right) = -\nabla^2 \frac{1}{2} |\Omega \wedge \mathbf{x}|^2, \tag{B.43}$$

and rearranging the different terms, the pressure equation is given by

$$\nabla^2 \left(\frac{p}{2} + \frac{|\mathbf{u}|^2}{2} - \frac{1}{2} |\Omega \wedge \mathbf{x}|^2 \right) = \boldsymbol{\omega} (\boldsymbol{\omega} + 2\Omega) + \mathbf{u} \cdot \nabla^2 \mathbf{u}. \tag{B.44}$$

If one uses the change of variable (5.10) the pressure equation can also be written as

$$\nabla^2 \left(\frac{p}{2} + \frac{|\mathbf{u}|^2}{2} - \frac{1}{2} |\Omega \wedge \mathbf{x}|^2 \right) = \nabla \cdot \left(\mathbf{u} \wedge \boldsymbol{\omega}' \right), \tag{B.45}$$

which is the same as that given by Tsai and Colonius, 2015. For simplicity, it is going to be used the equation (B.44). So, developing term by term of the equation (B.44)

$$\omega^2 = \frac{1}{h_s^4}\left[\left(\frac{\partial(h_s v_r)}{\partial\theta}\right)^2 + \left(\frac{\partial(h_s v_\theta)}{\partial r}\right)^2 - 2\frac{\partial(h_s v_r)}{\partial\theta}\frac{\partial(h_s v_\theta)}{\partial r}\right], \tag{B.46}$$

$$\mathbf{u}\cdot\nabla^2\mathbf{u} = \frac{1}{h_s^2}\left[\left(\frac{\partial^2 v_r}{\partial r^2} + \frac{\partial^2 v_r}{\partial\theta^2}\right)v_r + \left(\frac{\partial^2 v_\theta}{\partial r^2} + \frac{\partial^2 v_\theta}{\partial\theta^2}\right)v_\theta\right], \tag{B.47}$$

$$\begin{aligned}\nabla^2\frac{|\mathbf{u}|^2}{2} = \frac{1}{h_s^2}\Bigg[&\left(\frac{\partial v_r}{\partial r}\right)^2 + \left(\frac{\partial v_r}{\partial\theta}\right)^2 + \left(\frac{\partial v_\theta}{\partial r}\right)^2 + \left(\frac{\partial v_\theta}{\partial\theta}\right)^2 + \\ & v_r\left(\frac{\partial^2 v_r}{\partial r^2} + \frac{\partial^2 v_r}{\partial\theta^2}\right) + v_\theta\left(\frac{\partial^2 v_\theta}{\partial r^2} + \frac{\partial^2 v_\theta}{\partial\theta^2}\right)\Bigg],\end{aligned} \tag{B.48}$$

$$\nabla^2\frac{1}{2}|\boldsymbol{\Omega}\wedge\mathbf{x}|^2 = 2\Omega^2, \tag{B.49}$$

and taking into account the relation between the velocity and the stream function

$$\mathbf{u} = v_r\mathbf{e}_r + v_\theta\mathbf{e}_\theta = (\nabla\wedge\psi)\mathbf{e}_z = \frac{1}{h_s}\frac{\partial\psi}{\partial\theta}\mathbf{e}_r - \frac{1}{h_s}\frac{\partial\psi}{\partial r}\mathbf{e}_\theta, \tag{B.50}$$

with the hypothesis of incompressible fluid, $(\nabla\cdot\mathbf{u}=0)$ and consequently

$$(\nabla\cdot\mathbf{u})^2 = \left(\frac{\partial(h_s v_r)}{\partial r}\right)^2 + \left(\frac{\partial(h_s v_\theta)}{\partial\theta}\right)^2 + 2\frac{\partial(h_s v_r)}{\partial r}\frac{\partial(h_s v_\theta)}{\partial\theta} = 0, \tag{B.51}$$

the pressure equation yields to

$$\begin{aligned}\nabla^2 p = 4\Omega(\omega+\Omega) + \frac{4}{h_s^4}\Bigg\{&\left(\frac{\partial^2\psi}{\partial r^2}\right)\left(\frac{\partial^2\psi}{\partial\theta^2}\right) - \frac{\partial^2\psi}{\partial r\partial\theta}\left(\frac{\partial^2\psi}{\partial r\partial\theta} - H_\theta\frac{\partial\psi}{\partial r} - H_r\frac{\partial\psi}{\partial\theta}\right) + \\ & H_\theta\frac{\partial\psi}{\partial\theta}\frac{\partial^2\psi}{\partial\theta^2} + H_r\frac{\partial\psi}{\partial r}\frac{\partial^2\psi}{\partial r^2} - \left(H_r^2 + H_\theta^2\right)\left[\left(\frac{\partial\psi}{\partial r}\right)^2 + \left(\frac{\partial\psi}{\partial\theta}\right)^2\right]\Bigg\},\end{aligned} \tag{B.52}$$

where H_r and H_θ are purely geometric functions given by

$$H_r := \frac{1}{h_s}\frac{\partial h_s}{\partial r}, \quad H_\theta := \frac{1}{h_s}\frac{\partial h_s}{\partial\theta}. \tag{B.53}$$

The right hand side of (B.52) is known and therefore, the pressure equation coincides with a Poisson equation which can be solved with the same 6COS that the Poisson equation for the stream function. For simplicity, the equation (B.52) can be written as

$$\nabla^2 p = S(\omega,\psi,\Omega), \tag{B.54}$$

where $S(\omega,\psi,\Omega)$ is the right hand side of (B.52), and it would only remain to impose the boundary conditions to solve the pressure equation. Apart from that, if one only is interested on the pressure surface, it is not necessary to solve the pressure equation if one projects the Navier-Stokes equation to the airfoil surface in the tangent direction, i.e,

$$\frac{1}{2}\nabla p\cdot\mathbf{n}_t = -\frac{1}{Re}(\nabla\wedge\boldsymbol{\omega})\cdot\mathbf{n}_t - \left[\mathbf{a}_y + \frac{d\boldsymbol{\Omega}}{dt}\wedge\mathbf{x} + \boldsymbol{\Omega}\wedge(\boldsymbol{\Omega}\wedge\mathbf{x})\right]\cdot\mathbf{n}_t, \tag{B.55}$$

where $\mathbf{n}_t$ is the unit tangent vector to the airfoil surface. Taking into account that $\mathbf{u} = 0$ on the surface. So, developing every component separately

$$\frac{1}{2}\nabla p \cdot \mathbf{n}_t = \frac{1}{2}\frac{1}{h_s}\frac{\partial p}{\partial \theta}, \tag{B.56}$$

$$-\frac{1}{Re}\left(\nabla \wedge \boldsymbol{\omega}\right) \cdot \mathbf{n}_t = \frac{1}{h_s}\frac{1}{Re}\frac{\partial \omega}{\partial r}, \tag{B.57}$$

$$-\mathbf{a}_y \cdot \mathbf{n}_t = -\ddot{h}(t)\frac{1}{h_s}\frac{\partial y}{\partial \theta}, \tag{B.58}$$

$$-\left(\frac{d\boldsymbol{\Omega}}{dt} \wedge \mathbf{x}\right) \cdot \mathbf{n}_t = \ddot{\alpha}(t)\frac{1}{h_s}\left[y\frac{\partial x}{\partial \theta} - (x-a)\frac{\partial y}{\partial \theta}\right], \tag{B.59}$$

$$-\left[\boldsymbol{\Omega} \wedge \left(\boldsymbol{\Omega} \wedge \mathbf{x}\right)\right] \cdot \mathbf{n}_t = \dot{\alpha}(t)^2\frac{1}{h_s}\left[y\frac{\partial y}{\partial \theta} + (x-a)\frac{\partial x}{\partial \theta}\right], \tag{B.60}$$

and replacing in the equation (B.55), it reduces to

$$\frac{1}{2}\frac{\partial p}{\partial \theta} = \frac{1}{Re}\frac{\partial \omega}{\partial r} - \ddot{h}(t)\frac{\partial y}{\partial \theta} + \ddot{\alpha}(t)\left[y\frac{\partial x}{\partial \theta} - (x-a)\frac{\partial y}{\partial \theta}\right] + \dot{\alpha}(t)^2\left[y\frac{\partial y}{\partial \theta} - (x-a)\frac{\partial x}{\partial \theta}\right], \tag{B.61}$$

where it would only remain to impose an arbitrary value of the pressure on the surface (e.g. $p = 0$ on the trailing edge) to obtain the pressure distribution. To ensure the periodicity of the pressure when there are high pressure gradients, specially at the edges, it is convenient to solve the equation (B.61) with high accuracy. For that, one option is to solve it using the FFT, i.e,

$$p = \mathrm{iFFT}\left[\frac{\mathrm{FFT}[rhs]}{-\hat{i}k}\right], \tag{B.62}$$

where rhs is the right hand side of the equation (B.61).

B.5 BOUNDARY CONDITIONS

One of the boundary conditions of particular interest is the boundary condition for the outlet. As the wake is highly unsteady, a much more passive boundary condition than the inlet is necessary for the outlet. The pressure gradient will be small to the output, neglecting it and if the viscosity is neglected too, the boundary condition at the outlet is given by

$$\frac{D}{Dt}\left(\frac{\partial \psi'}{\partial n}\right)\Bigg|_{outlet} = 0, \tag{B.63}$$

which in a similar way it will be considered for the vorticity. So, if one takes into account the definition of the material derivative

$$\frac{D}{Dt}(*) = \frac{\partial}{\partial t}(*) + \mathbf{u} \cdot \nabla(*), \tag{B.64}$$

the equation (B.63) can be written as

$$\frac{\partial v_\theta}{\partial t} + \frac{1}{h_s}\left(v_r\frac{\partial v_\theta}{\partial r} + v_\theta\frac{\partial v_\theta}{\partial \theta}\right) = 0, \tag{B.65}$$

where it has been used the relation (B.50). After some algebra and using the definitions (B.53) the boundary condition for the outlet can be wrttien as

$$\frac{\partial^2 \psi'}{\partial t \partial r}\Bigg|_{outlet} = \frac{1}{h_s^2}\left[H_r\frac{\partial \psi'}{\partial r} - \frac{\partial^2 \psi'}{\partial r^2}\right]\frac{\partial \psi'}{\partial \theta} - \frac{1}{h_s^2}\left[H_\theta\frac{\partial \psi'}{\partial r} - \frac{\partial^2 \psi'}{\partial r \partial \theta}\right]\frac{\partial \psi'}{\partial r}\Bigg|_{outlet}. \tag{B.66}$$

So, if one uses finite differences the equation (B.66) reduces to

$$\delta_r^- \psi_{Nr,j}^{n+1} = \delta_r^- \psi_{Nr,j}^{n} + \Delta t \Delta r F(\psi)|_{Nr,j}^{n}, \quad j = outlet, \tag{B.67}$$

where $F(\psi)$ is the right hand side of (B.66) and δ_r^- means backward finite differences. The other condition of particular interest is the boundary condition on the surface. In the case of the stream function is the no-slip, no penetration condition

$$\left.\frac{\partial \psi}{\partial s}\right|_{airfoil} = 0, \quad \left.\frac{\partial \psi}{\partial n}\right|_{airfoil} = 0. \tag{B.68}$$

From the first, it is obtained that $\psi = cte$ along the surface, which by default this constant is set to zero, and from the second one, which there is a maximun or minimun in the normal direction. For the vorticity, a physical boundary condition can not be defined. Thus, it has to be set from the Poisson equation for the stream function, i.e,

$$\omega_a = -\left.\frac{\partial^2 \psi}{\partial n^2}\right|_{airfoil}. \tag{B.69}$$

A typical solution for this boundary condition is the Jenson's formula (Jenson, 1959)

$$\omega_a' = \frac{7\psi_a - 8\psi_{a+1} + \psi_{a+2}}{2\Delta n^2} + 2\Omega, \tag{B.70}$$

but the equation (B.70) has $O(\Delta n^3)$ as it is discused in Spotz, 1998. Other boundary condition for the vorticity on the surface was derived by Briley, 1971 with $O(\Delta n^4)$ and it is given by

$$\omega_a' = \frac{1}{18\Delta n^2}\left[85\psi_a - 108\psi_{a+1} + 27\psi_{a+2} - 4\psi_{a+3}\right] + 2\Omega. \tag{B.71}$$

A sixth order boundary condition for the vorticity on the surface will be derivated below following both formulations. Beginning with the Jensen's formulation and using Taylor series for the point located on the surface, it can be written as

$$\begin{aligned}\psi_{a+1} + a\psi_{a+2} + b\psi_{a+3} + c\psi_{a+4} + d\psi_{a+5} + e\psi_{a+6} = (1+a+b+c+d+e)\psi_a + \\ \sum_{k=1}^{7}(1 + 2^k a + 3^k b + 4^k c + 5^k d + 6^k e)\frac{\Delta n^k}{k!}\frac{\partial^k \psi}{\partial n^k} + O(\Delta n^8).\end{aligned} \tag{B.72}$$

where a, b, c, d and e are arbitrary constants. To cancel the higher derivatives $(k = 3, .., 7)$, (B.72) provides the following algebraic system

$$\left.\begin{array}{ll} k=3, & 1 + 2^3 a + 3^3 b + 4^3 c + 5^3 d + 6^3 e = 0 \\ k=4, & 1 + 2^4 a + 3^4 b + 4^4 c + 5^4 d + 6^4 e = 0 \\ k=5, & 1 + 2^5 a + 3^5 b + 4^5 c + 5^5 d + 6^5 e = 0 \\ k=6, & 1 + 2^6 a + 3^6 b + 4^6 c + 5^6 d + 6^6 e = 0 \\ k=7, & 1 + 2^7 a + 3^7 b + 4^7 c + 5^7 d + 6^7 e = 0 \end{array}\right\}, \quad \rightarrow \quad \begin{array}{ll} a = -\frac{5}{8}, & b = \frac{10}{27}, \\ c = -\frac{5}{32}, & d = \frac{1}{25}, \\ e = -\frac{1}{216}, & \end{array} \tag{B.73}$$

So, replacing the constant values in (B.72) an applying the boundary condition (B.68), the vorticity on the surface is given by

$$\omega_a' = \frac{1}{\Delta n^2}\left[\frac{13489}{1800}\psi_a - 12\psi_{a+1} + \frac{15}{2}\psi_{a+2} - \frac{40}{9}\psi_{a+3} + \frac{15}{8}\psi_{a+4} - \frac{12}{25}\psi_{a+5} + \frac{1}{18}\psi_{a+6}\right] + 2\Omega. \tag{B.74}$$

Other option to implement a boundary condition for the vorticity on the surface is following the derivation of Briley, 1971. So, using one-sided difference approximation for the Neumann boundary condition for ψ given by (B.68),

$$\left.\frac{\partial\psi}{\partial n}\right|_a = \frac{1}{\Delta n}\left[-\frac{1}{6}\psi_{a-1,j} - \frac{77}{60}\psi_{a,j} + \frac{5}{2}\psi_{a+1,j} - \frac{5}{3}\psi_{a+2,j} + \frac{5}{6}\psi_{a+3,j} - \frac{1}{4}\psi_{a+4,j} + \frac{1}{30}\psi_{a+5,j}\right] + O(\Delta n^6) = 0, \quad \text{(B.75)}$$

solving $\psi_{a-1,j}$

$$\psi_{a-1,j} = -\frac{77}{10}\psi_{a,j} + 15\psi_{a+1,j} - 10\psi_{a+2,j} + 5\psi_{a+3,j} - \frac{3}{2}\psi_{a+4,j} + \frac{1}{5}\psi_{a+5,j}, \quad \text{(B.76)}$$

together with the one-side formula

$$\left.\frac{\partial^2\psi}{\partial n^2}\right|_a = \frac{1}{\Delta n^2}\left[\frac{137}{180}\psi_{a-1,j} - \frac{49}{60}\psi_{a,j} - \frac{17}{12}\psi_{a+1,j} + \frac{47}{18}\psi_{a+2,j} - \frac{19}{12}\psi_{a+3,j} + \frac{31}{60}\psi_{a+4,j} - \frac{13}{180}\psi_{a+5,j}\right] + O(\Delta n^6). \quad \text{(B.77)}$$

substituting (B.76) in (B.77), the boundary condition for the vorticity is given by

$$\omega'_a = \frac{1}{\Delta n^2}\left[\frac{12019}{1800}\psi_{a,j} - 10\psi_{a+1,j} + 5\psi_{a+2,j} - \frac{20}{9}\psi_{a+3,j} + \frac{5}{8}\psi_{a+4,j} - \frac{2}{25}\psi_{a+5,j}\right] + 2\Omega. \quad \text{(B.78)}$$

The problem with these boundary conditions of sixth order truncation errror, as for (B.74) as for (B.78), they produce oscillations in the numerical results for high Reynolds number and one has to decrease the time step to solve it. For that reason, it has been considered the (B.71) as boundary condition for the vorticity on the surface obtaining better results than the sixth order formulaes.

B.6 FORCES AND INPUT POWER

The nondimensional forces on the airfoil surface can be computed as follows

$$\mathbf{F}(t) = -\int_S p\mathbf{n}dS + \frac{2}{Re}\int_S \omega \wedge \mathbf{n}dS = F_x\mathbf{e}_x + F_y\mathbf{e}_y, \quad \text{(B.79)}$$

where each component of the force is given by

$$F_x(t) = -\int_0^{2\pi} p\frac{\partial x}{\partial r}d\theta + \frac{2}{Re}\int_0^{2\pi}\omega\frac{\partial x}{\partial\theta}d\theta, \quad \text{(B.80)}$$

$$F_y(t) = -\int_0^{2\pi} p\frac{\partial y}{\partial r}d\theta + \frac{2}{Re}\int_0^{2\pi}\omega\frac{\partial y}{\partial\theta}d\theta, \quad \text{(B.81)}$$

So, projecting the force components to the parallel and perpendicular axis of the free stream current, one obtains the drag and lift coefficients, i.e,

$$C_D(t) = F_x(t)\cos[\beta + \alpha(t)] - F_y(t)\sin[\beta + \alpha(t)], \quad \text{(B.82)}$$

$$C_L(t) = F_x(t)\sin[\beta + \alpha(t)] + F_y(t)\cos[\beta + \alpha(t)], \quad \text{(B.83)}$$

where β is the angle with which the free stream current points the airfoil. On the other hand, the nondimensional moment can be computed as follows

$$\mathbf{M}(t) = -\int_S p\,(\mathbf{x} \wedge \mathbf{n})\,dS + \frac{2}{Re}\int_S \mathbf{x} \wedge (\boldsymbol{\omega} \wedge \mathbf{n})\,dS, \tag{B.84}$$

which developing the integrals

$$\mathbf{M}(t) = -\int_0^{2\pi} p\left[(x-a)\frac{\partial y}{\partial r} - y\frac{\partial x}{\partial r}\right] d\theta + \frac{2}{Re}\int_0^{2\pi} \omega\left[(x-a)\frac{\partial y}{\partial \theta} - y\frac{\partial x}{\partial \theta}\right] d\theta, \tag{B.85}$$

which only has one component, perpendicular to the airfoil surface plane, in the present 2D flow. It will be defined as $C_M(t)$. Moreover, the input power coefficient is given by

$$C_P(t) = \int_S (p\mathbf{n})\frac{\partial z_0}{\partial t} dS - \frac{2}{Re}\int_S (\boldsymbol{\omega} \wedge \mathbf{n})\,\frac{\partial z_0}{\partial t} dS, \tag{B.86}$$

which developing the above integrals, it can be written as

$$C_P(t) = -\dot{h}(t)C_L(t) - \dot{\alpha}(t)C_M(t). \tag{B.87}$$

B.7 VALIDATION OF THE CODE

To validate the code and test that it is working correctly, some numerical simulations have been done comparing with experimental and numerical avalaible results in the bibliography. In the Figure B.3 has been shown the evolution of the drag coefficient for a impulsively started cylinder for $Re = 550$ with the numerical results from Koumoutsakos and Leonard, 1995. In Figure B.4, one can see the comparison of the closed wake length, the location of the main eddy core and the velocity at the mean line of the cylinder wake compared with the theory and the experimental results from Bouard and Coutanceau, 1980, for $Re = 550$ and $Re = 3000$. In addition, in the Figure B.5 is shown a snapshoot of the streamlines for three different Reynolds numbers in comparison with the experimental results from Bouard and Coutanceau, 1980.

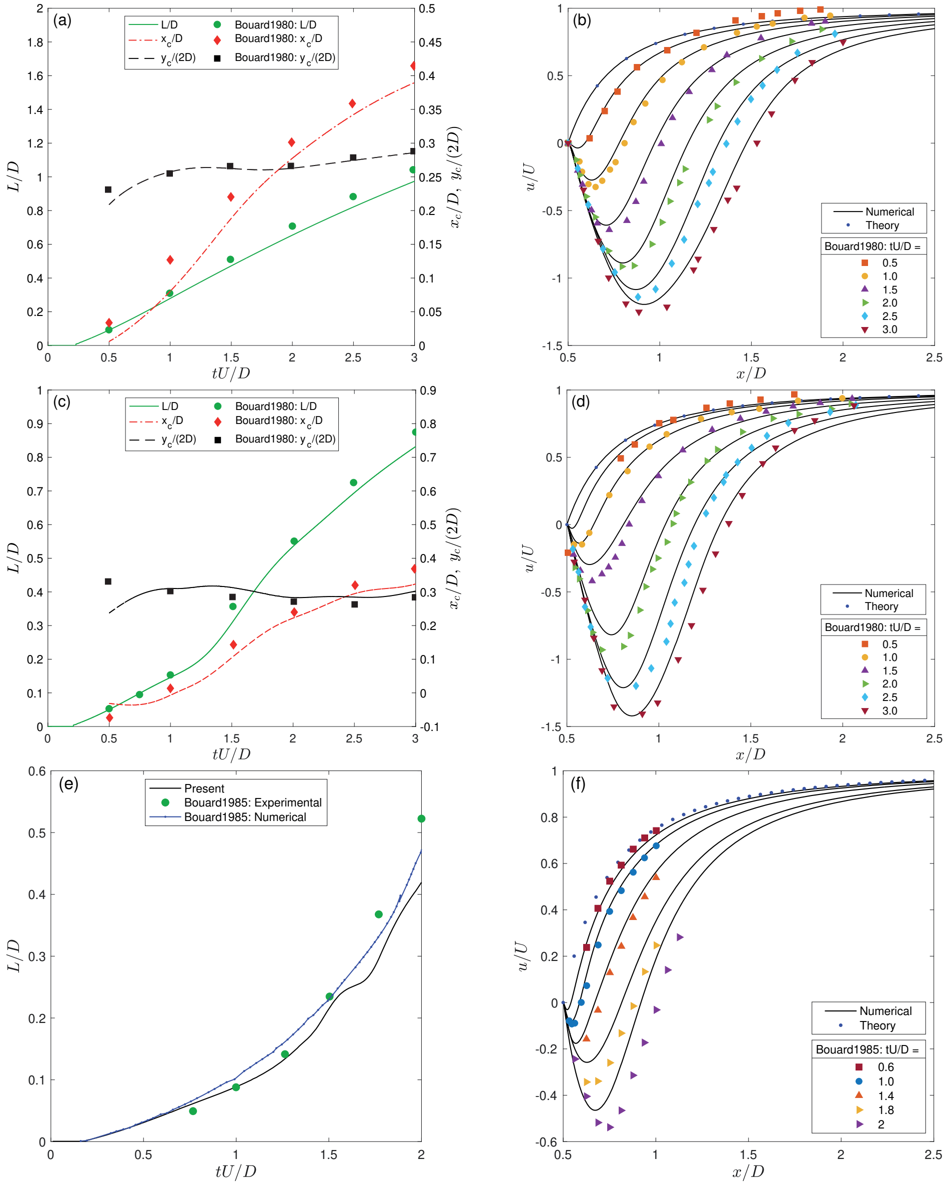

Figure B.4: (a) Comparison of the numerical results with the experimental data from Bouard and Coutanceau, 1980, for $Re = 550$ (a) and for $Re = 3000$ (c), and from Loc and Bouard, 1985, (e) of the closed wake length, L/D, and location of the main eddy core, $x_c/D, y_c/(2D)$ (measured from the most downstream point of the cylinder). Numerical results (continuous line) for the velocity at the mean line of the wake compared with the theory (dots), and the experimental data from Bouard and Coutanceau, 1980, for several moments of time (see the legend of the figure) for $Re = 550$ (b) and for $Re = 3000$ (d), and from Loc and Bouard, 1985, for $Re = 9500$ (f).

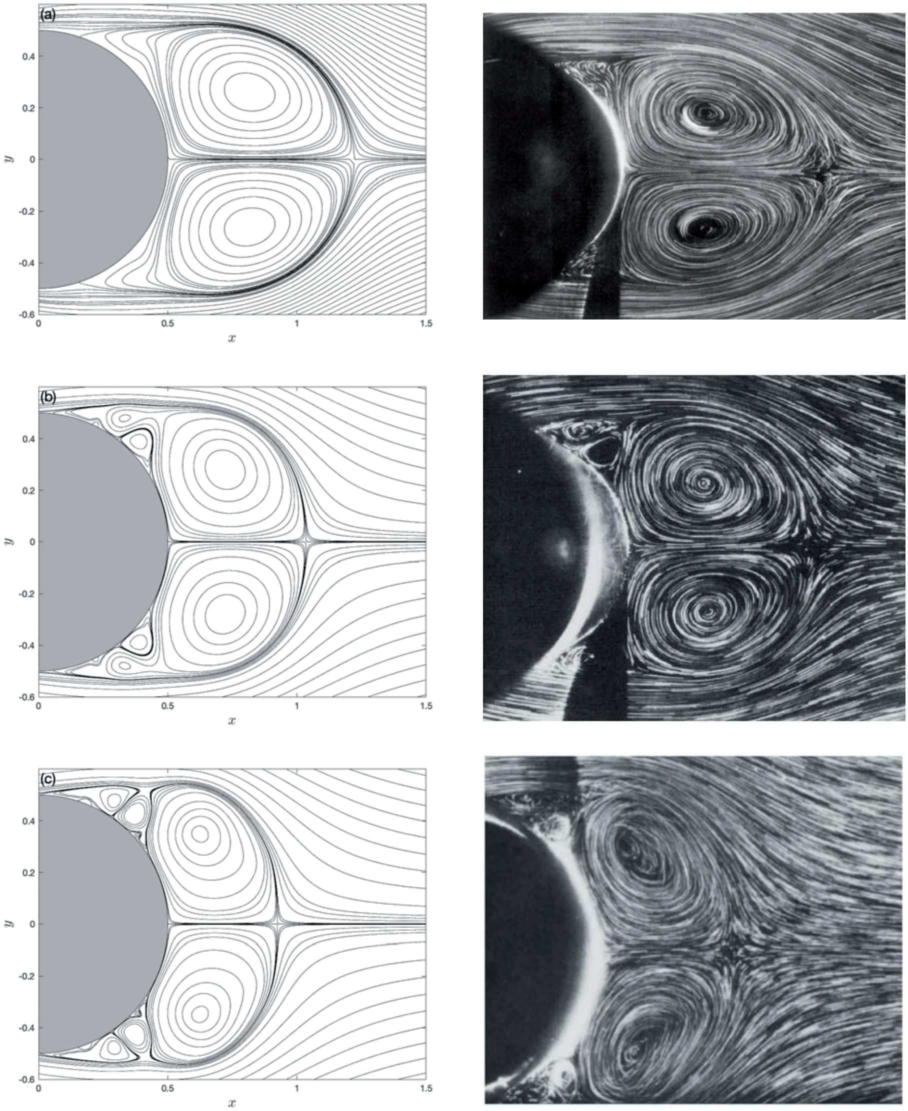

Figure B.5: Instantaneous streamlines for an impulsively started circular cylinder for (a) $Re = 300$ at $t = 2.5$ (top panels), for (b) $Re = 3000$ at $t = 2.5$ (middle panels) and for (c) $Re = 9500$ at $t = 2$ (bottom panels) compared with flow visualization results from Loc and Bouard, 1985.

C

TWO PLATES FUNCTIONS, INTEGRALS AND COEFFICIENTS

C.1 SOME INTEGRALS AND FUNCTIONS

Integrals and functions used in deriving the results of the thesis are summarized here.

$$\mathcal{A}_1(k,\varepsilon) := \int_{1-\varepsilon}^{-1} \frac{e^{-ik(\xi+\varepsilon)}}{\sqrt{\xi^2-1}} d\xi, \qquad \mathcal{A}_2(k,\varepsilon) := \int_{1+\varepsilon}^{\infty} \frac{e^{-ik(\xi-\varepsilon)}}{\sqrt{\xi^2-1}} d\xi, \tag{C.1}$$

$$\mathcal{Q}_1(k,\varepsilon) := \int_{1-\varepsilon}^{-1} e^{-ik(\xi+\varepsilon)} \sqrt{\xi^2-1} d\xi, \qquad \mathcal{Q}_2(k,\varepsilon) := \int_{1+\varepsilon}^{\infty} e^{-ik(\xi-\varepsilon)} \sqrt{\xi^2-1} d\xi, \tag{C.2}$$

$$\mathcal{K}(k,\varepsilon) := iH_1^{(2)}(k) + \frac{4i}{\pi k}\left[k\cos(k) - \sin(k)\right] + \frac{2}{\pi}\frac{e^{ik(\varepsilon-1)}}{k}\left[1 + ik(1-\varepsilon)\right]. \tag{C.3}$$

$$\mathsf{a}(k) := \frac{\pi}{2}\left[iH_0^{(2)}(k) + H_1^{(2)}(k)\right], \tag{C.4}$$

$$\mathsf{b}(k,\varepsilon) := \frac{i}{k}e^{-ik} + \left(1 + i\frac{d}{dk}\right)\mathcal{A}_2(k,\varepsilon), \tag{C.5}$$

$$\mathsf{c}(k,\varepsilon) := \frac{i}{k}e^{-ik} + \left(1 + i\frac{d}{dk}\right)\mathcal{A}_1(k,\varepsilon) - \mathsf{a}(k)e^{-ik\varepsilon}, \tag{C.6}$$

$$F_a(k,\varepsilon) := \frac{\mathsf{a}(k)}{\mathsf{a}(k) - \frac{\mathsf{b}(k,\varepsilon)}{\mathsf{a}(k)}\mathsf{c}(k,\varepsilon)}, \qquad F_b(k,\varepsilon) := \frac{\mathsf{b}(k,\varepsilon)}{\mathsf{a}(k) - \frac{\mathsf{b}(k,\varepsilon)}{\mathsf{a}(k)}\mathsf{c}(k,\varepsilon)}, \tag{C.7}$$

$$F_c(k,\varepsilon) := \frac{\mathsf{c}(k,\varepsilon)}{\mathsf{a}(k) - \frac{\mathsf{b}(k,\varepsilon)}{\mathsf{a}(k)}\mathsf{c}(k,\varepsilon)}, \tag{C.8}$$

$$\mathcal{C}_a := 1 - \frac{iH_0^{(2)}(k)F_a(k,\varepsilon)}{iH_0^{(2)}(k) + H_1^{(2)}(k)}, \quad \mathcal{C}_b := -\frac{iH_0^{(2)}(k)F_b(k,\varepsilon)}{iH_0^{(2)}(k) + H_1^{(2)}(k)}, \quad \mathcal{C}_c := -\frac{iH_0^{(2)}(k)F_c(k,\varepsilon)}{iH_0^{(2)}(k) + H_1^{(2)}(k)}, \tag{C.9}$$

$$C(k) := \frac{H_1^{(2)}(k)}{iH_0^{(2)}(k) + H_1^{(2)}(k)}, \qquad C_1(k) := \frac{\frac{1}{k}e^{-ik}}{iH_0^{(2)}(k) + H_1^{(2)}(k)}, \tag{C.10}$$

$$C_{1e}(k,\varepsilon) := \frac{\frac{1}{k}e^{-ik\varepsilon}}{iH_0^{(2)}(k) + H_1^{(2)}(k)}, \tag{C.11}$$

$$\mathcal{B}_1(k,\varepsilon) := \frac{\mathcal{Q}_2(k,\varepsilon)}{\mathsf{a}(k)} + \frac{2}{\pi}\left(\frac{1+ik}{k} + i\varepsilon\right)C_1(k), \quad \mathcal{B}_2(k,\varepsilon) := \mathcal{K}(k,\varepsilon)C_{1e}(k,\varepsilon) - \frac{\mathcal{Q}_1(k,\varepsilon)}{\mathsf{a}(k)}, \tag{C.12}$$

where $H_n^{(2)}(z) = J_n(z) - iY_n(z)$, $n = 0, 1$, are the Hankel functions of the second kind, related to the Bessel functions of the first and second kind J_n and Y_n, respectively (Olver et al., 2010). Other defined functions are the following

$$f_\gamma(x) := \frac{4}{\pi}\frac{K\left[4/\varepsilon^2\right]}{1+\varepsilon-x} + \frac{2}{\pi}\left(1 + \frac{2}{\varepsilon}\right)\left(\frac{(1-\varepsilon+x)(1-x)}{(1+\varepsilon-x)(1+x)}\Pi\left[\frac{2}{\varepsilon}\frac{1+\varepsilon-x}{1+x}, \frac{4}{\varepsilon^2}\right] - \Pi\left[-\frac{2}{\varepsilon}, \frac{4}{\varepsilon^2}\right]\right), \tag{C.13}$$

$$\begin{aligned} f_{\gamma\alpha}(x) \quad := \quad & 2\left\{\varepsilon E\left(\frac{4}{\varepsilon^2}\right) + \frac{2(2+x)+\varepsilon(1-\varepsilon+x)}{1+\varepsilon-x} K\left(\frac{4}{\varepsilon^2}\right) + \left(1+\frac{2}{\varepsilon}\right)(1+2x)\right. \\ & \left. \times \left[\frac{(1-\varepsilon+x)(1-x)}{(1+\varepsilon-x)(1+x)} \Pi\left(\frac{2}{\varepsilon}\frac{1+\varepsilon-x}{1+x}, \frac{4}{\varepsilon^2}\right) - \Pi\left(-\frac{2}{\varepsilon}, \frac{4}{\varepsilon^2}\right)\right]\right\}, \qquad \text{(C.14)} \end{aligned}$$

$$f_\Gamma := \frac{1}{\pi}\left[\varepsilon E\left(\frac{4}{\varepsilon^2}\right) + (2-\varepsilon)K\left(\frac{4}{\varepsilon^2}\right)\right] - 1, \qquad \text{(C.15)}$$

$$f_{\Gamma\alpha} := \varepsilon(1+\varepsilon)E\left(\frac{4}{\varepsilon^2}\right) + [6+(3-\varepsilon)\varepsilon]K\left(\frac{4}{\varepsilon^2}\right) - 4(2+\varepsilon)\Pi\left(-\frac{2}{\varepsilon}, \frac{4}{\varepsilon^2}\right), \qquad \text{(C.16)}$$

where $K(x), E(x)$ and $\Pi(x,y)$ are the complete elliptic integral of the first kind, the complete elliptic integral of the second kind and the incomplete elliptic integral of the third kind, respectively (Olver et al., 2010). Some integrals related to theses functions are the following

$$\mathcal{I}_{\gamma,n} := \frac{1}{\pi}\fint_{-1+\varepsilon}^{1+\varepsilon} (x-\varepsilon)^n \sqrt{\frac{1+\varepsilon-x}{1-\varepsilon+x}} f_\gamma(x)dx, \qquad \text{(C.17)}$$

$$\mathcal{I}_{\gamma\alpha,n} := \frac{1}{\pi}\fint_{-1+\varepsilon}^{1+\varepsilon} (x-\varepsilon)^n \sqrt{\frac{1+\varepsilon-x}{1-\varepsilon+x}} f_{\gamma\alpha}(x)dx. \qquad \text{(C.18)}$$

In addition, to compute (9), (10) and (13), one needs the following integrals:

$$\fint_{-1+\varepsilon_i}^{1+\varepsilon_i^*} (x-\varepsilon_i)\varpi_{sei}(x,t)dx = \int_{1+\varepsilon_i^*}^{\infty} \left[\sqrt{\frac{\xi+1-\varepsilon_i}{\xi-1-\varepsilon_i^*}}(\xi-1-\varepsilon_i-b_i) - (\xi-\varepsilon_i)\right]\varpi_{ei}(\xi,t)d\xi, \qquad \text{(C.19)}$$

$$\begin{aligned} \fint_{-1+\varepsilon_i}^{1+\varepsilon_i^*} (x-\varepsilon_i)^2\varpi_{sei}(x,t)dx = & \int_{1+\varepsilon_i^*}^{\infty} \left[\frac{1}{2}\sqrt{\frac{\xi+1-\varepsilon_i}{\xi-1-\varepsilon_i^*}} + (\xi-\varepsilon_i+b_i)\sqrt{(\xi+1-\varepsilon_i)(\xi-1-\varepsilon_i^*)}\right. \\ & \left. -(\xi-\varepsilon_i)^2\right]\varpi_{ei}(\xi,t)d\xi + b_i\left(1+\frac{3}{2}b_i\right)\left(\Gamma_{sei} + \int_{1+\varepsilon_i^*}^{\infty}\varpi_{ei}d\xi\right), \qquad \text{(C.20)} \end{aligned}$$

- Rear-wakes $(j > i)$

$$\fint_{-1+\varepsilon_i}^{1+\varepsilon_i^*} (x-\varepsilon_i)\varpi_{seji}(x,t)dx = \int_{1+\varepsilon_j^*}^{\infty} \left[\sqrt{\frac{\xi+1-\varepsilon_i}{\xi-1-\varepsilon_i^*}}(\xi-1-\varepsilon_i-b_i) - (\xi-\varepsilon_i)\right]\varpi_{ej}(\xi,t)d\xi, \qquad \text{(C.21)}$$

$$\begin{aligned} \fint_{-1+\varepsilon_i}^{1+\varepsilon_i^*} (x-\varepsilon_i)^2\varpi_{seji}(x,t)dx = & \int_{1+\varepsilon_j^*}^{\infty} \left[\frac{1}{2}\sqrt{\frac{\xi+1-\varepsilon_i}{\xi-1-\varepsilon_i^*}} + (\xi-\varepsilon_i+b_i)\sqrt{(\xi+1-\varepsilon_i)(\xi-1-\varepsilon_i^*)}\right. \\ & \left. -(\xi-\varepsilon_i)^2\right]\varpi_{ej}(\xi,t)d\xi + b_i\left(1+\frac{3}{2}b_i\right)\left(\Gamma_{seji} + \int_{1+\varepsilon_j^*}^{\infty}\varpi_{ej}d\xi\right), \qquad \text{(C.22)} \end{aligned}$$

- Front-wakes $(j < i)$

$$\begin{aligned} \fint_{-1+\varepsilon}^{1+\varepsilon^*} (x-\varepsilon_i)\varpi_{seji}(x,t)dx = & -\int_{1+\varepsilon_j^*}^{-1+\varepsilon_i} \left[\sqrt{\frac{\xi+1-\varepsilon_i}{\xi-1-\varepsilon_i^*}}(\xi-1-\varepsilon_i-b_i) + (\xi-\varepsilon_i)\right]\varpi_{ej}(\xi,t)d\xi + \\ & \int_{1+\varepsilon_i^*}^{\infty} \left[\sqrt{\frac{\xi+1-\varepsilon_i}{\xi-1-\varepsilon_i^*}}(\xi-1-\varepsilon_i-b_i) - (\xi-\varepsilon_i)\right]\varpi_{ej}(\xi,t)d\xi, \qquad \text{(C.23)} \end{aligned}$$

$$\fint_{-1+\varepsilon_i}^{1+\varepsilon_i^*}(x-\varepsilon_i)^2\varpi_{seji}(x,t)dx = -\int_{1+\varepsilon_j^*}^{-1+\varepsilon_i}\left[\frac{1}{2}\sqrt{\frac{\xi+1-\varepsilon_i}{\xi-1-\varepsilon_i^*}}+(\xi-\varepsilon_i+b_i)\sqrt{(\xi+1-\varepsilon_i)\left(\xi-1-\varepsilon_i^*\right)}\right.$$
$$\left.+(\xi-\varepsilon_i)^2\right]\varpi_{ej}(\xi,t)d\xi+\int_{1+\varepsilon_i^*}^{\infty}\left[\frac{1}{2}\sqrt{\frac{\xi+1-\varepsilon_i}{\xi-1-\varepsilon_i^*}}+\right.$$
$$\left.(\xi-\varepsilon_i+b_i)\sqrt{(\xi+1-\varepsilon_i)\left(\xi-1-\varepsilon_i^*\right)}-(\xi-\varepsilon_i)^2\right]\varpi_{ej}(\xi,t)d\xi+$$
$$b_i\left(1+\frac{3}{2}b_i\right)\left(\Gamma_{seji}+\int_{1+\varepsilon_i^*}^{\infty}\varpi_{ej}d\xi\right). \tag{C.24}$$

For the case of two airfoils in tandem configuration the integrals associated to ϖ_{12} are the following

$$\fint_{-1+\varepsilon}^{1+\varepsilon}(x-\varepsilon)^n\varpi_{12}(x,t)dx = \Gamma_{01}(t)\mathcal{I}_{\gamma,n}+\dot{\alpha}_1(t)\mathcal{I}_{\gamma\alpha,n}. \tag{C.25}$$

In the case of considering the first oscillating mode some new functions appears:

$$\mathcal{R}_1(k,\varepsilon) := \int_{1-\varepsilon}^{-1}e^{-ik(\xi+\varepsilon)}\xi\sqrt{\xi^2-1}d\xi,\quad \mathcal{R}_2(k,\varepsilon) := \int_{1+\varepsilon}^{\infty}e^{-ik(\xi-\varepsilon)}\xi\sqrt{\xi^2-1}d\xi, \tag{C.26}$$

$$C_2(k) := \frac{H_2^{(2)}(k)}{iH_0^{(2)}(k)+H_1^{(2)}(k)}, \tag{C.27}$$

$$\mathcal{B}_{1\delta}(k,\varepsilon) := \frac{\mathcal{R}_2(k,\varepsilon)}{\mathsf{a}(k,\varepsilon)}-\frac{2i}{\pi}\left\{1+\frac{1}{k^2}\left[2+2i(1+\varepsilon)k-(1+\varepsilon)^2k^2\right]\right\}C(k), \tag{C.28}$$

$$\mathcal{B}_{2\delta}(k,\varepsilon) := \mathcal{Q}_\delta(k,\varepsilon)C_{1e}(k,\varepsilon)-\frac{\mathcal{R}_1(k,\varepsilon)}{\mathsf{a}(k,\varepsilon)}-\frac{i}{\pi}C_1(k), \tag{C.29}$$

$$\mathcal{Q}_\delta := H_2^{(2)}(k)+\frac{2}{k^2}\left[2ik\sin(k)-i\left(k^2-2\right)\cos(k)\right]+$$
$$\frac{ie^{i(\varepsilon-1)k}}{k^2}\Big[(\varepsilon-1)k-1+i\Big]\Big[(\varepsilon-1)k+1+i\Big], \tag{C.30}$$

$$f_{\Gamma\delta} := 2\int_{-1}^{1}\sqrt{\frac{\xi+1-\varepsilon}{\xi-1-\varepsilon}}\xi\sqrt{1-\xi^2}d\xi, \tag{C.31}$$

$$\mathcal{I}_{\gamma\delta,n}(\varepsilon) := \frac{2}{\pi}\int_{-1+\varepsilon}^{1+\varepsilon}(x-\varepsilon)^n\sqrt{\frac{1+\varepsilon-x}{1-\varepsilon+x}}\int_{-1}^{1}\sqrt{\frac{\xi+1-\varepsilon}{\xi-1-\varepsilon}}\frac{\xi\sqrt{1-\xi^2}}{\xi-x}d\xi dx, \tag{C.32}$$

and the integrals associated to ϖ_{12} are the following

$$\fint_{-1+\varepsilon}^{1+\varepsilon}(x-\varepsilon)^n\varpi_{12}(x,t)dx = \Gamma_{01}(t)\mathcal{I}_{\gamma,n}-\mathcal{V}_1(t)\mathcal{I}_{\gamma\alpha,n}-\dot{\mathcal{D}}_1(t)\mathcal{I}_{\gamma\delta,n}. \tag{C.33}$$

The double integral (C.32) can be simplified to a single integral, integrating for x, i.e,

$$I_{\gamma\delta} = 2\int_{-1}^{1}\left(\sqrt{(\xi-\varepsilon)^2-1}+\xi-\varepsilon\right)\xi\sqrt{1-\xi^2}d\xi, \tag{C.34}$$

$$I_{\gamma\delta,2} = 2\int_{-1}^{1}\left(\frac{1}{2}\sqrt{\frac{\xi+1-\varepsilon}{\xi-1-\varepsilon}}+(\xi-\varepsilon)\sqrt{(\xi-\varepsilon)^2-1}+(\xi-\varepsilon)^2\right)\xi\sqrt{1-\xi^2}d\xi, \tag{C.35}$$

$$I_{\gamma\delta,3} = 2\int_{-1}^{1}\left[\sqrt{(\xi-\varepsilon)^2-1}\left(-\frac{1}{2}-(\xi-\varepsilon)^2\right)-(\xi-\varepsilon)^3\right]\xi\sqrt{1-\xi^2}d\xi. \tag{C.36}$$

C.2 LIFT, THRUST, MOMENT AND FLEXURAL COEFFICIENTS FOR TWO AIRFOILS

C.2.1 *Lift coefficient*

$$C_L^{(i)} = \mathcal{L}_0(t) + \Gamma_{01}(t)\mathcal{L}_{01} + \left[\Gamma_{02}(t) + \Gamma_{12}(t)\right]\mathcal{L}_{02}. \tag{C.37}$$

Only $\mathcal{L}_0(t)$ changes considering the first oscillation mode.

- Forewing

$$\mathcal{L}_0(t) = -\pi\left[\dot{\mathcal{U}}_1(t) + \frac{\ddot{\mathcal{D}}_1(t)}{2}\right], \tag{C.38}$$

$$\mathcal{L}_{01} = \mathcal{C}_a + F_c\left[\frac{\mathcal{A}_2}{\mathsf{a}} + \frac{2k}{\pi}\left(1 + \varepsilon - \sqrt{\varepsilon(\varepsilon+2)}\right)C_1\right], \tag{C.39}$$

$$\mathcal{L}_{02} = \mathcal{C}_b + F_a\left[\frac{\mathcal{A}_2}{\mathsf{a}} + \frac{2k}{\pi}\left(1 + \varepsilon - \sqrt{\varepsilon(\varepsilon+2)}\right)C_1\right]. \tag{C.40}$$

- Hindwing

$$\begin{aligned}\mathcal{L}_0(t) = -\pi\Bigg[&\dot{\mathcal{U}}_2(t) + \frac{\ddot{\mathcal{D}}_2(t)}{2} - 2\dot{\mathcal{U}}_1(t)\mathcal{I}_{\gamma,1} - \dot{\mathcal{V}}_1(t)\left(I_{\gamma,1} + \frac{I_{\gamma\alpha,1}}{\pi}\right) - \\ &\ddot{\mathcal{D}}_1(t)\left(I_{\gamma,1} + \frac{I_{\gamma\delta,1}}{\pi}\right)\Bigg],\end{aligned} \tag{C.41}$$

$$\begin{aligned}\mathcal{L}_{01} = \mathcal{C}_c + F_a\Bigg[&-\frac{\mathcal{A}_1}{\mathsf{a}} + \frac{2k}{\pi}\left(1 - \varepsilon + \sqrt{\varepsilon(\varepsilon-2)}\right)C_1 + \\ &\frac{2}{\pi}\left(-i\frac{\pi k}{2}H_0^{(2)}(k) - 2\sin(k) + 2k\cos(k)\right)C_{1e}\Bigg],\end{aligned} \tag{C.42}$$

$$\begin{aligned}\mathcal{L}_{02} = \mathcal{C}_a + F_b\Bigg[&-\frac{\mathcal{A}_1}{\mathsf{a}} + \frac{2k}{\pi}\left(1 - \varepsilon + \sqrt{\varepsilon(\varepsilon-2)}\right)C_1 + \\ &\frac{2}{\pi}\left(-i\frac{\pi k}{2}H_0^{(2)}(k) - 2\sin(k) + 2k\cos(k)\right)C_{1e}\Bigg].\end{aligned} \tag{C.43}$$

C.2.2 *Thrust coefficient*

$$C_T^{(i)} = \mathcal{E}_i C_L^{(i)} + \dot{\mathcal{E}}_i\mathcal{T}_0 + \mathcal{D}_i\mathcal{T}_{\delta 1} + \dot{\mathcal{D}}_i\mathcal{T}_{\delta 2} + \Gamma_{01}\mathcal{T}_{01} + \left[\Gamma_{02} + \Gamma_{12}\right]\mathcal{T}_{02},. \tag{C.44}$$

- Forewing

$$\mathcal{T}_0 = -\pi\left(\mathcal{U}_1 + \frac{\dot{\mathcal{D}}_1}{2}\right), \tag{C.45}$$

$$\mathcal{T}_{\delta 1} = -\frac{\pi}{2}\dot{\mathcal{V}}_1 - \Gamma_{01}\mathcal{T}_{\delta 01} - \left(\Gamma_{02} + \Gamma_{12}\right)\mathcal{T}_{\delta 02}, \tag{C.46}$$

$$\mathcal{T}_{\delta 2} = -\frac{\pi}{2}\mathcal{D}_1, \tag{C.47}$$

$$\begin{aligned}\mathcal{T}_{01} = F_a \Bigg\{ &\left[\dot{\mathcal{D}}_1 \left(\frac{2i}{k^2} - \frac{2+ik}{k}\right) - \frac{1+ik}{k}\mathcal{V}_1 - i\mathcal{U}_1\right] \frac{2}{\pi} F_a \mathcal{C}_1 - \frac{1}{k}\left[\dot{\mathcal{D}}_1 C_2 + i\mathcal{V}_1 C\right] \Bigg\} - \\ &F_c \left(\mathcal{V}_1 \mathcal{B}_1 + \dot{\mathcal{D}}_1 \mathcal{B}_{1\delta}\right),\end{aligned} \tag{C.48}$$

$$\begin{aligned}\mathcal{T}_{02} = F_b \Bigg\{ &\left[\dot{\mathcal{D}}_1 \left(\frac{2i}{k^2} - \frac{2+ik}{k}\right) - \frac{1+ik}{k}\mathcal{V}_1 - i\mathcal{U}_1\right] \frac{2}{\pi} F_a \mathcal{C}_1 - \frac{1}{k}\left[\dot{\mathcal{D}}_1 C_2 + i\mathcal{V}_1 C\right] \Bigg\} - \\ &F_a \left(\mathcal{V}_1 \mathcal{B}_1 + \dot{\mathcal{D}}_1 \mathcal{B}_{1\delta}\right),\end{aligned} \tag{C.49}$$

where the functions $\mathcal{T}_{\delta 01}$ and $\mathcal{T}_{\delta 01}$ are given by

$$\mathcal{T}_{\delta 01} = \mathcal{C}_a - 1 + F_c \left\{ \frac{\mathcal{A}_2}{\mathsf{a}} + \frac{2k}{\pi}\left[1 + 2(1+\varepsilon)\left(\sqrt{\varepsilon(\varepsilon+2)} - (1+\varepsilon)\right)\right] C_1 \right\}, \tag{C.50}$$

$$\mathcal{T}_{\delta 02} = \mathcal{C}_b + F_a \left\{ \frac{\mathcal{A}_2}{\mathsf{a}} + \frac{2k}{\pi}\left[1 + 2(1+\varepsilon)\left(\sqrt{\varepsilon(\varepsilon+2)} - (1+\varepsilon)\right)\right] C_1 \right\}. \tag{C.51}$$

- Hindwing

$$\mathcal{T}_0 = \pi \left[-\mathcal{U}_2 - \frac{\dot{\mathcal{D}}_2}{2} + 2\mathcal{U}_1 \mathcal{I}_{\gamma,1} + \mathcal{V}_1 \left(\mathcal{I}_{\gamma,1} + \frac{\mathcal{I}_{\gamma\alpha,1}}{\pi}\right) + \dot{\mathcal{D}}_1 \left(\mathcal{I}_{\gamma,1} + \frac{\mathcal{I}_{\gamma\delta,1}}{\pi}\right) \right], \tag{C.52}$$

$$\begin{aligned}\mathcal{T}_{\delta 1} = -\frac{\pi}{2}\dot{\mathcal{V}}_2 - 2\pi \Bigg[&\dot{\mathcal{U}}_1 \left(f_\Gamma - 2\mathcal{I}_{\gamma,2}\right) + \dot{\mathcal{V}}_1 \left(\frac{f_\Gamma}{2} + \frac{f_{\Gamma\alpha}}{2\pi} - \mathcal{I}_{\gamma,2} - \frac{\mathcal{I}_{\gamma\alpha,2}}{\pi}\right) + \\ &\ddot{\mathcal{D}}_1 \left(\frac{f_\Gamma}{2} + \frac{f_{\Gamma\delta}}{2\pi} - \mathcal{I}_{\gamma,2} - \frac{\mathcal{I}_{\gamma\delta,2}}{\pi}\right) \Bigg] - \Gamma_{01}\mathcal{T}_{\delta 01} - \left(\Gamma_{02} + \Gamma_{12}\right)\mathcal{T}_{\delta 02},\end{aligned} \tag{C.53}$$

$$\begin{aligned}\mathcal{T}_{\delta 2} = -\pi \Bigg[&\frac{\mathcal{D}_2}{2} + \mathcal{U}_1 \left(f_\Gamma - 2\mathcal{I}_{\gamma,2}\right) + \mathcal{V}_1 \left(\frac{f_\Gamma}{2} + \frac{f_{\Gamma\alpha}}{2\pi} - \mathcal{I}_{\gamma,2} - \frac{\mathcal{I}_{\gamma\alpha,2}}{\pi}\right) + \\ &\dot{\mathcal{D}}_1 \left(\frac{f_\Gamma}{2} + \frac{f_{\Gamma\delta}}{2\pi} - \mathcal{I}_{\gamma,2} - \frac{\mathcal{I}_{\gamma\delta,2}}{\pi}\right) \Bigg],\end{aligned} \tag{C.54}$$

$$\begin{aligned}\mathcal{T}_{01} = F_c \Bigg\{ &\left[\dot{\mathcal{D}}_2 \left(\frac{2i}{k^2} - \frac{2+ik}{k}\right) - \frac{1+ik}{k}\mathcal{V}_2 - i\mathcal{U}_2\right] \frac{2}{\pi} F_a \mathcal{C}_1 - \frac{1}{k}\left[\dot{\mathcal{D}}_2 C_2 + i\mathcal{V}_2 C\right] \Bigg\} - \\ &F_a \left(\mathcal{V}_2 \mathcal{B}_2 + \dot{\mathcal{D}}_2 \mathcal{B}_{2\delta}\right),\end{aligned} \tag{C.55}$$

$$\begin{aligned}\mathcal{T}_{02} = F_a \Bigg\{ &\left[\dot{\mathcal{D}}_2 \left(\frac{2i}{k^2} - \frac{2+ik}{k}\right) - \frac{1+ik}{k}\mathcal{V}_2 - i\mathcal{U}_2\right] \frac{2}{\pi} F_a \mathcal{C}_1 - \frac{1}{k}\left[\dot{\mathcal{D}}_2 C_2 + i\mathcal{V}_2 C\right] \Bigg\} - \\ &F_b \left(\mathcal{V}_2 \mathcal{B}_2 + \dot{\mathcal{D}}_2 \mathcal{B}_{2\delta}\right),\end{aligned} \tag{C.56}$$

where the functions $\mathcal{T}_{\delta 01}$ and $\mathcal{T}_{\delta 01}$ are given by

$$\begin{aligned}\mathcal{T}_{\delta 01} = \mathcal{C}_c + F_a \Bigg\{ &-\frac{\mathcal{A}_1}{\mathsf{a}} + \frac{2k}{\pi}\left[1 - 2(1-\varepsilon)\left(\sqrt{\varepsilon(\varepsilon-2)} + (1-\varepsilon)\right)\right] C_1 + \\ &\frac{2k}{\pi}\left(4i\sin(k) - \frac{\pi}{2} i H_0^{(2)}(k)\right) C_{1e} \Bigg\},\end{aligned} \tag{C.57}$$

$$\begin{aligned}\mathcal{T}_{\delta 02} = \mathcal{C}_a - 1 + F_b \Bigg\{ & -\frac{\mathcal{A}_1}{\mathsf{a}} + \frac{2k}{\pi}\left[1 - 2(1-\varepsilon)\left(\sqrt{\varepsilon(\varepsilon-2)} + (1-\varepsilon)\right)\right] C_1 + \\ & \frac{2k}{\pi}\left(4i\sin(k) - \frac{\pi}{2} i H_0^{(2)}(k)\right) C_{1e}\Bigg\}. \end{aligned} \tag{C.58}$$

C.2.3 *Moment coefficient*

$$C_M^{(i)} = \frac{a_i}{2} C_L^{(i)} + \mathcal{M}_0(t) + \Gamma_{01}\mathcal{M}_{01} + \left[\Gamma_{02}(t) + \Gamma_{12}(t)\right]\mathcal{M}_{02}. \tag{C.59}$$

Only $\mathcal{M}_0(t)$ changes considering the first oscillation mode.

- Forewing

$$\mathcal{M}_0(t) = \frac{\pi}{4}\left(\mathcal{V}_1 + \frac{\dot{\mathcal{V}}_1}{4} + \frac{\dot{\mathcal{D}}_1}{2}\right), \tag{C.60}$$

$$\mathcal{M}_{01} = \frac{1}{4}\left\{\mathcal{C}_a + F_c\left[\frac{\mathcal{A}_2}{\mathsf{a}} + \frac{2k}{\pi}\left(\frac{1}{2} + (1+\varepsilon)\sqrt{\varepsilon(\varepsilon+2)} - (1+\varepsilon)^2\right) C_1\right]\right\}, \tag{C.61}$$

$$\mathcal{M}_{02} = \frac{1}{4}\left\{\mathcal{C}_b + F_a\left[\frac{\mathcal{A}_2}{\mathsf{a}} + \frac{2k}{\pi}\left(\frac{1}{2} + (1+\varepsilon)\sqrt{\varepsilon(\varepsilon+2)} - (1+\varepsilon)^2\right) C_1\right]\right\}. \tag{C.62}$$

- Hindwing

$$\begin{aligned}\mathcal{M}_0(t) = & \frac{\pi}{4}\left(\mathcal{V}_2 + \frac{\dot{\mathcal{V}}_2}{4} + \frac{\dot{\mathcal{D}}_2}{2}\right) + \\ & \frac{1}{2}\left[-\Gamma_{01}\left(\mathcal{I}_{\gamma,1} + \frac{f_\Gamma}{2}\right) + \mathcal{B}_1\left(\mathcal{I}_{\gamma\alpha,1} + \frac{f_{\Gamma\alpha}}{2}\right) + \dot{\mathcal{D}}_1\left(\mathcal{I}_{\gamma\delta,1} + \frac{f_{\Gamma\delta}}{2}\right)\right] + \\ & \frac{1}{4}\left[\dot{\Gamma}_{01}\left(\mathcal{I}_{\gamma,2} - \frac{f_\Gamma}{2}\right) - \dot{\mathcal{B}}_1\left(\mathcal{I}_{\gamma\alpha,2} - \frac{f_{\Gamma\alpha}}{2}\right) - \ddot{\mathcal{D}}_1\left(\mathcal{I}_{\gamma\delta,2} - \frac{f_{\Gamma\delta}}{2}\right)\right], \end{aligned} \tag{C.63}$$

$$\begin{aligned}\mathcal{M}_{01} = \frac{1}{4}\Bigg\{ & \mathcal{C}_c + F_a\Bigg[-\frac{\mathcal{A}_1}{\mathsf{a}} + \frac{2k}{\pi}\left(\frac{1}{2} - (1-\varepsilon)\sqrt{\varepsilon(\varepsilon-2)} - (1-\varepsilon)^2\right) C_1 + \\ & \frac{2k}{\pi}\left(2i\sin(k) - i\frac{\pi}{2} H_0^{(2)}(k)\right) C_{1e}\Bigg]\Bigg\}, \end{aligned} \tag{C.64}$$

$$\begin{aligned}\mathcal{M}_{02} = \frac{1}{4}\Bigg\{ & \mathcal{C}_a + F_b\Bigg[-\frac{\mathcal{A}_1}{\mathsf{a}} + \frac{2k}{\pi}\left(\frac{1}{2} - (1-\varepsilon)\sqrt{\varepsilon(\varepsilon-2)} - (1-\varepsilon)^2\right) C_1 + \\ & \frac{2k}{\pi}\left(2i\sin(k) - i\frac{\pi}{2} H_0^{(2)}(k)\right) C_{1e}\Bigg]\Bigg\}. \end{aligned} \tag{C.65}$$

C.2.4 *Flexural coefficient*

$$C_F^{(i)} = p\left[4C_{Mp}^{(i)} - pC_L^{(i)}\right] + \mathcal{F}_0(t) + \Gamma_{01}(t)\mathcal{F}_{01} + \left[\Gamma_{02}(t) + \Gamma_{12}(t)\right]\mathcal{F}_{02}. \tag{C.66}$$

- Forewing

$$F_0(t) = -\frac{\pi}{4}\left[\dot{\mathcal{U}}_1 - \mathcal{V}_1 + \frac{\ddot{\mathcal{D}}_1}{3}\right], \tag{C.67}$$

$$F_{01} = \frac{1}{2}\left\{\mathcal{C}_a + \frac{\mathcal{A}_2}{\mathsf{a}}F_c + \frac{2}{3}\left[(1+\varepsilon)^3 - \left((1+\varepsilon)^2 + \frac{1}{2}\right)\sqrt{\varepsilon(\varepsilon+2)}\right]\frac{2k}{\pi}C_{1e}F_c\right\}, \tag{C.68}$$

$$F_{02} = \frac{1}{2}\left\{\mathcal{C}_b + \frac{\mathcal{A}_2}{\mathsf{a}}F_a + \frac{2}{3}\left[(1+\varepsilon)^3 - \left((1+\varepsilon)^2 + \frac{1}{2}\right)\sqrt{\varepsilon(\varepsilon+2)}\right]\frac{2k}{\pi}C_{1e}F_a\right\}. \tag{C.69}$$

- Hindwing

$$F_0(t) = -\frac{\pi}{4}\left[\dot{\mathcal{U}}_2 - \mathcal{V}_2 + \frac{\ddot{\mathcal{D}}_2}{3}\right] - \mathcal{V}_1\mathcal{I}_{\gamma\alpha,2} - \dot{\mathcal{D}}_1\mathcal{I}_{\gamma\delta,2} + \frac{\pi}{3}\left[2\dot{\mathcal{U}}_1\mathcal{I}_{\gamma,3} + \dot{\mathcal{V}}_1\left(\mathcal{I}_{\gamma,3} + \frac{\mathcal{I}_{\gamma,3}}{\pi}\right)\right], \tag{C.70}$$

$$\begin{aligned} F_{01} = \frac{1}{2}\Bigg\{&\mathcal{C}_c - \frac{\mathcal{A}_1}{\mathsf{a}}F_a - \left(ikH_0^{(2)}(k) - \frac{8k}{3\pi}\cos(k)\right)C_{1e}F_a + \\ &\frac{2}{3}\left[(1-\varepsilon)^3 + \left((1-\varepsilon)^2 + \frac{1}{2}\right)\sqrt{\varepsilon(\varepsilon-2)}\right]\frac{2k}{\pi}C_1F_a\Bigg\}, \end{aligned} \tag{C.71}$$

$$\begin{aligned} F_{02} = \frac{1}{2}\Bigg\{&\mathcal{C}_a - \frac{\mathcal{A}_1}{\mathsf{a}}F_b - \left(ikH_0^{(2)}(k) - \frac{8k}{3\pi}\cos(k)\right)C_{1e}F_b + \\ &\frac{2}{3}\left[(1-\varepsilon)^3 + \left((1-\varepsilon)^2 + \frac{1}{2}\right)\sqrt{\varepsilon(\varepsilon-2)}\right]\frac{2k}{\pi}C_1F_b\Bigg\}. \end{aligned} \tag{C.72}$$

C.3 TIME-AVERAGED COEFFICIENTS

C.3.1 *Thrust coefficient*

Full expressions for the time-averaged thrust coefficient for two airfoils in tandem configuration are given below. The superscripts R and I denote real and imaginary parts, respectively. The functions F, F_1, F_2 and G, G_1, G_2 are the real and the imaginary parts of the functions $C(k)$, $C_1(k)$ and $C_2(k)$, respectively, given by (C.10) and (A.33). The time-average thrust coefficient can be written in terms of the feathering paremeters as

$$\bar{C}_T^{(i)} = (kh_0)^2\left[t_h + t_{hp}\theta_i + t_p\theta_i^2 + \left(t_{hd} + t_{pd}\theta_i\right)\theta_{di} + t_d\theta_{di}^2\right], \tag{C.73}$$

where the functions t_h, t_{hp}, t_p, t_{hd}, t_{hd} and t_d are given by

$$t_h = F_{t1h} + \Theta_h\left[F_{t2h}\cos(\varphi) + F_{t3h}\sin(\varphi)\right], \tag{C.74}$$

$$t_{hp} = F_{t1hp} + \Theta_h F_{t2hp} + \Theta_a F_{t3hp}, \tag{C.75}$$

$$t_p = F_{t1p} + \Theta_a\left[F_{t2p}\cos(\varphi - \phi_i + \phi_j) + F_{t3p}\sin(\varphi - \phi_i + \phi_j)\right], \tag{C.76}$$

$$t_{hd} = \frac{1}{(1-p_i)^2}\left[F_{t1hd} + \Theta_h F_{t2hd} + \Theta_d F_{t3hd}\left(\frac{1-p_i}{1-p_j}\right)^2\right], \tag{C.77}$$

$$t_{pd} = \frac{1}{(1-p_i)^2}\left[F_{t1pd} + \Theta_a F_{t2pd} + \Theta_d F_{t3pd}\left(\frac{1-p_i}{1-p_j}\right)^2\right], \tag{C.78}$$

$$t_d = \frac{1}{(1-p_i)^4}\left\{F_{t1d} + \Theta_d\left(\frac{1-p_i}{1-p_j}\right)^2\left[F_{t2d}\cos(\varphi-\psi_i+\psi_j) + F_{t3d}\sin(\varphi-\psi_i+\psi_j)\right]\right\}. \tag{C.79}$$

The different functions F_t are specific for each airfoil and are given below.

- Forewing

$$F_{t1h} = -2\left(F_1F_a^I + F_1F_b^I f_\Gamma + F_a^R G_1 + F_b^R f_\Gamma G_1\right), \tag{C.80}$$

$$F_{t2h} = -2\left(F_1F_b^I + F_b^R G_1\right), \quad F_{t3h} = -2\left(F_b^I G_1 - F_1F_b^R\right), \tag{C.81}$$

$$\begin{aligned} F_{t1hp} = & \left\{ \left[4\left(\frac{3}{4}-a_1\right)F_1k + \pi F + 2G_1\right]\left(F_a^I + f_\Gamma F_b^I\right) + \frac{kf_{\Gamma\alpha}}{\pi}\left(G_1F_b^R + F_1F_b^I\right) \right. \\ & \left[4\left(\frac{3}{4}-a_1\right)G_1k - 2F_1 + \pi G\right]\left(F_a^R + f_\Gamma F_b^R\right) + \\ & \left. \pi\left[k\mathcal{B}_{01}^I\left(f_\Gamma F_a^I + F_c^I\right) - k\mathcal{B}_1^R\left(f_\Gamma F_a^R + F_c^R\right) - f_\Gamma\mathcal{L}_{02}^I - \mathcal{L}_1^I\right] \right\}\cos(\phi_1) + \\ & \left\{ (6F_1 - G_1k - \pi G)\left(F_a^I + f_\Gamma F_b^I\right) + (F_1k + \pi F + 6G_1)\left(F_a^R + f_\Gamma F_b^R\right) + \right. \\ & \pi\left[k\mathcal{B}_1^I\left(f_\Gamma F_a^R + F_c^R\right) + k\mathcal{B}_1^R\left(f_\Gamma F_a^I + F_c^I\right) + f_\Gamma\mathcal{L}_{02}^R + \mathcal{L}_{01}^R\right] + \\ & \left. \frac{kf_{\Gamma\alpha}}{\pi}\left(G_1F_b^I - F_1F_b^R\right) \right\}\sin(\phi_1), \end{aligned} \tag{C.82}$$

$$\begin{aligned} F_{t2hp} = & \left[\pi\left(k\mathcal{B}_{01}^I F_a^I - k\mathcal{B}_{01}^R F_a^R + GF_b^R + FF_b^I - \mathcal{L}_{02}^I\right) + 2(1-a_1)k\left(G_1F_b^R + F_1F_b^I\right) + \right. \\ & \left. 4\left(G_1F_b^I - F_1F_b^R\right)\right]\cos(\varphi - \phi_1) + \\ & \left[\pi\left(-k\mathcal{B}_1^I F_a^R - k\mathcal{B}_1^R F_a^I + GF_b^I - FF_b^R - \mathcal{L}_{02}^R\right) + 2(1-a_1)k\left(G_1F_b^I - F_1F_b^R\right) - \right. \\ & \left. 4\left(G_1F_b^R + F_1F_b^I\right)\right]\sin(\varphi - \phi_1), \end{aligned} \tag{C.83}$$

$$\begin{aligned} F_{t3hp} = & 2\left[\left(\frac{1}{2}-a_2\right)k\left(G_1F_b^R + F_1F_b^I\right) - G_1F_b^I + F_1F_b^R\right]\cos(\varphi + \phi_2) + \\ & 2\left[\left(\frac{1}{2}-a_2\right)k\left(G_1F_b^I - F_1F_b^R\right) + G_1F_b^R + F_1F_b^I\right]\sin(\varphi + \phi_2), \end{aligned} \tag{C.84}$$

$$
\begin{aligned}
F_{t1p} = &\Bigg\{\pi\left[G-\left(\frac{1}{2}-a_1\right)Fk\right]-2F_1\left[(1-a_1)\left(\frac{1}{2}-a_1\right)k^2+2\right]+2a_1G_1k\Bigg\}\left(F_a^I+f_\Gamma F_b^I\right)- \\
&\Bigg\{\pi\left[\left(\frac{1}{2}-a_1\right)Gk+F\right]+2a_1F_1k+2G_1\left[(1-a_1)\left(\frac{1}{2}-a_1\right)k^2+2\right]\Bigg\}\left(F_a^R+f_\Gamma F_b^R\right)+ \\
&\frac{kf_{\Gamma\alpha}}{\pi}\Bigg[\frac{1}{2}\pi\left(k\mathcal{B}_1^I F_a^i-k\mathcal{B}_1^R F_a^R+GF_b^R+FF_b^I-\mathcal{L}_{02}^I\right)+(1-a_1)\,k\left(G_1F_b^R+F_1F_b^I\right)+ \\
&2\left(G_1F_b^I-F_1F_b^R\right)\Bigg]+\pi\Bigg\{k\left[\left(\frac{1}{2}-a_1\right)k\mathcal{B}_1^I+\mathcal{B}_1^R\right]\left(f_\Gamma F_a^I+F_c^I\right)+f_\Gamma\mathcal{L}_{02}^R+\mathcal{L}_{01}^R+ \\
&k\left[\mathcal{B}_1^I-\left(\frac{1}{2}-a_1\right)k\mathcal{B}_1^R\right]\left(f_\Gamma F_a^R+F_c^R\right)-\left(\frac{1}{2}-a_1\right)k\left(f_\Gamma\mathcal{L}_{02}^I+\mathcal{L}_{01}^I\right)\Bigg\},
\end{aligned}
\tag{C.85}
$$

$$
\begin{aligned}
F_{t2p} = &\pi\Bigg[\left(\frac{1}{2}-a_2\right)k\left(-k\mathcal{B}_1^I F_a^I+k\mathcal{B}_1^R F_a^R-GF_b^R-FF_b^I+\mathcal{L}_{02}^I\right)-k\mathcal{B}_1^I F_a^R-k\mathcal{B}_1^R F_a^I+ \\
&GF_b^I-FF_b^R-\mathcal{L}_{02}^R\Bigg]-\left[2\,(1-a_1)\left(\frac{1}{2}-a_2\right)k^2+4\right]\left(G_1F_b^R+F_1F_b^I\right)+ \\
&2\,(a_1-2a_2)\,k\left(F_1F_b^R-G_1F_b^I\right),
\end{aligned}
\tag{C.86}
$$

$$
\begin{aligned}
F_{t3p} = &\pi\Bigg[\left(\frac{1}{2}-a_2\right)k\left(k\mathcal{B}_1^I F_a^R+k\mathcal{B}_1^R F_a^I-GF_b^I+FF_b^R+\mathcal{L}_{02}^R\right)-k\mathcal{B}_1^I F_a^I+k\mathcal{B}_1^R F_a^R- \\
&GF_b^R-FF_b^I+\mathcal{L}_{02}^I\Bigg]+\left[2\,(1-a_1)\left(\frac{1}{2}-a_2\right)k^2+4\right]\left(F_1F_b^R-G_1F_b^i\right)+ \\
&2\,(a_1-2a_2)\,k\left(G_1F_b^R+F_1F_b^I\right),
\end{aligned}
\tag{C.87}
$$

$$
\begin{aligned}
F_{t1hd} = &\Bigg\{2\pi(f_\Gamma F_a^R+F_c^R)\left[\mathcal{B}_1^I+k\left(\frac{\mathcal{B}_{1\delta}^R}{2}-p_1\mathcal{B}_1^R\right)\right]-\frac{2F_b^I}{\pi}\left[F_1k\left(\frac{f_{\Gamma\delta}}{2}-p_1f_{\Gamma\alpha}\right)-G_1f_{\Gamma\alpha}\right]- \\
&\frac{2F_b^R}{\pi}\left[F_1f_{\Gamma\alpha}+G_1k\left(\frac{f_{\Gamma\delta}}{2}-p_1f_{\Gamma\alpha}\right)\right]+2\pi(f_\Gamma F_a^I+F_c^I)\left[B_1^R-k\left(\frac{\mathcal{B}_\delta^I}{2}-p_1\mathcal{B}_1^I\right)\right]- \\
&2\pi\left[p_1\left(f_\Gamma\mathcal{L}_{02}^I+\mathcal{L}_{01}^I\right)+\frac{1}{2}\left(f_\Gamma T_{\delta02}^I+T_{\delta01}^I\right)\right]+2\pi(F_a^R+f_\Gamma F_b^R)\left(\frac{F}{k}+\frac{F_2}{2}+Gp_1\right)+ \\
&6k\left(1-\frac{2p_1}{3}\right)\left[(F_a^R+f_\Gamma F_b^R)\left(\frac{F_1}{k}+G_1p_1\right)-(F_a^I+f_\Gamma F_b^I)\left(\frac{G_1}{k}-F_1p_1\right)\right]+ \\
&\left(\frac{8}{k}-3k\right)\left[F_1(F_a^I+f_\Gamma F_b^I)+G_1(F_a^R+f_\Gamma F_b^R)\right]- \\
&2\pi(F_a^I+f_\Gamma F_b^I)\left(-Fp_1+\frac{G}{k}+\frac{G_2}{2}\right)\Bigg\}\cos\left(\psi_1\right)+ \\
&\Bigg\{2\pi(f_\Gamma F_a^R+F_c^R)\left[\mathcal{B}_1^R-k\left(\frac{\mathcal{B}_{1\delta}^I}{2}-p_1\mathcal{B}_1^I\right)\right]-\frac{2F_b^I}{\pi}\left[F_1f_{\Gamma\alpha}+G_1k\left(\frac{f_{\Gamma\delta}}{2}-p_1f_{\Gamma\alpha}\right)\right]+ \\
&\frac{2F_b^R}{\pi}\left[F_1k\left(\frac{f_{\Gamma\delta}}{2}-p_1f_{\Gamma\alpha}\right)-G_1f_{\Gamma\alpha}\right]-2\pi(f_\Gamma F_a^I+F_c^I)\left[\mathcal{B}_1^I+k\left(\frac{\mathcal{B}_\delta^R}{2}-p_1\mathcal{B}_1^R\right)\right]+ \\
&2\pi\left[p_1\left(f_\Gamma\mathcal{L}_2^R+\mathcal{L}_1^R\right)+\frac{1}{2}\left(f_\Gamma\mathcal{T}_{\delta02}^R+T_{\delta01}^R\right)\right]-2\pi(F_a^R+f_\Gamma F_b^R)\left(-Fp_1+\frac{G}{k}+\frac{G_2}{2}\right)+
\end{aligned}
$$

$$\begin{aligned}
&\left[\frac{8}{k} - 2k\left(\frac{1}{2} - p_1\right)\right]\left[F_1(F_a^R + f_\Gamma F_b^R) - G_1(F_a^I + f_\Gamma F_b^I)\right] - \\
&10\left(1 - \frac{6p_1}{5}\right)\left(F_1(F_a^I + f_\Gamma F_b^I) + G_1(F_a^R + f_\Gamma F_b^R)\right) - \\
&\left.2\pi(F_a^I + f_\Gamma F_b^I)\left(\frac{F}{k} + \frac{F_2}{2} + Gp_1\right)\right\}\sin\left(\psi_1\right),
\end{aligned} \tag{C.88}$$

$$\begin{aligned}
F_{t2hd} =& \left\{2\pi F_a^I\left[\mathcal{B}_1^R - k\left(\frac{\mathcal{B}_{1\delta}^i}{2} - p_1\mathcal{B}_1^i\right)\right] + 2\pi F_a^R\left[\mathcal{B}_1^I + k\left(\frac{\mathcal{B}_{1\delta}^R}{2} - p_1\mathcal{B}_1^R\right)\right] + \right.\\
&2\left(\frac{4}{k} - k\left(p_1 - 1\right)^2\right)\left(G_1F_b^R + F_1F_b^I\right) + 2\pi F_b^I\left(Fp_1 - \frac{G}{k} - \frac{G_2}{2}\right) + \\
&8\left(p_1 - 1\right)\left(G_1F_b^I - F_1F_b^R\right) + 2\pi F_b^R\left(\frac{F}{k} + \frac{F_2}{2} + Gp_1\right) - \\
&\left.\pi\left(2p_1\mathcal{L}_{02}^I + \mathcal{T}_{\delta 02}^I\right)\right\}\cos\left(\varphi - \psi_1\right) + \\
&\left\{2\pi F_a^I\left[\mathcal{B}_1^I + k\left(\frac{\mathcal{B}_{1\delta}^R}{2} - p_1\mathcal{B}_1^R\right)\right] + 2\pi F_a^R\left(k\left(\frac{\mathcal{B}_{1\delta}^I}{2} - p_1B_1^I\right) - \mathcal{B}_1^R\right) + \right.\\
&2\left(\frac{4}{k} - k\left(p_1 - 1\right)^2\right)\left(G_1F_b^I - F_1F_b^R\right) + 2\pi F_b^I\left(\frac{F}{k} + \frac{F_2}{2} + Gp_1\right) - \\
&8\left(p_1 - 1\right)\left(G_1F_b^R + F_1F_b^i\right) + 2\pi F_b^R\left(-Fp_1 + \frac{G}{k} + \frac{G_2}{2}\right) - \\
&\left.\pi\left(2p_1\mathcal{L}_{02}^R + \mathcal{T}_{\delta 02}^R\right)\right\}\sin\left(\theta - \psi_1\right),
\end{aligned} \tag{C.89}$$

$$\begin{aligned}
F_{t3hd} =& \left[4\left(\frac{1}{2} - p_2\right)\left(G_1F_b^I - F_1F_b^R\right) - 2k\left(\left(p_2 - 1\right)p_2 + \frac{1}{2}\right)\left(G_1F_b^R + F_1F_b^I\right)\right]\cos\left(\varphi + \psi_2\right) + \\
&\left[2k\left(\left(p_2 - 1\right)p_2 + \frac{1}{2}\right)\left(F_1F_b^R - G_1F_b^I\right) - 4\left(\frac{1}{2} - p_2\right)\left(G_1F_b^R + F_1F_b^I\right)\right]\sin\left(\varphi + \psi_2\right),
\end{aligned} \tag{C.90}$$

$$F_{t1pd} = F_{t1pd,1}\cos(\phi_1 - \psi_1) + F_{t1pd,2}\sin(\phi_1 - \psi_1), \tag{C.91}$$

$$
\begin{aligned}
F_{t1pd,1} = & k\Bigg\{ \left[\frac{Ff_{\Gamma\delta}}{2} + 2f_{\Gamma\alpha}\left(\frac{G_2}{4} - Fp_1\right)\right] F_b^I + \left[\frac{Gf_{\Gamma\delta}}{2} - 2f_{\Gamma\alpha}\left(\frac{F_2}{4} + Gp_1\right)\right] F_b^R + \\
& k\pi\left(\frac{1}{2} - a_1\right)\left[(f_\Gamma F_a^I + F_c^I)\mathcal{B}_{1\delta}^I - (f_\Gamma F_a^R + F_c^R)\mathcal{B}_{1\delta}^R\right] + \frac{2}{\pi}\left(F_b^I G_1 - F_1 F_b^R\right) \times \\
& \Bigg[f_{\Gamma\delta} + 4f_{\Gamma\alpha}\left(\frac{1}{4}(a_1+1) - p_1\right)\Bigg] + \frac{k}{\pi}\left(F_1 F_b^I + G_1 F_b^R\right)\Bigg[2\left(a_1 + \frac{p_1}{2} - 2\right)p_1 f_{\Gamma\alpha} + \\
& f_{\Gamma\alpha} + (1-a_1)f_{\Gamma\delta}\Bigg] + 2\pi\left[(f_\Gamma F_a^R + F_c^R)\mathcal{B}_1^I + (f_\Gamma F_a^I + F_c^I)\mathcal{B}_1^R\right](a_1 - 2p_1) + \\
& 2\left(k\mathcal{B}_1^I F_a^i - k\mathcal{B}_1^R F_a^R - \mathcal{L}_2^I\right)\left(\frac{f_{\Gamma\delta}}{4} - f_{\Gamma\alpha}p_1\right) + 2\left[(F_a^I + f_\Gamma F_b^I)G_1 - (F_a^R + f_\Gamma F_b^R)F_1\right] \times \\
& \left(p_1^2 + 2a_1p_1 - 3a_1 + \frac{4}{k^2} + 1\right) + \pi\Bigg[- \mathcal{L}_1^I - f_\Gamma\mathcal{L}_2^I + k\big[(f_\Gamma F_a^I + F_c^I)\mathcal{B}_1^I - \\
& (f_\Gamma F_a^R + F_c^R)\mathcal{B}_1^R\big]\Bigg]\left(p_1(2a_1 + p_1 - 2) + \frac{1}{2}\right) + \pi(F_a^I + f_\Gamma F_b^I)\Bigg[\frac{2F}{k^2} + \frac{F_2}{k} + \frac{4Gp_1}{k} + \\
& \frac{1}{2}(2(p_1-2)p_1F + F + G_2) - a_1\left(\frac{2G}{k} + G_2 - 2Fp_1\right)\Bigg] + \pi(F_a^R + f_\Gamma F_b^R) \times \\
& \left[\frac{2G}{k^2} + \frac{G_2}{k} + a_1\left(\frac{2F}{k} + F_2 + 2Gp_1\right) + \frac{1}{2}(2(p_1-2)p_1G + G - F_2) - \frac{4Fp_1}{k}\right] + \\
& \left[(F_a^I + f_\Gamma F_b^I)F_1 + (F_a^R + f_\Gamma F_b^R)G_1\right]\Bigg[-4\left(1 - \frac{3p_1}{4}\right)p_1k + 2k + a_1\Bigg(- 4kp_1^2 - \\
& 6k\left(\frac{1}{2} - p_1\right) + \frac{8}{k}\Bigg) + \frac{16}{k}\left(\frac{1}{2} - p_1\right)\Bigg] + f_{\Gamma\alpha}\left[\frac{L_2^R}{k} + \frac{1}{2}\left(k\mathcal{B}_\delta^I F_a^I - k\mathcal{B}_{1\delta}^R F_a^R + \mathcal{T}_{\delta02}^I\right)\right] + \\
& \Bigg[(f_\Gamma F_a^R + F_c^R)\mathcal{B}_{1\delta}^I + (f_\Gamma F_a^I + F_c^I)\mathcal{B}_{1\delta}^R + \left(\frac{1}{2} - a_1\right)\left(\mathcal{T}_{\delta01}^I + f_\Gamma\mathcal{T}_{\delta02}^I\right) + \frac{1}{k}\Bigg(- \mathcal{T}_{\delta01}^R - \\
& f_\Gamma\mathcal{T}_{\delta02}^R + 2\left[(f_\Gamma F_a^I + F_c^I)\mathcal{B}_1^I - (f_\Gamma F_a^R + F_c^R)\mathcal{B}_1^R\right] + \\
& 4\left(\mathcal{L}_1^R + f_\Gamma\mathcal{L}_2^R\right)\left(\frac{1}{4} - p_1\right)\Bigg) - \frac{k}{8}\Bigg]\pi\Bigg\},
\end{aligned}
\tag{C.92}
$$

$$
\begin{aligned}
F_{t1pd,2} = & k\Bigg\{\pi k\left[p_1(p_1 - 2a_1) + \frac{1}{2}\right]\Bigg[(f_\Gamma F_a^R + F_c^R)\mathcal{B}_1^I + (f_\Gamma F_a^I + F_c^I)B_1^R + \\
& \frac{1}{k}\left(f_\Gamma\mathcal{L}_2^R + F(F_a^R + f_\Gamma F_b^R) - G(F_a^I + f_\Gamma F_b^I) + \mathcal{L}_1^R\right)\Bigg] - \pi\left(\frac{1}{2} - a_1\right)k\Bigg[(f_\Gamma F_a^R + F_c^R)\mathcal{B}_{1\delta}^I + \\
& (f_\Gamma F_a^I + F_c^I)\mathcal{B}_{1\delta}^R + \frac{1}{k}\left(-f_\Gamma\mathcal{T}_{\delta02}^R + F_2(F_a^I + f_\Gamma F_b^I) + G_2(F_a^R + f_\Gamma F_b^R) - \mathcal{T}_{\delta01}^R\right)\Bigg] + \\
& 2\pi(1-a_1)\left[(f_\Gamma F_a^R + F_c^R)\mathcal{B}_1^R - (f_\Gamma F_a^I + F_c^I)\mathcal{B}_1^I - \frac{F(F_a^I + f_\Gamma F_b^I) + G(F_a^R + f_\Gamma F_b^R)}{k}\right] + \\
& \frac{1}{\pi}\left(F_1F_b^R - G_1F_b^I\right)\left[(1-a_1)kf_{\Gamma\delta} + f_{\Gamma\alpha}\left(\frac{8}{k} - k\left(-2a_1p_1 + p_1^2 + 1\right)\right)\right] + \\
& \frac{2}{\pi}\left[3\left(\frac{a_1}{3} - 1\right)f_{\Gamma\alpha} + f_{\Gamma\delta}\right]\left(G_1F_b^R + F_1F_b^I\right) + \frac{f_{\Gamma\delta}}{2}\left[k\left(\mathcal{B}_1^I F_a^R + \mathcal{B}_1^R F_a^I\right) + \mathcal{L}_2^R\right] +
\end{aligned}
$$

$$
\begin{aligned}
& f_{\Gamma\alpha} \Biggl[-F_a^I \left(2\mathcal{B}_1^I + \frac{k\mathcal{B}_{1\delta}^R}{2} \right) + F_a^R \left(2\mathcal{B}_1^R - \frac{k\mathcal{B}_{1\delta}^I}{2} \right) + \frac{\mathcal{L}_2^I}{k} + \frac{\mathcal{T}_{\delta 02}^R}{2} \Biggr] + \\
& k \left[a_1 \left(-\frac{8}{k^2} - 2p_1 + 1 \right) + p_1^2 \right] \Bigl(F_1 (F_a^R + f_\Gamma F_b^R) - G_1 (F_a^I + f_\Gamma F_b^I) \Bigr) - \\
& 2 \left(a_1 \left(6p_1 - 5 \right) + \frac{4}{k^2} - 3p_1^2 + 1 \right) \Bigl(F_1 (F_a^I + f_\Gamma F_b^I) + G_1 (F_a^R + f_\Gamma F_b^R) \Bigr) + \\
& \pi \Biggl[\frac{1}{k} \Biggl(-2 \Bigl((f_\Gamma F_a^R + F_c^R) \mathcal{B}_1^I + (f_\Gamma F_a^I + F_c^I) \mathcal{B}_1^R \Bigr) + f_\Gamma \mathcal{L}_2^I + f_\Gamma \mathcal{T}_{\delta 02}^I - \\
& (F_a^R + f_\Gamma F_b^R) \left(\frac{2F}{k} + F_2 \right) + (F_a^I + f_\Gamma F_b^I) \left(\frac{2G}{k} + G_2 \right) + \mathcal{L}_1^I + \mathcal{T}_{\delta 01}^I \Biggr) - \\
& (f_\Gamma F_a^R + F_c^R) \mathcal{B}_{1\delta}^R + (f_\Gamma F_a^I + F_c^I) \mathcal{B}_{1\delta}^I \Biggr] - F_b^I \left[2 f_{\Gamma\alpha} \left(\frac{F}{k} + \frac{F_2}{4} \right) + \frac{G f_{\Gamma\delta}}{2} \right] + \\
& F_b^R \left[\frac{F f_{\Gamma\delta}}{2} - 2 f_{\Gamma\alpha} \left(\frac{G}{k} + \frac{G_2}{4} \right) \right] \Biggr\},
\end{aligned}
\tag{C.93}
$$

$$
\begin{aligned}
F_{t2pd} = & k \Biggl\{ 2\pi \left(\frac{1}{2} - p_2 \right) \left[\mathcal{B}_1^I F_a^R + \mathcal{B}_1^R F_a^I + \frac{1}{k} \left(-G F_b^I + F F_b^R + \mathcal{L}_2^R \right) \right] + \\
& \pi \left[\left(p_2 - 1 \right) p_2 + \frac{1}{2} \right] \left(k\mathcal{B}_1^I F_a^I - k\mathcal{B}_1^R F_a^R + G F_b^R + F F_b^I - \mathcal{L}_2^I \right) + \\
& 2 \left[\frac{4}{k} \left(\frac{1}{2} - p_2 \right) - \left(a_1 - 1 \right) k \left(\left(p_2 - 1 \right) p_2 + \frac{1}{2} \right) \right] \left(G_1 F_b^R + F_1 F_b^I \right) + \\
& 4 \left[a_1 \left(\frac{1}{2} - p_2 \right) + p_2^2 \right] \left(G_1 F_b^I - F_1 F_b^R \right) \Biggr\} \cos \left(\varphi + \psi_2 - \phi_1 \right) - \\
& k \Biggl\{ 2\pi \left(\frac{1}{2} - p_2 \right) \left[-\mathcal{B}_1^I F_a^i + \mathcal{B}_1^R F_a^R + \frac{1}{k} \left(-G F_b^R - F F_b^i + \mathcal{L}_2^I \right) \right] + \\
& \pi \left(\left(p_2 - 1 \right) p_2 + \frac{1}{2} \right) \left(k\mathcal{B}_1^I F_a^R + k\mathcal{B}_1^R F_a^I - G F_b^I + F F_b^R + \mathcal{L}_2^R \right) + \\
& 2 \left[\frac{4}{k} \left(\frac{1}{2} - p_2 \right) - \left(a_1 - 1 \right) k \left(\left(p_2 - 1 \right) p_2 + \frac{1}{2} \right) \right] \left(F_1 F_b^R - G_1 F_b^I \right) + \\
& 4 \left[a_1 \left(\frac{1}{2} - p_2 \right) + p_2^2 \right] \left(G_1 F_b^R + F_1 F_b^I \right) \Biggr\} \sin \left(\varphi + \psi_2 - \phi_1 \right),
\end{aligned}
\tag{C.94}
$$

$$
F_{t3pd} = F_{t3pd,1} \cos \left(\varphi - \psi_1 + \phi_2 \right) + F_{t3pd,2} \sin \left(\varphi - \psi_1 + \phi_2 \right), \tag{C.95}
$$

$$\begin{aligned}
F_{t3pd,1} =& k\biggl\{2\pi\biggl[\frac{1}{k}\left(\mathcal{B}_1^I F_a^I - \mathcal{B}_1^R F_a^R + F_b^I\left(\frac{F_2}{2} + Gp_1\right) + F_b^R\left(-Fp_1 + \frac{G}{k} + \frac{G_2}{2}\right)\right) - p_1\mathcal{B}_1^I F_a^R - \\
& p_1\mathcal{B}_1^R F_a^I + \frac{1}{2}\left(F_a^R\mathcal{B}_{1\delta}^I + F_a^I\mathcal{B}_{1\delta}^R\right) + \frac{FF_b^I}{k^2}\biggr] + 2\pi\left(\frac{1}{2} - a_2\right)\biggl[F_a^I\left(\frac{k\mathcal{B}_{1\delta}^I}{2} - kp_1\mathcal{B}_1^I - \mathcal{B}_1^R\right) + \\
& F_a^R\left(-\mathcal{B}_1^I + kp_1\mathcal{B}_1^R - \frac{k\mathcal{B}_{1\delta}^R}{2}\right) + F_b^I\left(-Fp_1 + \frac{G}{k} + \frac{G_2}{2}\right) - F_b^R\left(\frac{F}{k} + \frac{F_2}{2} + Gp_1\right) + \\
& p_1\mathcal{L}_2^I + \frac{\mathcal{T}_{\delta 02}^I}{2}\biggr] + 2\left[(p_1 - 1)(4a_2 - p_1 - 1) + \frac{4}{k^2}\right]\left(G_1F_b^I - F_1F_b^R\right) + \\
& 2\left[\left(\frac{1}{2} - a_2\right)k(p_1 - 1)^2 + \frac{4\left(a_2 + \frac{1}{2}\right)}{k} - \frac{4p_1}{k}\right]\left(G_1F_b^R + F_1F_b^I\right) + \\
& \frac{2\pi}{k}\left(-p_1\mathcal{L}_2^R - \frac{\mathcal{T}_{\delta 02}^R}{2}\right)\biggr\},
\end{aligned} \tag{C.96}$$

$$\begin{aligned}
F_{t3pd,2} =& k\biggl\{2\pi\left(\frac{1}{2} - a_2\right)\biggl[F_a^I\left(\mathcal{B}_1^I - kp_1\mathcal{B}_1^R + \frac{k\mathcal{B}_{1\delta}^R}{2}\right) - F_a^R\left(-\frac{k\mathcal{B}_{1\delta}^I}{2} + kp_1\mathcal{B}_1^I + \mathcal{B}_1^R\right) + \\
& F_b^I\left(\frac{F}{k} + \frac{F_2}{2} + Gp_1\right) + F_b^R\left(-Fp_1 + \frac{G}{k} + \frac{G_2}{2}\right) - p_1\mathcal{L}_2^R - \frac{\mathcal{T}_{\delta 02}^R}{2}\biggr] + \\
& 2\left[(p_1 - 1)(4a_2 - p_1 - 1) + \frac{4}{k^2}\right]\left(G_1F_b^R + F_1F_b^I\right) + \\
& 2\left[\left(\frac{1}{2} - a_2\right)k(p_1 - 1)^2 + \frac{4\left(a_2 + \frac{1}{2}\right)}{k} - \frac{4p_1}{k}\right]\left(F_1F_b^R - G_1F_b^I\right) + \\
& \pi F_a^I\left(-\mathcal{B}_{1\delta}^I + 2p_1\mathcal{B}_1^I + \frac{2\mathcal{B}_1^R}{k}\right) + \pi F_a^R\left(\frac{2\mathcal{B}_1^I}{k} - 2p_1\mathcal{B}_1^R + \mathcal{B}_{1\delta}^R\right) + \\
& \frac{\pi}{k}F_b^I\left(2Fp_1 - \frac{2G}{k} - G_2\right) + \frac{\pi}{k}F_b^R\left(\frac{2F}{k} + F_2 + 2Gp_1\right) + \frac{2\pi}{k}\left(-p_1\mathcal{L}_2^I - \frac{\mathcal{T}_{\delta 02}^I}{2}\right)\biggr\},
\end{aligned} \tag{C.97}$$

$$\begin{aligned}
F_{t1d} =& Ff_{\Gamma\delta}F_b^R - f_{\Gamma\delta}\left(-kF_a^R\mathcal{B}_1^I - kF_a^I\mathcal{B}_1^R + GF_b^I\right) - f_{\Gamma\alpha}\left(kF_a^R\mathcal{B}_{1\delta}^I + kF_a^I\mathcal{B}_{1\delta}^R + F_2F_b^I\right) + \\
& \frac{8}{\pi}\left(\frac{f_{\Gamma\delta}}{2} - f_{\Gamma\alpha}\right)\left(F_1F_b^I + G_1F_b^R\right) + 2\biggl\{2\pi\biggl[-\frac{\mathcal{T}_{\delta 01}^R}{2} - f_\Gamma\left(p_1\mathcal{L}_2^R + \frac{\mathcal{T}_{\delta 02}^R}{2}\right) + \\
& \left(\mathcal{B}_1^I + \frac{k\mathcal{B}_{1\delta}^R}{2}\right)\left(f_\Gamma F_a^I + F_c^I\right) + \left(\frac{k\mathcal{B}_{1\delta}^I}{2} - \mathcal{B}_1^R\right)\left(f_\Gamma F_a^R + F_c^R\right)\biggr] + \\
& \frac{1}{k}\left[2\pi\left(G + \frac{kG_2}{2}\right) - 8F_1\right]\left(F_a^R + f_\Gamma F_b^R\right) + \frac{1}{k}\left(F_a^I + f_\Gamma F_b^I\right)\left[2\pi\left(F + \frac{kF_2}{2}\right) + 8G_1\right] + \\
& \pi\left(k\mathcal{L}_1^I - 2\mathcal{L}_1^R\right)p_1\biggr\}\left(p_1 - \frac{1}{2}\right) + 2\biggl\{k\left[F_1\left(F_a^I + f_\Gamma F_b^I\right) + \left(F_a^R + f_\Gamma F_b^R\right)G_1\right](p_1 - 1)^2 +
\end{aligned}$$

$$
\begin{aligned}
&\left[\frac{\mathcal{T}^I_{\delta 01}}{2} + \left(p_1 \mathcal{L}^I_2 + \frac{\mathcal{T}^I_{\delta 02}}{2}\right) f_\Gamma - \left(F^R_a + f_\Gamma F^R_b\right)\left(\frac{F_2}{2} + G p_1\right) + k\left(f_\Gamma F^R_a + F^R_c\right) \times\right.\\
&\left.\left(\mathcal{B}^R_1 p_1 - \frac{\mathcal{B}^R_{1\delta}}{2}\right) + \left(F^I_a + f_\Gamma F^I_b\right)\left(\frac{G_2}{2} - F p_1\right) + k\left(f_\Gamma F^I_a + F^I_c\right)\left(\frac{\mathcal{B}^I_{1\delta}}{2} - \mathcal{B}^I_1 p_1\right)\right]\pi \Bigg\} \times\\
&k\left[(1-p_1)\,p_1 - \frac{1}{2}\right] + 8\left[F_1\left(F^I_a + f_\Gamma F^I_b\right) + \left(F^R_a + f_\Gamma F^R_b\right) G_1\right]\left[(2-p_1)\,p_1 - \frac{1}{2}\right] +\\
&2k\left[F_1\left(F^R_a + f_\Gamma F^R_b\right) - \left(F^I_a + f_\Gamma F^I_b\right) G_1\right](1-p_1)\left[1 - 2\left(\frac{1}{2} - p_1\right) p_1\right] +\\
&2\pi\left[-G\left(F^I_a + f_\Gamma F^I_b\right) + F\left(F^R_a + f_\Gamma F^R_b\right) + \left(f_\Gamma F^R_a + F^R_c\right) k\mathcal{B}^I_1 + \left(f_\Gamma F^I_a + F^i_c\right) k\mathcal{B}^R_1\right] \times\\
&\left(\frac{1}{2} - p_1^2\right) - k\pi p_1\left(2p_1^2 \mathcal{L}^I_1 + \frac{k}{4}\right) + \frac{1}{\pi}\left(F_1 F^R_b - F^I_b G_1\right)\left[\frac{8 f_{\Gamma\alpha}}{k} + 2k\,(p_1 - 1) \times\right.\\
&\left.(3p_1 f_{\Gamma\alpha} + f_{\Gamma\alpha} - 2 f_{\Gamma\delta})\right] + \left(k\mathcal{B}^I_1 F^I_a - k\mathcal{B}^R_1 F^R_a + F F^I_b + G F^R_b\right)\left[k f_{\Gamma\delta} p_1 - 2 f_{\Gamma\alpha}\left(k p_1^2 + \frac{1}{k}\right)\right] +\\
&k\left(f_{\Gamma\alpha} p_1 - \frac{f_{\Gamma\delta}}{2}\right)\left[k\mathcal{B}^I_{1\delta} F^I_a - k\mathcal{B}^R_{1\delta} F^R_a + \mathcal{T}^I_{\delta 02} - F_2 F^R_b + \frac{2k\left(F_1 F^I_b + G_1 F^R_b\right)(p_1 - 1)^2}{\pi} +\right.\\
&\left.F^I_b G_2 + 2\mathcal{L}^I_2 p_1\right] + f_{\Gamma\alpha}\left(\mathcal{T}^R_{\delta 02} - F^R_b G_2 + 2\mathcal{L}^R_2 p_1\right),
\end{aligned} \tag{C.98}
$$

$$
\begin{aligned}
F_{t2d} = {}&\left[(p_2 - 1)\,p_2 + \frac{1}{2}\right]\Bigg\{\pi\left[2kF^I_a\left(-\frac{k\mathcal{B}^I_{1\delta}}{2} + k p_1 \mathcal{B}^I_1 + \mathcal{B}^R_1\right) + 2k^2 F^R_a\left(\frac{\mathcal{B}^R_{1\delta}}{2} - p_1 \mathcal{B}^R_1\right) +\right.\\
&\left.2F^I_b\left(F k p_1 - \frac{G_2 k}{2} - G\right) + 2F^R_b\left(\frac{F_2 k}{2} + F + G k p_1\right) - k\left(2p_1 \mathcal{L}^I_2 + \mathcal{T}^I_{\delta 02}\right)\right] -\\
&2k^2\,(p_1 - 1)^2\left(G_1 F^R_b + F_1 F^I_b\right)\Bigg\} + \pi\left(\frac{1}{2} - p_2\right)\Bigg\{4F^I_a\left[k\left(p_1 \mathcal{B}^R_1 - \frac{\mathcal{B}^R_{1\delta}}{2}\right) - \mathcal{B}^I_1\right] +\\
&4F^R_a\left[-\frac{k\mathcal{B}^I_{1\delta}}{2} + k\left(p_1 + \frac{1}{2}\right)\mathcal{B}^I_1 + \mathcal{B}^R_1\right] - 4F^I_b\left(\frac{F}{k} + \frac{F_2}{2} + G p_1\right) + 4F^R_b\left(F p_1 - \frac{G}{k} - \frac{G_2}{2}\right) +\\
&4p_1 \mathcal{L}^R_2 + 2\mathcal{T}^R_{\delta 02}\Bigg\} + 2\pi k p_2^2 \mathcal{B}^I_1 F^R_a + 2k\,(p_1 - 1)\left(G_1 F^I_b - F_1 F^R_b\right) +\\
&\left(\frac{1}{2} - p_2\right)\left[2\left(2k\,(p_1 - 1)\,(2p_2 - p_1) + \frac{8}{k}\right)\left(F_1 F^R_b - G_1 F^I_b\right) + 16 p_1\left(G_1 F^R_b + F_1 F^I_b\right)\right] +\\
&(8p_2\,(p_2 + 1) - 4)\left(G_1 F^R_b + F_1 F^I_b\right),
\end{aligned} \tag{C.99}
$$

$$\begin{aligned}
F_{t3d} = & \left[(p_2 - 1)\, p_2 + \frac{1}{2} \right] \Bigg\{ \pi \Bigg[2kF_a^I \left(\mathcal{B}_1^I - kp_1\mathcal{B}_1^R + \frac{k\mathcal{B}_{1\delta}^R}{2} \right) + 2kF_a^R \left(\frac{k\mathcal{B}_{1\delta}^I}{2} - kp_1\mathcal{B}_1^I - \mathcal{B}_1^R \right) + \\
& 2F_b^I \left(\frac{F_2k}{2} + F + Gkp_1 \right) + 2F_b^R \left(-Fkp_1 + \frac{G_2k}{2} + G \right) - 2k \left(p_1\mathcal{L}_2^R + \frac{\mathcal{T}_{\delta 02}^R}{2} \right) \Bigg] + \\
& 2k^2 (p_1 - 1)^2 \left(F_1F_b^R - G_1F_b^I \right) \Bigg\} + \left(\frac{1}{2} - p_2 \right) \Bigg\{ \pi \Bigg[4F_a^I \left(-\frac{k\mathcal{B}_{1\delta}^I}{2} + kp_1\mathcal{B}_1^I + \mathcal{B}_1^R \right) + \\
& 4F_a^R \left(\mathcal{B}_1^I - kp_1\mathcal{B}_1^R + \frac{k\mathcal{B}_{1\delta}^R}{2} \right) + F_b^I \left(4Fp_1 - \frac{4G}{k} - 2G_2 \right) + F_b^R \left(\frac{4F}{k} + 2F_2 + 4Gp_1 \right) - \\
& 4p_1\mathcal{L}_2^I - 2\mathcal{T}_{\delta 02}^I \Bigg] - 4k \left(p_1^2 - 1 \right) \left(G_1F_b^R + F_1F_b^I \right) + \frac{16\,(G_1F_b^R + F_1F_b^I)}{k} + \\
& 16 \left(\frac{1}{2} - p_1 \right) \left(F_1F_b^R - G_1F_b^I \right) \Bigg\} - 8k\,(p_1 - 1)\, p_2^2 \left(G_1F_b^R + F_1F_b^I \right) + 8p_2^2 \left(G_1F_b^I - F_1F_b^R \right).
\end{aligned} \tag{C.100}$$

- Hindwing

$$F_{t1h} = -2(F_1F_a^I + F_a^RG_1), \tag{C.101}$$

$$F_{t2h} = -2\left[F_1(F_a^I f_\Gamma + F_c^I) + G_1(F_a^R f_\Gamma + F_c^R) \right], \tag{C.102}$$

$$F_{t3h} = -2\left[F_1(F_a^R f_\Gamma + F_c^R) - G_1(F_a^I f_\Gamma + F_c^I) \right], \tag{C.103}$$

$$\begin{aligned}
F_{t1hp} = & \Bigg[\pi \left(GF_a^R + FF_a^I + kF_b^i\mathcal{B}_2^I - k\mathcal{B}_2^RF_b^R - \mathcal{L}_2^I \right) + 3 \left(1 - \frac{4a_2}{3} \right) k \left(G_1F_a^R + F_1F_a^I \right) + \\
& 2 \left(G_1F_a^I - F_1F_a^R \right) \Bigg] \cos(\phi_2) + \Bigg[\pi \left(-GF_a^I + FF_a^R + kF_b^R\mathcal{B}_2^i + k\mathcal{B}_2^RF_b^I + \mathcal{L}_2^R \right) + \\
& k \left(F_1F_a^R - G_1F_a^I \right) + 6 \left(G_1F_a^R + F_1F_a^I \right) \Bigg] \sin(\phi_2),
\end{aligned} \tag{C.104}$$

$$\begin{aligned}
F_{t2hp} = & \Bigg\{ \pi \left[kB_2^i \left(F_a^I + f_\Gamma F_b^i \right) - k\mathcal{B}_2^R \left(F_a^R + f_\Gamma F_b^R \right) - f_\Gamma\mathcal{L}_2^I - \mathcal{L}_1^I \right] + \\
& 4 \left[\frac{1}{2} (1 - a_2)\, F_1k + \frac{\pi F}{4} + G_1 \right] \left(f_\Gamma F_a^I + F_c^I \right) + 4 \left[\frac{1}{2} (1 - a_2)\, G_1k - F_1 + \frac{\pi G}{4} \right] \times \\
& \left(f_\Gamma F_a^R + F_c^R \right) \Bigg\} \cos(\varphi + \phi_2) + \Bigg\{ \pi \Bigg[k\mathcal{B}_2^I \left(F_a^R + f_\Gamma F_b^R \right) + k\mathcal{B}_2^R \left(F_a^I + f_\Gamma F_b^I \right) + \\
& f_\Gamma\mathcal{L}_2^R + \mathcal{L}_1^R \Bigg] + 4 \left[-\frac{1}{2} (1 - a_2)\, G_1k + F_1 - \frac{\pi G}{4} \right] \left(f_\Gamma F_a^I + F_c^I \right) + \\
& 4 \left[\frac{1}{2} (1 - a_2)\, F_1k + \frac{\pi F}{4} + G_1 \right] \left(f_\Gamma F_a^R + F_c^R \right) + \Bigg\} \sin(\varphi + \phi_2),
\end{aligned} \tag{C.105}$$

$$\begin{aligned} F_{t3hp} =& \left\{ -2\left[G_1 - \left(\frac{1}{2} - a_1\right) F_1 k\right] \left(f_\Gamma F_a^I + F_c^I\right) + 2\left[\left(\frac{1}{2} - a_1\right) G_1 k + F_1\right] \left(f_\Gamma F_a^R + F_c^R\right) + \right. \\ & \left. \frac{k f_{\Gamma\alpha}}{\pi} \left(G_1 F_a^R + F_1 F_a^I\right) \right\} \cos\left(\varphi - \phi_1\right) + \left\{ -2\left[\left(\frac{1}{2} - a_1\right) G_1 k + F_1\right] \left(f_\Gamma F_a^I + F_c^I\right) - \right. \\ & \left. 2\left[G_1 - \left(\frac{1}{2} - a_1\right) F_1 k\right] \left(f_\Gamma F_a^R + F_c^R\right) + \frac{k f_{\Gamma\alpha}}{\pi} \left(F_1 F_a^R - G_1 F_a^I\right) \right\} \sin\left(\varphi - \phi_1\right), \end{aligned} \tag{C.106}$$

$$\begin{aligned} F_{t1p} =& \pi\left[\left(\frac{1}{2} - a_2\right) k \left(-G F_a^R - F F_a^I - k F_b^I \mathcal{B}_2^I + k \mathcal{B}_2^R F_b^R + \mathcal{L}_2^I\right) + G F_a^I - F F_a^R - k F_b^R \mathcal{B}_2^I - \right. \\ & \left. k \mathcal{B}_2^R F_b^I - \mathcal{L}_2^R \right] + 2\left(\frac{1}{2} - a_2\right) \left(a_2 - 1\right) k^2 \left(G_1 F_a^R + F_1 F_a^I\right) + 2 a_2 k \left(G_1 F_a^I - F_1 F_a^R\right) - \\ & 4\left(G_1 F_a^R + F_1 F_a^I\right), \end{aligned} \tag{C.107}$$

$$\begin{aligned} F_{t2p} =& -\left(f_\Gamma F_a^R + F_c^R\right) \left\{ 2\left(2a_1 - a_2\right) F_1 k + \left(\frac{1}{2} - a_1\right) k^2 \left[2\left(1 - a_2\right) G_1 + \frac{\pi G}{k}\right] + \pi F + 4 G_1 \right\} + \\ & \left(f_\Gamma F_a^I + F_c^I\right) \left\{ -\left(\frac{1}{2} - a_1\right) k^2 \left[2\left(1 - a_2\right) F_1 + \frac{\pi F}{k}\right] + 2\left(2a_1 - a_2\right) G_1 k - 4 F_1 + \pi G \right\} - \\ & \pi (F_a^R + f_\Gamma F_b^R) k \left[B_2^I - \left(\frac{1}{2} - a_1\right) k \mathcal{B}_2^R\right] - \pi (F_a^I + f_\Gamma F_b^I) k \left[\left(\frac{1}{2} - a_1\right) k B_2^I + \mathcal{B}_2^R\right] - \\ & \frac{k f_{\Gamma\alpha} F_a^I}{\pi} \left[\left(1 - a_2\right) F_1 k + \frac{\pi F}{2} + 2 G_1\right] - \frac{k f_{\Gamma\alpha} F_a^R}{\pi} \left[\left(1 - a_2\right) G_1 k - 2 F_1 + \frac{\pi G}{2}\right] + \\ & \pi \left[\left(\frac{1}{2} - a_1\right) k \left(f_\Gamma \mathcal{L}_2^I + \mathcal{L}_1^I\right) - f_\Gamma \mathcal{L}_2^R - \mathcal{L}_1^R\right] + \frac{1}{2} k^2 f_{\Gamma\alpha} \left(-\mathcal{B}_2^I F_b^I + \mathcal{B}_2^R F_b^R + \frac{\mathcal{L}_2^I}{k}\right), \end{aligned} \tag{C.108}$$

$$\begin{aligned} F_{t3p} =& \left(f_\Gamma F_a^R + F_c^R\right) \left\{ -\left(\frac{1}{2} - a_1\right) k^2 \left[2\left(1 - a_2\right) F_1 + \frac{\pi F}{k}\right] + 2\left(2a_1 - a_2\right) G_1 k - 4 F_1 + \pi G \right\} + \\ & \left(f_\Gamma F_a^I + F_c^I\right) \left\{ 2\left(2a_1 - a_2\right) F_1 k + \left(\frac{1}{2} - a_1\right) k^2 \left[\frac{\pi G}{k} - 2\left(a_2 - 1\right) G_1\right] + \pi F + 4 G_1 \right\} - \\ & \pi (F_a^R + f_\Gamma F_b^R) k \left(\left(\frac{1}{2} - a_1\right) k \mathcal{B}_2^i + \mathcal{B}_2^R\right) + \pi (F_a^I + f_\Gamma F_b^I) k \left(\mathcal{B}_2^I - \left(\frac{1}{2} - a_1\right) k \mathcal{B}_2^R\right) - \\ & \frac{k f_{\Gamma\alpha} F_a^I}{\pi} \left[-\left(1 - a_2\right) G_1 k + 2 F_1 - \frac{\pi G}{2}\right] - \frac{k f_{\Gamma\alpha} F_a^R}{\pi} \left[\left(1 - a_2\right) F_1 k + \frac{\pi F}{2} + 2 G_1\right] - \\ & \pi \left[\left(\frac{1}{2} - a_1\right) k \left(f_\Gamma \mathcal{L}_2^R + \mathcal{L}_1^R\right) + f_\Gamma \mathcal{L}_2^I + \mathcal{L}_1^I\right] + \frac{1}{2} k^2 f_{\Gamma\alpha} \left(-F_b^R \mathcal{B}_2^I - \mathcal{B}_2^R F_b^I - \frac{\mathcal{L}_2^R}{k}\right), \end{aligned} \tag{C.109}$$

$$\begin{aligned}
F_{1hd} =& \Bigg\{ F_a^I \left[6\left(1-\frac{2p_2}{3}\right)(F_1 k p_2 - G_1) - 2\pi\left(-Fp_2+\frac{G}{k}+\frac{G_2}{2}\right) + F_1\left(\frac{8}{k}-3k\right)\right] + \\
& F_a^R \left[2\pi\left(\frac{F}{k}+\frac{F_2}{2}+Gp_2\right) + 6\left(1-\frac{2p_2}{3}\right)(F_1+G_1 k p_2) + G_1\left(\frac{8}{k}-3k\right)\right] + \\
& 2\pi F_b^I \left(-\frac{1}{2}k\mathcal{B}_{2\delta}^I + kp_2\mathcal{B}_2^I + \mathcal{B}_2^R\right) + 2\pi F_b^R \left(\mathcal{B}_2^I - kp_2\mathcal{B}_2^R + \frac{1}{2}k\mathcal{B}_{2\delta}^R\right) + \\
& 2\pi\left(\frac{\mathcal{T}_{\delta 02}^I}{2} - p_2\mathcal{L}_2^I\right)\Bigg\}\cos(\psi_2) + \Bigg\{ -2F_a^I \Bigg[\pi\left(\frac{F}{k}+\frac{F_2}{2}+Gp_2\right) + 5F_1\left(1-\frac{6p_2}{5}\right) - \\
& G_1 k\left(\frac{1}{2}-p_2\right) + \frac{4G_1}{k}\Bigg] + 2F_a^R\Bigg[-\pi\left(-Fp_2+\frac{G}{k}+\frac{G_2}{2}\right) - F_1 k\left(\frac{1}{2}-p_2\right) + \\
& \frac{4F_1}{k} - 5G_1\left(1-\frac{6p_2}{5}\right)\Bigg] + 2\pi F_b^R\left(-\frac{1}{2}k\mathcal{B}_{2\delta}^I + kp_2\mathcal{B}_2^I + \mathcal{B}_2^R\right) - \\
& 2\pi F_b^I\left(\mathcal{B}_2^I - kp_2\mathcal{B}_2^R + \frac{1}{2}k\mathcal{B}_{2\delta}^R\right) + 2\pi\left(p_2\mathcal{L}_2^R - \frac{\mathcal{T}_{\delta 02}^R}{2}\right)\Bigg\}\sin(\psi_2)\,,
\end{aligned} \tag{C.110}$$

$$\begin{aligned}
F_{t2hd} =& \Bigg\{ \pi\Bigg[3k\left(\mathcal{I}_{\gamma,2} - \frac{f_\Gamma}{2}\right) + 2(F_a^R + f_\Gamma F_b^R)\left(\mathcal{B}_2^I - kp_2\mathcal{B}_2^R + \frac{1}{2}k\mathcal{B}_{2\delta}^R\right) + 2(F_a^I + f_\Gamma F_b^I)\times \\
& \left(-\frac{1}{2}k\mathcal{B}_{2\delta}^I + kp_2\mathcal{B}_2^I + \mathcal{B}_2^R\right) - 2p_2\left(f_\Gamma\mathcal{L}_2^I + \mathcal{L}_1^I\right) + f_\Gamma\mathcal{T}_{\delta 02}^I + \mathcal{T}_{\delta 01}^I\Bigg] + 8(f_\Gamma F_a^R + F_c^R)\times \\
& \left[\frac{\pi}{4}\left(\frac{F}{k}+\frac{F_2}{2}+Gp_2\right) - F_1(p_2-1) + G_1\left(\frac{1}{k}-\frac{k}{4}(p_2-1)^2\right)\right] + 8(f_\Gamma F_a^I + F_c^I)\times \\
& \left[-\frac{\pi}{4}\left(-Fp_2+\frac{G}{k}+\frac{G_2}{2}\right) + F_1\left(\frac{1}{k}-\frac{k}{4}(p_2-1)^2\right) + G_1(p_2-1)\right]\Bigg\}\cos(\theta+\psi_2) + \\
& \Bigg\{8(f_\Gamma F_a^R + F_c^R)\left[-\frac{\pi}{4}\left(-Fp_2+\frac{G}{k}+\frac{G_2}{2}\right) + F_1\left(\frac{1}{k}-\frac{k}{4}(p_2-1)^2\right) + G_1(p_2-1)\right] + \\
& \pi\Bigg[2(F_a^R + f_\Gamma F_b^R)\left(-\frac{k}{2}\mathcal{B}_{2\delta}^i + kp_2\mathcal{B}_2^I + \mathcal{B}_2^R\right) - 2(F_a^I + f_\Gamma F_b^I)\left(\mathcal{B}_2^I - kp_2\mathcal{B}_2^R + \frac{k}{2}\mathcal{B}_{2\delta}^R\right) + \\
& 2p_2\left(f_\Gamma\mathcal{L}_2^R + \mathcal{L}_1^R\right) - f_\Gamma\mathcal{T}_{\delta 02}^R - \mathcal{T}_{\delta 01}^R\Bigg] - 8(f_\Gamma F_a^I + F_c^I)\Bigg[\frac{\pi}{4}\left(\frac{F}{k}+\frac{F_2}{2}+Gp_2\right) - \\
& F_1(p_2-1) + G_1\left(\frac{1}{k}-\frac{k}{4}(p_2-1)^2\right)\Bigg]\Bigg\}\sin(\theta+\psi_2)\,,
\end{aligned} \tag{C.111}$$

$$
\begin{aligned}
F_{t3hd} =& \Bigg\{ -\frac{2k}{\pi}\left(\frac{f_{\Gamma\delta}}{2} - p_1 f_{\Gamma\alpha}\right)\left(G_1 F_a^R + F_1 F_a^I\right) + \frac{2 f_{\Gamma\alpha}}{\pi}\left(G_1 F_a^I - F_1 F_a^R\right) - \\
& 2k\left[\left(p_1 - 1\right) p_1 + \frac{1}{2}\right]\left[(f_\Gamma F_a^R + F_c^R)G_1 + (f_\Gamma F_a^I + F_c^I)F_1\right] + \\
& 4\left(\frac{1}{2} - p_1\right)\left[(f_\Gamma F_a^I + F_c^I)G_1 - (f_\Gamma F_a^R + F_c^R)F_1\right]\Bigg\}\cos\left(\theta - \psi_1\right) + \\
& \Bigg\{\frac{2k}{\pi}\left(\frac{f_{\Gamma\delta}}{2} - p_1 f_{\Gamma\alpha}\right)\left(G_1 F_a^I - F_1 F_a^R\right) + \frac{2 f_{\Gamma\alpha}}{\pi}\left(G_1 F_a^R + F_1 F_a^I\right) + \\
& 2k\left(\left(p_1 - 1\right) p_1 + \frac{1}{2}\right)\left[(f_\Gamma F_a^I + F_c^I)G_1 - (f_\Gamma F_a^R + F_c^R)F_1\right] + \\
& 4\left(\frac{1}{2} - p_1\right)\left[(f_\Gamma F_a^R + F_c^R)G_1 + (f_\Gamma F_a^I + F_c^I)F_1\right]\Bigg\}\sin\left(\theta - \psi_1\right), \qquad \text{(C.112)}
\end{aligned}
$$

$$
\begin{aligned}
F_{t1pd} =& k\Bigg\{\pi\left[\frac{1}{k}\left(G_2 F_a^R + F_2 F_a^I + 2\mathcal{B}_2^I F_b^I - 2\mathcal{B}_2^R F_b^R + 4\left(\frac{1}{4} - p_2\right)\mathcal{L}_2^R - \mathcal{T}_{\delta 02}^R\right) + \frac{2}{k^2}\left(GF_a^R + FF_a^I\right) + \right. \\
& \left. F_b^R \mathcal{B}_{2\delta}^I + F_b^I \mathcal{B}_{2\delta}^R - \frac{k}{8}\right] + \pi\left[p_2\left(2a_2 + p_2 - 2\right) + \frac{1}{2}\right]\left(GF_a^R + FF_a^{+} k\mathcal{B}_2^I F_b^I - k\mathcal{B}_2^R F_b^R - \mathcal{L}_2^I\right) + \\
& 2\left(a_2 - 2p_2\right)\left[\pi\left(\frac{FF_a^R - GF_a^I}{k} + \mathcal{B}_2^I F_b^R + \mathcal{B}_2^R F_b^I\right) + \frac{4\left(G_1 F_a^R + F_1 F_a^I\right)}{k}\right] + \\
& \pi\left(\frac{1}{2} - a_2\right)\left(G_2 F_a^I - F_2 F_a^R + kF_b^I \mathcal{B}_{2\delta}^I - kF_b^R \mathcal{B}_{2\delta}^R + \mathcal{T}_{\delta 02}^I\right) + \\
& 2\left(2a_2 p_2 - 3a_2 + \frac{4}{k^2} + p_2^2 + 1\right)\left(G_1 F_a^I - F_1 F_a^R\right) + \left[3\left(1 - \frac{4a_2}{3}\right)kp_2^2 + \right. \\
& \left. 4\left(1 - \frac{3a_2}{2}\right)k\left(\frac{1}{2} - p_2\right) + \frac{8}{k}\right]\left(G_1 F_a^R + F_1 F_a^I\right)\Bigg\}\cos\left(\phi_2 - \psi_2\right) - \\
& k\Bigg\{\pi\left[\frac{2}{k}\left(\mathcal{B}_2^I F_b^R + \mathcal{B}_2^R F_b^I - \left(\left(a_2 - 1\right)F + \frac{G_2}{2}\right)F_a^I + \left(\left(1 - a_2\right)G + \frac{F_2}{2}\right)F_a^R - \frac{\mathcal{L}_2^I}{2} - \right.\right. \\
& \left. \frac{\mathcal{T}_{\delta 02}^I}{2}\right) - 2\left(a_2 - 1\right)\mathcal{B}_2^I F_b^I + 2\left(a_2 - 1\right)\mathcal{B}_2^R F_b^R + \frac{2\left(FF_a^R - GF_a^I\right)}{k^2} - Fp_2\left(p_2 - 2a_2\right)F_a^R - \\
& \left. \frac{FF_a^R}{2} - \left(\frac{1}{2} - a_2\right)\mathcal{T}_{\delta 02}^R - F_b^I \mathcal{B}_{2\delta}^i + F_b^R \mathcal{B}_{2\delta}^R\right] + \pi\left[p_2\left(p_2 - 2a_2\right) + \frac{1}{2}\right] \times \\
& \left[GF_a^I - k\left(\mathcal{B}_2^I F_b^R + \mathcal{B}_2^R F_b^I\right) - \mathcal{L}_2^R\right] + \pi\left(\frac{1}{2} - a_2\right)\left[G_2 F_a^R + F_2 F_a^I + k\left(F_b^R \mathcal{B}_{2\delta}^i + F_b^I \mathcal{B}_{2\delta}^R\right)\right] + \\
& k\left(\frac{8a_2}{k^2} - 2a_2\left(\frac{1}{2} - p_2\right) - p_2^2\right)\left(F_1 F_a^R - G_1 F_a^I\right) + \\
& 2\left[a_2\left(6p_2 - 5\right) + \frac{4}{k^2} - 3p_2^2 + 1\right]\left(G_1 F_a^R + F_1 F_a^I\right)\Bigg\}\sin\left(\phi_2 - \psi_2\right), \qquad \text{(C.113)}
\end{aligned}
$$

$$
F_{t2pd} = F_{t2pd,1} k\cos(\varphi - \phi_1 + \psi_2) + F_{t2pd,2} k\sin(\varphi - \phi_1 + \psi_2), \qquad \text{(C.114)}
$$

$$
\begin{aligned}
F_{t2pd,1} ={}& \pi \left(\frac{1}{2} - a_1\right) \Bigg\{ k \Bigg[\mathcal{I}_{\gamma,2} + (F_a^I + f_\Gamma F_b^I) \left(\mathcal{B}_{2\delta}^I - 2p_2 \mathcal{B}_2^I\right) + (F_a^R + f_\Gamma F_b^R) \left(2p_2 \mathcal{B}_2^R - \mathcal{B}_{2\delta}^R\right) - \\
& \frac{f_\Gamma}{2} \Bigg] - 2(F_a^R + f_\Gamma F_b^R)\mathcal{B}_2^I - 2(F_a^I + f_\Gamma F_b^I)\mathcal{B}_2^R + 2p_2 \left(f_\Gamma \mathcal{L}_2^I + \mathcal{L}_1^I\right) + f_\Gamma \mathcal{T}_{\delta 02}^I + \mathcal{T}_{\delta 01}^I \Bigg\} + \\
& \frac{k}{2} \mathcal{I}_{\gamma\alpha,2} + \left[(p_2 - 1)\,(4a_1 - p_2 - 1) + \frac{4}{k^2} \right] \left[2(f_\Gamma F_a^I + F_c^I) G_1 - 2(f_\Gamma F_a^R + F_c^R) F_1 \right] + \\
& \frac{8}{k} \left(a_1 - p_2 + \frac{1}{2}\right) \left[(f_\Gamma F_a^R + F_c^R) G_1 + (f_\Gamma F_a^I + F_c^I) F_1 \right] + \left(\frac{1}{2} - a_1\right) \times \\
& \Bigg\{ 2k\,(p_2 - 1)^2 \left((f_\Gamma F_a^R + F_c^R) G_1 + (f_\Gamma F_a^I + F_c^I) F_1 \right) + \pi \Bigg[(f_\Gamma F_a^I + F_c^I) \times \\
& \left(-2Fp_2 + \frac{2G}{k} + G_2 \right) - (f_\Gamma F_a^R + F_c^R) \left(\frac{2F}{k} + F_2 + 2Gp_2 \right) \Bigg] \Bigg\} + \\
& f_{\Gamma\alpha} \Bigg\{ \frac{1}{\pi} \left(k\,(p_2 - 1)^2 - \frac{4}{k} \right) \left(G_1 F_a^R + F_1 F_a^I \right) + F_a^I \left(-Fp_2 + \frac{G}{k} + \frac{G_2}{2} \right) + \\
& \frac{4}{\pi} (p_2 - 1) \left(F_1 F_a^R - G_1 F_a^I \right) - F_a^R \left(\frac{F}{k} + \frac{F_2}{2} + Gp_2 \right) + F_b^I \left(\frac{k}{2} \mathcal{B}_{2\delta}^I - kp_2 \mathcal{B}_2^I - \mathcal{B}_2^R \right) - \\
& F_b^R \left(\mathcal{B}_2^I - kp_2 \mathcal{B}_2^R + \frac{k}{2} \mathcal{B}_{2\delta}^R \right) + p_2 \mathcal{L}_2^I + \frac{\mathcal{T}_{\delta 02}^I}{2} - \frac{k}{4} \Bigg\} + \pi \Bigg\{ (f_\Gamma F_a^R + F_c^R) \times \\
& \left(\frac{G_2 - 2Fp_2}{k} + \frac{2G}{k^2} \right) + (f_\Gamma F_a^I + F_c^I) \left(\frac{F_2 + 2Gp_2}{k} + \frac{2F}{k^2} \right) + (F_a^R + f_\Gamma F_b^R) \times \\
& \left(\mathcal{B}_{2\delta}^I - 2p_2 \mathcal{B}_2^I - \frac{2\mathcal{B}_2^R}{k} \right) + (F_a^I + f_\Gamma F_b^I) \left(\frac{2\mathcal{B}_2^I}{k} - 2p_2 \mathcal{B}_2^R + \mathcal{B}_{2\delta}^R \right) + \\
& \frac{2}{k} \left[p_2 \left(-f_\Gamma \mathcal{L}_2^R - \mathcal{L}_1^R \right) + \frac{1}{2} \left(-f_\Gamma \mathcal{T}_{\delta 02}^R - \mathcal{T}_{\delta 01}^R \right) \right] \Bigg\},
\end{aligned}
\tag{C.115}
$$

$$
\begin{aligned}
F_{t2pd,2} =\pi\Bigg\{ & -\mathcal{I}_{\gamma,2}+\frac{2}{k}\Bigg[(f_\Gamma F_a^R+F_c^R)\left(\frac{F_2}{2}+Gp_2\right)+(f_\Gamma F_a^I+F_c^I)\left(Fp_2-\frac{G_2}{2}\right)+\\
& p_2\left(-f_\Gamma\mathcal{L}_2^I-\mathcal{L}_1^I\right)+\frac{1}{2}\left(-f_\Gamma\mathcal{T}_{\delta02}^I-\mathcal{T}_{\delta01}^I\right)\Bigg]+\frac{2}{k^2}[(f_\Gamma F_a^R+F_c^R)F-(f_\Gamma F_a^I+F_c^I)G]+\\
& (F_a^R+f_\Gamma F_b^R)\left(\frac{2\mathcal{B}_2^I}{k}-2p_2\mathcal{B}_2^R+\mathcal{B}_{2\delta}^R\right)+(F_a^I+f_\Gamma F_b^I)\left(-\mathcal{B}_{2\delta}^I+2p_2\mathcal{B}_2^I+\frac{2\mathcal{B}_2^R}{k}\right)+\frac{f_\Gamma}{2}\Bigg\}+\\
& 2\left[(p_2-1)\,(4a_1-p_2-1)+\frac{4}{k^2}\right]\Big[(f_\Gamma F_a^R+F_c^R)G_1+BF_1\Big]+\\
& \frac{8}{k}\left(a_1-p_2+\frac{1}{2}\right)\Big((f_\Gamma F_a^R+F_c^R)F_1-(f_\Gamma F_a^I+F_c^I)G_1\Big)+\left(\frac{1}{2}-a_1\right)\Bigg\{2k\,(p_2-1)^2\times\\
& \Big[(f_\Gamma F_a^R+F_c^R)F_1-(f_\Gamma F_a^I+F_c^I)G_1\Big]+\pi\Bigg[(f_\Gamma F_a^R+F_c^R)\left(-2Fp_2+\frac{2G}{k}+G_2\right)+\\
& (f_\Gamma F_a^I+F_c^I)\left(\frac{2F}{k}+F_2+2Gp_2\right)\Bigg]\Bigg\}+f_{\Gamma\alpha}\Bigg\{\frac{1}{\pi}\Bigg[\left(k\,(p_2-1)^2-\frac{4}{k}\right)\left(F_1F_a^R-G_1F_a^I\right)-\\
& 4\,(p_2-1)\left(G_1F_a^R+F_1F_a^I\right)\Bigg]+F_a^I\left(\frac{F}{k}+\frac{F_2}{2}+Gp_2\right)+F_a^R\left(-Fp_2+\frac{G}{k}+\frac{G_2}{2}\right)+\\
& F_b^R\left(\frac{1}{2}k\mathcal{B}_{2\delta}^I-kp_2\mathcal{B}_2^I-\mathcal{B}_2^R\right)+F_b^I\left(\mathcal{B}_2^I-kp_2\mathcal{B}_2^R+\frac{1}{2}k\mathcal{B}_{2\delta}^R\right)-p_2\mathcal{L}_2^R-\frac{\mathcal{T}_{\delta02}^R}{2}\Bigg\}+\\
& \pi\left(\frac{1}{2}-a_1\right)\Bigg\{2(F_a^R+f_\Gamma F_b^R)\left(\frac{1}{2}k\mathcal{B}_{2\delta}^I-kp_2\mathcal{B}_2^I-\mathcal{B}_2^R\right)+2(F_a^I+f_\Gamma F_b^I)\times\\
& \left(\mathcal{B}_2^I-kp_2\mathcal{B}_2^R+\frac{1}{2}k\mathcal{B}_{2\delta}^R\right)-2p_2\left(f_\Gamma\mathcal{L}_2^R+\mathcal{L}_1^R\right)-f_\Gamma\mathcal{T}_{\delta02}^R-\mathcal{T}_{\delta01}^R\Bigg\},
\end{aligned}
\tag{C.116}
$$

$$
\begin{aligned}
F_{t3pd} = & k\Bigg\{ \left(\frac{1}{2} - p_1\right) \Bigg[2(f_\Gamma F_a^R + F_c^R) \left(-2a_2F_1 + \frac{\pi F}{k} + \frac{4G_1}{k}\right) + 2(f_\Gamma F_a^I + F_c^I)\times \\
& \left(2a_2G_1 + \frac{4F_1}{k} - \frac{\pi G}{k}\right) + 2\pi \left((F_a^R + f_\Gamma F_b^R)\mathcal{B}_2^I + (F_a^I + f_\Gamma F_b^I)\mathcal{B}_2^R + \frac{f_\Gamma \mathcal{L}_2^R + \mathcal{L}_1^R}{k}\right)\Bigg] + \\
& \left[(p_1 - 1)\, p_1 + \frac{1}{2}\right] \Bigg[2\,(a_2 - 1)\, k \Big(-(f_\Gamma F_a^R + F_c^R)G_1 - (f_\Gamma F_a^I + F_c^I)F_1\Big) + \\
& \pi k\Bigg(\frac{G}{k}(f_\Gamma F_a^R + F_c^R) + \frac{F}{k}(f_\Gamma F_a^I + F_c^I) + (F_a^I + f_\Gamma F_b^I)\mathcal{B}_2^i - (F_a^R + f_\Gamma F_b^R)\mathcal{B}_2^R - \frac{f_\Gamma \mathcal{L}_2^I + \mathcal{L}_1^I}{k}\Bigg)\Bigg] + \\
& \left(\frac{f_{\Gamma\delta}}{2} - p_1 f_{\Gamma\alpha}\right) \Bigg[-\frac{2}{\pi}\,(a_2 - 1)\, k \Big(G_1F_a^R + F_1F_a^I\Big) + \frac{4}{\pi}\Big(G_1F_a^I - F_1F_a^R\Big) + GF_a^R + FF_a^I + \\
& k\Big(\mathcal{B}_2^I F_b^I - \mathcal{B}_2^R F_b^R\Big) - \mathcal{L}_2^I\Bigg] + f_{\Gamma\alpha}\Bigg[\frac{1}{k}\Big(FF_a^R - GF_a^I\Big) + \frac{4}{k\pi}\Big(G_1F_a^R + F_1F_a^I\Big) + \\
& \frac{2}{\pi}\,(a_2 - 1)\Big(G_1F_a^I - F_1F_a^R\Big) + \mathcal{B}_2^I F_b^R + \mathcal{B}_2^R F_b^I + \frac{\mathcal{L}_2^R}{k}\Bigg] + \\
& 4p_1^2\Big[(f_\Gamma F_a^I + F_c^I)G_1 - (f_\Gamma F_a^R + F_c^R)F_1\Big]\Bigg\} \cos(\varphi - \psi_1 + \phi_2) + \\
& k\Bigg\{ \left(\frac{1}{2} - p_1\right) \Bigg[(f_\Gamma F_a^R + F_c^R) \left(4a_2G_1 + \frac{8F_1}{k}\right) + (f_\Gamma F_a^I + F_c^I)\left(4a_2F_1 - \frac{8G_1}{k}\right) + \\
& \pi\Bigg(\frac{2}{k}\Big(-(f_\Gamma F_a^R + F_c^R)G - (f_\Gamma F_a^I + F_c^I)F + f_\Gamma \mathcal{L}_2^I + \mathcal{L}_1^I\Big) + \\
& 2\Big((F_a^R + f_\Gamma F_b^R)\mathcal{B}_2^R - (F_a^I + f_\Gamma F_b^I)\mathcal{B}_2^i\Big)\Bigg)\Bigg] + \left[(p_1 - 1)\, p_1 + \frac{1}{2}\right] \Bigg[2\,(a_2 - 1)\, k\times \\
& \Big((f_\Gamma F_a^I + F_c^I)G_1 - (f_\Gamma F_a^R + F_c^R)F_1\Big) + \pi\Bigg((f_\Gamma F_a^R + F_c^R)F - (f_\Gamma F_a^I + F_c^I)G + \\
& k(F_a^R + f_\Gamma F_b^R)\mathcal{B}_2^I + k(F_a^I + f_\Gamma F_b^I)\mathcal{B}_2^R + f_\Gamma\mathcal{L}_2^R + \mathcal{L}_1^R\Bigg)\Bigg] + \left(\frac{f_{\Gamma\delta}}{2} - p_1 f_{\Gamma\alpha}\right)\times \\
& \Bigg[\frac{2k}{\pi}\,(a_2 - 1)\Big(G_1F_a^I - F_1F_a^R\Big) + \frac{4}{\pi}\Big(G_1F_a^R + F_1F_a^I\Big) - GF_a^I + FF_a^R + \\
& k\Big(\mathcal{B}_2^I F_b^R + \mathcal{B}_2^R F_b^I\Big) + \mathcal{L}_2^R\Bigg] + f_{\Gamma\alpha}\Bigg[\frac{1}{k}\Bigg(\frac{4}{\pi}\Big(F_1F_a^R - G_1F_a^I\Big) - GF_a^R - FF_a^I\Bigg) + \\
& \frac{2}{\pi}\,(a_2 - 1)\Big(G_1F_a^R + F_1F_a^I\Big) - \mathcal{B}_2^I F_b^i + \mathcal{B}_2^R F_b^R + \frac{\mathcal{L}_2^I}{k}\Bigg] + \\
& 4p_1^2\Big[(f_\Gamma F_a^R + F_c^R)G_1 + (f_\Gamma F_a^I + F_c^I)F_1\Big]\Bigg\} \sin(\varphi - \psi_1 + \phi_2)\,, \qquad \text{(C.117)}
\end{aligned}
$$

$$
\begin{aligned}
F_{t1d} = &- k^2 \bigg[\left(p_2 - 1\right) p_2 + \frac{1}{2}\bigg] \Bigg\{\pi \Bigg[\frac{F_a^I \left(G_2 - 2Fp_2\right)}{k} - \frac{F_a^R \left(F_2 + 2Gp_2\right)}{k} + 2F_b^I \left(\frac{\mathcal{B}_{2\delta}^I}{2} - p_2 \mathcal{B}_2^I\right) + \\
&2F_b^R \left(p_2 \mathcal{B}_2^R - \frac{\mathcal{B}_{2\delta}^R}{2}\right) + \frac{2\left(p_2 \mathcal{L}_2^I + \frac{\mathcal{T}_{\delta 02}^I}{2}\right)}{k}\Bigg] + 2\left(p_2 - 1\right)^2 \left(G_1 F_a^R + F_1 F_a^I\right) \Bigg\} + \\
&\left(p_2 - \frac{1}{2}\right) \Bigg\{\pi \Bigg[2\left(\frac{2G}{k} + G_2\right) F_a^R + 2\left(\frac{2F}{k} + F_2\right) F_a^I + 4F_b^I \left(\mathcal{B}_2^I + \frac{1}{2} k \mathcal{B}_{2\delta}^R\right) + \\
&4F_b^R \left(\frac{1}{2} k \mathcal{B}_{2\delta}^I - \mathcal{B}_2^R\right) - 4\left(p_2 \mathcal{L}_2^R + \frac{\mathcal{T}_{\delta 02}^R}{2}\right)\Bigg] + \frac{16\left(G_1 F_a^I - F_1 F_a^R\right)}{k} \Bigg\} + \\
&2\pi \left(\frac{1}{2} - p_2^2\right) \left[-GF_a^I + FF_a^R + k\left(\mathcal{B}_2^I F_b^R + \mathcal{B}_2^R F_b^I\right)\right] + 4k\left(p_2 - 1\right) \left[\frac{1}{2} - \left(\frac{1}{2} - p_2\right) p_2\right] \times \\
&\left(G_1 F_a^I - F_1 F_a^R\right) - 8\left[\left(p_2 - 2\right) p_2 + \frac{1}{2}\right] \left(G_1 F_a^R + F_1 F_a^I\right) - \frac{1}{4}\pi k^2 p_2,
\end{aligned}
\tag{C.118}
$$

$$
\begin{aligned}
F_{t2d} = &\left(p_1 \mathcal{I}_{\gamma\alpha,2} - \frac{\mathcal{I}_{\gamma\delta,2}}{2}\right) k^2 - f_{\Gamma\alpha} \left[F_2 - kG_2 p_1 + 2G\left(p_2 - p_1\right) + 2F\left(kp_1 p_2 + \frac{1}{k}\right)\right] F_a^I + \\
&f_{\Gamma\alpha} \left[-G_2 - kF_2 p_1 + 2F\left(p_2 - p_1\right) - 2G\left(kp_1 p_2 + \frac{1}{k}\right)\right] F_a^R + +2\Bigg[\frac{\mathcal{T}_{\delta 02}^R}{2} + \mathcal{L}_2^R p_2 - \\
&\left(\mathcal{B}_2^I - kp_2 \mathcal{B}_2^R + \frac{1}{2} k \mathcal{B}_{2\delta}^R\right) F_b^I + \left(kp_2 \mathcal{B}_2^I + \mathcal{B}_2^R - \frac{1}{2} k \mathcal{B}_{2\delta}^i\right) F_b^R\Bigg] f_{\Gamma\alpha} + \\
&\frac{2f_{\Gamma\alpha}}{\pi} \left(F_1 F_a^I + G_1 F_a^R\right) \left[p_1 \left(k^2 \left(p_2 - 1\right)^2 - 4\right) + 4\left(p_2 - 1\right)\right] + \\
&\frac{2f_{\Gamma\alpha}}{\pi} \left(F_1 F_a^R - F_a^I G_1\right) \left[k\left(4p_1 - p_2 + 1\right)\left(p_2 - 1\right) + \frac{4}{k}\right] + \\
&8(f_\Gamma F_a^I + F_c^I) p_1^2 \left[-\frac{\pi G}{4} + F_1 + kG_1\left(p_2 - 1\right)\right] + \frac{4kf_{\Gamma\delta}}{\pi} \left(F_a^I G_1 - F_1 F_a^R\right)\left(p_2 - 1\right) + \\
&8(f_\Gamma F_a^R + F_c^R) p_1^2 \left[\frac{\pi F}{4} + G_1 - kF_1\left(p_2 - 1\right)\right] + \frac{f_{\Gamma\delta}}{\pi} \left(F_1 F_a^I + G_1 F_a^R\right) \left(4 - k^2\left(p_2 - 1\right)^2\right) + \\
&f_{\Gamma\delta} \left[F_a^R \left(F + \frac{kF_2}{2} + Gkp_2\right) - F_a^I \left(G + \frac{kG_2}{2} - Fkp_2\right)\right] + k\left(\frac{f_{\Gamma\delta}}{2} - f_{\Gamma\alpha} p_1\right) \times \\
&\left[\frac{k}{2} - 2\left(-kp_2 \mathcal{B}_2^I - \mathcal{B}_2^R + \frac{1}{2} k \mathcal{B}_{2\delta}^I\right) F_b^I + 2\left(\mathcal{B}_2^I - kp_2 \mathcal{B}_2^R + \frac{1}{2} k \mathcal{B}_{2\delta}^R\right) F_b^R - \mathcal{T}_{\delta 02}^I - 2\mathcal{L}_2^I p_2\right] + \\
&\left(\frac{1}{2} - p_1\right) \Bigg\{ - 16\left[(f_\Gamma F_a^I + F_c^I) F_1 + (f_\Gamma F_a^R + F_c^R) G_1\right] \left(\frac{1}{2} - p_2\right) + \\
&4\left[(f_\Gamma F_a^I + F_c^I) G_1 - (f_\Gamma F_a^R + F_c^R) F_1\right] \left[k\left(p_2 - 1\right)\left(p_2 + 1\right) - \frac{4}{k}\right] + \\
&\pi \Bigg[2\mathcal{T}_{\delta 01}^R + 2f_\Gamma \mathcal{T}_{\delta 02}^R - 4(f_\Gamma F_a^R + F_c^R) \left(\frac{G}{k} + \frac{G_2}{2}\right) - 4\left(\frac{F}{k} + \frac{F_2}{2}\right) (f_\Gamma F_a^I + F_c^I) + \\
&4\left(\mathcal{L}_1^R + f_\Gamma \mathcal{L}_2^R\right) p_2 + 4\left[(f_\Gamma F_a^R + F_c^R) F - (f_\Gamma F_a^I + F_c^I) G\right] \left(p_2 + \frac{1}{2}\right) +
\end{aligned}
$$

$$
\begin{aligned}
&4(F_a^R + f_\Gamma F_b^R)\left[\mathcal{B}_2^R + k\left(\mathcal{B}_2^I p_2 - \frac{\mathcal{B}_{2\delta}^I}{2}\right)\right] + 4(F_a^I + f_\Gamma F_b^I)\left[k\left(\mathcal{B}_2^R p_2 - \frac{\mathcal{B}_{2\delta}^R}{2}\right) - \mathcal{B}_2^I\right]\Bigg]\Bigg\}+ \\
&k\left[(p_1-1)\,p_1 + \frac{1}{2}\right]\Bigg\{\pi\Bigg[-\mathcal{T}_{\delta01}^I - f_\Gamma\mathcal{T}_{\delta02}^I + \frac{kf_\Gamma}{2} - 2\left(\mathcal{L}_1^I + f_\Gamma\mathcal{L}_2^I\right)p_2+ \\
&(f_\Gamma F_a^R + F_c^R)\,(F_2 + 2Gp_2) + k(F_a^I + f_\Gamma F_b^I)\left(2p_2\mathcal{B}_2^I + \frac{2\mathcal{B}_2^R}{k} - \mathcal{B}_{2\delta}^i\right) - \\
&(f_\Gamma F_a^I + F_c^I)\,(G_2 - 2Fp_2) + (F_a^R + f_\Gamma F_b^R)k\left(\frac{2\mathcal{B}_2^I}{k} - 2p_2\mathcal{B}_2^R + \mathcal{B}_{2\delta}^R\right) - k\mathcal{I}_{\gamma,2}\Bigg]- \\
&2k\left[(f_\Gamma F_a^I + F_c^I)F_1 + (f_\Gamma F_a^R + F_c^R)G_1\right](p_2-1)^2\Bigg\}, \qquad \text{(C.119)}
\end{aligned}
$$

$$
\begin{aligned}
F_{t3d} =& -8(f_\Gamma F_a^I + F_c^I)\left[\frac{\pi F}{4} + G_1 - kF_1\,(p_2-1)\right]p_1^2 - 8(f_\Gamma F_a^R + F_c^R)\times \\
&\left[\frac{\pi G}{4} - F_1 - kG_1\,(p_2-1)\right]p_1^2 - 2k\left(\frac{f_{\Gamma\delta}}{2} - f_{\Gamma\alpha}p_1\right)\Bigg[\left(\mathcal{B}_2^I - kp_2\mathcal{B}_2^R + \frac{1}{2}k\mathcal{B}_{2\delta}^R\right)F_b^I+ \\
&\left(-kp_2\mathcal{B}_2^I - \mathcal{B}_2^R + \frac{1}{2}k\mathcal{B}_{2\delta}^i\right)F_b^R + \frac{1}{\pi}\left(F_a^I G_1 - F_1 F_a^R\right)\left(\frac{4}{k} - k\,(p_2-1)^2\right) - \mathcal{L}_2^R p_2- \\
&\frac{\mathcal{T}_{\delta02}^R}{2} - \frac{4\left(F_1F_a^I + G_1F_a^R\right)(p_2-1)}{\pi}\Bigg] - f_{\Gamma\delta}\Bigg[\left(F + \frac{kF_2}{2} + Gkp_2\right)F_a^I+ \\
&\left(G + \frac{kG_2}{2} - Fkp_2\right)F_a^R\Bigg] - \left(\frac{1}{2} - p_1\right)\Bigg\{(f_\Gamma F_a^I + F_c^I)\Bigg[-4k\,(p_2-1)\,(p_2+1)\,F_1+ \\
&\frac{16F_1}{k} - 16G_1\left(\frac{1}{2} - p_2\right)\Bigg] + (f_\Gamma F_a^R + F_c^R)\Bigg[-4k\,(p_2-1)\,(p_2+1)\,G_1 + \frac{16G_1}{k}+ \\
&16F_1\left(\frac{1}{2} - p_2\right)\Bigg]\Bigg\} - f_{\Gamma\alpha}\Bigg\{\left[-G_2 - kF_2p_1 + 2F\,(p_2-p_1) - 2G\left(kp_1p_2 + \frac{1}{k}\right)\right]F_a^I+ \\
&\left[F_2 - kG_2p_1 + 2G\,(p_2-p_1) + 2F\left(kp_1p_2 + \frac{1}{k}\right)\right]F_a^R - T_{\delta02}^I + \frac{k}{2}+ \\
&\frac{2}{\pi}\left(F_1F_a^I + G_1F_a^R\right)\left(\frac{4}{k} - k\,(p_2-1)^2\right) + \frac{8}{\pi}\left(F_a^I G_1 - F_1F_a^R\right)(p_2-1) - 2\mathcal{L}_2^I p_2+ \\
&2F_b^I\left(kp_2\mathcal{B}_2^I + \mathcal{B}_2^R - \frac{1}{2}k\mathcal{B}_{2\delta}^I\right) + 2F_b^R\left(\mathcal{B}_2^I - kp_2\mathcal{B}_2^R + \frac{1}{2}k\mathcal{B}_{2\delta}^R\right)\Bigg\}- \\
&k\left[(p_1-1)\,p_1 + \frac{1}{2}\right]\Bigg\{2k\left[(f_\Gamma F_a^R + F_c^R)F_1 - (f_\Gamma F_a^I + F_c^I)G_1\right](p_2-1)^2+ \\
&\pi\Bigg[-2p_2\mathcal{L}_1^R - \mathcal{T}_{\delta01}^R - f_\Gamma\mathcal{T}_{\delta02}^R - 2f_\Gamma\mathcal{L}_2^R p_2 + (f_\Gamma F_a^I + F_c^I)\,(F_2 + 2Gp_2)+ \\
&(f_\Gamma F_a^R + F_c^R)\,(G_2 - 2Fp_2) + 2(F_a^R + f_\Gamma F_b^R)\left(-kp_2\mathcal{B}_2^I - \mathcal{B}_2^R + \frac{1}{2}k\mathcal{B}_{2\delta}^I\right)+ \\
&2(F_a^I + f_\Gamma F_b^I)\left(\mathcal{B}_2^I - kp_2\mathcal{B}_2^R + \frac{1}{2}k\mathcal{B}_{2\delta}^R\right)\Bigg]\Bigg\} - \pi\left(\frac{1}{2} - p_1\right)\Bigg\{-4p_2\mathcal{L}_1^I - 2\mathcal{T}_{\delta01}^I+
\end{aligned}
$$

$$(F_a^I + f_\Gamma F_b^I)\left(4kp_2\mathcal{B}_2^I + 4\mathcal{B}_2^R - 2k\mathcal{B}_{2\delta}^I\right) + (F_a^R + f_\Gamma F_b^R)\left(4\mathcal{B}_2^I - 4kp_2\mathcal{B}_2^R + 2k\mathcal{B}_{2\delta}^R\right) +$$
$$(f_\Gamma F_a^I + F_c^I)\left[-\frac{4G}{k} - 2G_2 + 4F\left(p_2 + \frac{1}{2}\right)\right] + (f_\Gamma F_a^R + F_c^R)\times$$
$$\left.\left[\frac{4F}{k} + 2F_2 + 4G\left(p_2 + \frac{1}{2}\right)\right] - 2f_\Gamma\left(2p_2\mathcal{L}_2^I + \mathcal{T}_{\delta 02}^I\right) + 2k\left(\frac{f_\Gamma}{2} - \mathcal{I}_{\gamma,2}\right)\right\} + k\mathcal{I}_{\gamma\alpha,2}, \tag{C.120}$$

C.3.2 *Input power coefficient*

Full expressions for the time-averaged input power coefficient for two airfoils in tandem configuration are given below. The superscripts R and I denote real and imaginary parts, respectively. The time-average input power coefficient can be written in terms of the feathering paremeters as

$$\bar{C}_P^{(i)} = (kh_0)^2\left[p_h + p_{hp}\theta_i + p_p\theta_i^2 + \left(p_{hd} + p_{pd}\theta_i\right)\theta_{di} + p_d\theta_{di}^2\right], \tag{C.121}$$

where the functions p_h, p_{hp}, p_p, p_{hd}, p_{hd} and p_d are given by

$$p_h = F_{p1h} + \Theta_h\left[F_{p2h}\cos(\varphi) + F_{p3h}\sin(\varphi)\right], \tag{C.122}$$

$$p_{hp} = F_{p1hp} + \Theta_h F_{p2hp} + \Theta_a F_{p3hp}, \tag{C.123}$$

$$p_p = F_{p1p} + \Theta_a\left[F_{p2p}\cos(\varphi - \phi_i + \phi_j) + F_{p3p}\sin(\varphi - \phi_i + \phi_j)\right], \tag{C.124}$$

$$p_{hd} = \frac{1}{(1-p_i)^2}\left[F_{p1hd} + \Theta_h F_{p2hd} + \Theta_d F_{p3hd}\left(\frac{1-p_i}{1-p_j}\right)^2\right], \tag{C.125}$$

$$p_{pd} = \frac{1}{(1-p_i)^2}\left[F_{p1pd} + \Theta_a F_{p2pd} + \Theta_d F_{p3pd}\left(\frac{1-p_i}{1-p_j}\right)^2\right], \tag{C.126}$$

$$p_d = \frac{1}{(1-p_i)^4}\left\{F_{p1d} + \Theta_d\left(\frac{1-p_i}{1-p_j}\right)^2\left[F_{p2d}\cos(\varphi - \psi_i + \psi_j) + F_{p3d}\sin(\varphi - \psi_i + \psi_j)\right]\right\}. \tag{C.127}$$

The different functions F_p are specific for each airfoil and are given below.

- Forewing

$$F_{p1h} = \pi\left(f_\Gamma\mathcal{L}_{02}^R + \mathcal{L}_{01}^R\right), \quad F_{p2h} = \pi\mathcal{L}_{02}^R, \quad F_{p2h} = -\pi\mathcal{L}_{02}^I, \tag{C.128}$$

$$F_{p1hp} = \left\{2\pi k\left[f_\Gamma(a_1\mathcal{L}_{02}^R + \mathcal{M}_{02}^R) - \left(\frac{1}{4} - a_1\right)\mathcal{L}_{01}^R - \frac{f_\Gamma\mathcal{L}_{02}^R}{4} + \mathcal{M}_{01}^R - \frac{1}{4}\right] -\right.$$
$$\left.\pi(f_\Gamma\mathcal{L}_{02}^I + \mathcal{L}_{01}^I) - \frac{f_{\Gamma\alpha}k}{2}\mathcal{L}_{02}^R\right\}\cos(\phi_1) + \left\{\frac{f_{\Gamma\alpha}k}{2}\mathcal{L}_{02}^I - \pi(f_\Gamma\mathcal{L}_{02}^R + \mathcal{L}_{01}^R) +\right.$$
$$\left.2\pi k\left(\frac{1}{4}(f_\Gamma\mathcal{L}_{02}^I + \mathcal{L}_{01}^I) + f_\Gamma\mathcal{M}_{02}^I + \mathcal{M}_{01}^I\right)\right\}\sin(\phi_1), \tag{C.129}$$

$$F_{p2hp} = \pi k \left[(a_1 \mathcal{L}_{02}^R + 2\mathcal{M}_{02}^R) \cos(\varphi - \phi_1) - (a_1 \mathcal{L}_{02}^I + 2\mathcal{M}_{02}^I) \sin(\varphi - \phi_1) \right], \tag{C.130}$$

$$F_{p3hp} = -\pi \left\{ \left[\left(\frac{1}{2} - a_2 \right) k\mathcal{L}_{02}^R + \mathcal{L}_{02}^I \right] \cos(\varphi + \phi_2) + \left[\mathcal{L}_{02}^R - \left(\frac{1}{2} - a_2 \right) k\mathcal{L}_{02}^I \right] \sin(\varphi + \phi_2) \right\}, \tag{C.131}$$

$$\begin{aligned} F_{p1p} =& - k^2 f_{\Gamma\alpha} \left(\frac{a_1 \mathcal{L}_{02}^R}{2} + \mathcal{M}_{02}^R \right) - k\pi \Big\{ a_1 (f_\Gamma \mathcal{L}_{02}^I + \mathcal{L}_{01}^I) + 2(f_\Gamma \mathcal{M}_{02}^I + \mathcal{M}_{01}^I) + \\ & (1 - 2\text{a1})k \left[\frac{1}{2} a_1 (f_\Gamma \mathcal{L}_{02}^R + \mathcal{L}_{01}^R) + f_\Gamma \mathcal{M}_{02}^R + \mathcal{M}_{01}^R - \frac{1}{4} \right] \Big\}, \end{aligned} \tag{C.132}$$

$$F_{p2p} = -k\pi \left[a_1 \left(\frac{1}{2} - a_2 \right) k\mathcal{L}_{02}^R + a_1 \mathcal{L}_{02}^I + 2 \left(\frac{1}{2} - a_2 \right) k\mathcal{M}_{02}^R + 2\mathcal{M}_{02}^I \right], \tag{C.133}$$

$$F_{p3p} = \pi k \left[a_1 \left(\frac{1}{2} - a_2 \right) k\mathcal{L}_{02}^I - a_1 \mathcal{L}_{02}^R + 2 \left(\frac{1}{2} - a_2 \right) k\mathcal{M}_{02}^I - 2\mathcal{M}_{02}^R \right], \tag{C.134}$$

$$\begin{aligned} F_{p1d} =& 4 f_{\Gamma\alpha} k p_1 \left(\frac{1}{4} p_1 (\mathcal{L}_{02}^I - k\mathcal{L}_{02}^R p_1) - k\mathcal{M}_{02}^R p_1 + \mathcal{M}_{02}^I \right) + 2 f_{\Gamma\delta} k^2 p_1 \left(\frac{\mathcal{L}_{02}^R p_1}{4} + \mathcal{M}_{02}^R \right) + \\ & \mathcal{F}_{02}^I k \left[2\pi f_\Gamma \left(\frac{1}{2} - p_1 \right) + f_{\Gamma\alpha} \right] + \mathcal{F}_{02}^R k^2 \left[\pi f_\Gamma \left((p_1 - 1) p_1 + \frac{1}{2} \right) - f_{\Gamma\alpha} p_1 + \frac{f_{\Gamma\delta}}{2} \right] + \\ & 2k\pi \mathcal{F}_{01}^I \left(\frac{1}{2} - p_1 \right) + \mathcal{F}_{01}^R k^2 \pi \left[(p_1 - 1) p_1 + \frac{1}{2} \right] + \\ & 8k\pi p_1 \left(\frac{1}{2} - p_1 \right) \left(\frac{p_1}{4} (f_\Gamma \mathcal{L}_{02}^I + \mathcal{L}_{01}^I) + f_\Gamma \mathcal{M}_{02}^I + \mathcal{M}_{01}^I \right) + \\ & 4k^2 \pi p_1 \left((p_1 - 1) p_1 + \frac{1}{2} \right) \left(\frac{p_1}{4} (f_\Gamma \mathcal{L}_{02}^R + \mathcal{L}_{01}^R) + f_\Gamma \mathcal{M}_{02}^R + \mathcal{M}_{01}^R - \frac{1}{4} \right), \end{aligned} \tag{C.135}$$

$$\begin{aligned} F_{p2d} =& k\pi \Big\{ \mathcal{F}_{02}^I (1 - 2p_2) + \mathcal{F}_{02}^R k \left[(p_2 - 1) p_2 + \frac{1}{2} \right] + p_1 (1 - 2p_2)(\mathcal{L}_{02}^I p_1 + 4\mathcal{M}_{02}^I) + \\ & k p_1 \left[(p_2 - 1) p_2 + \frac{1}{2} \right] (\mathcal{L}_{02}^R p_1 + 4\mathcal{M}_{02}^R) \Big\}, \end{aligned} \tag{C.136}$$

$$\begin{aligned} F_{p3d} =& k\pi \Big\{ \mathcal{F}_{02}^R (1 - 2p_2) - \mathcal{F}_{02}^I k \left[(p_2 - 1) p_2 + \frac{1}{2} \right] + p_1 (1 - 2p_2)(\mathcal{L}_{02}^R p_1 + 4\mathcal{M}_{02}^R) - \\ & k p_1 \left[(p_2 - 1) p_2 + \frac{1}{2} \right] (\mathcal{L}_{02}^I p_1 + 4\mathcal{M}_{02}^I) \Big\}, \end{aligned} \tag{C.137}$$

$$\begin{aligned}
F_{p1hd} =& \Bigg\{ \pi \left[\mathcal{F}_{01}^{R} k + \mathcal{F}_{02}^{R} f_{\Gamma} k + 2 \left(\frac{1}{2} - p_1 \right) \left(-k p_1 (f_{\Gamma} \mathcal{L}_{02}^{R} + \mathcal{L}_{01}^{R}) + f_{\Gamma} \mathcal{L}_{02}^{I} + \mathcal{L}_{01}^{I} \right) \right] + \\
& \pi \left[\frac{k}{2} (f_{\Gamma} \mathcal{L}_{02}^{R} + \mathcal{L}_{01}^{R}) + 4 k p_1 (f_{\Gamma} \mathcal{M}_{02}^{R} + \mathcal{M}_{01}^{R}) - k p_1 \right] + \\
& k \mathcal{L}_{02}^{R} \left(\frac{f_{\Gamma\delta}}{2} - f_{\Gamma\alpha} p_1 \right) + f_{\Gamma\alpha} \mathcal{L}_{02}^{I} \Bigg\} \cos(\psi_1) + \\
& \Bigg\{ \pi \left[\mathcal{F}_{01}^{I} k + \mathcal{F}_{02}^{I} f_{\Gamma} k + 2 \left(\frac{1}{2} - p_1 \right) \left(-\frac{k}{2} (f_{\Gamma} \mathcal{L}_{02}^{I} + \mathcal{L}_{01}^{I}) + f_{\Gamma} \mathcal{L}_{02}^{R} + \mathcal{L}_{01}^{R} \right) \right] + \\
& \pi \left[4 k p_1 (f_{\Gamma} \mathcal{M}_{02}^{I} + \mathcal{M}_{01}^{I}) \right] + k \mathcal{L}_{02}^{I} \left(f_{\Gamma\alpha} p_1 - \frac{f_{\Gamma\delta}}{2} \right) + f_{\Gamma\alpha} \mathcal{L}_{02}^{R} \Bigg\} \sin(\psi_1), \qquad (C.138)
\end{aligned}$$

$$\begin{aligned}
F_{p2hd} =& \pi k [\mathcal{F}_{02}^{R} + p_1 (\mathcal{L}_{02}^{R} p_1 + 4 \mathcal{M}_{02}^{R})] \cos(\varphi - \psi_1) - \\
& \pi k [\mathcal{F}_{02}^{I} + p_1 (\mathcal{L}_{02}^{I} p_1 + 4 \mathcal{M}_{02}^{I})] \sin(\varphi - \psi_1), \qquad (C.139)
\end{aligned}$$

$$\begin{aligned}
F_{p3hd} =& \pi \left[k \mathcal{L}_{02}^{R} \left((p_2 - 1) p_2 + \frac{1}{2} \right) + \mathcal{L}_{02}^{I} (1 - 2 p_2) \right] \cos(\varphi + \psi_2) + \\
& \pi \left[\mathcal{L}_{02}^{R} (1 - 2 p_2) - k \mathcal{L}_{02}^{I} \left((p_2 - 1) p_2 + \frac{1}{2} \right) \right] \sin(\varphi + \psi_2), \qquad (C.140)
\end{aligned}$$

$$\begin{aligned}
F_{p1pd} =& \Bigg\{ f_{\Gamma\alpha} \left(a_1 \mathcal{L}_{02}^{I} - \frac{\mathcal{F}_{02}^{R} k}{2} + 2 \mathcal{M}_{02}^{I} \right) + k \mathcal{L}_{02}^{R} \left[\frac{a_1 f_{\Gamma\delta}}{2} - f_{\Gamma\alpha} p_1 \left(a_1 + \frac{p_1}{2} \right) \right] + \\
& 4 k \mathcal{M}_{02}^{R} \left(\frac{f_{\Gamma\delta}}{4} - f_{\Gamma\alpha} p_1 \right) - \pi \left(\frac{1}{2} - a_1 \right) k (\mathcal{F}_{01}^{R} + \mathcal{F}_{02}^{R} f_{\Gamma}) - \pi \mathcal{F}_{01}^{I} - \pi \mathcal{F}_{02}^{I} f_{\Gamma} - \frac{\pi k}{4} + \\
& \pi k p_1 \left(-a_1 - \frac{p_1}{2} + 1 \right) + \pi \left[2 a_1 \left(\frac{1}{2} - p_1 \right) - p_1^2 \right] (f_{\Gamma} \mathcal{L}_{02}^{I} + \mathcal{L}_{01}^{I}) + \\
& \pi k \left[a_1 \left(\frac{1}{2} - p_1 \right) - 2 \left(\frac{1}{4} - a_1 \right) p_1^2 \right] (f_{\Gamma} \mathcal{L}_{02}^{R} + \mathcal{L}_{01}^{R}) + \\
& \pi k \left[4 p_1 \left(a_1 + \frac{p_1}{2} - 1 \right) + 1 \right] (f_{\Gamma} \mathcal{M}_{02}^{R} + \mathcal{M}_{01}^{R}) + \\
& 2 \pi (1 - 4 p_1) (f_{\Gamma} \mathcal{M}_{02}^{I} + \mathcal{M}_{01}^{I}) \Bigg\} \cos(\phi_1 - \psi_1) + \\
& \Bigg\{ f_{\Gamma\alpha} \left(-a_1 \mathcal{L}_{02}^{R} + \frac{\mathcal{F}_{02}^{I} k}{2} - 2 \mathcal{M}_{02}^{R} \right) + k \mathcal{L}_{02}^{I} \left[f_{\Gamma\alpha} p_1 \left(\frac{p_1}{2} - a_1 \right) + \frac{a_1 f_{\Gamma\delta}}{2} \right] + \\
& f_{\Gamma\delta} k \mathcal{M}_{02}^{I} + \pi \left(\frac{1}{2} - a_1 \right) k (\mathcal{F}_{01}^{I} + \mathcal{F}_{02}^{I} f_{\Gamma}) - \pi \mathcal{F}_{01}^{R} - \pi \mathcal{F}_{02}^{R} f_{\Gamma} + \frac{\pi}{2} + \\
& \pi k \left[a_1 \left(\frac{1}{2} - p_1 \right) + \frac{p_1^2}{2} \right] (f_{\Gamma} \mathcal{L}_{02}^{I} + \mathcal{L}_{01}^{I}) - \pi \left[2 a_1 \left(\frac{1}{2} - p_1 \right) + p_1^2 \right] (f_{\Gamma} \mathcal{L}_{02}^{R} + \mathcal{L}_{01}^{R}) + \\
& \pi k \left[4 p_1 \left(\frac{p_1}{2} - a_1 \right) + 1 \right] (f_{\Gamma} \mathcal{M}_{02}^{I} + \mathcal{M}_{01}^{I}) - 2 \pi (f_{\Gamma} \mathcal{M}_{02}^{R} + \mathcal{M}_{01}^{R}) \Bigg\} \sin(\phi_1 - \psi_1), \\
& \qquad (C.141)
\end{aligned}$$

$$\begin{aligned} F_{p2pd} =& -\pi\left\{\left(\frac{1}{2}-a_2\right)k\left[\mathcal{F}_{02}^R+4p_1\left(\frac{\mathcal{L}_{02}^R p_1}{4}+\mathcal{M}_{02}^R\right)\right]+\mathcal{F}_{02}^I+\right.\\ &\left. 4p_1\left(\frac{\mathcal{L}_{02}^I p_1}{4}+\mathcal{M}_{02}^I\right)\right\}\cos(\varphi-\psi_1+\phi_2)-\pi\left\{\mathcal{F}_{02}^R+4p_1\left(\frac{\mathcal{L}_{02}^R p_1}{4}+\mathcal{M}_{02}^R\right)-\right.\\ &\left.\left(\frac{1}{2}-a_2\right)k\left[\mathcal{F}_{02}^I+4p_1\left(\frac{\mathcal{L}_{02}^I p_1}{4}+\mathcal{M}_{02}^I\right)\right]\right\}\sin(\theta-\psi_1+\phi_2), \end{aligned} \tag{C.142}$$

$$\begin{aligned} F_{p3pd} =& \pi\left\{k\left[(p_2-1)p_2+\frac{1}{2}\right](a_1\mathcal{L}_{02}^R+2\mathcal{M}_{02}^R)+2\left(\frac{1}{2}-p_2\right)(a_1\mathcal{L}_{02}^I+2\mathcal{M}_{02}^I)\right\}\times\\ &\cos(\varphi+\psi_2-\phi_1)+\pi\left\{2\left(\frac{1}{2}-p_2\right)(a_1\mathcal{L}_{02}^R+2\mathcal{M}_{02}^R)-\right.\\ &\left. k\left[(p_2-1)p_2+\frac{1}{2}\right](a_1\mathcal{L}_{02}^I+2\mathcal{M}_{02}^I)\right\}\sin(\varphi+\psi_2-\phi_1). \end{aligned} \tag{C.143}$$

- Hindwing

$$F_{p1h}=\pi\mathcal{L}_{02}^R,\quad F_{p2h}=\pi\left(f_\Gamma\mathcal{L}_{02}^R+\mathcal{L}_{01}^R\right),\quad F_{p2h}=\pi\left(f_\Gamma\mathcal{L}_{02}^I-\mathcal{I}_\gamma k+\mathcal{L}_{01}^I\right), \tag{C.144}$$

$$\begin{aligned} F_{p1hp} =& \pi\left[-\left(\frac{1}{2}-2a_2\right)k\mathcal{L}_{02}^R+2k\mathcal{M}_{02}^R-\frac{k}{2}-\mathcal{L}_{02}^I\right]\cos(\phi_2)+\\ &\pi\left(\frac{k\mathcal{L}_{02}^I}{2}+2k\mathcal{M}_{02}^I-\mathcal{L}_{02}^R\right)\sin(\phi_2), \end{aligned} \tag{C.145}$$

$$\begin{aligned} F_{p2hp} =& \pi k\left(a_2(f_\Gamma\mathcal{L}_{02}^R+\mathcal{L}_{01}^R)+2(f_\Gamma\mathcal{M}_{02}^R+\mathcal{M}_{01}^R)-\frac{f_\Gamma}{2}-\mathcal{I}_\gamma\right)\cos(\varphi+\phi_2)+\\ &\pi k\left[k\left(-a_2\mathcal{I}_\gamma-\frac{f_\Gamma}{4}+\frac{\mathcal{I}_{\gamma,2}}{2}\right)+a_2(f_\Gamma\mathcal{L}_{02}^I+\mathcal{L}_{01}^I)+2(f_\Gamma\mathcal{M}_{02}^I+\mathcal{M}_{01}^I)\right]\sin(\varphi+\phi_2), \end{aligned} \tag{C.146}$$

$$\begin{aligned} F_{p3hp} =& -\left\{\pi\left[\left(\frac{1}{2}-a_1\right)k(f_\Gamma\mathcal{L}_{02}^R+\mathcal{L}_{01}^R)+(f_\Gamma\mathcal{L}_{02}^I+\mathcal{L}_{01}^I)-\mathcal{I}_\gamma k\right]+\right.\\ &\left.\frac{f_{\Gamma\alpha}k\mathcal{L}_{02}^R}{2}\right\}\cos(\varphi-\phi_1)+\left\{\pi\left[\left(\frac{1}{2}-a_1\right)k(-f_\Gamma\mathcal{L}_{02}^I+\mathcal{I}_\gamma k-\mathcal{L}_{01}^I)+f_\Gamma\mathcal{L}_{02}^R+\mathcal{L}_{01}^R\right]+\right.\\ &\left.\frac{1}{2}k(\mathcal{I}_{\gamma\alpha}k-f_{\Gamma\alpha}\mathcal{L}_{02}^I)\right\}\sin(\varphi-\phi_1), \end{aligned} \tag{C.147}$$

$$F_{p1p}=\pi k\left[\left(\frac{1}{2}-a_2\right)k\left(-a_2\mathcal{L}_{02}^R-2\mathcal{M}_{02}^R+\frac{1}{2}\right)-a_2\mathcal{L}_{02}^I-2\mathcal{M}_{02}^I\right], \tag{C.148}$$

$$\begin{aligned}
F_{p2p} =& k\Bigg\{ \pi\Bigg[2\left(\frac{1}{2}-a_1\right)k\left(-\frac{a_2}{2}(f_\Gamma\mathcal{L}^R_{02}+\mathcal{L}^R_{01})-f_\Gamma\mathcal{M}^R_{02}+\frac{\mathcal{I}_\gamma}{2}-\mathcal{M}^R_{01}\right)+\frac{1}{2}(1-a_1)f_\Gamma k+ \\
& a_2(-f_\Gamma\mathcal{L}^I_{02}+\mathcal{I}_\gamma k-\mathcal{L}^I_{01})-2(f_\Gamma\mathcal{M}^I_{02}+\mathcal{M}^I_{01})-\frac{\mathcal{I}_{\gamma,2}k}{2}\Bigg]+\frac{\mathcal{I}_{\gamma\alpha}k}{2}+ \\
& f_{\Gamma\alpha}k\left(-\frac{a_2\mathcal{L}^R_{02}}{2}-\mathcal{M}^R_{02}+\frac{1}{4}\right)\Bigg\}, \qquad \text{(C.149)}
\end{aligned}$$

$$\begin{aligned}
F_{p3p} =& k\Bigg\{ \pi\Bigg[\left(\frac{1}{2}-a_1\right)k\left(a_2(-f_\Gamma\mathcal{L}^I_{02}+\mathcal{I}_\gamma k-\mathcal{L}^I_{01})+\frac{f_\Gamma k}{4}-2f_\Gamma\mathcal{M}^I_{02}-\frac{\mathcal{I}_{\gamma,2}k}{2}-2\mathcal{M}^I_{01}\right)+ \\
& a_2(f_\Gamma\mathcal{L}^R_{02}+\mathcal{L}^R_{01})+2(f_\Gamma\mathcal{M}^R_{02}+\mathcal{M}^R_{01})-\frac{f_\Gamma}{2}-\mathcal{I}_\gamma\Bigg]+f_{\Gamma\alpha}k\left(-\frac{a_2\mathcal{L}^I_{02}}{2}+\frac{k}{8}-\mathcal{M}^I_{02}\right)+ \\
& \frac{k^2}{2}\left(a_2\mathcal{I}_{\gamma\alpha}-\frac{\mathcal{I}_{\gamma\alpha,2}}{2}\right)\Bigg\}, \qquad \text{(C.150)}
\end{aligned}$$

$$\begin{aligned}
F_{p1d} =& \pi k\Bigg\{(1-2p_2)\left[\mathcal{F}^I_{02}+4p_2\left(\frac{\mathcal{L}^I_{02}p_2}{4}+\mathcal{M}^I_{02}\right)\right]+k\left[(p_2-1)p_2+\frac{1}{2}\right]\times \\
& \left[\mathcal{F}^R_{02}+4p_2\left(\frac{\mathcal{L}^R_{02}p_2}{4}+\mathcal{M}^R_{02}-\frac{1}{4}\right)\right]\Bigg\}, \qquad \text{(C.151)}
\end{aligned}$$

$$\begin{aligned}
F_{p2d} =& \pi k\Bigg\{(1-2p_1)\Bigg[\mathcal{F}^I_{01}+\mathcal{F}^I_{02}f_\Gamma+p_2^2(f_\Gamma\mathcal{L}^I_{02}-\mathcal{I}_\gamma k+\mathcal{L}^I_{01})+4p_2\Bigg(-\frac{f_\Gamma k}{4}+f_\Gamma\mathcal{M}^I_{02}+ \\
& \frac{\mathcal{I}_{\gamma,2}k}{4}+\frac{k\mathcal{M}^R_{01}}{2}+\mathcal{M}^I_{01}\Bigg)-\frac{\mathcal{I}_{\gamma,3}k}{3}\Bigg]+k\left((p_1-1)p_1+\frac{1}{2}\right)\Bigg[\mathcal{F}^R_{01}+\mathcal{F}^R_{02}f_\Gamma+ \\
& 4p_2\left(f_\Gamma\mathcal{M}^R_{02}-\frac{\mathcal{I}_\gamma}{2}\right)+p_2^2(f_\Gamma\mathcal{L}^R_{02}+\mathcal{L}^R_{01})\Bigg]+4kp_1^2p_2\left(\mathcal{M}^R_{01}-\frac{f_\Gamma}{4}\right)\Bigg\}+ \\
& k\Bigg\{\mathcal{F}^I_{02}f_{\Gamma\alpha}+k\left(\frac{f_{\Gamma\delta}}{2}-f_{\Gamma\alpha}p_1\right)\left[\mathcal{F}^R_{02}+4p_2\left(\frac{\mathcal{L}^R_{02}p_2}{4}+\mathcal{M}^R_{02}\right)\right]- \\
& k\Bigg[p_2\left(f_{\Gamma\alpha}\left(\frac{1}{2}-p_1\right)+\frac{f_{\Gamma\delta}}{2}+\mathcal{I}_{\gamma\delta}\right)+\mathcal{I}_{\gamma\alpha}p_2(p_2-2p_1)+\mathcal{I}_{\gamma\alpha,2}(p_1-p_2)+ \\
& \frac{\mathcal{I}_{\gamma\alpha,3}}{3}-\frac{\mathcal{I}_{\gamma\delta,2}}{2}\Bigg]+4f_{\Gamma\alpha}p_2\left(\frac{\mathcal{L}^I_{02}p_2}{4}+\mathcal{M}^I_{02}\right)\Bigg\}, \qquad \text{(C.152)}
\end{aligned}$$

$$\begin{aligned}
F_{p3d} =&\pi k^2\Bigg\{ \left[(p_1-1)p_1+\frac{1}{2}\right]\Bigg[\mathcal{F}^I_{01}+\mathcal{F}^I_{02}f_\Gamma+p_2^2(f_\Gamma\mathcal{L}^I_{02}-\mathcal{I}_\gamma k+\mathcal{L}^I_{01})+\\
&p_2\left(-\frac{f_\Gamma k}{2}+4f_\Gamma\mathcal{M}^I_{02}+\mathcal{I}_{\gamma,2}k+4\mathcal{M}^I_{01}\right)-\frac{\mathcal{I}_{\gamma,3}k}{3}\Bigg]\Bigg\}-\\
&\pi k(1-2p_1)\left[\mathcal{F}^R_{01}+\mathcal{F}^R_{02}f_\Gamma+p_2(4f_\Gamma\mathcal{M}^R_{02}-f_\Gamma-2\mathcal{I}_\gamma+4\mathcal{M}^R_{01})+p_2^2(f_\Gamma\mathcal{L}^R_{02}+\mathcal{L}^R_{01})\right]+\\
&k\Bigg\{k\left(\frac{f_{\Gamma\delta}}{2}-f_{\Gamma\alpha}p_1\right)\left[\mathcal{F}^I_{02}+4p_2\left(\frac{\mathcal{L}^I_{02}p_2}{4}+\mathcal{M}^I_{02}\right)\right]-\mathcal{F}^R_{02}f_{\Gamma\alpha}+\\
&f_{\Gamma\alpha}p_2\left(\frac{k^2p_1}{2}+1\right)-4f_{\Gamma\alpha}p_2\left(\frac{\mathcal{L}^R_{02}p_2}{4}+\mathcal{M}^R_{02}\right)+\\
&k^2\left[\frac{p_2}{2}\left(\frac{f_{\Gamma\delta}}{2}-\mathcal{I}_{\gamma\delta}p_2+\mathcal{I}_{\gamma\delta,2}\right)+\frac{\mathcal{I}_{\gamma\alpha,3}p_1}{3}-\frac{\mathcal{I}_{\gamma\delta,3}}{6}\right]+\\
&\mathcal{I}_{\gamma\alpha}p_2\left(k^2p_1p_2+2\right)-\mathcal{I}_{\gamma\alpha,2}\left(k^2p_1p_2+1\right)\Bigg\},
\end{aligned} \tag{C.153}$$

$$\begin{aligned}
F_{p1hd} =&\pi\Bigg\{\left[\mathcal{F}^R_{02}k+(1-2p_2)(\mathcal{L}^I_{02}-k\mathcal{L}^R_{02}p_2)+k\left(\frac{\mathcal{L}^R_{02}}{2}-(1-4\mathcal{M}^R_{02})p_2\right)\right]\cos(\psi_2)+\\
&\left[\mathcal{F}^I_{02}k+\left(\frac{1}{2}-p_2\right)(2\mathcal{L}^R_{02}-k\mathcal{L}^I_{02})+4k\mathcal{M}^I_{02}p_2\right]\sin(\psi_2)\Bigg\},
\end{aligned} \tag{C.154}$$

$$\begin{aligned}
F_{p2hd} =&\pi k\Bigg\{\Bigg[\mathcal{F}^R_{01}+\mathcal{F}^R_{02}f_\Gamma-2p_2\left(\frac{f_\Gamma}{2}+\mathcal{I}_\gamma\right)+p_2^2(f_\Gamma\mathcal{L}^R_{02}+\mathcal{L}^R_{01})+\\
&4p_2(f_\Gamma\mathcal{M}^R_{02}+\mathcal{M}^R_{01})\Bigg]\cos(\varphi+\psi_2)-\Bigg[\mathcal{F}^I_{01}+\mathcal{F}^I_{02}f_\Gamma+p_2^2(f_\Gamma\mathcal{L}^I_{02}-\mathcal{I}_\gamma k+\mathcal{L}^I_{01})+\\
&p_2\left(-\frac{f_\Gamma}{2}k+4(f_\Gamma\mathcal{M}^I_{02}+\mathcal{M}^I_{01})+\mathcal{I}_{\gamma,2}k\right)-\frac{\mathcal{I}_{\gamma,3}k}{3}\Bigg]\sin(\varphi+\psi_2)\Bigg\},
\end{aligned} \tag{C.155}$$

$$\begin{aligned}
F_{p3hd} =&\Bigg\{\pi\left[(1-2p_1)(f_\Gamma\mathcal{L}^I_{02}-\mathcal{I}_\gamma k+\mathcal{L}^I_{01})+k\left((p_1-1)p_1+\frac{1}{2}\right)(f_\Gamma\mathcal{L}^R_{02}+\mathcal{L}^R_{01})\right]+\\
&k\mathcal{L}^R_{02}\left(\frac{f_{\Gamma\delta}}{2}-f_{\Gamma\alpha}p_1\right)+f_{\Gamma\alpha}\mathcal{L}^I_{02}-\mathcal{I}_{\gamma\alpha}k\Bigg\}\cos(\varphi-\psi_1)+\\
&\Bigg\{\pi\left[k\left((p_1-1)p_1+\frac{1}{2}\right)(f_\Gamma\mathcal{L}^I_{02}-\mathcal{I}_\gamma k+\mathcal{L}^I_{01})-(1-2p_1)(f_\Gamma\mathcal{L}^R_{02}+\mathcal{L}^R_{01})\right]+\\
&k\mathcal{L}^I_{02}\left(\frac{f_{\Gamma\delta}}{2}-f_{\Gamma\alpha}p_1\right)-f_{\Gamma\alpha}\mathcal{L}^R_{02}+k^2\left(\mathcal{I}_{\gamma\alpha}p_1-\frac{\mathcal{I}_{\gamma\delta}}{2}\right)\Bigg\}\sin(\varphi-\psi_1),
\end{aligned} \tag{C.156}$$

$$\begin{aligned}
F_{p1pd} = &-\pi\Bigg\{\left(\frac{1}{2}-a_2\right)\mathcal{F}^R_{02}k+\left[\frac{p_2^2}{2}-a_2\left(\frac{1}{2}-p_2\right)\right](k\mathcal{L}^R_{02}+2\mathcal{L}^I_{02})-2a_2k\mathcal{L}^R_{02}p_2^2+\\
&k(1-4\mathcal{M}^R_{02})\left[p_2\left(a_2+\frac{p_2}{2}-1\right)+\frac{1}{4}\right]+\mathcal{F}^I_{02}-2\mathcal{M}^I_{02}(1-4p_2)\Bigg\}\cos(\phi_2-\psi_2)+\\
&\pi\Bigg\{\left(\frac{1}{2}-a_2\right)\mathcal{F}^I_{02}k+\left[a_2\left(\frac{1}{2}-p_2\right)+\frac{p_2^2}{2}\right](k\mathcal{L}^I_{02}-2\mathcal{L}^R_{02})+\\
&2k\mathcal{M}^I_{02}p_2(p_2-2a_2)-\mathcal{F}^R_{02}+k\mathcal{M}^I_{02}-2\mathcal{M}^R_{02}+\frac{1}{2}\Bigg\}\sin(\phi_2-\psi_2),
\end{aligned}\tag{C.157}$$

$$\begin{aligned}
F_{p2pd} = &-\Bigg\{\pi\Bigg[\left(\frac{1}{2}-a_1\right)k\Bigg[\mathcal{F}^R_{01}+\mathcal{F}^R_{02}f_\Gamma+4p_2\left(f_\Gamma\mathcal{M}^R_{02}-\frac{\mathcal{I}_\gamma}{2}+\mathcal{M}^R_{01}\right)+\\
&p_2^2(f_\Gamma\mathcal{L}^R_{02}+\mathcal{L}^R_{01})\Bigg]+4p_2\left(\frac{1}{4}k((a_1-1)f_\Gamma+\mathcal{I}_{\gamma,2})+f_\Gamma\mathcal{M}^I_{02}+\mathcal{M}^I_{01}\right)+\\
&\mathcal{F}^I_{01}+\mathcal{F}^I_{02}f_\Gamma+p_2^2(f_\Gamma\mathcal{L}^I_{02}-\mathcal{I}_\gamma k+\mathcal{L}^I_{01})-\frac{\mathcal{I}_{\gamma,3}k}{3}\Bigg]+\frac{1}{2}k(\mathcal{F}^R_{02}f_{\Gamma\alpha}+\mathcal{I}_{\gamma\alpha,2})-\\
&kp_2\left[f_{\Gamma\alpha}\left(-\frac{\mathcal{L}^R_{02}p_2}{2}-2\mathcal{M}^R_{02}+\frac{1}{2}\right)+\mathcal{I}_{\gamma\alpha}\right]\Bigg\}\cos(\varphi+\psi_2-\phi_1)+\\
&\Bigg\{\pi\Bigg[-\left(\frac{1}{2}-a_1\right)k\Bigg(\mathcal{F}^I_{01}+\mathcal{F}^I_{02}f_\Gamma-p_2^2(-f_\Gamma\mathcal{L}^I_{02}+\mathcal{I}_\gamma k-\mathcal{L}^I_{01})+\\
&p_2\left(-\frac{f_\Gamma k}{2}+4f_\Gamma\mathcal{M}^I_{02}+\mathcal{I}_{\gamma,2}k+4\mathcal{M}^I_{01}\right)-\frac{\mathcal{I}_{\gamma,3}k}{3}\Bigg)+\mathcal{F}^R_{01}+\mathcal{F}^R_{02}f_\Gamma+\\
&2p_2\left(\frac{p_2}{2}(f_\Gamma\mathcal{L}^R_{02}+\mathcal{L}^R_{01})+2(f_\Gamma\mathcal{M}^R_{02}+\mathcal{M}^R_{01})-\frac{f_\Gamma}{2}-\mathcal{I}_\gamma\right)\Bigg]+\frac{k}{2}\left(\frac{\mathcal{I}_{\gamma\alpha,3}k}{3}-\mathcal{F}^I_{02}f_{\Gamma\alpha}\right)+\\
&kp_2\left[f_{\Gamma\alpha}\left(\frac{k}{4}-\frac{\mathcal{L}^I_{02}p_2}{2}-2\mathcal{M}^I_{02}\right)+\frac{k}{2}(\mathcal{I}_{\gamma\alpha}p_2-\mathcal{I}_{\gamma\alpha,2})\right]\Bigg\}\sin(\varphi+\psi_2-\phi_1),
\end{aligned}\tag{C.158}$$

$$
\begin{aligned}
F_{p3pd} = &\Biggl\{ \pi \biggl[(1-2p_1) \biggl(2f_\Gamma \biggl(\frac{a_2 \mathcal{L}_{02}^I}{2} + \mathcal{M}_{02}^I \biggr) - a_2 \mathcal{I}_\gamma k + a_2 \mathcal{L}_{01}^I + \frac{\mathcal{I}_{\gamma,2} k}{2} + 2\mathcal{M}_{01}^I \biggr) + \\
& k \biggl((p_1-1)p_1 + \frac{1}{2} \biggr) \biggl(2f_\Gamma \biggl(\frac{a_2 \mathcal{L}_{02}^R}{2} + \mathcal{M}_{02}^R \biggr) + a_2 \mathcal{L}_{01}^R - \mathcal{I}_\gamma + 2\mathcal{M}_{01}^R \biggr) - \frac{k}{2} f_\Gamma (p_1-1)^2 \biggr] - \\
& k \biggl(-a_2 \mathcal{L}_{02}^R - 2\mathcal{M}_{02}^R + \frac{1}{2} \biggr) \biggl(\frac{f_{\Gamma\delta}}{2} - f_{\Gamma\alpha} p_1 \biggr) + f_{\Gamma\alpha} \biggl(a_2 \mathcal{L}_{02}^I - \frac{k}{4} + 2\mathcal{M}_{02}^I \biggr) + \\
& k \biggl(-a_2 \mathcal{I}_{\gamma\alpha} + \mathcal{I}_{\gamma\alpha} p_1 + \frac{\mathcal{I}_{\gamma\alpha,2}}{2} - \frac{\mathcal{I}_{\gamma\delta}}{2} \biggr) \Biggr\} \cos(\varphi - \psi_1 + \phi_2) + \\
& \Biggl\{ \pi \biggl[k \biggl((p_1-1)p_1 + \frac{1}{2} \biggr) \biggl(f_\Gamma \biggl(a_2 \mathcal{L}_{02}^I - \frac{k}{4} + 2\mathcal{M}_{02}^I \biggr) + a_2 (\mathcal{L}_{01}^I - \mathcal{I}_\gamma k) + \frac{\mathcal{I}_{\gamma,2} k}{2} + \\
& 2\mathcal{M}_{01}^I \biggr) + (1-2p_1) \biggl(f_\Gamma (-(a_2 \mathcal{L}_{02}^R + 2\mathcal{M}_{02}^R)) - (a_2 \mathcal{L}_{01}^R + 2\mathcal{M}_{01}^R) + \frac{f_\Gamma}{2} + \mathcal{I}_\gamma \biggr) \biggr] + \\
& k (a_2 \mathcal{L}_{02}^I + 2\mathcal{M}_{02}^I) \biggl(\frac{f_{\Gamma\delta}}{2} - f_{\Gamma\alpha} p_1 \biggr) + f_{\Gamma\alpha} \biggl(-a_2 \mathcal{L}_{02}^R - 2\mathcal{M}_{02}^R + \frac{1}{2} \biggr) + \\
& \mathcal{I}_{\gamma\alpha} \left(a_2 k^2 p_1 + 1 \right) + \frac{1}{2} k^2 \biggl(-a_2 \mathcal{I}_{\gamma\delta} - \mathcal{I}_{\gamma\alpha,2} p_1 + \frac{\mathcal{I}_{\gamma\delta,2}}{2} \biggr) + \\
& \frac{k^2}{4} \biggl(f_{\Gamma\alpha} p_1 + \frac{f_{\Gamma\delta}}{2} \biggr) \Biggr\} \sin(\varphi - \psi_1 + \phi_2). \qquad \text{(C.159)}
\end{aligned}
$$

BIBLIOGRAPHY

Akhtar, Imran, Rajat Mittal, George V. Lauder, and Elliot Drucker (2007). “Hydrodynamics of a biologically inspired tandem flapping foil configuration.” In: *Theoretical and Computational Fluid Dynamics* 21.3, pp. 155–170. issn: 09354964. doi: 10.1007/s00162-007-0045-2.

Alaminos-Quesada, J. and R. Fernandez-Feria (2017). “Effect of the angle of attack on the transient lift during the interaction of a vortex with a flat plate. Potential theory and experimental results.” In: *Journal of Fluids and Structures* 74, pp. 130–141. doi: 10.1016/j.jfluidstructs.2017.07.013.

Alben, Silas (2008). “Optimal flexibility of a flapping appendage in an inviscid fluid.” In: *Journal of Fluid Mechanics* 614, 355–380. doi: 10.1017/S0022112008003297.

Alben, Silas (2009). “Wake-mediated synchronization and drafting in coupled flags.” In: *Journal of Fluid Mechanics* 641, p. 489.

Alexander, David E (1984). “Unusual phase relationships between the forewings and hindwings in flying dragonflies.” In: *Journal of Experimental Biology* 109.1, pp. 379–383.

Anderson, JM, K Streitlien, DS Barrett, and MS Triantafyllou (1998). “Oscillating foils of high propulsive efficiency.” In: *Journal of Fluid mechanics* 360, pp. 41–72.

Arranz, G., O. Flores, and M. Garcia-Villalba (2020). “Three-dimensional effects on the aerodynamic performance of flapping wings in tandem configuration.” In: *Journal of Fluids and Structures* 94, p. 102893.

Ascher, U. M., S. J. Ruuth, and B. T.R. Wetton (1995). “Implicit-explicit methods for time-dependent partial differential equations.” In: *SIAM Journal on Numerical Analysis* 32.3, pp. 797–823.

Azuma, A. and T. Watanabe (1988). “Flight Performance of a Dragonfly.” In: *Journal of Experimental Biology* 137, pp. 221–252. issn: 0022-0949.

Baik, Yeon Sik, Luis P Bernal, Kenneth Granlund, and Michael V Ol (2012). “Unsteady force generation and vortex dynamics of pitching and plunging aerofoils.” In: *Journal of Fluid Mechanics* 709, pp. 37–68.

Bajec, Iztok Lebar and Frank H. Heppner (2009). “Organized flight in birds.” In: *Animal Behaviour* 78.4, pp. 777–789. issn: 00033472. doi: 10.1016/j.anbehav.2009.07.007.

Booth Jr, Earl R (1990). “Experimental observations of two-dimensional blade-vortex interaction.” In: *AIAA journal* 28.8, pp. 1353–1359.

Bosch, Helmut (1978). “Interfering Airfoils in Two-Dimensional Unsteady, Incompressible Flow.” In: *AGARD Tech Rept*.

Boschitsch, Birgitt M., Peter A. Dewey, and Alexander J. Smits (2014). “Propulsive performance of unsteady tandem hydrofoils in an in-line configuration.” In: *Physics of Fluids* 26.5, p. 051901.

Bouard, R. and M. Coutanceau (1980). “The early stage of development of the wake behind an impulsively started cylinder for $40 < \mathrm{Re} < 10^4$.” In: *Journal of Fluid Mechanics* 101.3, pp. 583–607. issn: 14697645.

Breder Jr, CM (1926). “The locomotion of fishes.” In: *Zoologica* 4, pp. 159–291.

Briley, W. Roger (1971). “A numerical study of laminar separation bubbles using the Navier-Stokes equations.” In: *Journal of Fluid Mechanics* 47.4, pp. 713–736. issn: 14697645. doi: 10.1017/S0022112071001332.

Broering, Timothy M. and Yong Sheng Lian (2012). "The effect of phase angle and wing spacing on tandem flapping wings." In: *Acta Mechanica Sinica/Lixue Xuebao* 28.6, pp. 1557–1571. ISSN: 16143116. DOI: 10.1007/s10409-012-0210-8.

Broering, Timothy M and Yongsheng Lian (2015). "Numerical study of tandem flapping wing aerodynamics in both two and three dimensions." In: *Computers & Fluids* 115, pp. 124–139.

Broering, Timothy M., Yongsheng Lian, and William Henshaw (2012). "Numerical investigation of energy extraction in a tandem flapping wing configuration." In: *AIAA Journal* 50.11, pp. 2295–2307. ISSN: 00011452. DOI: 10.2514/1.J051104.

Brown, C.E. and W.H. Michael (1954). "Effect of leading-edge separation on the lift of a delta wing." In: *Journal of the Aeronautical Sciences* 21.10, pp. 690–694.

Butcher, J. C. (1964). "On Runge-Kutta processes of high order." In: *Journal of the Australian Mathematical Society* 4.2, 179–194. DOI: 10.1017/S1446788700023387.

Butkov, E. and G. Sposito (1969). "Mathematical Physics." In: *Physics Today*. ISSN: 0031-9228. DOI: 10.1063/1.3035806.

Chang, X., L. Zhang, and X. He (2012). "Numerical study of the thunniform mode of fish swimming with different Reynolds number and caudal fin shape." In: *Computers and Fluids* 68, pp. 54–70. ISSN: 00457930. DOI: 10.1016/j.compfluid.2012.08.004.

Clements, RR (1973). "An inviscid model of two-dimensional vortex shedding." In: *Journal of Fluid Mechanics* 57.2, pp. 321–336.

Cong, L., B. Teng, and L. Cheng (2020). "Hydrodynamic behavior of two-dimensional tandem-arranged flapping flexible foils in uniform flow." In: *Physics of Fluids* 32.2, p. 021903. ISSN: 10897666. DOI: 10.1063/1.5133794.

Cordes, Ulrike, G. Kampers, T. Meißner, C. Tropea, J. Peinke, and M. Hölling (2017). "Note on the limitations of the Theodorsen and Sears functions." In: *Journal of Fluid Mechanics* 811, R1. DOI: 10.1017/jfm.2016.780.

DeVoria, Adam C and Kamran Mohseni (2017). "On the mechanism of high-incidence lift generation for steadily translating low-aspect-ratio wings." In: *Journal of Fluid Mechanics* 813, pp. 110–126.

Dewey, Peter A., Birgitt M. Boschitsch, Keith W. Moored, Howard A. Stone, and Alexander J. Smits (2013). "Scaling laws for the thrust production of flexible pitching panels." In: *Journal of Fluid Mechanics* 732, pp. 29–46. ISSN: 00221120. DOI: 10.1017/jfm.2013.384.

Dickinson, Michael H and Karl G Gotz (1993). "Unsteady aerodynamic performance of model wings at low Reynolds numbers." In: *Journal of experimental biology* 174.1, pp. 45–64.

Dong, Gen-Jin and Xi-Yun Lu (2007). "Characteristics of flow over traveling wavy foils in a side-by-side arrangement." In: *Physics of fluids* 19.5, p. 057107.

Ellington, C. P. (1984). "The aerodynamics of hovering insect flight. IV. Aerodynamic mechanisms." In: *Philosophical Transactions of the Royal Society of London. B, Biological Sciences* 305.1122, pp. 79–113.

Ellington, C. P., C. Van Den Berg, A. P. Willmott, and A. LR Thomas (1996). "Leading-edge vortices in insect flight." In: *Nature* 384.6610, pp. 626–630.

Eloy, C. (2013). "On the best design for undulatory swimming." In: *Journal of Fluid Mechanics* 717, pp. 48–89. ISSN: 00221120. DOI: 10.1017/jfm.2012.561.

Eloy, C. and L. Schouveiler (2011). "Optimisation of two-dimensional undulatory swimming at high Reynolds number." In: *International Journal of Non-Linear Mechanics* 46.4, pp. 568–576. ISSN: 00207462. DOI: 10.1016/j.ijnonlinmec.2010.12.007.

Fernandez-Feria, R (2016). "Linearized propulsion theory of flapping airfoils revisited." In: *Physical Review Fluids* 1.8, p. 084502.

Fernandez-Feria, R (2017). “Note on optimum propulsion of heaving and pitching airfoils from linear potential theory.” In: *Journal of Fluid Mechanics* 826, pp. 781–796.

Fernandez-Feria, R. and J. Alaminos-Quesada (2018). “Unsteady thrust, lift and moment of a two-dimensional flapping thin airfoil in the presence of leading-edge vortices: a first approximation from linear potential theory.” In: *Journal of Fluid Mechanics* 851, pp. 344–373. doi: 10.1017/jfm.2018.505.

Fernandez-Feria, R. and E. Sanmiguel-Rojas (2019). “Comparison of aerodynamic models for two-dimensional pitching foils with experimental data.” In: *Physics of Fluids* 31.5, p. 057104. issn: 10897666. doi: 10.1063/1.5096337.

Floryan, D. and C. W. Rowley (2018). “Clarifying the relationship between efficiency and resonance for flexible inertial swimmers.” In: *Journal of Fluid Mechanics* 853, pp. 271–300. issn: 14697645. doi: 10.1017/jfm.2018.581. arXiv: 1807.07499.

Ford, CW Pitt and Holger Babinsky (2013). “Lift and the leading-edge vortex.” In: *Journal of Fluid Mechanics* 720, pp. 280–313.

Garrick, I. E. (1938). “On some reciprocal relations in the theory of nonstationary flows.” In: 629, pp. 347–350.

Garrick, I.E. et al. (1936). “Propulsion of a flapping and oscillating airfoil.” In: *Report National Advisory Committee for Aeronautics, NACA Report* 567, pp. 419–427.

Gong, Wu Qi, Bo Bo Jia, and Guang Xi (2015). “Experimental study on mean thrust of two plunging wings in tandem.” In: *AIAA Journal* 53.6, pp. 1693–1705. issn: 00011452. doi: 10.2514/1.J053452.

Gong, Wu Qi, Bo Bo Jia, and Guang Xi (2016). “Experimental study on instantaneous thrust and lift of two plunging wings in tandem.” In: *Experiments in Fluids* 57.1, pp. 1–11. issn: 07234864. doi: 10.1007/s00348-015-2096-2.

Gonzalo, A., G. Arranz, M. Moriche, M. Garcia-Villalba, and O. Flores (2018). “From flapping to heaving: A numerical study of wings in forward flight.” In: *Journal of Fluids and Structures* 83, pp. 293–309. issn: 10958622. doi: 10.1016/j.jfluidstructs.2018.09.006.

Graham, JMR (1983). “The lift on an aerofoil in starting flow.” In: *Journal of Fluid Mechanics* 133, pp. 413–425.

Graham, William Richard, CW Pitt Ford, and Holger Babinsky (2017). “An impulse-based approach to estimating forces in unsteady flow.” In: *Journal of Fluid Mechanics* 815, pp. 60–76.

Heathcote, S. and I. Gursul (2007). “Flexible flapping airfoil propulsion at low reynolds numbers.” In: *AIAA Journal* 45.5, pp. 1066–1079. issn: 00011452. doi: 10.2514/1.25431.

Heathcote, S., D Martin, and I Gursul (2004). “Flexible flapping airfoil propulsion at zero freestream velocity.” In: *AIAA journal* 42.11, pp. 2196–2204.

Hemati, Maziar S, Jeff D Eldredge, and Jason L Speyer (2014). “Improving vortex models via optimal control theory.” In: *Journal of Fluids and Structures* 49, pp. 91–111.

Hoover, A. P., R. Cortez, E. D. Tytell, and L. J. Fauci (2018). “Swimming performance, resonance and shape evolution in heaving flexible panels.” In: *Journal of Fluid Mechanics* 847, pp. 386–416. issn: 14697645. doi: 10.1017/jfm.2018.305.

Howe, M. S. (2003). *Theory of vortex sound*. Vol. 33. Cambridge university press.

Howe, M.S. (1996). “Emendation of the Brown & Michael equation, with application to sound generation by vortex motion near a half-plane.” In: *Journal of Fluid Mechanics* 329, pp. 89–101.

Huera-Huarte, F. J. (2018a). “On the Impulse Produced by Chordwise Flexible Pitching Foils in a Quiescent Fluid.” In: *Journal of Fluids Engineering, Transactions of the ASME* 140.4, p. 041206. issn: 1528901X. doi: 10.1115/1.4038168.

Huera-Huarte, F. J. (2018b). “Propulsive performance of a pair of pitching foils in staggered configurations.” In: *Journal of Fluids and Structures* 81, pp. 1–13.

Jenson, VG (1959). “Viscous flow round a sphere at low Reynolds numbers (< 40).” In: *Proceedings of the Royal Society of London. Series A. Mathematical and Physical Sciences* 249.1258, pp. 346–366.

Jones, K and M Platzer (1999). “An experimental and numerical investigation of flapping-wing propulsion.” In: *37th aerospace sciences meeting and exhibit*, p. 995.

Jones, Marvin A (2003). “The separated flow of an inviscid fluid around a moving flat plate.” In: *Journal of Fluid Mechanics* 496, pp. 405–441.

Kang, C.-K., H. Aono, C. E. S. Cesnik, and W. Shyy (2011). “Effects of flexibility on the aerodynamic performance of flapping wings.” In: *Journal of Fluid Mechanics* 689, 32–74. DOI: 10.1017/jfm.2011.428.

Kármán, Th H von and William R Sears (1938). “Airfoil theory for non-uniform motion.” In: *Journal of the Aeronautical Sciences* 5.10, pp. 379–390.

Katz, J and D Weihs (1978). “Hydrodynamic propulsion by large amplitude oscillation of an airfoil with chordwise flexibility.” In: *Journal of Fluid Mechanics* 88.3, pp. 485–497.

Koumoutsakos, P. and A. Leonard (1995). “High-Resolution simulations of the flow around an impulsively started cylinder using vortex methods.” In: *Journal of Fluid Mechanics* 296, pp. 1–38. ISSN: 14697645. DOI: 10.1017/S0022112095002059.

Kurt, Melike and Keith W Moored (2018). “Flow interactions of two-and three-dimensional networked bio-inspired control elements in an in-line arrangement.” In: *Bioinspiration & biomimetics* 13.4, p. 045002.

Lan, C. E. (1979). “The unsteady quasi-vortex-lattice method with applications to animal propulsion.” In: *Journal of Fluid Mechanics* 93.4, pp. 747–765. ISSN: 14697645. DOI: 10.1017/S0022112079002019.

Lan, SL and M Sun (2001). “Aerodynamic interactions of two airfoils in unsteady motion.” In: *Acta mechanica* 150.1-2, pp. 39–51.

Le, T. Q., J. H. Ko, D. Byun, S. H. Park, and H. C. Park (2010). “Effect of Chord Flexure on Aerodynamic Performance of a Flapping Wing.” In: *Journal of Bionic Engineering* 7.1, pp. 87–94. ISSN: 16726529. DOI: 10.1016/S1672-6529(09)60196-7.

Lehmann, Fritz Olaf (2009). “Wing-wake interaction reduces power consumption in insect tandem wings.” In: *Experiments in Fluids* 46.5, pp. 765–775. ISSN: 07234864. DOI: 10.1007/s00348-008-0595-0.

Li, Juan and Zi-Niu Wu (2015). “Unsteady lift for the Wagner problem in the presence of additional leading/trailing edge vortices.” In: *Journal of Fluid Mechanics* 769, 182–217. DOI: 10.1017/jfm.2015.118.

Li, Juan and Zi-Niu Wu (2016). “A vortex force study for a flat plate at high angle of attack.” In: *Journal of Fluid Mechanics* 801, 222–249. DOI: 10.1017/jfm.2016.349.

Lighthill, M. J. (1969). “Hydromechanics of aquatic animal propulsion.” In: *Annual review of fluid mechanics* 1.1, pp. 413–446. DOI: 10.1146/annurev.fl.01.010169.002213.

Lighthill, M. J. (1970). “Aquatic animal propulsion of high hydromechanical efficiency.” In: *Journal of Fluid Mechanics* 44.2, pp. 265–301. ISSN: 14697645.

Lighthill, M. J. (1975). *Mathematical biofluiddynamics*. Society for Industrial and Applied Mathematics.

Lin, C. L., D. W. Pepper, and S. C. Lee (1976). “Numerical Methods for Separated Flow Solutions around a Circular Cylinder.” In: *AIAA Journal* 14.7, pp. 900–907. ISSN: 0001-1452. DOI: 10.2514/3.61431. URL: http://arc.aiaa.org/doi/10.2514/3.61431.

Lin, Xingjian, Jie Wu, Tongwei Zhang, and Liming Yang (2019). “Phase difference effect on collective locomotion of two tandem autopropelled flapping foils.” In: *Physical Review Fluids* 4.5, p. 054101.

Loc, Ta Phuoc and R. Bouard (1985). "Numerical solution of the early stage of the unsteady viscous flow around a circular cylinder: A comparison with experimental visualization andmeasurements." In: *Journal of fluid Mechanics* 160.1985, pp. 93–117. ISSN: 14697645. DOI: 10.1017/S0022112085003408.

Lua, K. B., H. Lu, X. H. Zhang, T. T. Lim, and K. S. Yeo (2016). "Aerodynamics of two-dimensional flapping wings in tandem configuration." In: *Physics of Fluids* 28.12, p. 121901. ISSN: 10897666. DOI: 10.1063/1.4971859.

Mackowski, A. W. and C. H. K. Williamson (2015). "Direct measurement of thrust and efficiency of an airfoil undergoing pure pitching." In: *Journal of Fluid Mechanics* 765, 524–543. DOI: 10.1017/jfm.2014.748.

Mackowski, A. W. and C. H. K. Williamson (Jan. 2017). "Effect of pivot location and passive heave on propulsion from a pitching airfoil." In: *Phys. Rev. Fluids* 2 (1), p. 013101. DOI: 10.1103/PhysRevFluids.2.013101. URL: https://link.aps.org/doi/10.1103/PhysRevFluids.2.013101.

Maertens, Audrey P, Amy Gao, and Michael S Triantafyllou (2017). "Optimal undulatory swimming for a single fish-like body and for a pair of interacting swimmers." In: *Journal of Fluid Mechanics* 813, pp. 301–345.

Martín-Alcántara, A., R. Fernandez-Feria, and E. Sanmiguel-Rojas (2015). "Vortex flow structures and interactions for the optimum thrust efficiency of a heaving airfoil at different mean angles of attack." In: *Physics of Fluids* 27.7, p. 073602. DOI: 10.1063/1.4926622. URL: https://doi.org/10.1063/1.4926622.

Martínez-Muriel, C. and O. Flores (2020). "Analysis of vortical gust impact on airfoils at low Reynolds number." In: *Journal of Fluids and Structures* 99, p. 103138. ISSN: 0889-9746. DOI: 10.1016/j.jfluidstructs.2020.103138. URL: http://www.sciencedirect.com/science/article/pii/S0889974620306071.

Martín-Alcántara, A. and R. Fernandez-Feria (2019). "Assessment of two vortex formulations for computing forces of a flapping foil at high Reynolds numbers." In: *Physical Review Fluids* 4.2, p. 024702. ISSN: 2469990X. DOI: 10.1103/PhysRevFluids.4.024702.

Maxworthy, T. (2007). "The formation and maintenance of a leading-edge vortex during the forward motion of an animal wing." In: *Journal of Fluid Mechanics* 587, 471–475. DOI: 10.1017/S0022112007007616.

McGowan, Gregory Z., Kenneth Granlund, Michael V. Ol, Ashok Gopalarathnam, and Jack R. Edwards (2011). "Investigations of Lift-Based Pitch-Plunge Equivalence for Airfoils at Low Reynolds Numbers." In: *AIAA Journal* 49.7, pp. 1511–1524. DOI: 10.2514/1.J050924. URL: https://doi.org/10.2514/1.J050924.

Mehra, Mani and Kuldip Singh Patel (2017). "Algorithm 986: A suite of compact finite difference schemes." In: *ACM Transactions on Mathematical Software* 44.2. ISSN: 15577295. DOI: 10.1145/3119905.

Michelin, Sébastien and Stefan G. Llewellyn Smith (2009). "An unsteady point vortex method for coupled fluid–solid problems." In: *Theoretical and Computational Fluid Dynamics* 23.2, pp. 127–153.

Milne-Thomson, Louis Melville (1996). *Theoretical hydrodynamics*. Courier Corporation.

Minotti, F. O. (Nov. 2002). "Unsteady two-dimensional theory of a flapping wing." In: *Phys. Rev. E* 66 (5), p. 051907. DOI: 10.1103/PhysRevE.66.051907. URL: https://link.aps.org/doi/10.1103/PhysRevE.66.051907.

Moore, M. Nicholas J. (2014). "Analytical results on the role of flexibility in flapping propulsion." In: *Journal of Fluid Mechanics* 757, pp. 599–612. ISSN: 14697645. DOI: 10.1017/jfm.2014.533.

Moore, M. Nicholas J. (2015). "Torsional spring is the optimal flexibility arrangement for thrust production of a flapping wing." In: *Physics of Fluids* 27.9, p. 091701. ISSN: 10897666. DOI: 10.1063/1.4930235.

Moore, M. Nicholas J. (2017). "A fast Chebyshev method for simulating flexible-wing propulsion." In: *Journal of Computational Physics* 345, pp. 792–817. ISSN: 10902716. DOI: 10.1016/j.jcp.2017.05.052. arXiv: 1612.08448.

Muscutt, L. E., G. Dyke, G. D. Weymouth, D. Naish, C. Palmer, and B. Ganapathisubramani (2017). "The four-flipper swimming method of plesiosaurs enabled efficient and effective locomotion." In: *Proceedings of the Royal Society B: Biological Sciences* 284.1861, p. 20170951.

Muscutt, L. E., G. D. Weymouth, and B. Ganapathisubramani (2017). "Performance augmentation mechanism of in-line tandem flapping foils." In: *Journal of Fluid Mechanics* 827, pp. 484–505. ISSN: 14697645. DOI: 10.1017/jfm.2017.457.

Nagai, Hiroto, Koki Fujita, and Masahiko Murozono (2019). "Experimental Study on Forewing–Hindwing Phasing in Hovering and Forward Flapping Flight." In: *AIAA journal* 57.9, pp. 3779–3790.

Newbolt, Joel W., Jun Zhang, and Leif Ristroph (2019). "Flow interactions between uncoordinated flapping swimmers give rise to group cohesion." In: *Proceedings of the National Academy of Sciences of the United States of America* 116.7, pp. 2419–2424. ISSN: 10916490. DOI: 10.1073/pnas.1816098116.

Newman, J. N. (1977). *Marine Hydrodynamics*. MIT Press.

Olivier, Mathieu and Guy Dumas (2016). "A parametric investigation of the propulsion of 2D chordwise-flexible flapping wings at low Reynolds number using numerical simulations." In: *Journal of Fluids and Structures* 63, pp. 210–237.

Olver, Frank WJ, Daniel W Lozier, Ronald F Boisvert, and Charles W Clark (2010). *NIST handbook of mathematical functions hardback and CD-ROM*. Cambridge university press.

Ortega-Casanova, J. and R. Fernandez-Feria (2016). "Analysis of the aerodynamic interaction between two plunging plates in tandem at low Reynolds number for maximum propulsive efficiency." In: *Journal of Fluids and Structures* 63, pp. 351–373. ISSN: 10958622. DOI: 10.1016/j.jfluidstructs.2016.03.011.

Ortega-Casanova, J. and R. Fernandez-Feria (2019). "Maximum propulsive efficiency of two pitching and plunging plates in tandem at low Reynolds number." In: *International Journal of Numerical Methods for Heat & Fluid Flow* 29.11, pp. 4013–4033.

Paraz, F., L. Schouveiler, and C. Eloy (2016). "Thrust generation by a heaving flexible foil: Resonance, nonlinearities, and optimality." In: *Physics of Fluids* 28.1, p. 011903. ISSN: 10897666. DOI: 10.1063/1.4939499.

Park, Sung Goon and Hyung Jin Sung (2018). "Hydrodynamics of flexible fins propelled in tandem, diagonal, triangular and diamond configurations." In: *Journal of Fluid Mechanics* 840, p. 154.

Pederzani, J. and H. Haj-Hariri (2006). "Numerical analysis of heaving flexible airfoils in a viscous flow." In: *AIAA Journal* 44.11, pp. 2773–2779. ISSN: 00011452. DOI: 10.2514/1.21203.

Pelletier, A. and T. J Mueller (2000). "Low Reynolds number aerodynamics of low-aspect-ratio, thin/flat/cambered-plate wings." In: *Journal of aircraft* 37.5, pp. 825–832.

Peng, Di and James W Gregory (2015). "Vortex dynamics during blade-vortex interactions." In: *Physics of Fluids* 27.5, p. 053104.

Peng, Di and James W Gregory (2017). "Asymmetric distributions in pressure/load fluctuation levels during blade-vortex interactions." In: *Journal of Fluids and Structures* 68, pp. 58–71.

Platzer, M. F., K. D. Jones, J. Young, and J. C.S. Lai (2008). “Flapping-wing aerodynamics: Progress and challenges.” In: *AIAA Journal* 46.9, pp. 2136–2149. issn: 00011452. doi: 10.2514/1.29263.

Poling, David R, Leo Dadone, and Demetri P Telionis (1989). “Blade-vortex interaction.” In: *AIAA journal* 27.6, pp. 694–699.

Polyanin, A. (1998). *Handbook of Integral Equations*. doi: 10.1201/9781420050066.

Prempraneerach, P, FS Hover, and Michael S Triantafyllou (2003). “The effect of chordwise flexibility on the thrust and efficiency of a flapping foil.” In: *Proc. 13th Int. Symp. on Unmanned Untethered Submersible Technology: special session on bioengineering research related to autonomous underwater vehicles, New Hampshire*. Vol. 152, pp. 152–170.

Pullin, D. I. and Z. Jane Wang (2004). “Unsteady forces on an accelerating plate and application to hovering insect flight.” In: *Journal of Fluid Mechanics* 509, 1–21. doi: 10.1017/S0022112004008821.

Quinn, Daniel B, George V Lauder, and Alexander J Smits (2015). “Maximizing the efficiency of a flexible propulsor using experimental optimization.” In: *Journal of Fluid Mechanics* 767, pp. 430–448.

Ramananarivo, S., F. Fang, A. Oza, J. Zhang, and L. Ristroph (2016). “Flow interactions lead to orderly formations of flapping wings in forward flight.” In: *Physical Review Fluids* 1.7, p. 071201. issn: 2469990X. doi: 10.1103/PhysRevFluids.1.071201.

Ramananarivo, S., R. Godoy-Diana, and B. Thiria (2011). “Rather than resonance, flapping wing flyers may play on aerodynamics to improve performance.” In: *Proceedings of the National Academy of Sciences of the United States of America*. issn: 10916490. doi: 10.1073/pnas.1017910108. arXiv: 1011.4688.

Ramesh, Kiran, Ashok Gopalarathnam, Jack R. Edwards, Michael V. Ol, and Kenneth Granlund (2013). “An unsteady airfoil theory applied to pitching motions validated against experiment and computation.” In: *Theoretical and Computational Fluid Dynamics* 27.6, pp. 843–864.

Rival, David, Roland Manejev, and Cam Tropea (2010). “Measurement of parallel blade–vortex interaction at low Reynolds numbers.” In: *Experiments in Fluids* 49.1, pp. 89–99.

Rockwell, Donald (1998). “Vortex-body interactions.” In: *Annual review of fluid mechanics* 30.1, pp. 199–229.

Ryu, J., J. Yang, S. G. Park, and H. J. Sung (2020). “Phase-mediated locomotion of two self-propelled flexible plates in a tandem arrangement.” In: *Physics of Fluids* 32.4, p. 041901. issn: 10897666. doi: 10.1063/5.0005489.

Saffman, P. G. (1992). *Vortex Dynamics*. Cambridge University Press.

Saffman, P. G. and J. S. Sheffield (1977). “Flow over a wing with an attached free vortex.” In: *Studies in Applied Mathematics* 57.2, pp. 107–117.

Schmidt, Wilhelm (1965). “Der wellpropeller ein neuer antrieb fur wasser-land-und luftfahrzeuge.” In: *Zeitschrift fur Flugwissenschaften* 13.12, p. 472.

Senturk, Utku and Alexander J. Smits (2019). “Reynolds number scaling of the propulsive performance of a pitching airfoil.” In: *AIAA Journal* 57.7, pp. 2663–2669. issn: 00011452. doi: 10.2514/1.J058371.

Shyy, W., H. Aono, S. K. Chimakurthi, P. Trizila, C-K Kang, C. ES Cesnik, and H. Liu (2010). “Recent progress in flapping wing aerodynamics and aeroelasticity.” In: *Progress in Aerospace Sciences* 46.7, pp. 284–327.

Shyy, W., H. Aono, C. Kang, and H. Liu (2013). *An Introduction to Flapping Wing Aerodynamics*. doi: 10.1017/cbo9781139583916.

Shyy, Wei and Hao Liu (2007). “Flapping Wings and Aerodynamic Lift: The Role of Leading-Edge Vortices.” In: *AIAA Journal* 45.12, pp. 2817–2819. doi: 10.2514/1.33205. url: https://doi.org/10.2514/1.33205.

Smits, A. J. (2019). “Undulatory and oscillatory swimming.” In: *Journal of Fluid Mechanics* 874, P1. doi: 10.1017/jfm.2019.284.

Spotz, William F. (1998). “Accuracy and performance of numerical wall boundary conditions for steady, 2D, incompressible streamfunction vorticity.” In: *International Journal for Numerical Methods in Fluids* 28.4, pp. 737–757. issn: 02712091.

Streitlien, Knut, George S Triantafyllou, and Michael S Triantafyllou (1996). “Efficient foil propulsion through vortex control.” In: *Aiaa journal* 34.11, pp. 2315–2319.

Sutmann, Godehard (2007). “Compact finite difference schemes of sixth order for the Helmholtz equation.” In: *Journal of Computational and Applied Mathematics* 203.1, pp. 15–31. issn: 03770427. doi: 10.1016/j.cam.2006.03.008.

Tanida, Yoshimichi (2003). “Locomotion by tandem and parallel wings.” In: *JSME International Journal, Series B: Fluids and Thermal Engineering* 46.2, pp. 244–249. issn: 13408054. doi: 10.1299/jsmeb.46.244.

Tchieu, Andrew A. and Anthony Leonard (2011). “A discrete-vortex model for the arbitrary motion of a thin airfoil with fluidic control.” In: *Journal of Fluids and Structures* 27.5, pp. 680 –693. issn: 0889-9746. doi: 10.1016/j.jfluidstructs.2011.02.008. url: http://www.sciencedirect.com/science/article/pii/S0889974611000260.

Theodorsen, Theodore (1935). *General theory of aerodynamic instability and the mechanism of flutter*. Tech. rep. No. 496, p. 24. doi: 10.1017/CBO9781107415324.004. arXiv: arXiv:1011.1669v3.

Thomas, A. LR, G. K. Taylor, R. B. Srygley, R. L. Nudds, and R. J. Bomphrey (2004). “Dragonfly flight: free-flight and tethered flow visualizations reveal a diverse array of unsteady lift-generating mechanisms, controlled primarily via angle of attack.” In: *Journal of Experimental Biology* 207.24, pp. 4299–4323.

Tsai, Hsieh-Chen and Tim Colonius (2015). “Coriolis Effect on Dynamic Stall in a Vertical Axis Wind Turbine.” In: *AIAA Journal* 54.1, pp. 216–226. issn: 0001-1452. doi: 10.2514/1.j054199.

Tuncer, Ismail H and Max F Platzer (1996). “Thrust generation due to airfoil flapping.” In: *AIAA journal* 34.2, pp. 324–331.

Tytell, E. D. and G. V. Lauder (2004). “The hydrodynamics of eel swimming: I. Wake structure.” In: *Journal of Experimental Biology* 207.11, pp. 1825–1841. issn: 00220949. doi: 10.1242/jeb.00968.

Tzezana, G. A. and K. S. Breuer (2019). “Thrust, drag and wake structure in flapping compliant membrane wings.” In: *Journal of Fluid Mechanics* 862, pp. 871–888. issn: 14697645. doi: 10.1017/jfm.2018.966.

Usherwood, James R and Fritz-Olaf Lehmann (2008). “Phasing of dragonfly wings can improve aerodynamic efficiency by removing swirl.” In: *Journal of The Royal Society Interface* 5.28, pp. 1303–1307.

Vogel, S. (1981). “Life in moving fluids: the physical biology of flow.” In: issn: 00220981. doi: 10.1016/0022-0981(96)02487-2.

Wang, Chengjie and Jeff D. Eldredge (2013). “Low-order phenomenological modeling of leading-edge vortex formation.” In: *Theoretical and Computational Fluid Dynamics* 27.5, pp. 577–598.

Wang, Shizhao, Guowei He, and Xing Zhang (2016). *Self-propulsion of flapping bodies in viscous fluids: Recent advances and perspectives*. doi: 10.1007/s10409-016-0578-y.

Wang, Z. J. and D. Russell (2007). "Effect of forewing and hindwing interactions on aerodynamic forces and power in hovering dragonfly flight." In: *Physical Review Letters* 99.14, p. 148101. issn: 00319007. doi: 10.1103/PhysRevLett.99.148101.

Wang, Z. Jane (2000). "Vortex shedding and frequency selection in flapping flight." In: *Journal of Fluid Mechanics* 410, 323–341. doi: 10.1017/S0022112099008071.

Wang, Z. Jane (2005). "Dissecting insect flight." In: *Annual Review of Fluid Mechanics* 37.1, pp. 183–210. doi: 10.1146/annurev.fluid.36.050802.121940. url: https://doi.org/10.1146/annurev.fluid.36.050802.121940.

Warkentin, Jonathan and James DeLaurier (2007). "Experimental aerodynamic study of tandem flapping membrane wings." In: *Journal of Aircraft* 44.5, pp. 1653–1661. issn: 00218669. doi: 10.2514/1.28160.

Weihs, D. (1973). "Hydromechanics of fish schooling." In: *Nature* 241.5387, pp. 290–291. issn: 00280836. doi: 10.1038/241290a0.

Wilder, MC and DP Telionis (1998). "Parallel blade–vortex interaction." In: *Journal of fluids and structures* 12.7, pp. 801–838.

Wu, J. C. (1981). "Theory for Aerodynamic Force and Moment in Viscous Flows." In: *AIAA Journal* 19.4, pp. 432–441. doi: 10.2514/3.50966. url: https://doi.org/10.2514/3.50966.

Wu, J.-Z., H.-Y. Ma, and M.-D. Zhou (2006). *Vorticity and Vortex Dynamics*. Springer.

Wu, T. Y. (1961). "Swimming of a waving plate." In: *Journal of Fluid Mechanics* 10.3, 321–344. doi: 10.1017/S0022112061000949.

Wu, T. Y. (1971a). "Hydromechanics of swimming propulsion. Part 1. Swimming of a two-dimensional flexible plate at variable forward speeds in an inviscid fluid." In: *Journal of Fluid Mechanics* 46.2, 337–355. doi: 10.1017/S0022112071000570.

Wu, T. Y. (1971b). "Hydromechanics of swimming propulsion. Part 2. Some optimum shape problems." In: *Journal of Fluid Mechanics* 46.3, 521–544.

Wu, T. Y. (2011). "Fish swimming and bird/insect flight." In: *Annual Review of Fluid Mechanics* 43, pp. 25–58.

Wu, T. Y., C. J. Brokaw, and C. Brennen (1975). *Swimming and Flying in Nature vol. 1 and 2*. Cambridge university press.

Xia, X. and K. Mohseni (2013). "Lift evaluation of a two-dimensional pitching flat plate." In: *Physics of Fluids* 25.9, p. 091901. doi: 10.1063/1.4819878. url: https://doi.org/10.1063/1.4819878.

Xia, X. and K. Mohseni (2017). "Unsteady aerodynamics and vortex-sheet formation of a two-dimensional airfoil." In: *Journal of Fluid Mechanics* 830, 439–478. doi: 10.1017/jfm.2017.513.

Yang, D., B. Pettersen, and Y. L. Xiong (2016). "Interactions between two flat plates at different positions in a current." In: *Ocean Engineering* 119, pp. 75–85. issn: 00298018. doi: 10.1016/j.oceaneng.2016.04.029.

Yükselen, M. A. and M. Z. Erim (1984). "A general iterative method to design Kármán-Trefftz and Joukowsky airfoils." In: *International Journal for Numerical Methods in Engineering* 20.7, pp. 1349–1360. issn: 10970207. doi: 10.1002/nme.1620200712.

Zannetti, Luca and Alexandre Gourjii (2014). "Two-vortex equilibrium in the flow past a flat plate at incidence." In: *Journal of fluid mechanics* 755, pp. 50–61.

Zhang, D., G. Pan, L. Chao, and Y. Zhang (2018). "Effects of Reynolds number and thickness on an undulatory self-propelled foil." In: *Physics of Fluids* 30.7, p. 071902. issn: 10897666. doi: 10.1063/1.5034439.

Zhang, Li Jeany and Jeff D. Eldredge (2009). "A viscous vortex particle method for deforming bodies with application to biolocomotion." In: *International Journal for Numerical Methods in Fluids* 59.12, pp. 1299–1320. issn: 02712091. doi: 10.1002/fld.1867.

Zheng, Yingying, Yanhua Wu, and Hui Tang (2016). "An experimental study on the forewing–hindwing interactions in hovering and forward flights." In: *International Journal of Heat and Fluid Flow* 59, pp. 62–73.

Zhu, Q. (2007). "Numerical simulation of a flapping foil with chordwise or spanwise flexibility." In: *AIAA Journal*. ISSN: 00011452. DOI: 10.2514/1.28565.

Ziada, S. and D. Rockwell (1982). "Vortex–leading-edge interaction." In: *Journal of Fluid Mechanics* 118, pp. 79–107.

DECLARACIÓN

El profesor Dr. Ramón Fernández Feria Catedrático de Universidad en el departamento de Ingeniería Mecánica, Térmica y de Fluidos de la Universidad de Málaga,

INFORMA:

Que el trabajo de investigación que se ha desarrollado durante la tesis doctoral de D. Javier Alaminos Quesada es original y las publicaciones que avalan esta tesis no han sido utilizadas en tesis anteriores.

Málaga, España, 2021

Dr. D. Ramón Fernández Feria

COLOPHON

Javier Alaminos Quesada: *Aerodynamic vortex interaction with a flapping foil and between multiple flapping foils, and its application to the design of aerial and aquatic small vehicles,* Ph.D Thesis, Universidad de Málaga © 2021.

Final version as of February 10, 2021.